

processes

Industrial Chemistry Reactions

Kinetics, Mass Transfer and Industrial Reactor Design

Edited by
Elio Santacesaria, Riccardo Tesser and Vincenzo Russo

Printed Edition of the Special Issue Published in *Processes*

Industrial Chemistry Reactions: Kinetics, Mass Transfer and Industrial Reactor Design

Industrial Chemistry Reactions: Kinetics, Mass Transfer and Industrial Reactor Design

Editors

Elio Santacesaria

Riccardo Tesser

Vincenzo Russo

MDPI • Basel • Beijing • Wuhan • Barcelona • Belgrade • Manchester • Tokyo • Cluj • Tianjin



Editors

Elio Santacesaria
Eurochem Engineering
Italy

Riccardo Tesser
University FEDERICO II
of Naples
Italy

Vincenzo Russo
University FEDERICO II
of Naples
Italy

Editorial Office

MDPI
St. Alban-Anlage 66
4052 Basel, Switzerland

This is a reprint of articles from the Special Issue published online in the open access journal *Processes* (ISSN 2227-9717) (available at: https://www.mdpi.com/journal/processes/special_issues/Industrial_Reactor_Design).

For citation purposes, cite each article independently as indicated on the article page online and as indicated below:

LastName, A.A.; LastName, B.B.; LastName, C.C. Article Title. <i>Journal Name</i> Year , Volume Number, Page Range.
--

ISBN 978-3-0365-4155-6 (Hbk)

ISBN 978-3-0365-4156-3 (PDF)

© 2022 by the authors. Articles in this book are Open Access and distributed under the Creative Commons Attribution (CC BY) license, which allows users to download, copy and build upon published articles, as long as the author and publisher are properly credited, which ensures maximum dissemination and a wider impact of our publications.

The book as a whole is distributed by MDPI under the terms and conditions of the Creative Commons license CC BY-NC-ND.

Contents

About the Editors	vii
Elio Santacesaria, Riccardo Tesser and Vincenzo Russo	
Special Issue on “Industrial Chemistry Reactions: Kinetics, Mass Transfer and Industrial Reactor Design”	
Reprinted from: <i>Processes</i> 2022 , <i>10</i> , 411, doi:10.3390/pr10020411	1
Somchart Chantasiriwan	
Modification of Conventional Sugar Juice Evaporation Process for Increasing Energy Efficiency and Decreasing Sucrose Inversion Loss	
Reprinted from: <i>Processes</i> 2020 , <i>8</i> , 765, doi:10.3390/pr8070765	7
Alessandro Rosengart, Carlo Pirola and Sofia Capelli	
Hydrogenation of <i>Trans,Trans</i> -Muconic Acid to Bio-Adipic Acid: Mechanism Identification and Kinetic Modelling	
Reprinted from: <i>Processes</i> 2020 , <i>8</i> , 929, doi:10.3390/pr8080929	19
Elio Santacesaria, Rosa Turco, Vincenzo Russo, Riccardo Tesser and Martino Di Serio	
Soybean Oil Epoxidation: Kinetics of the Epoxide Ring Opening Reactions	
Reprinted from: <i>Processes</i> 2020 , <i>8</i> , 1134, doi:10.3390/pr8091134	29
Nikhil H. Margi and Ganapati D. Yadav	
Design and Development of Novel Continuous Flow Stirred Multiphase Reactor: Liquid–Liquid–Liquid Phase Transfer Catalysed Synthesis of Guaiacol Glycidyl Ether	
Reprinted from: <i>Processes</i> 2020 , <i>8</i> , 1271, doi:10.3390/pr8101271	53
Tapio Salmi, Esko Tirronen, Johan Wärnå, Jyri-Pekka Mikkola, Dmitry Murzin and Valerie Eta	
A Robust Method for the Estimation of Kinetic Parameters for Systems Including Slow and Rapid Reactions—From Differential-Algebraic Model to Differential Model	
Reprinted from: <i>Processes</i> 2020 , <i>8</i> , 1552, doi:10.3390/pr8121552	69
Riccardo Tesser and Elio Santacesaria	
Revisiting the Role of Mass and Heat Transfer in Gas–Solid Catalytic Reactions	
Reprinted from: <i>Processes</i> 2020 , <i>8</i> , 1599, doi:10.3390/pr8121599	85
Kang Yu, Yumei Yong and Chao Yang	
Numerical Study on Bubble Rising in Complex Channels Saturated with Liquid Using a Phase-Field Lattice-Boltzmann Method	
Reprinted from: <i>Processes</i> 2020 , <i>8</i> , 1608, doi:10.3390/pr8121608	121
Linda Nikoshvili, Elena S. Bakhvalova, Alexey V. Bykov, Alexander I. Sidorov, Alexander L. Vasiliev, Valentina G. Matveeva, Mikhail G. Sulman, Valentin N. Sapunov and Liubov Kiwi-Minsker	
Study of Deactivation in Suzuki Reaction of Polymer-Stabilized Pd Nanocatalysts	
Reprinted from: <i>Processes</i> 2020 , <i>8</i> , 1653, doi:10.3390/pr8121653	147
Hee-Chul Yang, Hyeon-Oh Park, Kyu-Tae Park, Sung-Jun Kim, Hyung-Ju Kim, Hee-Chul Eun and Keunyoung Lee	
Development of Carbonization and a Relatively High-Temperature Halogenation Process for the Removal of Radionuclides from Spent Ion Exchange Resins	
Reprinted from: <i>Processes</i> 2021 , <i>9</i> , 96, doi:10.3390/pr9010096	161

Ravisut Vitidsant, Satoshi Kodama and Hidetoshi Sekiguchi Transesterification Using Ultrasonic Spray of Triolein Containing CaO Particles into Methanol Vapor in a 3-Phase Reactor Reprinted from: <i>Processes</i> 2021 , <i>9</i> , 181, doi:10.3390/pr9010181	177
Jasper Spitters, Jonathan C. Gonçalves, Rui P. V. Faria and Alírio E. Rodrigues Optimization of the Production of 1,1-Diethoxybutane by Simulated Moving Bed Reactor Reprinted from: <i>Processes</i> 2021 , <i>9</i> , 189, doi:10.3390/pr9020189	189
Zemeng Zhao, Zhibang Liu, Yang Xiang, Moses Arowo and Lei Shao Removal of Dissolved Oxygen from Water by Nitrogen Stripping Coupled with Vacuum Degassing in a Rotor–Stator Reactor Reprinted from: <i>Processes</i> 2021 , <i>9</i> , 1354, doi:10.3390/pr9081354	209

About the Editors

Elio Santacesaria

Elio Santacesaria, Professor, Chemistry Degree from the University of Pavia in 1966 with a Thesis developed under the guidance of the Nobel Prize-winning Giulio Natta. He worked as researcher at the Polytechnic of Milano from 1969 to 1986 developing studies in the fields of: chemistry of propellants, catalysis, kinetics, reactors design and simulation, and separation science. In 1986 he earned the chair of Industrial Chemistry at the University of Naples "FEDERICO II". He continued his research on almost all the above-mentioned research themes. Santacesaria had been National Coordinator of the research on "Colloid, Interphase and Surfactants" providing a great contribution to the improvement of the research efforts in these fields. He was the founder of GICI, the Italian Group of Colloid and Interphase Science of the Italian Chemical Society, and he has been the Coordinator of this Group for more than ten years (1985–1995). He has been the organizer of many national and international Congresses, workshops, and post-doctoral schools. He has been a member of the Scientific Committee of the Industrial Chemistry Division of the Italian Chemical Society for 10 years. Then, he was elected President of the Industrial Chemistry Division of the Italian Chemical Society for the period 2004–2006, renewed for the 2007–2009, and was a member of the Council as Past President in 2010–2012. He has been President of the Council of the Industrial Chemistry Degree Course from 1994 until 2009. He has collaborated with many Italian and foreign chemical industries. He published more than 260 papers in qualified journals and is the coauthor of more than 30 Patents. In 2011 he was awarded by the Italian Chemical Society with the Gold Medal entitled "Emanuele Paternò" In November 2012 he retired from the University and started a new activity where he was responsible for a Spin Off Company named Eurochem Engineering Ltd located in Milano. In September 2016 he was awarded by the Italian Group of Catalysis (GIC) of Italian Chemical Society (SCI) with the Silver Plate entitled Giacomo Fauser for taking the lead on the related Conference.

Riccardo Tesser

Riccardo Tesser, Associate Professor, Industrial Chemistry Master Degree from the University of Napoli in 1989. He has ten years of industrial experience at the Montefibre Research Centre (NA) developing research activities and technological improvements on dimethyl terephthalate production and batch and continuous PET polymerization. Then, he obtained an Associate Professor position at the Chemical Sciences Department of the University of Naples "Federico II" in Industrial Chemistry. His main fields of research in Industrial Chemistry are industrial catalysis and kinetic studies, reaction and reactor modeling of multiphase systems, kinetic investigation of catalytic reactions, optimization algorithms in chemical engineering, and design and realization of lab-scale pilot plants. More recently, his main field of activity has been biofuel production and the use of renewable resources as raw materials for the chemical industry. The results of these scientific activities have been published in 164 papers in a wide range of international peer-reviewed chemistry journals, 3 books, and 11 international patents.

Vincenzo Russo

Vincenzo Russo, Assistant professor, obtained a PhD in Chemical Sciences from the University of Napoli Federico II (Italy) in 2014 and a PhD in Chemical Engineering from Åbo Akademi (Finland). He has been an Assistant Professor in the Department of Chemical Sciences of the University of Naples Federico II since November 2019. His research activity can be summarized as "Bridging the

Fundamentals of Molecular Phenomena with Modern Concepts of Chemical Reactor Engineering". The research topics are treated with methodology, starting from the investigation of the chemical and physical phenomena occurring in the reaction network. Detailed kinetic investigations are carried out, describing quantitatively the experimental data in lab-scale reactors, both continuous and discontinuous. The kinetic models are based on the investigation of both the physical properties of the catalysts tested (homogeneous or heterogeneous) and the mass and heat transfer phenomena involved in the reaction network. Advanced reactor modeling activity leads to the design and optimization of pilot-scale chemical plants, allowing for the scale-up of the overall process. Novel reactor concepts are tested and designed with the aim of optimizing and intensifying the chemical plant (i.e., reactive chromatography, microreactors). The results of these scientific activities have been published in 109 papers in a wide range of international peer-reviewed chemistry journals, 2 books, and 4 book chapters.

Editorial

Special Issue on “Industrial Chemistry Reactions: Kinetics, Mass Transfer and Industrial Reactor Design”

Elio Santacesaria ^{1,*}, Riccardo Tesser ² and Vincenzo Russo ²

¹ Eurochem Engineering Ltd., 20139 Milano, Italy

² NICL—Department of Chemical Science, University of Naples Federico II, 80126 Naples, Italy; riccardo.tesser@unina.it (R.T.); v.russo@unina.it (V.R.)

* Correspondence: elio.santacesaria@eurochemengineering.com

The impressive developments in commercially available technologies, in terms of new equipment and faster computers, allow us to solve ever-more complicated chemical and technical issues within industrial chemistry and reaction engineering fields. More sophisticated approaches to catalysis, kinetics, reactor design and simulation have been developed thanks to the newly available powerful equipment and calculation methods. It is well known that many chemical reactions are of great interest for industrial processes and must be conducted on a large scale to obtain the necessary information in thermodynamics, kinetics, and transport phenomena related to mass, energy, and momentum. The aim of this Special Issue, entitled “Industrial Chemistry Reactions: Kinetics, Mass Transfer and Industrial Reactor Design”, was to collect worldwide contributions from recognized experts in the field of chemical reaction engineering. The following areas/sections were covered by the call for original papers:

- Kinetic studies for complex reaction schemes;
- Mass transfer aspects in multifunctional reactors;
- Reactions in mass-transfer-dominated regimes (fluid–solid and intraparticle diffusive limitations);
- Kinetics and mass-transfer modeling with alternative approaches.

The interest in the topics could be verified by considering the information extracted from the Scopus database, related to the number of publications per year, as demonstrated in Figure 1A.

Citation: Santacesaria, E.; Tesser, R.; Russo, V. Special Issue on “Industrial Chemistry Reactions: Kinetics, Mass Transfer and Industrial Reactor Design”. *Processes* **2022**, *10*, 411. <https://doi.org/10.3390/pr10020411>

Received: 11 February 2022

Accepted: 17 February 2022

Published: 20 February 2022

Publisher’s Note: MDPI stays neutral with regard to jurisdictional claims in published maps and institutional affiliations.



Copyright: © 2022 by the authors. Licensee MDPI, Basel, Switzerland. This article is an open access article distributed under the terms and conditions of the Creative Commons Attribution (CC BY) license (<https://creativecommons.org/licenses/by/4.0/>).

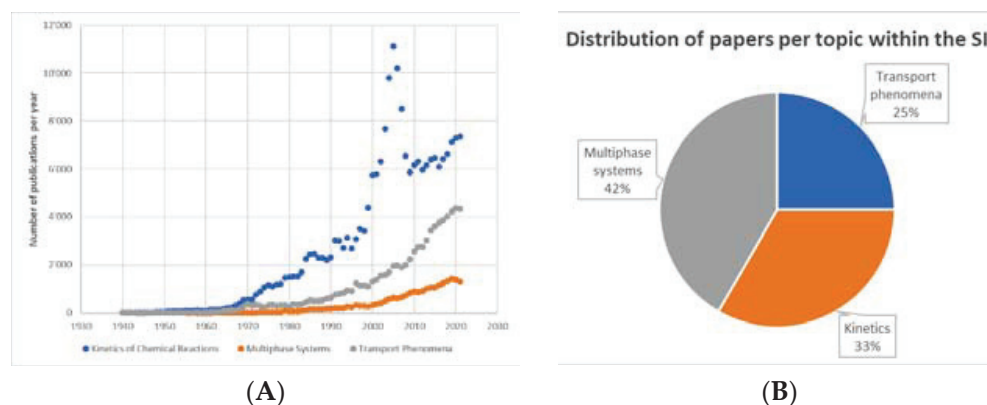


Figure 1. Statistical information related to the Special Issue “Industrial Chemistry Reactions: Kinetics, Mass Transfer and Industrial Reactor Design”. (A) Number of publications per year related to each specific macro area (Scopus Database). (B) Distribution of papers per macro area.

The Special Issue collated twelve papers, which could be framed within different macro areas, whose distribution is depicted in Figure 1B. As revealed, the trends are all

exponentially increasing, proving the effective scientific interest in the selected topics. Moreover, the distribution is well-balanced along three different macro areas, namely: (i) transport phenomena; (ii) kinetics; and (iii) multiphase systems. In the following sections, the main contributions published in the SI are reviewed and summarized, highlighting the novelty for each macro area.

Four articles devoted to the kinetics of chemical reactions have been published in this Special Issue. The first article, published by Tapio Salmi et al. [1], proposes a robust method for the estimation of kinetic parameters for systems including slow and rapid reactions. These systems require the solution of differential–algebraic equation systems. The authors simplified the approach by converting all the equations to a system of ordinary differential equations, enabling easier determination avoiding problems of numerical stability in the kinetic parameters by mathematical regression analysis. Two examples illustrate the method in practice, showing the good performance of the developed numerical strategy. A second article by Santacesaria et al. [2] examined the kinetics of epoxide ring opening reactions in detail. These are side reactions in the epoxidation of unsaturated vegetable oils, reducing the yields of the industrial process. All the factors affecting the reaction have been considered and experimentally tested, while a reliable kinetic model has been developed for simulating all the performed kinetic runs (Figure 2A).

Linda Nikoshvili et al. [3] studied a polymer-Pd nanocatalyst deactivation in the Suzuki–Miyaura cross-coupling reaction. This reaction is widely applied in industry for C–C bond formation. The authors found methods for increasing the catalyst stability. The last article of this topic written by Rosengart et al. [4] deals with the hydrogenation of trans, trans-muconic acid to bio-adipic acid promoted by Pd/C 5% (wt). The authors studied the reaction in batch conditions and developed an LHHW kinetic model for interpreting all the experimental kinetic data. The most reliable reaction mechanism was individuated and discussed, resulting in a proper description of the collected experimental data (Figure 2B).

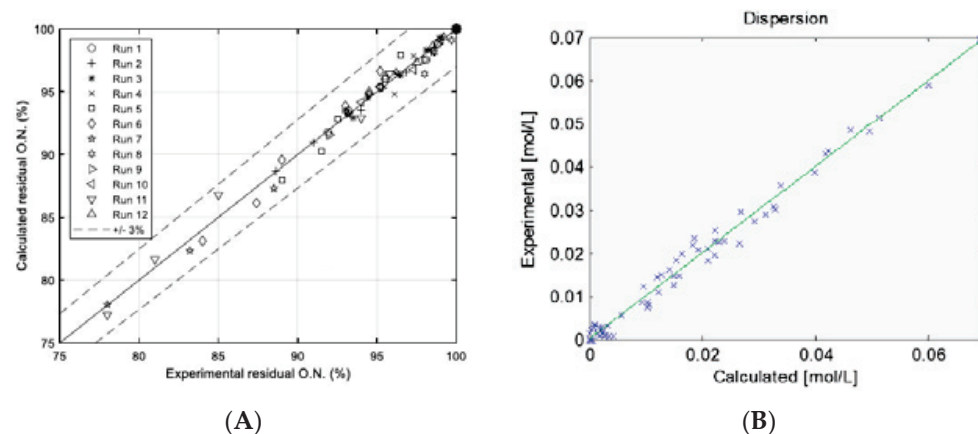


Figure 2. Parity plots for: (A) epoxidized soybean oil ring opening tests in the presence of sulfuric acid as catalyst [2]; (B) hydrogenation of trans, trans-muconic acid to bio-adipic acid promoted by Pd/C 5% (wt) [4].

Three articles of the Special Issue were devoted to problems of transport phenomena. First of all, Tesser and Santacesaria [5] published a brief review on the role of mass and heat transfer in gas–solid catalytic reactions, updating the knowledge on this topic by considering the considerable progress in computing power has occurred in the last 20 years. This progress has favored the use of numerical methods in the simulation of complex systems involving kinetics and mass transfer, as in gas–solid catalytic reactions, starting from a generic treatment of the multiphase system (see the sketch in Figure 3A). Somchart Chantasiriwan [6] published a study on sugar juice evaporation, aiming to increase the energy efficiency and decrease the sucrose inversion loss through modification of the conventional method. Finally, Hee-Chul Yang [7] investigated the two-step thermochemical

treatment of carbonization and halogenation for the removal of radionuclides from spent cation-exchange resins, developing a reliable model useful to describe the dependence of unburned hydrocarbon content as a function of both reactor temperature and length (Figure 3B).

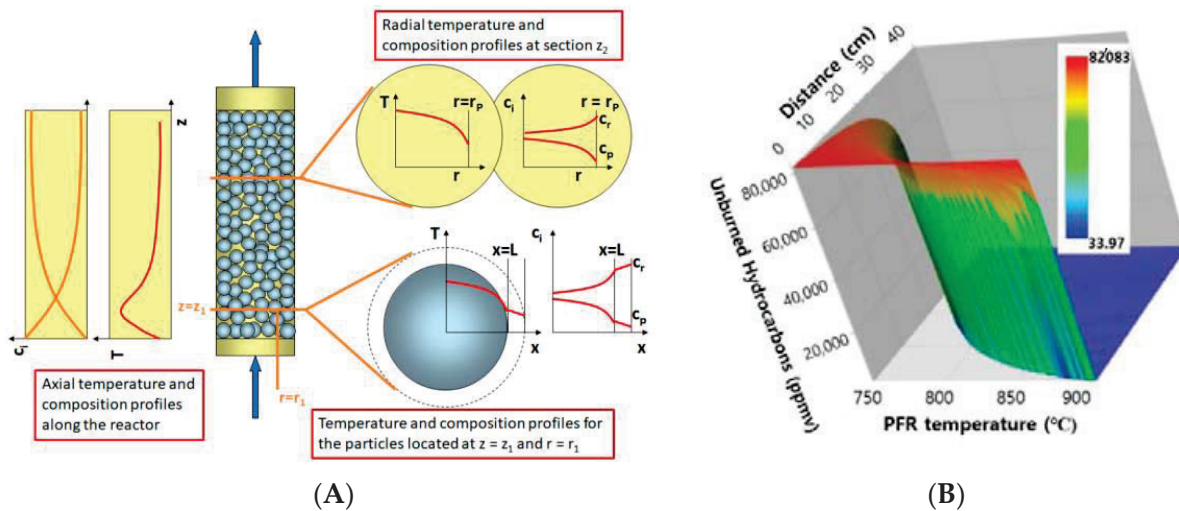


Figure 3. (A) Sketch concentration and temperature gradients along both the catalyst particle radius and reactor length [5]. (B) Unburned hydrocarbon concentration at the center of the reactor as a function of the plug flow reactor length and temperature [7].

Finally, five articles of the Special Issue were devoted to the study of multiphase systems. In particular, Margi and Yadav [8] published research on the design and development of a novel continuous flow stirred multiphase reactor, by studying the phase transfer catalyzed reaction of guaiacol with epichlorohydrin to obtain guaiacol glycidyl ether.

Figure 4A is a singular example of liquid–liquid–liquid phase reaction conducted in a novel continuous reactor, as proposed by Margi and Yadav.

Yu et al. [9] studied a system gas–liquid–solid with a numerical approach to define the bubble of gas rising in channels saturated with liquid. A mathematical model avoiding numerical instability has been proposed by the authors. Ravisut Vitidsant et al. [10] studied the transesterification of triolein, containing solid CaO particles, with methanol. The oil and solid particles were injected through an ultrasonic spray into an atmosphere of methanol. This three-phase reactor produced methyl ester with yields higher than the conventional reactors. Spitters et al. published an article concerning the optimization of the production of 1,1-diethoxybutane (DEB) by a simulated moving bed reactor (SMBR) [11], showing that this approach results in a high level of productivity and high purity of the desired product. The data collected were described quantitatively with sophisticated models (Figure 4B). The last study of this section, by Zemeng Zhao et al. [12], is devoted to the removal of dissolved oxygen from water by stripping with nitrogen coupled with vacuum degassing in a novel rotor–stator reactor. The performance of the mentioned reactor has been carefully determined and interpreted.

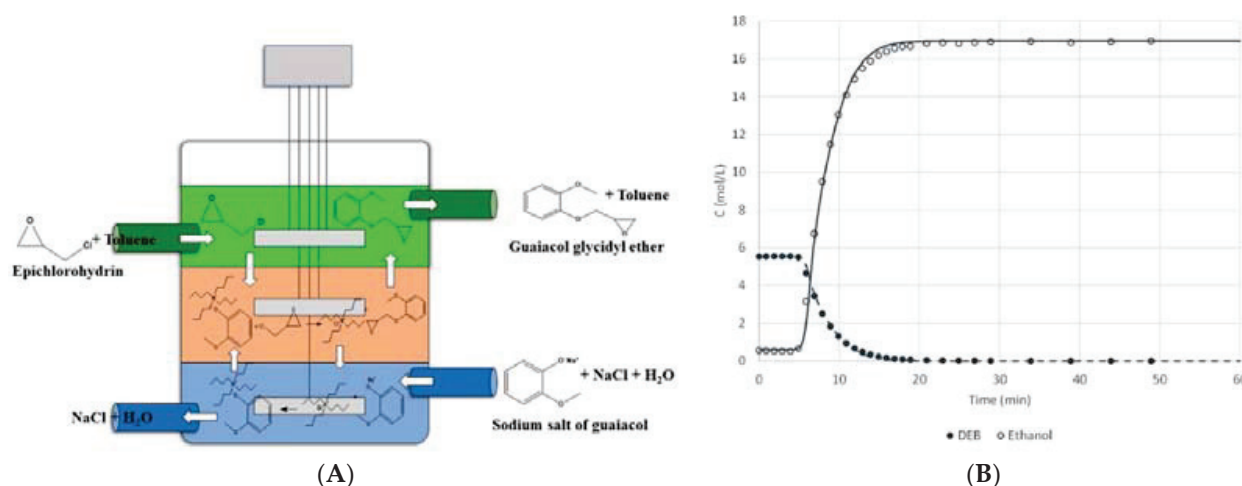


Figure 4. (A) Liquid–liquid–liquid reaction system in a continuous flow stirred reactor [8]. (B) Break-through curve between ethanol and DEB within an SMBR [11].

As it can be seen, although high in quality, the studies published in this first edition of the Special Issue entitled “Industrial Chemistry Reactions: Kinetics, Mass Transfer, and Industrial Reactor Design” are rather heterogeneous for their contents. This is due to the many different options that can possibly be obtained when chemical reactions, catalysis, kinetics, transport phenomena, and multiphase systems are considered without focusing on a single aspect. On the other hand, to have an open view on all the mentioned subjects is useful to be ready to understand what the best approach for any possible system could be: gas–solid, liquid–solid, liquid–liquid, gas–liquid–solid, etc., both in chemical regimes and limited by transport phenomena. The multiple approach of this Special Issue is, therefore, useful when presenting the approaches followed by eminent scientists in studying the kinetics of different reactions in many different situations. It would be desirable to further enlarge the casuistry of possible examples under study. For this reason, a second edition of this Special Issue with the same title has been recently launched.

Author Contributions: Conceptualization, E.S., R.T. and V.R. equally; writing—review and editing, E.S., R.T. and V.R. equally. All authors have read and agreed to the published version of the manuscript.

Funding: This research received no external funding.

Institutional Review Board Statement: Not applicable.

Informed Consent Statement: Not applicable.

Data Availability Statement: Data sharing not applicable.

Conflicts of Interest: The authors declare no conflict of interest.

References

1. Salmi, T.; Tirronen, E.; Wärnå, J.; Mikkola, J.P.; Murzin, D.; Eta, V. A Robust Method for the Estimation of Kinetic Parameters for Systems Including Slow and Rapid Reactions—From Differential-Algebraic Model to Differential Model. *Processes* **2020**, *8*, 1552. [\[CrossRef\]](#)
2. Santacesaria, E.; Turco, R.; Russo, V.; Tesser, R.; Di, M. Soybean Oil Epoxidation: Kinetics of the Epoxide Ring Opening Reactions. *Processes* **2020**, *8*, 1134. [\[CrossRef\]](#)
3. Nikoshvili, L.; Bakhvalova, E.S.; Bykov, A.V.; Sidorov, A.I.; Vasiliev, A.L.; Matveeva, V.G.; Sulman, M.G.; Sapunov, V.N.; Kiwi-Minsker, L. Study of Deactivation in Suzuki Reaction of Polymer-Stabilized Pd Nanocatalysts. *Processes* **2020**, *8*, 1653. [\[CrossRef\]](#)
4. Rosengart, A.; Pirola, C.; Capelli, S. Hydrogenation of Trans, Trans-Muconic Acid to Bio-Adipic Acid: Mechanism Identification and Kinetic Modelling. *Processes* **2020**, *8*, 929. [\[CrossRef\]](#)
5. Tesser, R.; Santacesaria, E. Revisiting the Role of Mass and Heat Transfer in Gas–Solid Catalytic Reactions. *Processes* **2020**, *8*, 1599. [\[CrossRef\]](#)

6. Chantasiriwan, S. Modification of Conventional Sugar Juice Evaporation Process for Increasing Energy Efficiency and Decreasing Sucrose Inversion Loss. *Processes* **2020**, *8*, 765. [[CrossRef](#)]
7. Yang, H.C.; Park, H.O.; Park, K.T.; Kim, S.J.; Kim, H.J.; Eun, H.C.; Lee, K. Development of Carbonization and a Relatively High-Temperature Halogenation Process for the Removal of Radionuclides from Spent Ion Exchange Resins. *Processes* **2021**, *9*, 96. [[CrossRef](#)]
8. Margi, N.H.; Yadav, G.D. Design and Development of Novel Continuous Flow Stirred Multiphase Reactor: Liquid–Liquid–Liquid Phase Transfer Catalysed Synthesis of Guaiacol Glycidyl Ether. *Processes* **2020**, *8*, 1271. [[CrossRef](#)]
9. Yu, K.; Yong, Y.; Yang, C. Numerical Study on Bubble Rising in Complex Channels Saturated with Liquid Using a Phase-Field Lattice-Boltzmann Method. *Processes* **2020**, *8*, 1608. [[CrossRef](#)]
10. Vitidsant, R.; Kodama, S.; Sekiguchi, H. Transesterification Using Ultrasonic Spray of Triolein Containing CaO Particles into Methanol Vapor in a 3-Phase Reactor. *Processes* **2021**, *9*, 181. [[CrossRef](#)]
11. Spitters, J.; Gonçalves, J.C.; Faria, R.P.V.; Rodrigues, A.E. Optimization of the Production of 1,1-Diethoxybutane by Simulated Moving Bed Reactor. *Processes* **2021**, *9*, 189. [[CrossRef](#)]
12. Zhao, Z.; Liu, Z.; Xiang, Y.; Arowo, M.; Shao, L. Removal of Dissolved Oxygen from Water by Nitrogen Stripping Coupled with Vacuum Degassing in a Rotor–Stator Reactor. *Processes* **2021**, *9*, 1354. [[CrossRef](#)]

Article

Modification of Conventional Sugar Juice Evaporation Process for Increasing Energy Efficiency and Decreasing Sucrose Inversion Loss

Somchart Chantasiriwan

Department of Mechanical Engineering, Thammasat University, Pathum Thani 12121, Thailand;
somchart@engr.tu.ac.th

Received: 15 June 2020; Accepted: 28 June 2020; Published: 30 June 2020

Abstract: The evaporation process, boiler, and turbine are the main components of the cogeneration system of the sugar factory. In the conventional process, the evaporator requires extracted steam from the turbine, and bled vapor from the evaporator is supplied to the juice heater and the pan stage. The evaporation process may be modified by using extracted steam for the heating duty in the pan stage. This paper is aimed at the investigation of the effects of this process modification. Mathematical models of the conventional and modified processes were developed for this purpose. It was found that, under the conditions that the total evaporator area is 13,000 m², and the inlet juice flow rate is 125 kg/s, the optimum modified evaporation process requires extracted steam at a pressure of 157.0 kPa. Under the condition that the fuel consumption rate is 21 kg/s, the cogeneration system that uses the optimum modified evaporation process yields 2.3% more power output than the cogeneration system that uses a non-optimum conventional cogeneration process. Furthermore, sugar inversion loss of the optimum modified process is found to be 63% lower than that of the non-optimum conventional process.

Keywords: heat exchanger; mathematical model; energy efficiency; inversion loss; process design; mass transfer

1. Introduction

The evaporation process, boiler, and steam turbine are the main components of the cogeneration system in the sugar industry. Diluted sugar juice becomes raw sugar and molasses in the evaporation process after a specified amount of water is removed by evaporation. Thermal energy required for water evaporation is provided by steam condensation. The boiler generates high-pressure steam that is supplied to the steam turbine for power generation. Older cogeneration systems use the back-pressure turbine, in which steam is exhausted at a lower pressure, whereas modern cogeneration systems use the extraction–condensing steam turbine, in which some steam is extracted at lower pressure, and the remaining steam is sent to the condenser. Kamate and Gangavati [1] have shown that a cogeneration system using the extraction–condensing steam turbine is more energy efficient than a cogeneration system using the back-pressure steam turbine.

The multiple-effect evaporator is used in the evaporation process. The evaporator is designed to increase the juice concentration from approximately 15% to 70%. The removal of the remaining water content in sugar occurs in the pan stage. The multiple-effect evaporator requires a supply of saturated steam extracted from an extraction–condensing steam turbine at a specified pressure. An adverse consequence of the exposure of sugar juice to high-temperature steam and vapor in the multiple-effect evaporator is sucrose inversion loss, which converts sucrose to glucose and fructose. In order to increase the profitability of raw sugar manufacturing, the amount of required steam and sugar inversion loss should be minimized without compromising the capacity of the process.

There have been several suggestions to improve the energy efficiency of the evaporation process. Urbaniec et al. [2] have suggested that heat recovery can be improved by retrofitting the evaporation process. Ensinas et al. [3] have used a thermo-economic procedure to reduce steam consumption by the evaporation process. An analysis by Higa et al. [4] shows that increasing the number of effects can decrease steam consumption. Bapat et al. [5] have shown that steam consumption can be reduced by using heat recovery devices. Sharan and Bandyopadhyay [6] have shown that steam consumption by the entire plant can be minimized by integrating the evaporator with the background process. Mechanical vapor compression [7] and thermal vapor compression [8] have been suggested as methods to increase the energy efficiency of the multiple-effect evaporator. The energy efficiency of the multiple-effect evaporator can also be increased by the optimum distribution of heating surface areas [9–12]. Recently, Chantasiriwan has shown that the energy efficiency of the cogeneration system, in which the evaporation process is a component, can be increased by replacing the forward-feed evaporator with the backward-feed evaporator [13]. Investigations of sucrose inversion loss in sugar juice evaporation process have yielded conclusions that increased time between cleanings of the evaporator results in more inversion loss [14]; inversion loss may be reduced by replacing Robert evaporators with falling-film evaporators [15]; and using smaller diameter and longer tubes decrease inversion loss due to shorter residence time of juice in the evaporator [16]. In addition, Rein [17] has suggested that decreasing the temperature profile across the effects of the evaporator can also reduce inversion loss.

Energy efficiency of the evaporation process can be improved not only by reducing the steam consumption of a given pressure, which is the subject of most of the previous investigations, but also by decreasing extracted steam pressure. There is a lower limit of extracted steam pressure because the thermal energy input required for an evaporation process is approximately equal to the product of the total heating surface area of the evaporator and the difference between the steam temperature at the evaporator inlet and the vapor temperature at the evaporator outlet. The lower limit can be decreased by increasing the total heating surface area. Furthermore, it is interesting to note that vapor is usually bled from the first effect of the multiple-effect evaporator in order to be used for heating duty in the pan stage. This requirement imposes an additional constraint on the lower limit of the extracted steam pressure. It is possible to remove this constraint by using extracted steam instead of bled vapor for this purpose. A consequence of this constraint removal is further reduction of extracted steam pressure. Reduced extracted steam pressure results in not only higher energy efficiency but also lower sucrose inversion loss due to decreased temperature profile across the effects of the evaporator [17].

In this paper, the performance of the conventional process, in which vapor bled from the multiple-effect evaporator is used for the pan stage, is compared with that of a modified sugar juice evaporation process, which uses extracted steam instead of bled vapor for heating duty in the pan stage. Mathematical models of the conventional and modified processes are presented in Sections 2 and 3. Both processes operate in cogeneration systems described in Section 4. Section 5 shows that, under the same conditions, differences in energy efficiency and sucrose inversion loss can be attributed to the process modification.

2. Conventional Evaporation Process

The conventional sugar juice evaporation process is shown in Figure 1. The components of the process are 4 effects of the evaporator (E1, E2, E3, and E4), 2 heat exchangers of the juice heater (H1 and H2), the flash tanks (FC, F1, F2, and F3), and the pan stage (P). Sugar juice at the ambient temperature ($T_{h,2}$) is heated in H2 and H1 to the saturation temperature ($T_{h,0}$), which is 103 °C. This temperature corresponds to a pressure slightly larger than the atmospheric pressure (p_{atm}). Juice pressure is decreased to p_{atm} in FC before entering E1. Sugar juice and saturated steam or vapor flow from E1 to E4. The steam turbine (not shown in Figure 1) supplies extracted steam at pressure p_0 to E1. Vapor from E1 is sent to P, H1, and E2. Vapor from E2 is sent to H2 and E3. Vapor from E3 is sent to E4. Vapor from

E4 is sent to the condenser (not shown in Figure 1). In effect i , water evaporation at pressure p_{i+1} is caused by vapor condensation at pressure p_i . Concentrated sugar juice from E4 is sent to P.

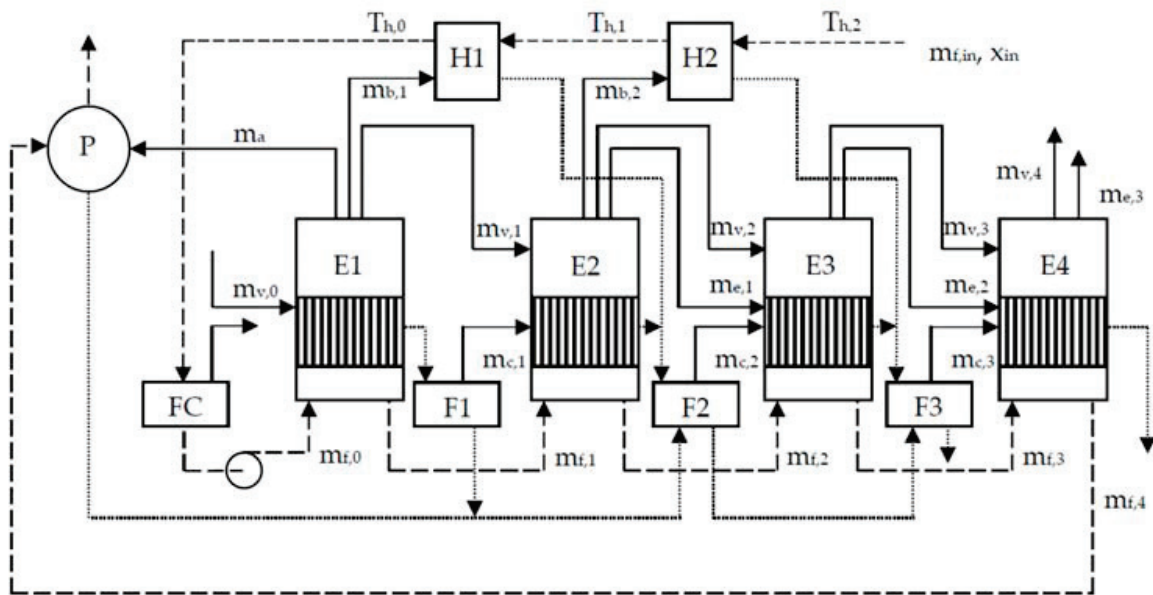


Figure 1. Conventional evaporation process.

In order to improve the energy efficiency of the process, condensates from E1, E2, and E3 are sent, respectively, to F1, F2, and F3. F2 also receives condensates from P, F1, and H1, and F3 also receives condensates from F2 and H2. Flash tanks (F1, F2, and F3) produce vapor and condensate at a lower pressure from condensate at a higher pressure.

The model of the conventional evaporation process in Figure 1 is similar to the model presented by Chantasiriwan [13]. The difference between the two models is the treatment of condensate from E1. In the model presented by Chantasiriwan [13], the condensate is sent to the boiler. In the model shown in Figure 1, the condensate is sent to F1. It can be shown that this treatment increases the overall energy efficiency of the process.

Due to the similarity between this model and the model presented by Chantasiriwan [13], only different equations are shown for the sake of concise presentation. The different treatment of condensate in this paper gives rise to the following energy equations:

$$(1 - \varepsilon)(m_{v,0} - m_{x,0})h_{vl}(p_0) + m_{f,0}(h_{f,1}^{(in)} - h_{f,1}^{(out)}) = (m_a + m_{v,1} + m_{b,1})[h_v(p_1) - h_{f,1}^{(out)}], \quad (1)$$

$$(1 - \varepsilon)(m_{v,1} + m_{c,1})h_{vl}(p_1) + m_{f,1}(h_{f,2}^{(in)} - h_{f,2}^{(out)}) = (m_{v,2} + m_{b,2})[h_v(p_2) - h_{f,2}^{(out)}], \quad (2)$$

$$(1 - \varepsilon)(m_{v,2} + m_{e,1} + m_{c,2})h_{vl}(p_2) + m_{f,2}(h_{f,3}^{(in)} - h_{f,3}^{(out)}) = m_{v,3}[h_v(p_3) - h_{f,3}^{(out)}], \quad (3)$$

$$(1 - \varepsilon)(m_{v,3} + m_{e,2} + m_{c,3})h_{vl}(p_3) + m_{f,3}(h_{f,4}^{(in)} - h_{f,4}^{(out)}) = m_{v,4}[h_v(p_4) - h_{f,4}^{(out)}], \quad (4)$$

$$m_{c,1} = m_{v,0}f(p_0, p_1), \quad (5)$$

$$m_{c,2} = (m_{v,0} + m_{v,1} + m_{b,1} + m_a)f(p_1, p_2), \quad (6)$$

$$m_{c,3} = (m_{v,0} + m_a + m_{v,1} + m_{b,1} + m_{v,2} + m_{b,2} + m_{e,1})f(p_2, p_3). \quad (7)$$

Expressions for the other parameters are the same as those in the model presented by Chantasiriwan [13], and an interested reader is asked to consult that reference. The heat

transfer equations in this model are also slightly different from those in the model presented by Chantasiriwan [13]. They are shown as follows.

$$U_1(A_1 - A_{x,0})[T_{sat}(p_0) - T_{f,1}^{(out)}] = (1 - \varepsilon)(m_{v,0} - m_{x,0})h_{vl}(p_0). \quad (8)$$

$$U_2A_2[T_{sat}(p_1) - T_{f,2}^{(out)}] = (1 - \varepsilon)(m_{v,1} + m_{c,1})h_{vl}(p_1), \quad (9)$$

$$U_3A_3[T_{sat}(p_2) - T_{f,3}^{(out)}] = (1 - \varepsilon)(m_{v,2} + m_{e,1} + m_{c,2})h_{vl}(p_2), \quad (10)$$

$$U_4A_4[T_{sat}(p_3) - T_{f,4}^{(out)}] = (1 - \varepsilon)(m_{v,3} + m_{e,2} + m_{c,3})h_{vl}(p_3). \quad (11)$$

3. Modified Evaporation Process

The conventional evaporation process uses bled vapor from the first effect of the evaporator for the pan stage. A consequence of this requirement is that the extracted steam pressure (p_0) must not be lower than the minimum value that corresponds to a specified juice mass flow rate. It is possible to remove this constraint by using extracted steam instead of bled vapor for the pan stage in the modified evaporation process.

The modified evaporation process is depicted in Figure 2. It can be seen that extracted steam at pressure p_a is supplied to the pan stage. The model of this process is the same as that of the conventional process with m_a deleted from Equation (1). The mass flow rate of extracted steam required by the pan stage is

$$m_a = \frac{2m_{f,A}(1 - x_4/91)h_{vl}(p_4)}{h_{vl}(p_a)}. \quad (12)$$

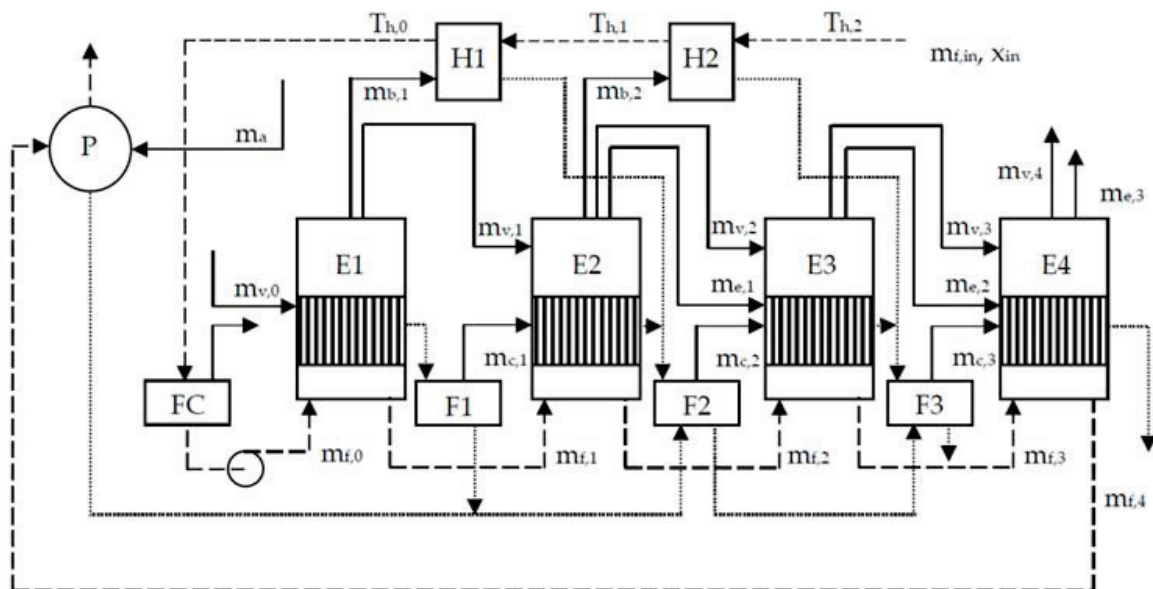


Figure 2. Modified evaporation process.

It is interesting to note that, under the same operating conditions, $m_{f,A}$, x_4 , and p_4 of the modified and conventional evaporation processes are identical. Therefore, the values of m_a of both processes are the same if $p_a = 150$ kPa.

4. Performance Parameters

This paper is intended to demonstrate that the modified evaporation process requires extracted steam at a lower pressure than the conventional evaporation process, which leads to the enhanced performance of the modified evaporation process compared with the conventional process. Comparison between both processes is based on two performance parameters, which are turbine power output of the cogeneration system and sucrose inversion loss.

4.1. Turbine Power Output

Steam economy is the performance parameter that may be used to evaluate the energy efficiency of an evaporation process. It is equal to the ratio of the mass flow rate of evaporated water to the mass flow rate of extracted steam. Therefore,

$$SE = \frac{2m_{f,in}(1 - x_4/91)}{m_{v,0}} \quad (13)$$

for the conventional evaporation process, and

$$SE = \frac{2m_{f,in}(1 - x_4/91)}{m_{v,0} + m_a} \quad (14)$$

for the modified evaporation process.

Steam economy is an appropriate parameter for comparing different conventional evaporation processes because the extracted steam pressure in the first effect of the multiple-effect evaporator is fixed. The process having larger steam economy is considered to be more energy efficient. However, steam economy should not be used to compare the conventional and modified evaporation processes because extracted steam pressures in both processes may be different. To identify a more suitable performance parameter, it is necessary to consider the cogeneration system.

The cogeneration systems for the conventional and modified evaporation processes are depicted in Figure 3. In each system, the mass flow rate, pressure, and temperature of steam generated by the boiler (B) are, respectively, m_s , p_s , T_s . Steam is extracted at the pressure of p_0 in the conventional evaporation process. The mass flow rate of extracted steam is $m_{v,0}$. The extracted steam is used for evaporation in the first effect of the evaporator. The remaining steam is condensed at the pressure of p_c . The mass flow rate of condensed steam (m_c) is, therefore, $m_s - m_{v,0}$. The modified evaporation process requires not only extracted steam at the pressure of p_0 for evaporation in the first effect of the evaporator but also extracted steam at the pressure of p_a for evaporation in the pan stage. The corresponding mass flow rates of extracted steam are $m_{v,0}$ and m_a . The remaining steam is condensed at the pressure of p_c . The mass flow rate of condensed steam (m_c) is, therefore, $m_s - m_{v,0} - m_a$.

Inspection of Figure 3 reveals that the inputs of both systems are sugar juice and bagasse, and the outputs are turbine power, sugar, and molasses. Both systems are assumed to have the same juice processing capacity. This means that $m_{f,in}$, x_{in} , and x_4 are the same in both the conventional evaporation process and the modified evaporation process. Moreover, both systems are assumed to consume the same amount of fuel (m_{fuel}) in their boilers. Based on these assumptions, the only difference between both systems is turbine power output, which is expressed as

$$P = m_{v,0}(h_s - h_0) + m_a(h_s - h_a) + m_c(h_s - h_c), \quad (15)$$

$$h_0 = h_s - \eta_t(h_s - h_{0s}), \quad (16)$$

$$h_a = h_s - \eta_t(h_s - h_{as}), \quad (17)$$

$$h_c = h_s - \eta_t(h_s - h_{cs}), \quad (18)$$

where η_t is isentropic efficiency of the steam turbine, h_s is specific enthalpy at pressure p_s , and temperature T_s , h_{0s} , h_{as} , and h_{cs} are specific enthalpies at, respectively, pressures p_0 , p_a , and p_c , and the same entropy as the inlet steam. It should be noted that m_a is zero in the cogeneration system for the conventional evaporation process.

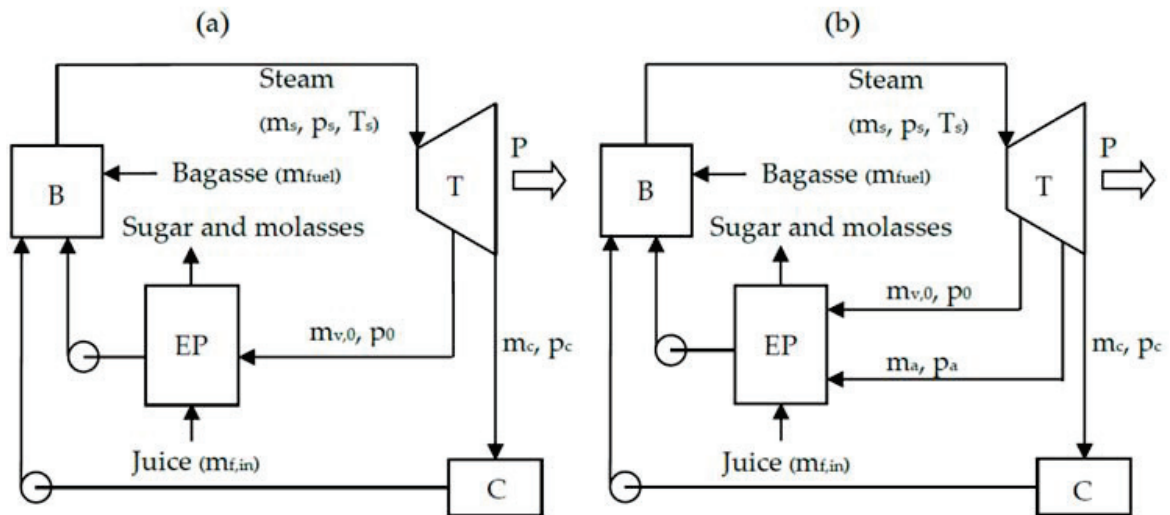


Figure 3. Cogeneration systems for (a) the conventional evaporation process and (b) the modified evaporation process.

4.2. Sucrose Inversion Loss

Sucrose inversion is the chemical reaction that transforms sucrose into glucose and fructose, which do not crystallize and cannot be recovered as sugar. Main factors that influence sucrose inversion in the multiple-effect evaporator are temperature, time, juice acidity, and juice concentration. Sucrose inversion loss may be estimated by using the Vukov model [18]. According to this model, the mass fraction of lost sucrose is expressed as

$$I = 1 - e^{-kt}, \quad (19)$$

where t is retention time (in minutes) of sugar juice in an evaporator vessel. The reaction rate (k) is determined from

$$\log k = 16.91 - \log \left[\frac{\rho(100 - x)}{100} \right] - \frac{5670}{T_f} - pH. \quad (20)$$

Equation (20) is applicable when the juice temperature is 25 °C. At a different temperature, the corrected pH value is

$$pH = pH_{25} + (T_f - 25)(-0.0339 + 0.015pH_{25} - 0.0017pH_{25}^2). \quad (21)$$

For simulation purposes, pH_{25} is assumed to be 6.0. The retention time (t) is proportional to the evaporator surface area (A), and inversely proportional to sugar juice mass flow rate (m_f). It may be approximated by assuming that sugar juice flows through N tubes, of which diameter and length are D and L , in an evaporator vessel at the speed of V . The expression of V is

$$V = \frac{4m_f}{N\rho\pi D^2}. \quad (22)$$

Consequently,

$$t = \frac{N\rho\pi D^2 L}{240m_f}. \quad (23)$$

If tube thickness is negligible, the heating surface of the evaporator vessel (A) is $N\pi DL$, and Equation (23) becomes

$$t = \frac{\rho DA}{240m_f}. \quad (24)$$

Typical tube diameter varies from 38 to 51 mm. It is assumed that D is 45 mm in this paper.

5. Results and Discussion

The parameters of both evaporation processes are $x_{in} = 15\%$, $x_{out} = 70\%$, $p_4 = 16$ kPa, and $T_{h,2} = 30$ °C. In each process, the total surface areas of the multiple-effect evaporator and the juice heater are, respectively, 13,000 and 2500 m². Multiple-effect evaporators in both systems are designed to process 125 kg/s (or 450 t/h) of juice. The optimum distribution of the total evaporator surface area that maximizes the steam economy at a specified extracted steam pressure (p_0) may be determined for each system.

The procedure for determining the optimum distribution of the evaporator surface area in the conventional evaporation process that maximizes the steam economy (SE) is shown in Figure 4. Figure 4a shows that, for the first-effect area (A_1) of 6000 m² and the second-effect area (A_2) of 1200 m², the optimum value of the third-effect area (A_3) that yields the required juice mass flow rate of 125 kg/s and the maximum steam economy (SE) is 1233 m². Figure 4b shows that, for the same value of A_1 , the optimum value of A_2 that results in maximum SE is 1251 m². Figure 4c shows that, as A_1 increases, SE decreases, and first-effect pressure (p_1) increases. By requiring that p_1 is 150 kPa, the optimum value of A_1 is found to be 4518 m². The corresponding value of SE is 2.508. Therefore, the mass flow rate of extracted steam for the evaporator ($m_{v,0}$) is 41.63 kg/s.

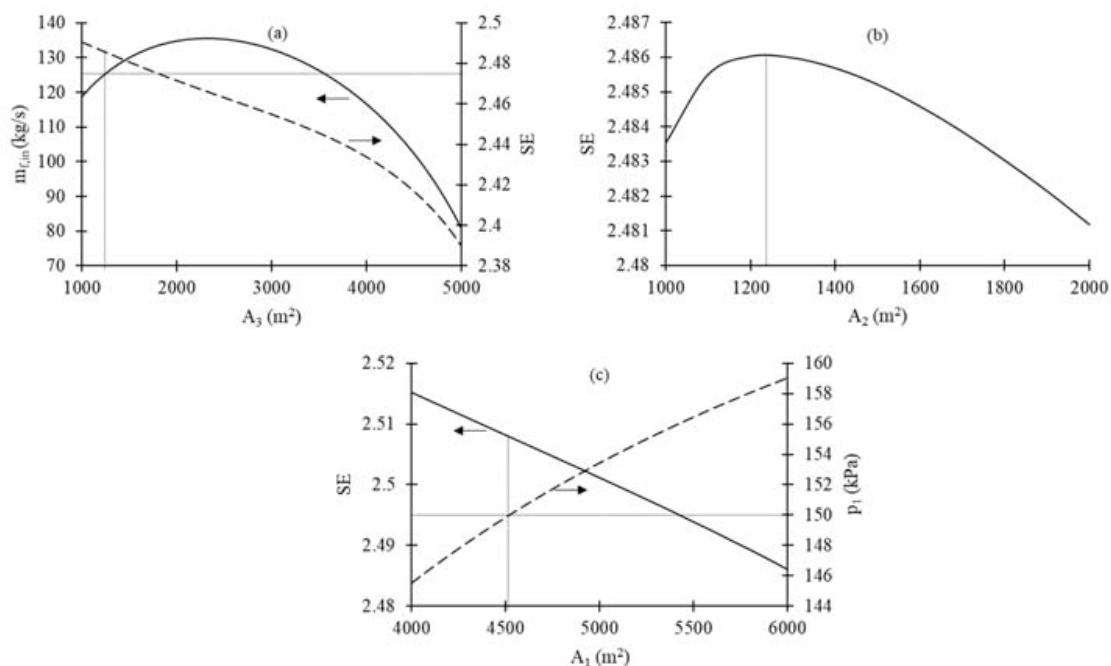


Figure 4. Procedure for determining the optimum distribution of evaporator area in the conventional evaporation process driven by extracted steam at a pressure (p_0) of 200 kPa: (a) finding third-effect area (A_3) corresponding to the inlet juice mass flow rate ($m_{f,in}$) of 125 kg/s and the maximum steam economy (SE) corresponding to first-effect area (A_1) = 6000 m², and second-effect area (A_2) = 1200 m²; (b) finding A_2 that maximizes SE corresponding to A_1 = 6000 m²; and (c) finding A_1 corresponding to the first-effect pressure (p_1) of 150 kPa.

The procedure for determining the optimum distribution of evaporator surface area in the modified evaporation process that maximizes SE is shown in Figure 5. Figure 5a shows that, for the first-effect area (A_1) of 4000 m² and the second-effect area (A_2) of 1100 m², the optimum value of the third-effect area (A_3) that yields the required juice mass flow rate of 125 kg/s and the maximum SE is 1723 m². Figure 5b shows that, for the same value of A_1 , the optimum value of A_2 that results in the maximum SE is 1342 m². Figure 5c shows the optimum value of A_1 that results in the maximum SE is 2074 m². The corresponding value of SE is 2.345. Since the mass flow rate of juice leaving E4 ($m_{f,4}$) is 26.79 kg/s, and the mass flow rate of extracted steam for the pan stage (m_a) is 13.16 kg/s, the value of $m_{v,0}$ is found to be 31.53 kg/s.

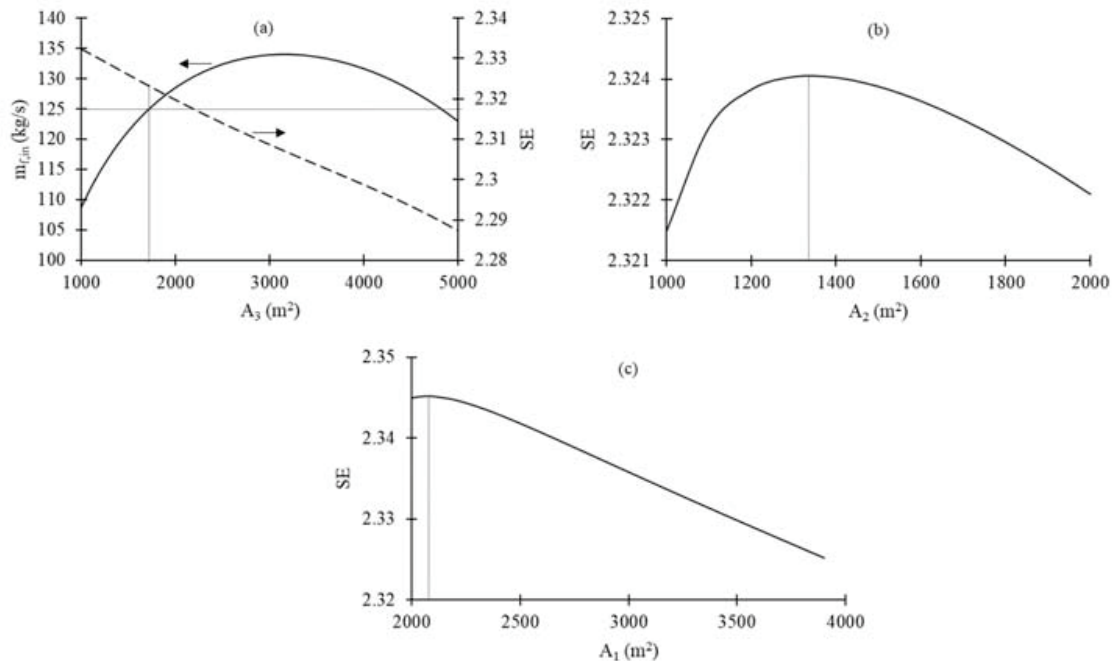


Figure 5. Procedure for determining the optimum distribution of evaporator area in the modified evaporation process driven by extracted steam at a pressure (p_0) of 200 kPa: (a) finding A_3 corresponding to the inlet juice mass flow rate ($m_{f,in}$) of 125 kg/s and the maximum steam economy (SE) corresponding to $A_1 = 4000$ m², and $A_2 = 1100$ m²; (b) finding A_2 that maximizes SE corresponding to $A_1 = 4000$ m²; and (c) finding A_1 that maximizes SE .

The calculation of the turbine power output (P) of a cogeneration system requires information about the fuel, the boiler, and the steam turbine. It is assumed that the fuel consumption rate in the boiler of each system is 21 kg/s, the higher heating value of fuel is 9000 kJ/kg, the boiler efficiency is 70%, the pressure and temperature of superheated steam generated by the boiler are 4.5 MPa and 440 °C, and the turbine efficiency is 85%. Figure 6 shows variations of $m_{v,0}$ and P with p_0 in cogeneration systems for the conventional and modified evaporation processes that have the optimum distributions of evaporator surface areas. It can be seen that, in each system, there exists the optimum value of p_0 ($p_{0,opt}$) that results in the maximum turbine power output (P_{max}). In the cogeneration system for the optimum conventional evaporation process, $p_{0,opt}$ is 186.8 kPa, and P_{max} is 29,286 kW. In the cogeneration system for the optimum modified evaporation process, $p_{0,opt}$ is 157.0 kPa, and P_{max} is 29,442 kW. It is interesting to compare the cogeneration systems for the optimum modified evaporation process and a non-optimum conventional evaporation process, in which p_0 is 200 kPa. The non-optimum conventional process has the same juice processing capacity as the optimum conventional process, but it is less energy efficient. The value of SE in this process is 2.411, and the value of $m_{v,0}$ is 43.31 kg/s. The turbine power output of the cogeneration system that uses this process is 28,789 kW, which is 2.3% lower than the turbine power output of the cogeneration system that uses the optimum modified

evaporation process. Table 1 shows simulation results of cogeneration systems for the non-optimum conventional evaporation process, the optimum conventional evaporation process, and the optimum modified evaporation process.

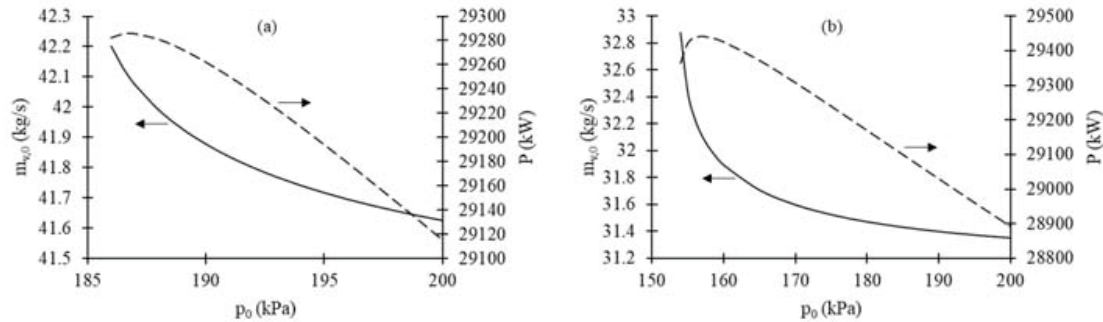


Figure 6. Variations with extracted steam pressure (p_0) of extracted steam consumption ($m_{v,0}$) and turbine power output (P) of the cogeneration systems that have the optimum distributions of evaporator surface areas for (a) the conventional evaporation process and (b) the modified evaporation process.

Table 1. Simulation results of cogeneration systems for the non-optimum conventional evaporation process, the optimum conventional evaporation process, and the optimum modified evaporation process.

	Conventional EP		Optimum Modified EP
	Non-Optimum	Optimum	
A_1 (m ²)	4695	6611	4634
A_2 (m ²)	4266	1558	2409
A_3 (m ²)	2729	1335	1932
A_4 (m ²)	1310	3496	4025
$A_{h,1}$ (m ²)	80	469	1399
$A_{h,2}$ (m ²)	2420	2031	1101
p_0 (kPa)	200.0	186.8	157.0
p_1 (kPa)	150.0	150.0	122.6
p_2 (kPa)	113.4	85.8	79.4
p_3 (kPa)	81.5	44.2	44.6
p_4 (kPa)	16.0	16.0	16.0
$m_{f,in}$ (kg/s)	125.0	125.0	125.0
$m_{v,0}$ (kg/s)	43.31	42.09	32.11
m_a (kg/s)	13.16 ¹	13.16 ¹	13.16 ²
m_{fuel} (kg/s)	21.00	21.00	21.00
P (kW)	28,789	29,286	29,442

¹ Vapor bled from the first effect at 150 kPa. ² Extracted steam from turbine at 150 kPa.

Table 1 shows that steam and vapor pressures in the optimum modified evaporation process are lower than those in the non-optimum and optimum conventional evaporation processes. Sucrose inversion losses in all effects of evaporators in the three processes are compared in Table 2. It can be seen that sugar inversion loss is largest in the first effect of each process. Sucrose inversion loss in the first effect of the optimum modified evaporation process has the lowest value due to the smallest extracted steam pressure and temperature. As a consequence, the total sucrose inversion loss of the optimum modified evaporation process is 63% lower than that of the non-optimum conventional evaporation process.

Table 2. Comparison of sucrose inversion losses in the non-optimum conventional evaporation process, the optimum conventional evaporation process, and the optimum modified evaporation process.

Effect Number	Conventional EP		Optimum Modified EP
	Non-Optimum	Optimum	
1	$2.95 \times 10^{-3}\%$	$4.16 \times 10^{-3}\%$	$1.58 \times 10^{-3}\%$
2	$1.79 \times 10^{-3}\%$	$2.93 \times 10^{-4}\%$	$3.29 \times 10^{-4}\%$
3	$6.38 \times 10^{-5}\%$	$5.50 \times 10^{-5}\%$	$7.46 \times 10^{-5}\%$
4	$6.15 \times 10^{-6}\%$	$1.59 \times 10^{-5}\%$	$1.77 \times 10^{-5}\%$
Total	$5.38 \times 10^{-3}\%$	$4.52 \times 10^{-3}\%$	$2.00 \times 10^{-3}\%$

6. Conclusions

The comparison between the cogeneration system that used the conventional evaporation process and the cogeneration system that used the modified evaporation process was investigated in this paper. Bled vapor and steam extracted from the turbine were used, respectively, by the first and the second systems for heating duty in pan stages. Both conventional and modified evaporation processes had the total evaporator surface area of 13,000 m² and total juice heater surface area of 2500 m². They were designed to process 125 kg/s of inlet sugar juice. The distribution of evaporator surface area of the optimum modified evaporation process resulted in the maximum steam economy. The pressures of extracted steam supplied to the optimum modified evaporation process were chosen so that the turbine power output of the cogeneration system that used this process was maximized. According to simulation results obtained from the mathematical models developed for this investigation, extracted steam at a mass flow rate of 31.53 kg/s and a pressure of 157.0 kPa was required for the evaporator of the optimum modified evaporation process, and extracted steam at a mass flow rate of 13.16 kg/s and a pressure of 150.0 kPa was required for the pan stage of this process. The turbine power output was 29,442 kW for the cogeneration system that used the optimum modified evaporation process. This power output was 2.3% larger than the power output of the cogeneration system that used a non-optimum conventional evaporation process. Furthermore, since the pressure profile in the evaporator of the optimum modified process was lower than that of the non-optimum conventional process, sucrose inversion loss in the modified process was 63% lower.

Funding: This research received no external funding.

Conflicts of Interest: The authors declare no conflict of interest.

Nomenclature

A	heat transfer surface of evaporator, m ²
A_h	heat transfer surface of juice heater, m ²
c_p	specific heat capacity, kJ/kg·°C
h	specific enthalpy, kJ/kg
I	mass fraction of lost sugar due to inversion
m	mass flow rate, kg/s
P	turbine power output, kW
p	pressure, kPa
SE	steam economy
T	temperature, °C
t	retention time, min
U	heat transfer coefficient, kW/m ² ·°C
x	concentration of sugar juice, %

Greek Symbols

ε	heat loss coefficient in evaporator
η_τ	turbine efficiency
ρ	density, kg/m ³

Subscripts

<i>a</i>	vapor to pan stage
<i>b</i>	vapor to juice heater
<i>c</i>	vapor from flash tank, condenser
<i>e</i>	flash evaporation
<i>f</i>	sugar juice
<i>h</i>	juice heater
<i>i</i>	effect number
<i>l</i>	saturated liquid
<i>s</i>	steam
<i>v</i>	saturated vapor
<i>vl</i>	vapor-to-liquid
<i>x</i>	juice heating inside evaporator vessels

Superscripts

<i>in</i>	inlet of an effect
<i>out</i>	outlet of an effect

References

1. Kamate, S.C.; Gangavati, P.B. Exergy analysis of cogeneration power plants in sugar industries. *Appl. Therm. Eng.* **2009**, *29*, 1187–1194. [[CrossRef](#)]
2. Urbaniec, K.; Zalewski, P.; Zhu, X.X. A decomposition approach for retrofit design of energy systems in the sugar industry. *Appl. Therm. Eng.* **2000**, *20*, 1431–1442. [[CrossRef](#)]
3. Ensinas, A.V.; Nebra, S.A.; Lozano, M.A.; Serra, L. Design of evaporation systems and heaters networks in sugar cane factories using a thermoeconomic optimization procedure. *Int. J. Thermodyn.* **2007**, *10*, 97–105.
4. Higa, M.; Freitas, A.J.; Bannwart, A.C.; Zemp, R.J. Thermal integration of multiple effect evaporator in sugar plant. *Appl. Therm. Eng.* **2009**, *29*, 515–522. [[CrossRef](#)]
5. Bapat, S.M.; Majali, V.S.; Ravindranath, G. Exergetic evaluation and comparison of quintuple effect evaporation units in Indian sugar industries. *Int. J. Energy Res.* **2013**, *37*, 1415–1427. [[CrossRef](#)]
6. Sharan, P.; Bandyopadhyay, S. Integration of multiple effect evaporators with background process. *Chem. Eng. Trans.* **2015**, *45*, 1591–1596.
7. Palacios-Bereche, R.; Ensinas, A.V.; Modesto, M.; Nebra, S.A. Mechanical vapour recompression incorporated to the ethanol production from sugarcane and thermal integration to the overall process applying pinch analysis. *Chem. Eng. Trans.* **2014**, *39*, 374–402.
8. Chen, T.; Ruan, Q. Modeling and energy reduction of multiple effect evaporator system with thermal vapor compression. *Comp. Chem. Eng.* **2016**, *92*, 204–215. [[CrossRef](#)]
9. Chantasiriwan, S. Optimum surface area distribution in co-current multiple-effect evaporator. *J. Food Eng.* **2015**, *161*, 48–54. [[CrossRef](#)]
10. Chantasiriwan, S. Distribution of juice heater surface for optimum performance of evaporation process in raw sugar manufacturing. *J. Food Eng.* **2017**, *195*, 21–30. [[CrossRef](#)]
11. Chantasiriwan, S. Determination of optimum vapor bleeding arrangements for sugar juice evaporation process. *J. Food Proc. Eng.* **2018**, *41*, e12616. [[CrossRef](#)]
12. Chantasiriwan, S. Distribution of heating surface areas in sugar juice evaporation process for maximum energy efficiency. *J. Food Proc. Eng.* **2019**, *42*, e12998. [[CrossRef](#)]
13. Chantasiriwan, S. Increased energy efficiency of backward-feed multiple-effect evaporator compared with forward-feed multiple-effect evaporator in cogeneration system of sugar factory. *Processes* **2020**, *8*, 342. [[CrossRef](#)]
14. Eggleston, G.; Monge, A. How time between cleanings affects performance and sucrose losses in robert's evaporators. *J. Food Process. Preserv.* **2007**, *31*, 52–72. [[CrossRef](#)]
15. Rackemann, D.W.; Broadfoot, R. Evaluation of sucrose loss in evaporators for different processing configurations. *Int. Sugar J.* **2018**, *120*, 366–372.
16. Thaval, O.P.; Broadfoot, R.; Kent, G.A.; Rackemann, D.W. Determination of optimum tube dimensions for Robert evaporators. *Int. Sugar J.* **2018**, *120*, 524–530.

17. Rein, P. *Cane Sugar Engineering*, 2nd ed.; Verlag Dr. Albert Bartens KG: Berlin, Germany, 2017.
18. Vukov, K. Kinetic aspects of sucrose hydrolysis. *Int. Sugar J.* **1965**, *67*, 172–175.



© 2020 by the author. Licensee MDPI, Basel, Switzerland. This article is an open access article distributed under the terms and conditions of the Creative Commons Attribution (CC BY) license (<http://creativecommons.org/licenses/by/4.0/>).

Article

Hydrogenation of *Trans,Trans*-Muconic Acid to Bio-Adipic Acid: Mechanism Identification and Kinetic Modelling

Alessandro Rosengart ^{1,†}, Carlo Pirola ² and Sofia Capelli ^{2,*,†}

¹ Chemistry Department, Università degli Studi di Milano, Via Golgi 19, 20133 Milan, Italy; alessandro.rosengart@vtu.com

² VTU Engineering, Via G. di Vittorio n. 16, 39100 Bolzano, Italy; carlo.pirola@unimi.it

* Correspondence: sofia.capelli@unimi.it; Tel.: +39-3349026284

† These Authors have equally contributed to the present work.

Received: 13 July 2020; Accepted: 31 July 2020; Published: 2 August 2020

Abstract: The hydrogenation of *trans,trans*-muconic acid was investigated on a Pt/C 5% (wt) catalyst in a batch slurry reactor at constant hydrogen pressure (4 bar) and temperature (323, 333 and 343 K), with the purpose of developing a kinetic model able to predict conversions and product distributions. A dual-site Langmuir–Hinshelwood–Hougen–Watson (LHHW) model with hydrogen dissociation provided good fitting of the experimental data. The model parameters were regressed by robust numerical methods to overcome the computational challenges of the model parameters' collinearity. Different reaction mechanisms were tested; the best model involved two subsequent hydrogenation steps. The first step yielded from *trans,trans*-muconic acid a monounsaturated intermediate (*trans*-2-hexenedioic acid), which was further hydrogenated to adipic acid in the second step. The intermediate was subjected to an equilibrium isomerization with *cis*-2-hexenedioic acid. The activation energy values and the rate constants were calculated for the reactions, providing the first reference for *trans,trans*-muconic acid hydrogenation.

Keywords: hydrogenation; slurry reactor; muconic acid; adipic acid; LHHW model; kinetics

1. Introduction

Muconic acid (MA) is a bio-derived dicarboxylic acid, which has the potential for becoming a strategic intermediate for the polyamide and polyester industry [1–3]. Intensive biotechnological research has identified a number of genetically engineered strains able to produce *cis,cis*-muconic acid (ccMA) in quantitatively significant amounts from different feedstock [4–6]. Some engineered strains have achieved the best conversions to date, in particular, strains of *Escherichia coli* starting from glucose [7,8] and of *Pseudomonas putida* from aromatics [9,10]. The feedstock flexibility is particularly relevant as both the cellulosic and lignin fractions of the biomass could be employed as cheap and abundant raw materials, opening the door to second generation biorefinery applications for fully sustainable adipic acid production [11]. Additionally, *Saccharomyces cerevisiae* was proved effective in converting sugars to MA, paving the way to future low-cost industrial fermentations [12,13]. The reason for the strong interest toward the efficient production of ccMA and its *cis,trans* and *trans,trans* isomers is explained by the versatility of these compounds for the production of strategic bulk chemicals. For example, MA and its partially hydrogenated derivative 3-hexenedioic acid can be used for the production of unsaturated polyesters (UPE) [14–16]. Upon undergoing the Diels–Alder reaction, MA provides a class of aromatic monomers including terephthalic acid and esters [17,18]. However, the most attractive application in the short term is the possibility to use MA to produce adipic acid (AA) [19], the main building block in the polyamide industry (PA6 and PA6,6). This can be achieved by

performing a complete hydrogenation of the unsaturated MA bonds [6]. The bio-derived AA would enter a market of 2.6 Mton/year, offering a green alternative to the traditional petro-chemical process, which still causes serious safety and environmental concerns [20]. A consistent number of scientific publications has addressed the catalytic hydrogenation of MA: Table 1 provides a short overview of the most relevant contributions in the literature. Surprisingly, only qualitative insights into the reaction's mechanism have been published to date [21], and very few attempts have been made to ensure the technological scalability of the reaction [22]. In fact, these early studies on catalyst selection aimed at demonstrating the reaction's feasibility, rather than performing the optimization of the reaction's parameters such as temperature, pressure catalyst/substrate ratio and reaction duration. Focusing on the data of Table 1, it is possible to see how the reaction scalability is subject to a complicated trade-off. As a general indication, to achieve good yields and short reaction times, high concentrations of noble catalysts or higher pressures and temperatures are required, which, however, would result in higher production costs. Additionally, the choice of the reaction solvent is important: organic solvents allow more concentrated reactions, but aqueous hydrogenations are still preferable due to safety and environmental reasons. Recently, the authors achieved the complete conversion of MA to AA on a commercial Pt/C (5% wt) catalyst in aqueous media, in a batch stirred reactor at mild temperature (50–70 °C) and mild hydrogen pressure (4 bar) [23]. These promising results, together with the development of robust analytical methods to identify the reaction intermediates [24], encouraged this first detailed kinetic study on muconic acid hydrogenation, here presented. The problem of estimating the hydrogenation kinetic constants has been treated only cursorily in the literature, focusing on limited data points and providing an indication of the sole muconic acid hydrogenation apparent activation energy [10]. Still, a kinetic study is a necessary step from the perspective of a scale up of the reaction, as the definition of a reaction model can provide also better insights into the pathways of MA hydrogenation by comparing different reaction mechanisms, leading to a rational optimization of the reaction conditions. Additionally, a reaction model can be useful for simulating and comparing industrial reactor configurations, to better assess the economics of catalytic hydrogenation against those of technologies concurrently under development, such as the recently proposed electrocatalytic hydrogenation [24].

Table 1. Selected publications on muconic acid catalytic hydrogenation.

Catalyst	T (°C)	P (bar)	Time (h)	Conversion (%)	AA yield (%)	Solvent	Ref.
Pt/C 10%	25	3.5	3	100	90	Water	[25]
Pt/C 10%	25	34	2.5	100	97	Water	[8]
Ru ₁₀ Pt ₂ /SiO ₂	80	30	5	91	96	Ethanol	[26]
Pt/C 5%	160	n.a.	12	n.a.	99	Pentanol	[27]
Re/TiO ₂	210	68	5	100	90	Methanol	[28]
Pd/C 10%	25	7	4	n.a.	62	n-butanol	[29]
Royer	37	25	18	n.a.	75		[30]
Pd/C 1%	24	24	0.3	>97	>97	Water	[10]
Ni/Al ₂ O ₃ 14.2%	60	10	5	100	>99		[22]
Ni electrode	25	25	1	50	<5	Acidic solution	[24]
Pt/C 5%	60	4	2.5	100	100	Water	[23]

2. Materials and Methods

2.1. Experimental

The used reactants were *trans,trans*-muconic acid (ttMA) (Sigma Aldrich) and ultra-high-purity hydrogen (Sapio 99.9%). AA was prepared by the hydrogenation of ttMA over a commercial 5% Pt/C catalyst (Sigma Aldrich). The catalyst is characterized by a mean grain size of about 40 µm. The hydrogenation of ttMA was performed in an autoclave equipped with temperature and pressure control. The catalyst (in the amount of 0.1 g) was pre-treated in a hydrogen atmosphere at 6 bar and 260 °C for 3 h. Then, it was cooled to room temperature, and 10 mL of a 0.07 M aqueous solution

of ttMA (sodium salt) was added. The reaction mixture was heated at the desired temperature and stirred with a magnetic stirrer at 800 rpm. All the tests were performed at 4 bar of static hydrogen. The reaction was then quenched with nitrogen at different reaction times, and the catalyst was removed immediately by filtration. ttMA conversion was measured by UV-Vis analysis on the filtered sample, while selectivity was evaluated after performing a Fischer esterification reaction on the dried sample for 48 h in methanol. The analysis of the esterified products was performed with a gas chromatograph (GC Master Dani) equipped with a column Supelcowax 10 (60 m × 0.53 mm i.d., 1 µm) and a thermal conductivity detector (TCD) detector. Details of the UV-Vis and GC/TCD analyses, together with an extensive characterization of the catalyst and the reaction equipment, are reported by Capelli et al. [23]. The reactor was demonstrated to guarantee a kinetic regime, which excludes any mass transfer limitation between the gas, liquid and solid phases [23].

The kinetic experimental points were taken by tracking the conversion profiles at different temperatures (323, 333 and 343 K), maintaining the other reaction conditions unaltered. The dissolved-hydrogen-in-water values were calculated in PRO/II 9.1 (Invensys systems Inc) using the NRTL model with Henry's law expression. As the hydrogen pressure was kept constant (4 bar) and the solvent/substrate ratio was high (70:1 by weight), the dissolved hydrogen concentration could be assumed to be constant throughout the reaction [31]. Finally, the kinetic study was performed only on the ttMA isomer, to simplify the design of experiments and reduce the degrees of freedom of the reaction. An application on a real fermentation broth would probably deal with mixtures of MA isomers (*cis,cis/cis,trans/trans,trans*), because the MA-producing microorganisms yield the *cis,cis* form, which can isomerize during the product recovery steps [32].

However, the analysis of the sole ttMA has many advantages. In the first place, due to the lower solubility and higher heat of formation, ttMA is the most stable of the possible isomers [24].

Hence, the temperature and pressure optimized for ttMA hydrogenation can be readily applied for the other isomers, leaving space for further optimization. Second, the formation of other possible intermediates (i.e., 3-hexanedioic acid), which were detected during ccMA hydrogenation [21], is limited, as their amount is negligible during ttMA reduction [28,33]. Third, with the purpose of mechanism modelling, the use of ttMA allows the exclusion of the sterically hindered isomerization equilibria between *cis,cis*, *cis,trans* and *trans,trans*, which allows the removal of parallel or concurrent pathways. This further simplifies the parameter regression. The original dataset used for the model parameter regression is reported in Table S1.

2.2. Kinetic Modelling

The Langmuir–Hinshelwood–Hougen–Watson (LHHW) model was selected to define the reaction rate equations, assuming the reaction on the surface as the rate-determining step [34]. This expression decomposes the adsorption–reaction–desorption mechanism occurring on the catalyst surface into several elementary steps, allowing the consideration of the competitive adsorption equilibria of the species and the testing of the hypotheses of molecular or dissociated hydrogen reactions on the active metal. A preliminary study at constant temperature identified an LHHW competitive adsorption with a hydrogen dissociation mechanism [33]. The generic reaction rate equation is [34]:

$$R_j = \frac{k_j \cdot C_t \cdot K_{H_2} \cdot C_{H_2} \cdot K_i \cdot C_i}{(1 + \sum_k K_k \cdot C_k)^n} \quad (1)$$

K_{H_2} and K_i are the adsorption constants for hydrogen and the species i , respectively. C_i is the concentration of the species i , k_j is the kinetic constant of reaction j , and C_t is concentration of the active sites. According to the parameter tables developed by Yang and Hougen, $n = 3$ expresses the hydrogen dissociation mechanism.

The temperature dependence of the kinetic constant can be expressed using the Arrhenius equation:

$$k_j = A_j \cdot \exp\left(\frac{-E_{att,j}}{R \cdot T}\right) \quad (2)$$

The adsorption constant K_k 's temperature dependence can be modelled using the Van't Hoff equation, but in the case of high surface coverage, the temperature dependence of the adsorption can be neglected, operating a liquid-phase hydrogenation [35]; the number of parameters can therefore be reduced. However, even if LHHW is one of the most used models in reaction engineering, its mathematical structure is barely suitable for application in nonlinear regression, because of the strongly collinear nature of the parameters, which leads to ill-conditioning problems [36]. This means that while carrying out the parameter regression, the minimization of the squared error becomes challenging even for robust solvers, and the obtained results can be deeply affected by small perturbations of the input data, which are inevitable due to the experimental error. These weaknesses are particularly important for models with many adaptive parameters and reaction steps, which involve the solution of large-size nonlinear regression problems, together with the dynamic solution of the stiff ordinary differential equations (ODEs) system derived from the material balances of the chemical species.

To reduce the computational work, a common and well-established approach is the re-parametrization of the model and the removal of the less significant parameters when possible. Equation (1) was therefore re-parametrized as:

$$R_j = \frac{k_j^* C_i C_{H_2}}{(1 + \sum_k K_k \cdot C_k)^3} \quad (3)$$

where the kinetic constant of the numerator (k_j^*) is expressed as a modified Arrhenius formula (Equation (4)):

$$k_j^* = \exp\left[\widetilde{A}_j - \frac{E_{att,j}}{R} \left(\frac{1}{T} - \frac{1}{\bar{T}}\right)\right] \quad (4)$$

where \bar{T} is the average of the explored temperatures (i.e., 333 K). The constant contributions in the numerator of Equation (1) (i.e., K_{H_2} , K_{ttMA} and C_i) were all combined in the factor \widetilde{A}_j , which appears as one of the arguments of the exponential function. Equation (4) is therefore equivalent to Equation (2), but, from a mathematical viewpoint, it helps in reducing the number of conditions by simplifying the optimization problem [36]. These equations could be further re-parametrized, but this would result in a difficult interpretation of the parameters, which does not allow the definition of physical constraints to the kinetic constants. The advantage of Equation (3) is that the adsorption constants of the LHHW model (or the activation energies of the Arrhenius equations) can be constrained in the known ranges available in the literature. In particular, a range between 10 and 120 kJ mol⁻¹ for the apparent activation energy of double-bond hydrogenations on noble metal catalysts can be considered [10,31,37–39]. As for the adsorption constants, concentration values between 10⁻¹ and 10⁴ L mol⁻¹ can be taken into account [31,40,41]. This broad range is sufficient to considerably reduce the convergence time.

The calculation of the parameters can be performed by minimizing the objective function, which is the sum of squared errors (SSE):

$$SSE = \sum_i (C_{i,exp} - C_{i,calc})^2 \quad (5)$$

where $C_{i,calc}$ and $C_{i,exp}$ are, respectively, the calculated and the experimental concentration of species i .

The quality of the model was evaluated by comparing the final value of the SSE and the coefficient of determination, defined as:

$$R^2(\%) = 1 - \frac{SSE}{\sum_i (C_{i,exp} - \overline{C_{i,exp}})^2} \quad (6)$$

where $\overline{C_{i,exp}}$ is the average experimental value.

The optimization method used to reach the best parameter optimization is based on the class of robust minimization of the C++ language and BzzMath library [36]. The least squares method analysis tools were used to calculate the 95% confidence interval on the regressed. Finally, to confirm the results, different solvers were used in Matlab (lsqnonlin function) and C++ (BzzMath nonLinReg).

3. Results and Discussion

Figure 1 shows the hypothesized reaction mechanism obtained after several preliminary tests [33]. The first step converts ttMA to two isomers ((2Z)-2-hexenedioic acid (tHDA) and (2E)-2-hexenedioic acid (cHDA)). The reactions R_h01 and R_h02 are assumed to be irreversible. The concentration of the intermediates is regulated by an equilibrium isomerization reaction (R_i12). The second step of the reaction leads to the formation of adipic acid from both the intermediates (R_h13 and R_h23).

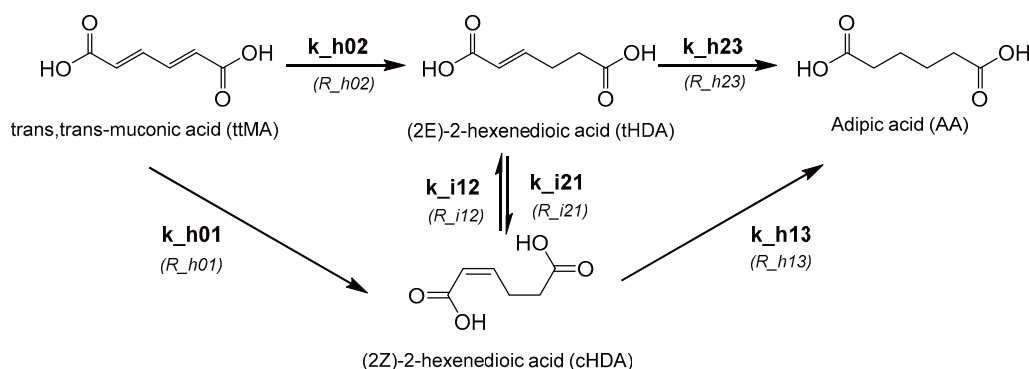


Figure 1. Reaction pathway of model LHHW_17P.

The set of ordinary differential equations defines the above mechanism (LHHW_17P), and it has 17 adaptive parameters (Table 2).

Table 2. Material balance equations solved for the model LHHW_17P.

Species	Kinetic Equation
ttMA	$\frac{dC_{ttMA}}{dt} = -R_{h01} - R_{h02} = -\frac{\overrightarrow{k}_{h01} \cdot C_{ttMA} \cdot C_{H_2}}{(1 + \sum K_i C_i)^3} - \frac{\overrightarrow{k}_{h02} \cdot C_{ttMA} \cdot C_{H_2}}{(1 + \sum K_i C_i)^3}$ (7)
cHDA	$\frac{dC_{cHDA}}{dt} = +R_{h01} - R_{h13} - R_{i12} = -\frac{\overrightarrow{k}_{h01} \cdot C_{ttMA} \cdot C_{H_2}}{(1 + \sum K_i C_i)^3} - \frac{\overrightarrow{k}_{h13} \cdot C_{cHDA} \cdot C_{H_2}}{(1 + \sum K_i C_i)^3} - \frac{\overrightarrow{k}_{i12} \cdot C_{cHDA} - \overrightarrow{k}_{i21} \cdot C_{tHDA}}{(1 + \sum K_i C_i)^3}$ (8)
tHDA	$\frac{dC_{tHDA}}{dt} = +R_{h02} - R_{h23} + R_{i12} = -\frac{\overrightarrow{k}_{h02} \cdot C_{ttMA} \cdot C_{H_2}}{(1 + \sum K_i C_i)^3} - \frac{\overrightarrow{k}_{h23} \cdot C_{tHDA} \cdot C_{H_2}}{(1 + \sum K_i C_i)^3} - \frac{\overrightarrow{k}_{i12} \cdot C_{cHDA} - \overrightarrow{k}_{i21} \cdot C_{tHDA}}{(1 + \sum K_i C_i)^3}$ (9)
AA	$\frac{dC_{AA}}{dt} = R_{h13} + R_{h23} = -\frac{\overrightarrow{k}_{h13} \cdot C_{cHDA} \cdot C_{H_2}}{(1 + \sum K_i C_i)^3} - \frac{\overrightarrow{k}_{h23} \cdot C_{tHDA} \cdot C_{H_2}}{(1 + \sum K_i C_i)^3}$ (10)
H ₂	$\frac{dC_{H_2}}{dt} = 0$ (11)

The results of the regression are listed in Table S2 and appear encouraging (supporting information). An R^2 close to 99% was obtained, and the results of the fitting can be also appreciated considering the concentration profiles and the dispersion diagram (Figure 2).

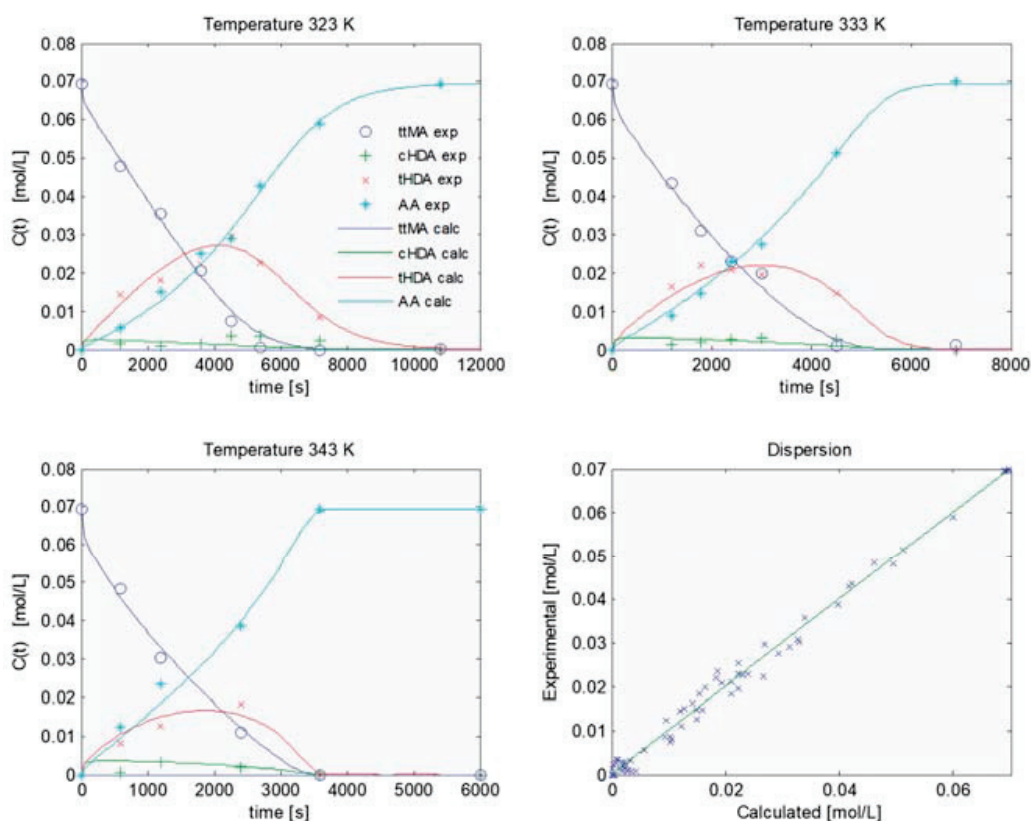


Figure 2. Results of the regression with the model LHHW_17P.

However, the statistical analysis on the obtained parameters showed little consistency, with a large value of the confidence interval for all the parameters. This result underlines the limit of the available experimental data, which lack the calculation of the experimental error due to the long and difficult experimental workup (72 h per point).

In addition, the wide confidence intervals point out the limits of this flexible model that is able to follow the concentration profile in virtue of the many adaptive parameters (which, in case of $E_{a_{h01}}$, are also close to the boundary limit). Therefore, the LHHW_17P model was abandoned, with the view of chasing a simpler and more stable formulation.

The model was reformulated in the following way: the R_{h01} reaction was excluded from the mechanism, obtaining a model with 15 parameters. In fact, the R_{h01} reaction combines ttMA hydrogenation with its isomerization. However, an isomerization to a higher-energy structure in a strong reducing environment is unlikely to occur.

Despite the model LHHW_15P having a lower number of parameters, the coefficient of determination decreased by only 0.6%. At the same time, the uncertainty of the parameters sensibly decreased. Moreover, the apparent energy values were lower and in line with the value previously calculated. On the other hand, the results of the confidence limits were still unsatisfactory for gaining a reliable indication of the kinetic constants, and the model needed further simplification.

The contribution of the group $K_{H_2}C_{H_2}$ can be neglected considering a constant H_2 concentration and the value of the adsorption constant, which are small and close to lower limit [31]. Additionally, the group $K_{AA}C_{AA}$ was neglected, since the adsorption constants of unsaturated compounds are much higher than those of the saturated ones.

Even though it was simplified in subsequent steps, the approximated model formulation (LHHW_13P) proved to be far more stable than the others, with a strong decrease in parameter collinearity. Only A_{h02} shows unacceptable values of confidence intervals, but in this case, the reason should be identified in merely numerical disturbances, as this parameter converges to a value close to

0. The susceptibility of Arrhenius constants to numerical issues can be found in the formulation of \tilde{A}_j , itself, which combines all those catalyst properties not explicitly included in the model formulation (as number of active sites). Another reason is the position of the adsorption constants of the reacting species at the numerator, which makes their value little interpretable by physical or chemical reasoning. A numerical sensitivity analysis on the regressed parameter was therefore performed, constraining the lower limit of A_{h02} to the values of 10^{-5} , 10^{-3} and 10^{-1} (this latter with the same order of magnitude of the similar parameter A_{h23}). The results are reported in Table 3; as predictable, the solver always converges to the boundary value for A_{h0} . Noticeably, the other parameters do not vary substantially with the major fluctuations of the other Arrhenius pre-exponential parameters, which, as already stated, carry all the approximations of the model simplification. Still, the quality of the regression did not worsen in any of the three cases, which makes all the sets of parameters acceptable. On the other hand, the third case becomes more interesting considering the narrower 95% confidence intervals. The regression results are graphically shown in Figure S1. In conclusion, it is possible to use the results of the sensitivity analysis to draw some reasonable boundaries for the estimates of the activation energy of muconic acid hydrogenation. E_{ah02} (ttMA to tHDA) is between the values of 27.3 and 27.5 kJ/mol, E_{ah23} (tHDA to AA) is between 39.7 and 40.1 kJ mol⁻¹, E_{ai12} (cHDA to tHDA) is between 20.5 and 29.2 kJ mol⁻¹, and E_{ai21} (tHDA to cHDA) is between 751 and 825 kJ mol⁻¹. Taking into consideration the isomerization reaction, it is evident how the cis to trans reaction is favored. Considering the overall results, the regression shows how the estimated activation energy of the hydrogenation reaction R_{h02} (first double bond) is lower than the R_{h23} one (complete hydrogenation). This means that the first hydrogenation reaction is the fastest reaction step, while to completely hydrogenate the intermediates, more energy is required [42]. This also explains the measured longer persistency of the intermediate tHDA with respect to ttMA. The ease of the isomerization of cHDA to tHDA explains instead why no cHDA accumulation was observed even at low temperature. Therefore, reactions R_{h01} , R_{i12} and R_{h13} are disadvantaged using 5%Pt/AC and water as reaction media, and also can be possibly excluded when modelling the hydrogenation of *cis,cis* muconic acid.

Table 3. Sensitivity analysis performed on the constrained regression increasing the lower acceptable value of parameter A_{h02} to three test values: 1.00×10^{-5} , 1.00×10^{-3} and 1.00×10^{-1} . The divergence columns highlight the little limited variation on the calculated parameters despite imposing new boundary limits to A_{h02} .

	LHHW_13P	Case 1		Case 2		Case 3	
	Reference Parameters	Calculated Parameters	Divergence	Calculated Parameters	Divergence	Calculated Parameters	Divergence
KttMA	9.40×10^0	9.40×10^0	0.00%	9.41×10^0	+0.11%	9.85×10^0	+4.79%
KcHDA	3.44×10^4	3.21×10^4	-6.69%	3.59×10^4	+4.36%	4.95×10^4	+43.90%
KtHDA	2.28×10^1	2.27×10^1	-0.44%	2.28×10^1	0.00%	2.52×10^1	+10.53%
Ah02	8.86×10^{-6}	1.00×10^{-5}	limited	1.00×10^{-3}	limited	1.00×10^{-1}	limited
Eah02	2.75×10^4	2.75×10^4	0.00%	2.75×10^4	0.00%	2.73×10^4	-0.73%
Ah23	1.39×10^{-1}	1.39×10^{-1}	0.00%	1.40×10^{-1}	+0.72%	2.40×10^{-1}	+72.66%
Eah23	4.01×10^4	4.01×10^4	0.00%	4.01×10^4	0.00%	3.97×10^4	-1.00%
Ai12	2.23×10^1	2.23×10^1	0.00%	2.23×10^1	0.00%	2.30×10^1	+3.14%
Ai21	5.17×10^0	5.23×10^0	+1.16%	5.24×10^0	+1.35%	5.02×10^0	-2.90%
Eai12	2.95×10^4	2.05×10^4	-30.51%	2.92×10^4	-1.02%	2.60×10^4	-11.86%
Eai21	7.63×10^5	7.53×10^5	-1.31%	7.51×10^5	-1.57%	8.25×10^5	+8.13%
Ah13	8.66×10^0	8.66×10^0	0.00%	8.72×10^0	+0.69%	8.89×10^0	-2.66%
Eah13	3.89×10^4	3.29×10^4	-15.42%	3.80×10^4	-2.31%	4.67×10^4	+20.05%
RR	7.76×10^{-4}	7.69×10^{-4}		7.69×10^{-4}		7.71×10^{-4}	

4. Conclusions

A temperature-dependent dual-site LHHW model was successfully applied to the case of the dissociative hydrogenation of ttMA salts to obtain adipic acid. The hypothesized mechanism involves a two-step reaction with the formation of two intermediates, (2Z)-2-hexenedioic acid and

(2E)-2-hexenedioic acid, that are in isomerization equilibrium. As expected, the use of a dual-site dissociative LHHW model led to computational regression issues, which were overcome by simplifying the model to reduce the number of regressed parameters, without losing the model's representativeness. The final model is able to well fit the experimental data, providing the first set of reference intervals for the kinetic constants of this hydrogenation reaction, in line with the values of other similar systems. This study opens the door to further investigations, to integrate the proposed LHHW model with, for example, direct estimates of the species adsorption constants or with extended reaction conditions, paving the way toward a sustainable adipic acid industry.

Supplementary Materials: The following are available online at <http://www.mdpi.com/2227-9717/8/8/929/s1>. Figure S1: Results of the regression with the model LHHW_13P (Case 3). Table S1: Experimental data at different temperatures for trans,trans-muconic acid hydrogenation on Pt/C 5% at 4 bar of hydrogen. Table S2: Calculated values for the different models with 95% confidence intervals and regression metrics.

Author Contributions: Conceptualization, A.R. and S.C.; methodology, A.R.; software, A.R.; formal analysis S.C.; writing—original draft preparation, A.R. and S.C.; writing—review and editing, S.C. and C.P.; supervision, C.P. All authors have read and agreed to the published version of the manuscript.

Funding: This research received no external funding.

Conflicts of Interest: The authors declare no conflict of interest.

Abbreviations

ttMA	<i>trans,trans</i> -muconic acid
tHDA	(2E)-2-hexenedioic acid
cHDA	(2Z)-2-hexenedioic acid
AA	adipic acid
LHHW	Langmuir–Hinshelwood–Hougen–Watson model
SSE	sum of squared errors
R ²	coefficient of determination

References

- Bart, J.C.J.; Cavallaro, S. Transitioning from adipic acid to bioadipic acid. 1, Petroleum-based processes. *Ind. Eng. Chem. Res.* **2015**, *54*, 1–46. [[CrossRef](#)]
- Becker, J.; Lange, A.; Fabarius, C.; Wittmann, C. Top value platform chemicals: Bio-based production of organic acids. *Curr. Opin. Biotechnol.* **2015**, *36*, 168–175. [[CrossRef](#)]
- Collias, D.I.; Harris, A.M.; Nagpal, V.; Cottrell, L.W.; Schultheis, M.W. Biobased terephthalic acid technologies: A literature review. *Ind. Biotechnol.* **2014**, *10*, 91–105. [[CrossRef](#)]
- Xie, N.-Z.; Liang, H.; Huang, R.-B.; Xu, P. Biotechnological production of muconic acid: Current status and future prospects. *Biotechnol. Adv.* **2014**, *32*, 615–622. [[CrossRef](#)] [[PubMed](#)]
- Kruyer, N.S.; Peralta-Yahya, P. Metabolic engineering strategies to bio-adipic acid production. *Curr. Opin. Biotechnol.* **2017**, *45*, 136–143. [[CrossRef](#)] [[PubMed](#)]
- Polen, T.; Spelberg, M.; Bott, M. Toward biotechnological production of adipic acid and precursors from biorenewables. *J. Biotechnol.* **2013**, *167*, 75–84. [[CrossRef](#)] [[PubMed](#)]
- Bui, V.; Lau, M.K.; Macrare, D.; Schweitzer, D. Methods for Producing Isomers of Muconic Acid and Muconate Salts. U.S. Patent 20130030215 A1, 1 January 2013.
- Niu, W.; Draths, K.M.M.; Frost, J.W.W. Benzene-free synthesis of adipic acid. *Biotechnol. Prog.* **2002**, *1*, 201–211. [[CrossRef](#)] [[PubMed](#)]
- Johnson, C.W.; Salvachúa, D.; Khanna, P.; Smith, H.; Peterson, D.J.; Beckham, G.T.; Salvachua, D.; Khanna, P.; Smith, H.; Peterson, D.J.; et al. Enhancing muconic acid production from glucose and lignin-derived aromatic compounds via increased protocatechuate decarboxylase activity. *Metab. Eng. Commun.* **2016**, *3*, 111–119. [[CrossRef](#)] [[PubMed](#)]
- Vardon, D.R.; Franden, M.A.; Johnson, C.W.; Karp, E.M.; Guarnieri, M.T.; Linger, J.G.; Salm, M.J.; Strathmann, T.J.; Beckham, G.T. Adipic acid production from lignin. *Energy Environ. Sci.* **2015**, *8*, 617–628. [[CrossRef](#)]

11. Tuck, C.O.; Perez, E.; Horváth, I.T.; Sheldon, R.A.; Poliakoff, M. Valorization of biomass: Deriving more value from waste. *Science* **2012**, *337*, 695–699. [[CrossRef](#)]
12. Aversch, N.J.H.; Krömer, J.O. Tailoring strain construction strategies for muconic acid production in *S. Cerevisiae* and *E. Coli*. *Metab. Eng. Commun.* **2014**, *1*, 19–28. [[CrossRef](#)]
13. Suástegui, M.; Yu Ng, C.; Chowdhury, A.; Sun, W.; Cao, M.; House, E.; Maranas, C.D.; Shao, Z. Multilevel engineering of the upstream module of aromatic amino acid biosynthesis in *saccharomyces cerevisiae* for high production of polymer and drug precursors. *Metab. Eng.* **2017**, *42*, 134–144. [[CrossRef](#)] [[PubMed](#)]
14. Rorrer, N.A.; Dorgan, J.R.; Vardon, D.R.; Martinez, C.R.; Yang, Y.; Beckham, G.T. Renewable unsaturated polyesters from muconic acid. *ACS Sustain. Chem. Eng.* **2016**, *4*, 6867–6876. [[CrossRef](#)]
15. Rorrer, N.A.; Vardon, D.R.; Dorgan, J.R.; Gjersing, E.J.; Beckham, G.T. Biomass-derived monomers for performance-differentiated fiber reinforced polymer composites. *Green Chem.* **2017**, *19*, 2812–2825. [[CrossRef](#)]
16. Matthiesen, J.E.; Suástegui, M.; Wu, Y.; Viswanathan, M.; Qu, Y.; Cao, M.; Rodriguez-Quiroz, N.; Okerlund, A.; Kraus, G.; Raman, D.R.; et al. Electrochemical conversion of biologically produced muconic acid: Key considerations for scale-up and corresponding techno-economic analysis. *ACS Sustain. Chem. Eng.* **2016**, *4*, 7098–7109. [[CrossRef](#)]
17. Lu, R.; Lu, F.; Chen, J.; Yu, W.; Huang, Q.; Zhang, J.; Xu, J.; Rui, L.; Lu, F.; Chen, J.; et al. Production of diethyl terephthalate from biomass-derived muconic acid. *Angew. Chemie Int. Ed.* **2015**, *55*, 249–253. [[CrossRef](#)]
18. Frost, J.W.; Miermont, A.; Schweitzer, D.; Bui, V.; Wicks, D.A. Terephthalic and Trimellitic Based Acids and Carboxylate Derivatives Thereof. U.S. Patent US8367858 B2, 5 February 2013.
19. Capelli, S.; Motta, D.; Evangelisti, C.; Dimitratos, N.; Prati, L.; Pirola, C.; Villa, A. Bio Adipic Acid Production from Sodium Muconate and Muconic Acid: A Comparison of Two Systems. *ChemCatChem* **2019**, *11*, 3075–3084. [[CrossRef](#)]
20. Bart, J.C.J.; Cavallaro, S. Transiting from adipic acid to bioadipic acid. part II. Biosynthetic pathways. *Ind. Eng. Chem. Res.* **2015**, *54*, 567–576. [[CrossRef](#)]
21. Vardon, D.R.; Rorrer, N.A.; Salvachua, D.; Settle, A.E.; Johnson, C.W.; Menart, M.J.; Cleveland, N.S.; Ciesielski, P.N.; Steirer, K.X.; Dorgan, J.R.; et al. Cis,cis-muconic acid: Separation and catalysis to bio-adipic acid for nylon-6,6 polymerization. *Green Chem.* **2016**, *18*, 3397–3413. [[CrossRef](#)]
22. Scelfo, S.; Pirone, R.; Russo, N. Highly efficient catalysts for the synthesis of adipic acid from cis,cis-muconic acid. *Catal. Commun.* **2016**, *84*, 98–102. [[CrossRef](#)]
23. Capelli, S.; Rosengart, A.; Villa, A.; Citterio, A.; Di Michele, A.; Bianchi, C.L.L.; Prati, L.; Pirola, C. Bio-adipic acid production by catalysed hydrogenation of muconic acid in mild operating conditions. *Appl. Catal. B Environ.* **2017**, *218*, 220–229. [[CrossRef](#)]
24. Matthiesen, J.E.; Carraher, J.M.; Vasiliu, M.; Dixon, D.A.; Tessonnier, J.P. Electrochemical conversion of muconic acid to biobased diacid monomers. *ACS Sustain. Chem. Eng.* **2016**, *4*, 3575–3585. [[CrossRef](#)]
25. Draths, K.M.; Frost, J.W. Environmentally compatible synthesis of adipic acid from D-glucose. *J. Am. Chem. Soc.* **1994**, *116*, 399–400. [[CrossRef](#)]
26. Thomas, J.M.; Raja, R.; Johnson, B.F.G.; O'Connell, T.J.; Sankar, G.; Khimyak, T. Bimetallic nanocatalysts for the conversion of muconic acid to adipic acid. *Chem. Commun.* **2003**, 1126–1127. [[CrossRef](#)]
27. Li, X.; Wu, D.; Lu, T.; Yi, G.; Su, H.; Zhang, Y. Highly efficient chemical process to convert mucic acid into adipic acid and DFT studies of the mechanism of the rhenium-catalyzed deoxydehydration. *Angew. Chemie-Int. Ed.* **2014**, *53*, 4200–4204. [[CrossRef](#)]
28. She, X.; Brown, H.M.; Zhang, X.; Ahring, B.K.; Wang, Y. Selective hydrogenation of trans,trans-muconic acid to adipic acid over a titania-supported rhenium catalyst. *ChemSusChem* **2011**, *4*, 1071–1073. [[CrossRef](#)]
29. Shiramizu, M.; Toste, F.D. Expanding the scope of biomass-derived chemicals through tandem reactions based on oxorhenium-catalyzed deoxydehydration. *Angew. Chemie Int. Ed.* **2013**, *52*, 12905–12909. [[CrossRef](#)]
30. Sirasani, G.; Tong, L.; Balskus, E.P. A biocompatible alkene hydrogenation merges organic synthesis with microbial metabolism. *Angew. Chemie-Int. Ed.* **2014**, *53*, 7785–7788. [[CrossRef](#)]
31. Neri, G.; Musolino, M.G.; Milone, C.; Galvagno, S. Kinetic modeling of 2,4-dinitrotoluene hydrogenation over Pd/C. *Ind. Eng. Chem. Res.* **1995**, *34*, 2226–2231. [[CrossRef](#)]
32. Carraher, J.M.; Pfennig, T.; Rao, R.G.; Shanks, B.H.; Tessonnier, J.-P. Cis,cis-muconic acid isomerization and catalytic conversion to biobased Cyclic-C₆-1,4-Diacid monomers. *Green Chem.* **2017**, 21–25. [[CrossRef](#)]

33. Rosengart, A.; Capelli, S.; Pirola, C.; Citterio, A.; Bianchi, C.L.; Prati, L.; Villa, A. Renewable adipic acid from the hydrogenation of trans, trans-muconic acid: Selection of a three phases kinetic model. *Chem. Eng. Trans.* **2017**, *57*, 931–936. [[CrossRef](#)]
34. Froment, G.F.; Bischoff, K.B.; De Wilde, J. *Chemical Reactor Analysis and Design*, 3rd ed.; Wiley: New York, NY, USA, 2011.
35. Lylykangas, M.S.; Rautanen, P.A.; Krause, A.O.I. Hydrogenation and deactivation kinetics in the liquid-phase hydrogenation of isooctenes on Pt/Al₂O₃. *Ind. Eng. Chem. Res.* **2004**, *43*, 1641–1648. [[CrossRef](#)]
36. Buzzi-Ferraris, G.; Manenti, F. *Interpolation and Regression Models for the Chemical Engineer: Solving Numerical Problems*; John Wiley & Sons: Hoboken, NJ, USA, 2010.
37. Veldsink, J.W.; Bouma, M.J.; Schöön, N.H.; Beenackers, A.C.M. Heterogeneous hydrogenation of vegetable oils: A literature review. *Catal. Rev.* **1997**, *39*, 253–318. [[CrossRef](#)]
38. Rajashekharam, M.V.; Nikalje, D.D.; Jaganathan, R.; Chaudhari, R.V. Hydrogenation of 2,4-dinitrotoluene using a Pd/Al₂O₃ catalyst in a slurry reactor: A molecular level approach to kinetic modeling and nonisothermal effects. *Ind. Eng. Chem. Res.* **1997**, *36*, 592–604. [[CrossRef](#)]
39. Jones, W.H. *Catalysis in Organic Syntheses*; Science, E., Ed.; Academic Press: Cambridge, MA, USA, 2013. [[CrossRef](#)]
40. Chaudhari, R.V.; Rode, C.V.; Deshpande, R.M.; Jaganathan, R.; Leib, T.M.; Mills, P.L. Kinetics of hydrogenation of maleic acid in a batch slurry reactor using a bimetallic Ru-Re/C catalyst. *Chem. Eng. Sci.* **2003**, *58*, 627–632. [[CrossRef](#)]
41. Zhan, Z.; Jackson, J.E.; Miller, D.J.; Zhang, Z. Kinetics of aqueous-phase hydrogenation of lactic acid to propylene glycol. *Ind. Eng. Chem. Res.* **2002**, *41*, 691–696. [[CrossRef](#)]
42. Feng, Y.; Zhou, L.; Wan, Q.; Lin, S.; Guo, H. Selective Hydrogenation of 1,3-Butadiene Catalyzed by a Single Pd Atom Anchored on Graphene: The Importance of Dynamics. *Chem. Sci.* **2018**, *9*, 5890–5896. [[CrossRef](#)]



© 2020 by the authors. Licensee MDPI, Basel, Switzerland. This article is an open access article distributed under the terms and conditions of the Creative Commons Attribution (CC BY) license (<http://creativecommons.org/licenses/by/4.0/>).

Article

Soybean Oil Epoxidation: Kinetics of the Epoxide Ring Opening Reactions

Elio Santacesaria ^{1,*}, Rosa Turco ², Vincenzo Russo ², Riccardo Tesser ² and Martino Di Serio ²

¹ CEO of Eurochem Engineering Ltd., 20139 Milano, Italy

² NICL—Department of Chemical Science, University of Naples Federico II, 80126 Naples, Italy; rosa.turco@unina.it (R.T.); vincenzo.russo@unina.it (V.R.); riccardo.tesser@unina.it (R.T.); martino.diserio@unina.it (M.D.S.)

* Correspondence: elio.santacesaria@eurochemengineering.com

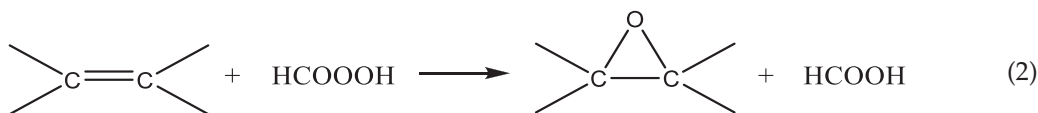
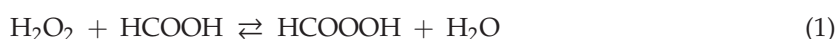
Received: 7 July 2020; Accepted: 9 September 2020; Published: 11 September 2020

Abstract: The epoxide ring opening reaction (ROR) can be considered as the most important side reaction occurring in the epoxidation of soybean oil reaction network. This reaction consistently reduces the selectivity to epoxidized soybean oil (ESBO). The reaction is also important for producing polyols and lubricants. In this work, the reaction was studied in different operative conditions to evaluate the effect on ROR rate respectively: (i) The Bronsted acidity of the mineral acid (H₂SO₄ or H₃PO₄), used as catalyst for promoting the oxidation with hydrogen peroxide of formic to performic acid, that is, the reactant in the epoxide formation; (ii) the concentration of the nucleophilic agents, normally present during the ESBO synthesis like HCOOH, HCOOOH, H₂O, H₂O₂; (iii) the stirring rate that changes the oil–water interface area and affects the mass transfer rate; (iv) the adopted temperature. Many different kinetic runs were made in different operative conditions, starting from an already epoxidized soybean oil. On the basis of these runs two different reaction mechanisms were hypothesized, one promoted by the Bronsted acidity mainly occurring at the oil–water interface and one promoted by the nucleophilic agents, in particular by formic acid. As it will be seen, the kinetic laws corresponding to the two mentioned mechanisms are quite different and this explain the divergent data reported in the literature on this subject. All the kinetic runs were correctly interpreted with a new developed biphasic kinetic model.

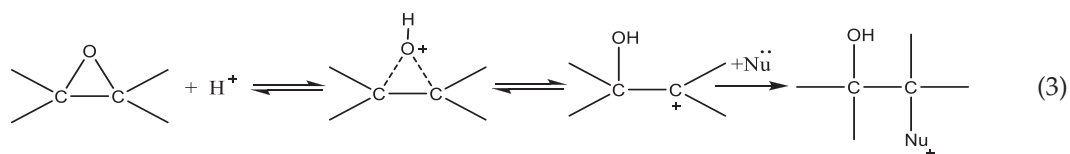
Keywords: epoxides; soybean oil; hydrogen peroxide; kinetics; ring opening reaction

1. Introduction

The epoxide ring opening reaction (ROR) of epoxidized vegetable oils has been intensively studied by many researchers interested in the production of polyols [1] or to the use as lubricants [2] or as intermediates for polyurethanes production [3]. In this case the scope is to find a good catalyst for promoting the reaction in a short time. On the contrary, in the epoxidation of vegetable oils (Prileschajew reaction [4]), ROR is an undesired side reaction lowering the yield in the production of epoxidized vegetable oils and the studies are, therefore, focused to hinder the reaction as much as possible. An example of epoxidation reaction network can be summarized as follows:



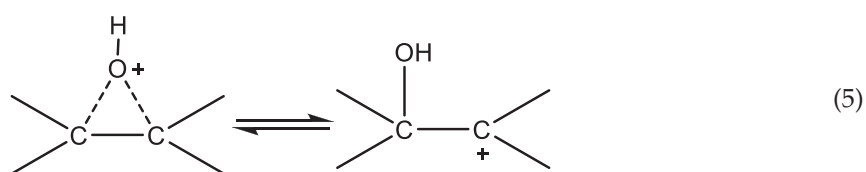
and according to our previous insights [5,6];



The sequence of reaction is the same if acetic acid is used instead of formic acid. As it can be seen, according to this mechanism, the oxirane cleavage step occurs in series with the epoxidation reaction and is promoted by a Bronsted acid environment. Considering that the reaction of formic to performic acid is catalyzed by mineral acids, such as sulfuric or phosphoric acid, the same catalyst seems to promote also the ring opening side reaction. It is important to point out that reaction (1) occurs in the aqueous phase, where the mineral acid is dissolved, while epoxide rings are dissolved in the oil phase. Therefore, it is reasonable to assume that reaction (3) occurs at the water/oil interface as suggested by us in two of our previous works [5,6] and also by other authors [7–11]. Then, considering that reaction (3) is deleterious to obtain epoxidized products at high yield, a detailed study dealing with the kinetics of this reaction can be useful in order to find the best operative conditions and to minimize the negative influence of this reaction. Different studies have already been performed, on the subject, investigating the influence of several parameters, such as the pH, the temperature, and composition of the reaction mixture [7,12]. According to these works, at a given pH, both formic and performic acids (in alternative acetic and peracetic) hydrogen peroxide and water can influence the reaction rate. From the collected experimental data, different previously cited authors proposed a global third-order reaction rate expression (4) such as:

$$r = k c_{\text{EpoX}} c_{\text{Nu}}^2 \quad (4)$$

At a first glance, it is hard to explain theoretically a second order for the nucleophilic reagents, for this reason a more reliable kinetic approach could be useful to better interpret the experimental data. Another important observation comes out from the literature analysis, that is, the pH of the reaction environment is a key feature in promoting the oxirane ring opening reaction. Moreover, according to the already mentioned authors [5–12] the ring opening reaction mainly occurs at the water–oil interface. Starting from these two observations, the reaction scheme (3) can be simplified by assuming the carbocation formation, following the protonic attack, as the rate determining step. On the basis of this conclusion, we can write:



Far from the equilibrium, the corresponding rate can be written as follows:

$$r = k c_{\text{EpoX}^+} \quad (6)$$

But, the c_{EpoX^+} concentration, can be determined by considering the first reaction in (3) nearly at equilibrium. Therefore, we can write:

$$c_{\text{EpoX}^+} = K_{\text{eq}} c_{\text{EpoX}} c_{\text{H}^+} \quad (7)$$

Then, the resulting rate law becomes:

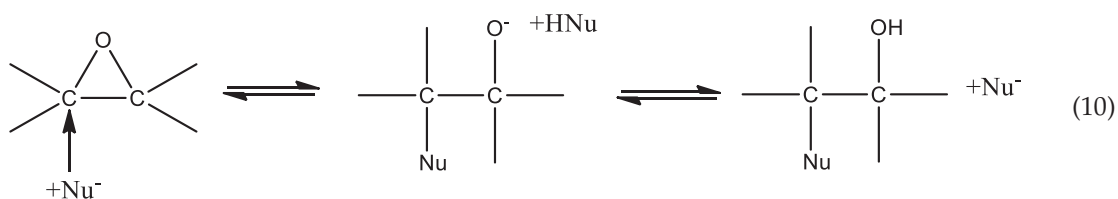
$$r = k K_{\text{eq}} c_{\text{EpoX}} c_{\text{H}^+} = k_d c_{\text{EpoX}} c_c \quad (8)$$

k_d , the overall pseudo-kinetic constant, contains also the reacting interfacial area changing according to the fluid dynamic conditions (for example the stirring speed). On the contrary, if the successive step is rate determining, that is, the nucleophilic attack to the protonated epoxide ring we can write:

$$r_{\text{Nu1}} = k_{\text{Nu1}} c_{\text{EpoX}^+} c_{\text{Nu}} = k_{\text{Nu1}} K_{\text{eq}} c_{\text{EpoX}} c_{\text{Nu}} c_{\text{H}^+} \quad (9)$$

Clearly, any nucleophilic component could have a different effect in the attack and therefore a different ring opening rate. In this case, the overall ring opening rate will result as the sum of different contributions to the reaction of respectively H_2O , HCOOH , HCOOOH , and H_2O_2 .

When the aqueous solution, in contact with ESBO, contains a strong acid like H_2SO_4 , the described mechanism and kinetics seems the most reliable, but in less acid environment also another reaction mechanism could become competitive, that is, a direct nucleophilic attack to one of the two carbon atoms of the oxirane ring, the formation of an intermediate with a negative charge and the abstraction of a proton from another nucleophilic molecule, such as:

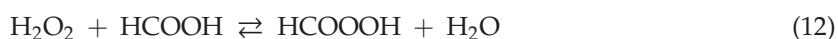


In this case, the reaction rate becomes independent of the protonic concentration but has a dependence on the square concentration of the nucleophilic molecules, that is:

$$r_{\text{Nu2}} = k_{\text{Nu2}} c_{\text{EpoX}} c_{\text{Nu}}^2 \quad (11)$$

Also in this case the nucleophilic power of the involved molecules (reactants and products) can be different and the overall ROR rate, occurring with this mechanism, is again the sum of the contributions of the different involved components (H_2O , HCOOH , HCOOOH , and H_2O_2). In conclusion, in the most general cases, the overall ring opening rate will be the sum of the two contributions $r_{\text{Nu1}} + r_{\text{Nu2}}$ related to the occurrence of respectively the two mentioned different mechanisms.

In this work, starting from an already epoxidized soybean oil, many different kinetic runs have been performed in the presence of different concentrations of mineral acids such as H_2SO_4 and H_3PO_4 , in the absence of mineral acids (auto-catalysis), in the presence of different concentrations of all the possible nucleophilic agents, in particular: HCOOH , HCOOOH , H_2O_2 , and H_2O . Moreover, also the effect of both the stirring rate (interface area) and the temperature on the reaction rate has been verified. Almost all the runs have successfully been simulated with the previously described kinetic laws and the related parameters have been determined by mathematical regression analysis. A kinetic model has been developed taking into account, when necessary, also the reactions of performic acid formation and decomposition, occurring according to the following two reactions [13]:



This last reaction consumes directly the reactant HCOOH and indirectly H₂O₂, therefore, this must be considered when ROR is performed in the presence of both formic acid and hydrogen peroxide, because, the composition of the aqueous solution changes along the time. The kinetics of these reactions have been studied in detail in a previously published work [13] and the kinetic laws and related parameters reported there have been employed in the present ROR model.

At last, another aspect arising in the ROR kinetic interpretation is the role of mass transfer, considering that epoxidized soybean oil is a viscous liquid and the epoxidized molecules are bulky molecules that diffuse slowly from the oil bulk to the interface. As it will be seen, also this aspect has been considered in the developed kinetic model.

2. Experimental Section

Materials

Epoxidized soybean oil (ESBO), with an oxirane number of 6.58 (grams of oxygen for 100 g of sample) and an iodine value of 2.0 (grams of reacted iodine per 100 g of sample) was purchased by KCHIMICA S.r.L. Hydrogen peroxide (60%) was supplied by Solvay Italia S.p.A. Formic acid (96%), sulfuric acid (97%), phosphoric acid (85%), all numbers are given as mass fraction %. All other employed reagents were provided by Merck at the highest level of purity available (>99.9%) and were used as received without further purification.

3. Apparatus

The kinetic runs have been carried out in a well stirred cylindrical jacketed glass reactors (purchased by Vetrochimica Srl, Casandrino (Naples), Italy) of 500 cm³ of volume and equipped with both a thermocouple for the reaction temperature control and a magnetically driven stirrer. The temperature control in the reactor was made by using recirculating thermostatted water.

4. Methods

The ring opening runs were carried out by working with aqueous solution of H₂O₂, water, and formic acid in the presence of sulfuric acid, phosphoric acid or in the absence of mineral acids. Degradation tests were carried out in the experimental conditions normally reached in the final part (digestion phase) of the soybean oil epoxidation process, where hydrogen peroxide and sulfuric or phosphoric acids are more diluted. In particular, a classical experimental procedure is described as it follows: a mixture containing 36.7 g of hydrogen peroxide (with a mass fraction of 20%), 5.4 g of formic acid (mass fraction 95%), and 0.64 g of sulfuric acid (mass fraction 98%) or in alternative phosphoric acid (mass fraction 85%), was added to 100 g of well mixed epoxidized soybean oil, heated at a desired temperature (normally 70 °C). As soon as the substrate reached the established temperature, the aqueous mixture was fed to the reactor (time = 0) and samples were periodically withdrawn during the 4–5 h of reaction. Then, the withdrawn samples have been cooled, a sodium bicarbonate solution was added to neutralize the residual acidity and finally anhydrous magnesium sulfate was added to remove the water. The oil of the withdrawn samples was analyzed for determining the oxirane number (ON), according to an analytical method reported by the literature [14–16]. The average titration error is inferior to 0.6%. A list of the experimental conditions for all the performed degradation runs are detailed in Table 1.

Table 1. List of ring opening experimental runs performed. 100 g of ESBO was used for all the runs. rpm = number of stirrer revolutions per minute. w = mass fraction %.

Run	Type Catalyst	Catalyst (g)	Temperature (°C)	Stirring Rate (rpm)	HCOOH (w = 96%) (g)	H ₂ O ₂ (w = 20%) (g)
1	H ₂ SO ₄ (w = 97%)	0.65	70	750	5.38	36.7
2		0.65	70	1 000	5.38	36.7
3		0.65	70	500	5.38	36.7
4		0.65	70	250	5.38	36.7
5		0.65	80	750	5.38	36.7
6		0.65	90	750	5.38	36.7
7		1.29	70	750	5.38	36.7
8		0.32	70	750	5.38	36.7
9		0.65	70	750	5.38	36.7
10		0.65	70	750	5.38	36.7
11		0.65	70	750	10.76	36.7
12		0.65	70	750	2.69	36.7
13	H ₃ PO ₄ (w = 85%)	0.65	70	250	5.16	36.7
14		0.65	70	500	5.16	36.7
15		0.65	70	750	5.16	36.7
16		1.30	70	500	5.16	36.7
17		0.79	70	500	5.16	36.7
18		0.65	70	500	10.33	36.7
19		0.65	60	500	5.16	36.7
20		0.65	80	500	5.16	36.7
21		0.65	70	500	5.16	36.7 ^a
22	None	-	70	750	4.25	H ₂ O 1.13 g ^b
23		-	70	750	4.25	7.34
24		-	70	750	4.25	H ₂ O 38.47 ^b

^a: Hydrogen peroxide 30 wt.% was used for this run. ^b: No H₂O₂ added but different amounts of water.

5. Results and Discussion

5.1. Runs Performed in the Presence of H₂SO₄

Twelve kinetic runs were performed in the presence of H₂SO₄ to evaluate the effect on the epoxide ROR rate of the following factors: (1) stirring rate (Interfacial area); (2) content of sulfuric acid; (3) temperature; (4) content of formic acid.

The list of the experimental runs performed in the presence of sulfuric acid as catalyst is reported on Table 1.

5.2. Stirring Rate Effect

In order to investigate the effect of the interfacial area, some runs, at different stirring rates, were performed, as it can be seen in Table 1. In Figure 1 the profiles along the time of the oxirane number, obtained at different stirring rates, are reported. From this figure it is evident that, in the presence of sulfuric acid (a strong Bronsted acid), by increasing the stirring rate, that is, by increasing the liquid–liquid interfacial area, the ring-opening reaction rate increases, too. This behavior means that reaction rates, in this case, are more or less affected by the mass transfer, the migration of the epoxide molecules from the bulk of the oil to the oil-water reacting interface being relatively slow. This aspect is quantitatively interpreted by the developed kinetic model that is described later.

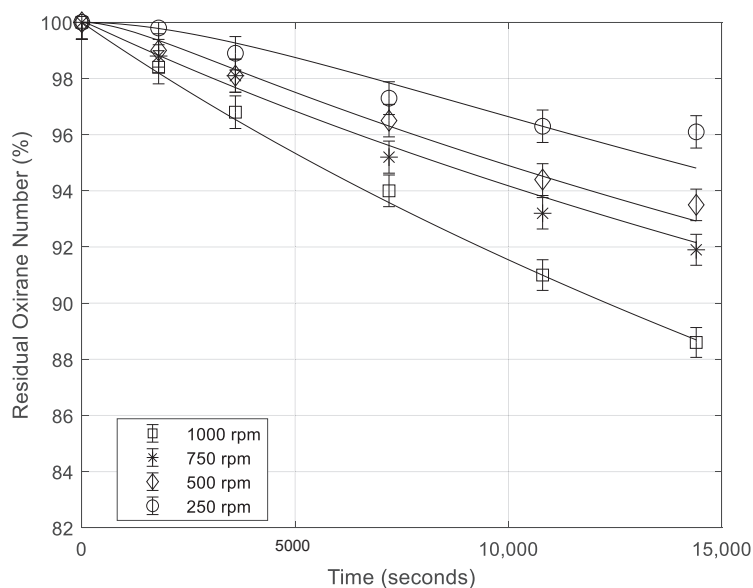


Figure 1. Residual oxirane number profiles vs. time for different stirring rate (rpm = rotations per minute). Points are experimental data lines that are calculated with the developed model (mass of catalyst 0.65 g; temperature 70 °C; mass of formic acid 5.38 g).

5.3. Effect of H_2SO_4 Concentration

In order to investigate the effect of the catalyst content, runs at different H_2SO_4 concentrations were performed, as it can be seen in Table 1. In Figure 2, the oxirane number profiles decreasing for the degradation reaction as a consequence of different catalyst concentrations are reported. As it can be seen, H_2SO_4 concentration has a great influence on the degradation rate, but the behavior is not linear.

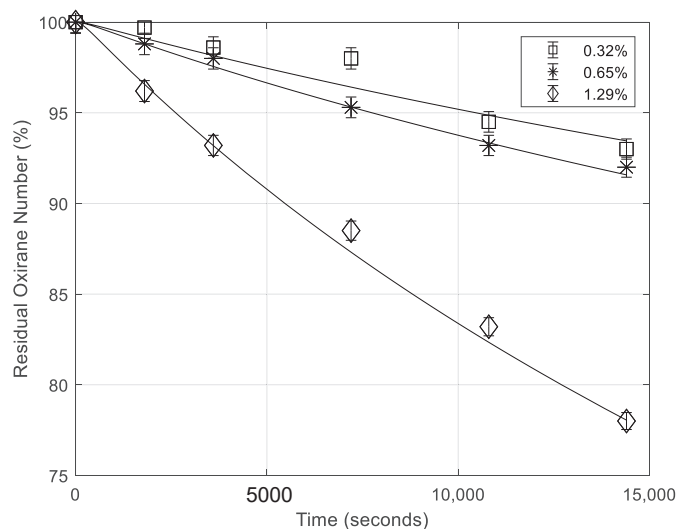


Figure 2. Residual oxirane number profiles vs. time for different sulfuric acid concentrations. Points are experimental data lines are calculated with the developed model. (temperature 70 °C; rate of agitation 750 rpm (rpm = revolutions per minute); mass of formic acid 5.38 g).

5.4. Effect of the Temperature

Runs at different temperatures were performed, taking the other conditions the same as before. In Figure 3, the obtained results are reported as profiles of the oxirane numbers, decreasing for the degradation reaction, at different temperatures.

As it can be seen, temperature has a great influence on the rate of the epoxide ring opening, in particular on the initial reaction rate.

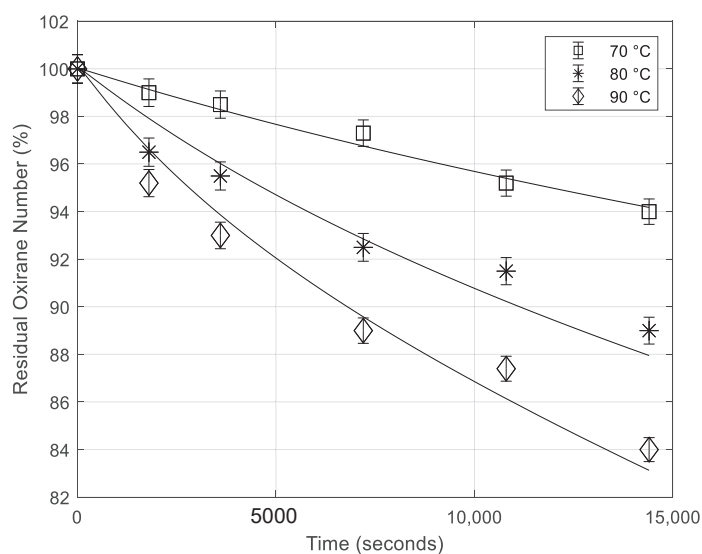


Figure 3. Residual oxirane number profiles obtained at different temperatures. Points are experimental data lines that are calculated with the developed model (mass of catalyst 0.65 g; rate of agitation 750 rpm; mass of formic acid 5.38 g).

5.5. Effect of Formic Acid Concentration

The profiles of oxirane numbers obtained for different initial formic acid concentrations, keeping constant the other conditions, are reported in Figure 4. As it can be observed also formic concentration has a relevant effect on the degradation rate of ESBO.

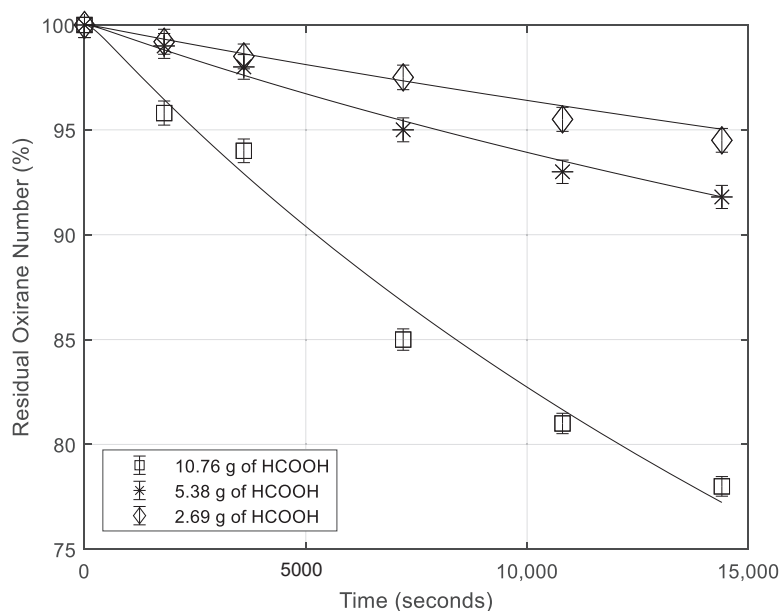


Figure 4. Residual oxirane number profiles obtained for different initial concentrations of formic acid. Points are experimental data lines that are calculated with the developed model (mass of catalyst 0.65 g; temperature 70 °C; rate of agitation 750 rpm).

5.6. Remarks on the Kinetic Results Obtained in the Presence of Sulfuric Acid

Figures 1 and 2 confirm that in the presence of a strong Bronsted acid, like sulfuric acid, the ROR occurs mainly at the liquid–liquid interface, because, the reaction rate is very sensible to the stirring rate. The effect of H_2SO_4 concentration seems not linear, because, a small difference has been observed by doubling the concentration at the lower levels and a threshold limit seems to occur at higher concentration. These findings are in agreement with Cai et al. [17], although their investigation was related to a different oil (cottonseed) and the use of acetic instead of formic acid.

As expected, the effect of the temperature is significant, while, it was not expected the remarkable influence of formic acid probably acting as nucleophilic agent. This means that our previously suggested mechanism (see relation 5) is not respected and the rate determining step seems to be the nucleophilic attack to the protonated oxirane ring. This would correspond to a kinetic law of the type:

$$r = k_{Nu} c_{Epoxy} c_{Nu} \quad (14)$$

$$\text{but } c_{Epoxy} = K_{eq} c_{Epoxy} c_{H^+} \quad (15)$$

$$\text{therefore, } r = k_{Nu} K_{eq} c_{Epoxy} c_{H^+} c_{Nu} \quad (16)$$

where c_{Nu} corresponds to the cumulative concentration of all the nucleophilic agents present in the reacting mixture. Therefore, considering that each nucleophilic agent acts with a different power, we can differentiate their contribution by writing:

$$r_{10} = k_{10} c_{Epoxy} c_{H^+} (\alpha_1 c_{FA} + \alpha_2 c_{H_2O_2} + \alpha_3 c_{PFA} + \alpha_4 c_{H_2O}) \left(\text{mol}/\text{cm}^3 \text{ s} \right) \quad (17)$$

The reaction rate is referred to the oil volume unit expressed in cm^3 .

Clearly, all these observations must be demonstrated through an opportune kinetic model able to simulate all the performed runs.

6. Runs Performed in the Presence of H_3PO_4

The kinetic runs, performed in the presence of H_3PO_4 , have been made according to the experimental conditions as reported in Table 1. The following variables have been considered, in this case: (1) the stirring rate; (2) the content of phosphoric acid; (3) the temperature; (4) the content of formic acid; (5) the content of hydrogen peroxide.

6.1. Stirring Rate Effect

In order to investigate the effect of the interfacial area, runs at different stirring rates were performed (see in Table 1 the adopted experimental conditions). In Figure 5 the oxirane number profiles, obtained for different stirring rates are reported. As it can be seen, in the presence of H_3PO_4 , this factor is poorly influent. The simulation of the different runs reported in the figure has been obtained with just a small change of the mass transfer coefficient β .

6.2. Effect of H_3PO_4 Concentration

Some runs have been performed in the presence of different H_3PO_4 concentrations (see Table 1). The obtained results are reported in the usual way in Figure 6. As it can be seen, also the phosphoric acid concentration poorly affects the degradation rate, probably, because the pH changes little by changing phosphoric acid concentration.

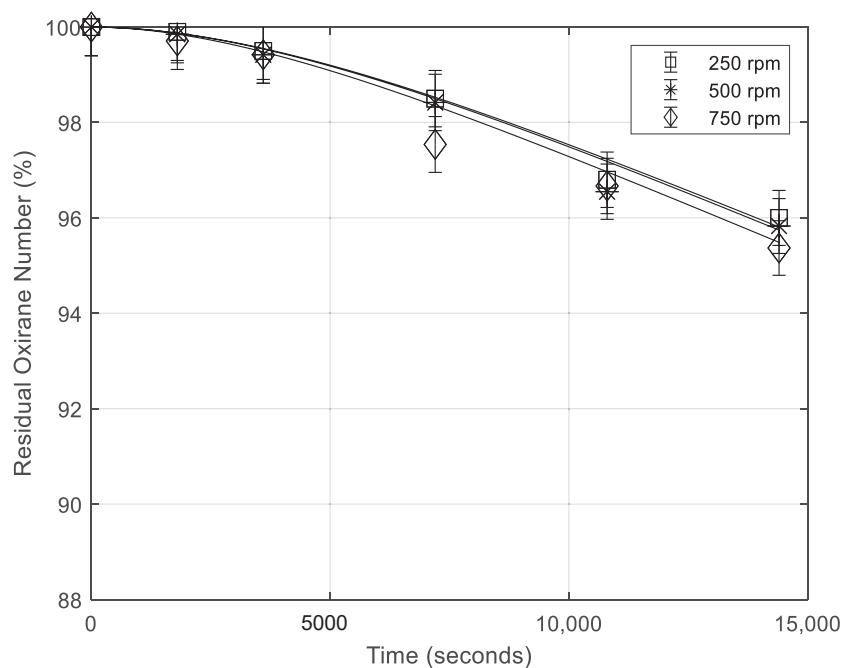


Figure 5. Residual oxirane number profiles in the presence of the same amount of H_3PO_4 for different stirring rates (rpm = number of stirrer revolution per minute). Points are experimental data lines that are calculated with the developed model (mass of catalyst 0.65 g; temperature 70 °C; mass of formic acid 5.16 g).

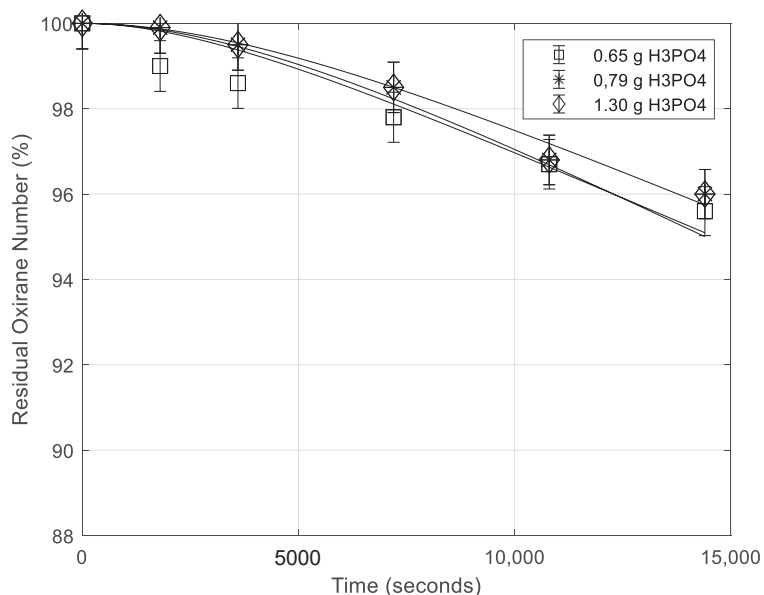


Figure 6. Residual oxirane number profiles for different contents of H_3PO_4 . All the other conditions are the same (temperature 70 °C; rate of agitation 500 rpm; mass of formic acid 5.16 g). Points are experimental data lines that are calculated with the developed model.

6.3. Effect of the Temperature

The effect of the temperature in the presence of H_3PO_4 catalyst is similar to the one observed for H_2SO_4 as it can be appreciated in Figure 7.

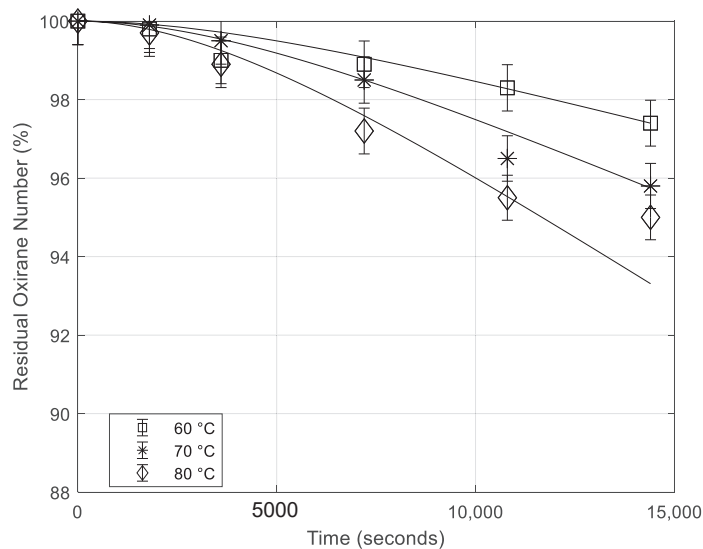


Figure 7. Residual oxirane number profiles for different temperatures. All the other conditions are the same (mass of catalyst 0.65 g; rate of agitation 500 rpm; mass of formic acid 5.16 g). Points are experimental data lines that are calculated with the developed model.

6.4. Effect of Formic Acid Content

The oxirane number profiles for different formic acid concentration are reported in Figure 8. Again, a significant effect of the HCCOH concentration on the ESBO degradation rate has been observed.

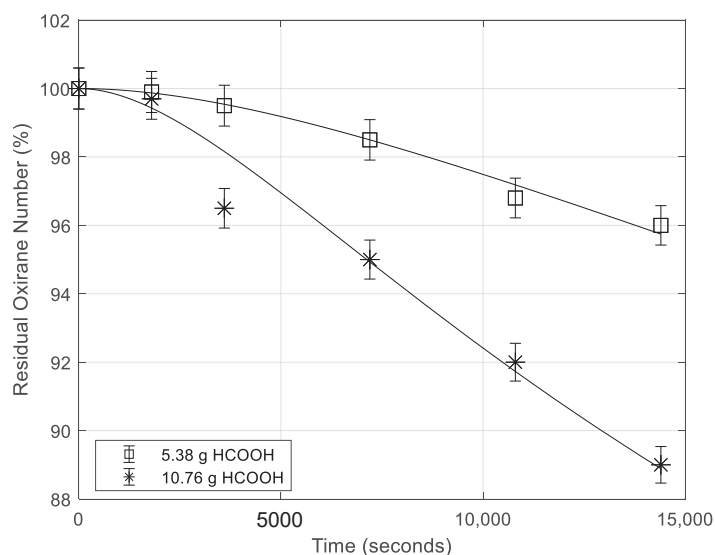


Figure 8. Residual oxirane profiles for different contents of formic acid being the same for all the other conditions (mass of catalyst 0.65 g; temperature 70 °C; rate of agitation 500 rpm). Points are experimental data lines that are calculated with the developed model.

6.5. Effect of Hydrogen Peroxide Concentration

The effect of hydrogen peroxide concentration on the ROR rate is moderate (see Figure 9), probably affecting the rate by oxidizing formic to performic acid being this last less active as nucleophilic agent. Therefore, the amount of formic acid in the reaction mixture is reduced.

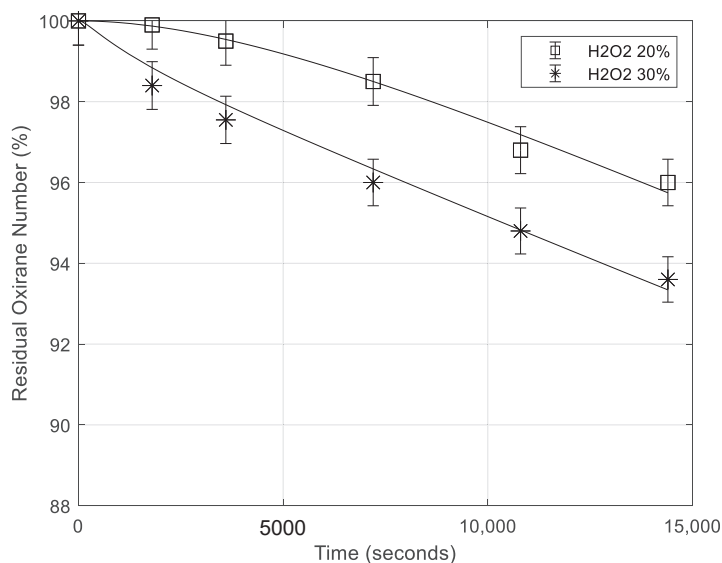


Figure 9. Residual oxirane profiles for different concentrations of hydrogen peroxide, being the same all the other conditions (mass of catalyst 0.65 g; rate of agitation 500 rpm; temperature 70 °C, mass of formic acid 5.16 g). Points are experimental data lines that are calculated with the developed model.

6.6. Remarks on the Kinetic Results Obtained in the Presence of H_3PO_4 Catalyst

We observed a great difference in the runs performed in the presence of H_3PO_4 with respect to the ones made in the presence of H_2SO_4 , in particular for what concerns the effect of stirring rate. While, in the presence of sulfuric acid the effect of the interface area was significant, and in the case of phosphoric acid a very small influence was observed, this behavior can be explained by assuming that phosphoric acid strongly interacts with the oxygen of the epoxide ring stabilizing it and giving place to a complex having good surfactant properties. In this case, a high interface area is formed also at low stirring rates but this is not followed by an increase in the degradation rate.

Another difference observed is the very low influence of the phosphoric acid concentration on the epoxide ring opening rate, although this behavior could be in agreement with the small influence of sulfuric acid concentration that has been observed at low concentration levels.

However, the kinetic behavior of ROR in the presence of H_3PO_4 suggests the prevalence of the already suggested mechanism (10), characterized by the attack of a nucleophilic anion to one of the two carbon atoms of the epoxide ring followed by a proton abstraction by the negatively charged oxygen. A mechanism of this type is in agreement with the kinetic law previously reported in relation (11) and with the observation made by different authors [7,8,11–13]. We can write now relation (11) in a more detailed way as:

$$r_{11} = k_{11} c_{\text{EpoX}} \left(\sum_i \gamma_i c_{\text{Nu}_i}^2 \right) \text{ (mol/(cm}^3 \text{ s))} \quad (18)$$

As for r_{10} the reaction rate is referred to the oil volume unit expressed in cm^3 .

Clearly, it cannot be excluded, in certain operative conditions, the intervention of both the described mechanisms, in this case the ROR reaction rate becomes the sum of the two contributions r_{10} and r_{11} .

Then, for what concerns the influence of formic acid, one of the four nucleophilic components, the behavior can be considered similar to the one observed for sulfuric acid but with a somewhat lower activity, confirming the protective effect of phosphoric acid molecule on the stability of the epoxide rings. Hydrogen peroxide seems to have an indirect effect on ROR rate by converting formic acid into performic acid, hence reducing its concentration. Finally, a relevant effect of the temperature has been observed.

7. Runs Performed in the Absence of Mineral Acids

Some runs have been performed in the absence of mineral acid with the scope to evaluate separately the contribution of formic acid or of the other nucleophilic components to the ring opening reaction. In Table 1, the runs performed, at this purpose, are summarized. In Run 22 of Table 1 only formic acid has been put in contact with ESBO. The obtained ESBO degradation for this run is shown in Figure 10. As it can be seen, the effect of concentrated formic acid is considerable in promoting the oxirane ring degradation rate, in agreement with the large effect previously observed by changing the HCOOH concentration in the presence of mineral acids. Run 23 was performed in absence of mineral acids but in the presence of both formic acid and hydrogen peroxide, which means to operate in the presence of three components and the third one being performic acid formed in situ. The obtained results are shown in Figure 10 for a useful comparison. By comparing these two runs it can be observed that in the last case the rate of oxirane ring opening is much slower probably because HCOOH is more diluted and consistently substituted by the performic acid which is much less acidic and less active as nucleophile. On the other hand, the effect of HCOOH dilution is again confirmed with run 24 always reported in Figure 10, occurring in the presence of a consistent amount of water.

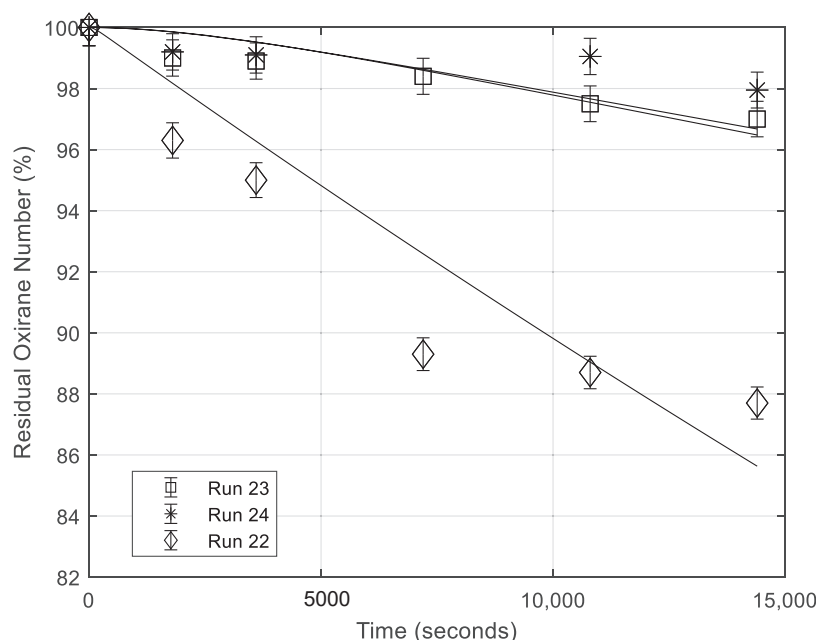


Figure 10. Evolution with time of the residual oxirane number in the presence of HCOOH alone (run 22), at much lower concentration because diluted with water (run 24), in the presence of H₂O₂, and performic acid (run 23).

8. Elaboration of the Experimental Kinetic Data of Ring Opening Reactions (ROR)

Description of the Adopted Kinetic Model

The selectivity of the soybean oil epoxidation is significantly lowered by the occurrence of some undesired side reactions characterized by the oxirane ring opening. These reactions become important in particular during the maturation step of the epoxidation process that has the scope of reaching the target values of both the oxirane number (greater than 6.5) and the iodine number (lower than 1–1.5). This phase of the ESBO production requires a long reaction time, at relatively high temperature (70–75 °C). Moreover, consider also that the epoxidation rate decreases with the double bonds disappearance, while, the ring opening reaction rate increases for the increase of the oxirane ring concentration. During this phase of the industrial process, an aqueous solution containing: HCOOH,

HCOOOH, H₂O₂ and H₂O, and H₂SO₄ or H₃PO₄ remains in contact with the epoxidized oil for at least 2–3 h. During this time epoxidation reaction continues consuming HCOOOH and indirectly H₂O₂ but, as we have previously seen, HCOOOH also decomposes to CO₂ and H₂O, further decreasing the H₂O₂ concentration and decreasing the HCOOH concentration, too. Therefore, the kinetic runs of the ring opening reaction (ROR) have been made by putting in contact an already epoxidized soybean oil with an aqueous solution of a composition similar to the one that we can find during the maturation phase of the process. As seen, runs have been made in the presence of sulfuric acid, phosphoric acid and in the absence of mineral acids to evaluate the role of both the solution acidity and the nucleophilic components concentrations. All the runs made have been simulated with a unique kinetic model and the parameters giving the best agreement with the experimental data have been determined. The model is based on the solution of the following differential equations system:

$$\frac{dc_{FA}}{dt} = -r_1 \text{ Rate of formic acid transforming in HCOOOH (mol/(L s))} \quad (19)$$

$$\frac{dc_{H_2O_2}}{dt} = -r_1 \text{ Rate of H}_2\text{O}_2 \text{ consumption to give HCOOOH (mol/(L s))} \quad (20)$$

$$\frac{dc_{PFA}}{dt} = r_1 - r_2 \text{ (} r_1 = \text{PFA formation } r_2 = \text{PFA decomposition) (mol/(L s))} \quad (21)$$

$$\frac{dc_{H_2O}}{dt} = r_1 + r_2 \text{ Rate of water formation (mol/L s)} \quad (22)$$

$$\frac{dc_{ESBO-bulk}}{dt} = -r_t \text{ Rate of ESBO molecules mass transfer} \quad (23)$$

$$\frac{dc_{ESBO-interface}}{dt} = r_t - r_g \text{ ESBO accumulation at the interface} \quad (24)$$

where, we have:

$$r_1 = k_1 c_{H^+} c_{FA} c_{H_2O_2} \left(1 - \frac{1}{K_{eq}} \frac{c_{PFA} c_{H_2O}}{c_{FA} c_{CO_2}} \right) \quad (25)$$

$$r_2 = k_2 c_{PFA} \quad (26)$$

The rates of these reactions occurring in the aqueous phase are referred to as the aqueous volume unit expressed in liter (L).

$$\begin{aligned} K_{eq} &= K_{eq,ref} \exp\left[\left(\frac{-\Delta H}{R}\right)\left(\frac{1}{298} - \frac{1}{T}\right)\right] \\ &= (1.6 \pm 0.1) \exp\left[\left(\frac{10,000 \pm 900}{8.314}\right)\left(\frac{1}{298} - \frac{1}{T}\right)\right] \end{aligned} \quad (27)$$

The dimensions are k_1 (L²/(mol² s)) and k_2 (L/s). Equations (25)–(27) are relationships determined in a previous work published by the same authors⁶. r_1 being the rate of performic acid formation and r_2 the decomposition rate, the volume is referred to as the aqueous phase.

The kinetic parameters reported in the already mentioned work⁶ are somewhat different in the presence of sulfuric acid, phosphoric acid or in the absence of mineral acids as it can be seen in Table 2. On the contrary, the equilibrium constant is obviously independent of the employed catalyst and are reported in relation (27).

Table 2. Kinetic parameters for the formation and decomposition of performic acid in different environment taken from [13]. Here, 323 K has been taken as the reference temperature.

Catalyst	k_{1-323} (L ² /mol ² s)	k_{2-323} (L/s)	ΔE_1 (J/mol)	ΔE_2 (J/mol)
H ₂ SO ₄	$(1.03 \pm 0.05) \times 10^{-3}$	$(9.61 \pm 1.56) \times 10^{-5}$	$47,518 \pm 3061$	$87,497 \pm 2374$
H ₃ PO ₄	$(1.16 \pm 0.13) \times 10^{-3}$	$(1.36 \pm 0.32) \times 10^{-4}$	$83,816 \pm 2905$	$98,989 \pm 3014$
NONE	$(1.20 \pm 0.16) \times 10^{-3}$	$(1.60 \pm 0.32) \times 10^{-4}$	$55,304 \pm 1288$	$105,073 \pm 8419$

The term r_g is the overall ring opening reaction rate considering as the sum of the contribution of the two described mechanisms, that is:

$$r_g = (r_{10} + r_{11}) \text{ (mol/cm}^3 \text{ s)} \quad (28)$$

$$r_{10} = k_{10} c_{\text{EpoX}} c_{\text{H}^+} (\alpha_1 c_{\text{FA}} + \alpha_2 c_{\text{H}_2\text{O}_2} + \alpha_3 c_{\text{PFA}} + \alpha_4 c_{\text{H}_2\text{O}}) \text{ (mol/(cm}^3 \text{ s))} \quad (29)$$

r_{10} is the ring opening rate promoted by the acid environment in which the rate-determining step is the reaction of the protonated ring reacting with the nucleophilic agent. The parameters from α_1 to α_4 differentiate the contribution given by each nucleophilic molecule.

$$r_{11} = k_{11} c_{\text{EpoX}} (\gamma_1 c_{\text{FA}}^2 + \gamma_2 c_{\text{H}_2\text{O}_2}^2 + \gamma_3 c_{\text{PFA}}^2 + \gamma_4 c_{\text{H}_2\text{O}}^2) \text{ (mol/cm}^3 \text{ s)} \quad (30)$$

r_{11} is the ring opening rate directly promoted by the nucleophilic agents. The parameters from γ_1 to γ_4 differentiate the contribution of each nucleophilic molecule.

Both r_{10} and r_{11} are referred to the oil volume unit expressed in cm^3 . k_{10} and k_{11} dimensions are both ($\text{l}^2/(\text{mol}^2 \text{ s})$). Finally, r_t is the mass transfer rate of the ESBO molecules from the liquid bulk to the interface where the ring opening reactions occur.

$$r_t = \beta (c_e - c_f) \text{ (mol/(cm}^3 \text{ s))} \quad (31)$$

The H^+ concentration changes more or less according to the acid used as catalyst and the temperature and for a correct simulation we have to evaluate such concentration.

9. Determination of the Hydrogen Ions Concentration at Different Temperature

As we have seen, r_1 and r_{10} are both promoted by the acid environment. A rigorous approach would be to calculate what is the H^+ concentration at the reaction temperature and how the H^+ concentration changes along the time in the aqueous reactants by adding a solution of hydrogen peroxide and formic acid to the acid catalyst. At this purpose, we have developed three different program codes for solving the set of algebraic equations (multiple protonation equilibria) for determining respectively the H^+ concentration in a solution of formic acid (the solution to be added), in a solution of concentrated sulfuric acid or phosphoric acid (solutions in contact with the oil), and in a solution containing both formic and sulfuric or phosphoric acids (solution formed by adding the oxidant mixture to oil and catalyst). Before considering the three mentioned cases, in Table 3, the dissociation constants are reported at 25°C for all the acids involved in the reaction.

Table 3. Ionic dissociation constants at 25°C .

Type of Dissociation	Dissociation Constant at 25°C and Ionic Product
$\text{HCOOH} \rightarrow \text{H}^+ + \text{HCOO}^-$	1.77×10^{-4}
$\text{HCOOOH} \rightleftharpoons \text{H}^+ + \text{HCOOO}^-$	7.90×10^{-8}
$\text{H}_3\text{PO}_4 \rightleftharpoons \text{H}^+ + \text{H}_2\text{PO}_4^-$	7.11×10^{-3}
$\text{H}_2\text{PO}_4^- \rightleftharpoons \text{H}^+ + \text{HPO}_4^{2-}$	6.31×10^{-8}
$\text{HPO}_4^{2-} \rightleftharpoons \text{H}^+ + \text{PO}_4^{3-}$	4.80×10^{-13}
$\text{H}_2\text{SO}_4 \rightleftharpoons \text{H}^+ + \text{HSO}_4^-$	2.40×10^6
$\text{HSO}_4^- \rightleftharpoons \text{H}^+ + \text{SO}_4^{2-}$	1.20×10^{-2}
$\text{H}_2\text{O} \rightleftharpoons \text{H}^+ + \text{OH}^-$	$K_w = c_{\text{H}^+} c_{\text{OH}^-} = 10^{-14}$

10. Hydrogen Ion Concentration in the System Formic–Performic Acid

In the absence of mineral acids the acidity is only due to the dissociation of formic acid:



The dissociation constant of performic acid is too low and therefore can be neglected.

Hence, we can write:

$$K_{aFA} = \frac{c_{H^+} c_{HCOO^-}}{c_{FA}} \quad (33)$$

To evaluate correctly the pH of the solution at different temperatures, it is required to know the dependence of both K_{aFA} and K_w on this parameter. K_w is highly temperature dependent, hence increasing with the temperature. Different exhaustive studies have been devoted to this subject [18–20].

The following relation, although has not physical mean, well interpolates the K_w values at different temperatures:

$$K_w = 8.754 \times 10^{-10} e^{-\left(\frac{1.01 \times 10^6}{T^2}\right)} \quad (34)$$

Different works have been published on the dissociation constant of HCOOH [21,22] According to Harned and Embree [21] the dissociation constant of HCOOH as a function of temperature can be determined with the following relationship:

$$\lg K_{aFA} = -\left(\frac{173.624}{T}\right) + 17.88348 \lg T - 0.0280397 T - 39.06123 \quad (35)$$

More recently, Hwa Kim et al. [22] have proposed the following relation:

$$pK_{aFa} = -57.528 + \frac{2773.9}{T} + 9.1232 \lg T \quad (36)$$

that correctly reproduces to a larger extent the dependence of K_{aFa} on the temperature.

In order to evaluate the c_{H^+} concentration for different HCOOH concentrations and different temperatures the following algebraic four equations system, containing both mass and charge balances equations, must be solved:

$$\begin{aligned} (1) \quad & (c_{H^+} c_{HCOO^-}) - K_{aFA} c_{FA} = 0 \\ (2) \quad & (c_{H^+} c_{OH^-}) - K_w = 0 \\ (3) \quad & c_{FA} + c_{HCOO^-} - c_{FA}^0 = 0 \\ (4) \quad & c_{HCOO^-} + c_{OH^-} - c_{H^+} = 0 \end{aligned} \quad (37)$$

in which K_w and K_{aFA} can be calculated with the previously reported equations.

11. Hydrogen Ion Concentration in the System H₂SO₄-Formic Acid

Sulfuric acid is completely dissociated as:



The second dissociation constant (Relation (39)) is equal to $K_{2sulf} = 1.2 \times 10^{-2}$ at 25 °C, that is a dissociation constant greater than the one of formic acid:



The dependence of this second dissociation constant on the temperature has been studied by three different works respectively published by: (Dickson et al. [23]; Wu and Feng, [24]; Marshall and Jones, [25]). Marshall and Jones determined K_{2sulf} in a very large range of temperature. The data have been interpolated with the relation:

$$\lg K_{2sulf} = 56.889 - 19.8858 \lg T - \frac{2307.9}{T} - 0.006473 T \quad (40)$$

or alternatively with the more approximated relation:

$$\lg K_{2\text{sulf}} = 91.471 - 33.0024 \lg T - \frac{3520.3}{T} \quad (41)$$

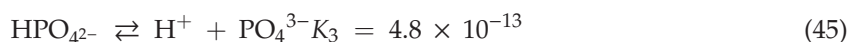
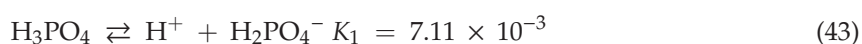
Also in this case for evaluating the H^+ concentration the following system of algebraic equations, containing both mass and charge balances equations, must be solved:

$$\begin{aligned} (1) \quad & (c_{\text{H}^+} c_{\text{HSO}_4^-}) - K_{1\text{sulf}} c_{\text{H}_2\text{SO}_4} = 0 \\ (2) \quad & (c_{\text{H}^+} c_{\text{HSO}_4^-}) - K_{2\text{sulf}} c_{\text{HSO}_4^-} = 0 \\ (3) \quad & (c_{\text{H}^+} c_{\text{OH}^-}) - K_w = 0 \\ (4) \quad & c_{\text{H}_2\text{SO}_4} + c_{\text{HSO}_4^-} + c_{\text{SO}_4^{2-}} - c_{\text{H}_2\text{SO}_4}^0 = 0 \\ (5) \quad & c_{\text{HSO}_4^-} + 2 c_{\text{SO}_4^{2-}} + c_{\text{OH}^-} + c_{\text{HCOO}^-} - c_{\text{H}^+} = 0 \\ (6) \quad & (c_{\text{H}^+} c_{\text{HCOO}^-}) - K_{\text{aFA}} c_{\text{FA}} = 0 \\ (7) \quad & c_{\text{HCOO}^-} + c_{\text{FA}} - c_{\text{FA}}^0 = 0 \end{aligned} \quad (42)$$

in which K_w , $K_{2\text{sulf}}$, and K_{aFA} can be calculated with the previously reported equations.

12. Hydrogen Ion Concentration in the System H_3PO_4 -Formic Acid

In this case the acidity of the system is the result of the contribution of both H_3PO_4 and HCOOH . H_3PO_4 gives place to three different dissociation equilibria:



As it can be seen K_1 is comparable with the dissociation constant of formic acid

$K_{\text{aFA}} = 1.8 \times 10^{-4}$, therefore, the H^+ concentration can be calculated rigorously by considering all the equilibrium constants but in particular K_1 , K_{aFA} , and their dependence on the temperature. The dependence of K_1 on the temperature was determined by R. Bates [26] for which data were interpolated with the following relationship:

$$-\lg K_1 = \frac{799.31}{T} - 4.5535 + 0.013486 T \quad (46)$$

C.A. Vega et al. [27] have determined both K_1 and K_2 as a function of the temperature and data determined have been fitted with the relation:

$$pK_1 = \frac{A}{T} + B + C \lg T \quad (47)$$

The parameters A, B, and C are reported in their work.

However, the equilibrium constants K_2 and K_3 are too small and their dependence on the temperature can be neglected, so we have considered only the dependence of K_1 and K_{aFA} adopting respectively the relations (46) and (35).

To obtain the c_{H^+} concentration in a solution containing H_3PO_4 and HCOOH requires to solve the following system of eight algebraic equations containing both mass and charge balances equations:

$$\begin{aligned}
(1) \quad & (c_{\text{H}^+} c_{\text{H}_2\text{PO}_4^-}) - K_1 c_{\text{H}_3\text{PO}_4} = 0 \\
(2) \quad & (c_{\text{H}^+} c_{\text{HPO}_4^{2-}}) - K_2 c_{\text{H}_2\text{PO}_4^-} = 0 \\
(3) \quad & (c_{\text{H}^+} c_{\text{PO}_4^{3-}}) - K_3 c_{\text{HPO}_4^{2-}} = 0 \\
(4) \quad & (c_{\text{H}^+} c_{\text{OH}^-}) - K_w = 0 \\
(5) \quad & c_{\text{H}_3\text{PO}_4} + c_{\text{H}_2\text{PO}_4^-} + c_{\text{HPO}_4^{2-}} + c_{\text{PO}_4^{3-}} - c_{\text{H}_3\text{PO}_4}^0 = 0 \\
(6) \quad & c_{\text{H}_2\text{PO}_4^-} + 2 c_{\text{HPO}_4^{2-}} + 3 c_{\text{PO}_4^{3-}} + c_{\text{OH}^-} + c_{\text{HCOO}^-} - c_{\text{H}^+} = 0 \\
(7) \quad & (c_{\text{H}^+} c_{\text{HCOO}^-}) - K_{\text{aFA}} c_{\text{FA}} = 0 \\
(8) \quad & c_{\text{HCOO}^-} + c_{\text{FA}} - c_{\text{FA}}^0 = 0
\end{aligned} \tag{48}$$

13. Simulation of the Runs Performed in the Presence of Sulfuric Acid

The runs performed in the presence of sulfuric acid have already been described. The adopted operative conditions of the runs considered are summarized in Table 1. As it can be seen, 12 runs have been performed by changing: the stirring rate, the sulfuric acid concentration, the temperature, the formic acid concentration, and the hydrogen peroxide concentration. In the presence of sulfuric acid as a catalyst, the contribution of formic acid to the protonic concentration is practically null and the pH of the solution changes very little along the time. Moreover, the contribution of r_{11} to the ring opening rate is negligible and we can put $r_{11} \approx 0$. All the 12 runs of Table 1, made in the presence of sulfuric acid, were simulated with the described model and the obtained agreements are reported in Figures 1–4, while, the kinetic parameters giving the best fitting are reported in Table 4.

Table 4. Kinetic parameters and initial protonic concentration used for simulating the ring opening reaction (ROR) runs performed in the presence of sulfuric acid.

Run	$k_{10} (\times 10^6)$	$\beta (\times 10^3)$	$c_{\text{H}^+}^0$
1	0.656 ± 0.013	6.06 ± 0.12	0.1675
2	0.929 ± 0.018	15.15 ± 0.30	0.1675
3	0.606 ± 0.011	0.50 ± 0.02	0.1675
4	0.545 ± 0.010	0.13 ± 0.01	0.1675
5	1.111 ± 0.022	5.05 ± 0.11	0.1660
6	1.939 ± 0.037	5.05 ± 0.11	0.1658
7	0.990 ± 0.019	3.23 ± 0.06	0.3258
8	1.010 ± 0.020	2.22 ± 0.05	0.0869
9	0.656 ± 0.013	2.42 ± 0.05	0.1667
10	0.636 ± 0.012	3.03 ± 0.02	0.1667
11	1.515 ± 0.030	2.82 ± 0.05	0.1450
12	0.626 ± 0.011	3.83 ± 0.04	0.1730

k_1 , k_2 , and K_{eq} have been imposed on the basis of the relations (25)–(27) and the parameters of Table 2, already reported in our previous work [13]. k_{10} and β have been obtained by regression analysis on the experimental data, while, the α values have been roughly estimated from all the runs made resulting approximately: $\alpha_1 = 40$ and α_2 , α_3 , and α_4 all equal to about 1. These values show the greater nucleophilic power of formic acid with respect to the other molecules (H_2O , H_2O_2 , HCOOOH) and have been estimated considering all the runs made also in the presence of phosphoric acid and HCOOH alone.

Runs 1–4 have been performed all at 70 °C, in the same operative conditions changing only, the stirring rate, 250 rpm for run 4500 rpm for run 31,000 rpm for run 2 and 750 for run 1. k_{10} resulted about the same for runs 1, 3, and 4 with an average value of 6×10^{-7} , while, run 4 requires a somewhat greater but reasonable parameter of 9.2×10^{-7} . We can conclude that for these runs the rate changes for the effect of mass transfer, changing the interface area with the stirring speed. As a matter of fact,

the β parameter changes from 1.3×10^{-4} at 250 rpm to 5×10^{-4} at 500 rpm, 6×10^{-3} at 750 rpm and 1.5×10^{-2} at 1000 rpm. All the other runs have been performed at 750 rpm.

Run 1, 5, and 6 have been made at different temperatures of respectively 70, 80, and 90 °C. Again k_1 , k_2 , and K_{eq} have been imposed on the basis of the relations (25)–(27) and parameters of Table 2. On the contrary, k_{10} and β have been obtained by regression analysis on the experimental data. α_1 has been kept constant equal to 40 and α_2 , α_3 , and α_4 all equal to 1 giving only to k_{10} the possibility to change with the temperature. Considering the small number of runs available this approximation is reasonable. As it can be seen, k_{10} correctly increases with the temperature, while, the mass transfer parameter remains approximately constant. The dependence of k_{10} can be calculated from the slope of the Arrhenius plot related to the runs 1, 5, and 6 that resulted quite linear. The activation energy resulted $\Delta E_{10} = 55,000 \pm 2500$ Joule/mole.

Runs 7, 8, and 9 have been performed in the same conditions changing only the amount of sulfuric acid added to the aqueous solution that is 1.29 g for run 7, 0.32 g for run 8, and 0.65 for run 9. Moreover, run 9 is identical to run 1. The simulations of these runs show a little change of k_{10} and β value and this confirms that H^+ concentration strongly affects the ring opening reaction rate and that the adopted model is correct. The small observed differences can be due to the interface area that is the other factor influencing the reaction rate.

Finally, runs 10, 11, and 12 have been made in the same conditions changing only the formic acid concentration. As we have already seen, HCOOH concentration has a strong effect on the ring opening reaction rate. This observation imposes to differentiate its contribution as the most efficient nucleophilic component. We estimated that the nucleophilic power of HCOOH is at least 40 times that of the other components. This difference is satisfactory expressed by the α_1 parameter. Run 10 containing 0.65 g of HCOOH (79 wt.%) was performed in the identical conditions as run 1 and 9 and is well simulated with very similar parameters. Run 12 was performed in the presence of 2.69 g of HCOOH and is correctly simulated with parameters similar to the ones of run 10. Run 11, containing an excess of HCOOH corresponding to 10.76 g, gives a k_{10} value that is about double of the previous one. This probably could be due to the fact that we neglected the possibility of the occurrence of the ring opening reaction also inside the oil bulk and hence correlated with the component solubilities although, according to Campanella and Baltanás (Campanella and Baltanás, 2008), the formic acid dissolved in oil is only 3–4% of the total amount. However, by averaging the obtained kinetic parameters in the optimal fitting of all the different performed runs we can write finally:

$$k_{10} = (6.56 \pm 0.27) \times 10^{-7} \exp\left[\left(\frac{-55,000 \pm 2500}{8.314}\right)\left(\frac{1}{T} - \frac{1}{343}\right)\right] (L^2 / (\text{Mol}^2 \text{ s})) \quad (49)$$

14. Simulation of the Runs Performed in the Presence of Phosphoric Acid

A set of nine different kinetic runs was made in the presence of phosphoric acid for testing the effect respectively: stirring rate, phosphoric acid concentration, temperature, formic acid concentration, and hydrogen peroxide concentration. All the mentioned runs have been simulated and the parameters giving the best fitting are reported in Table 5.

Table 5. Kinetic parameters and initial protonic concentration used for simulating the runs performed in the presence of phosphoric acid.

Run	$k_{10} (\times 10^7)$	$k_{11} (\times 10^9)$	$\beta (\times 10^4)$	$C_{H^+}^0$
13, 14, 15	1.62 ± 0.04	4.04 ± 0.09	1.00 ± 0.02	0.0343
16	1.60 ± 0.04	4.74 ± 0.09	1.01 ± 0.02	0.0455
17	1.58 ± 0.04	4.04 ± 0.09	1.01 ± 0.02	0.0370
18	1.64 ± 0.05	11.61 ± 0.25	1.01 ± 0.02	0.0372
19	0.86 ± 0.03	2.52 ± 0.06	1.01 ± 0.02	0.0344
20	5.55 ± 0.95	6.16 ± 0.12	1.01 ± 0.02	0.0343
21	1.62 ± 0.04	4.54 ± 0.09	40.4 ± 0.9	0.0365

Again k_1 , k_2 , and K_{eq} were imposed as already explained. Runs 13, 14, and 15 were performed in the same conditions with the exclusion of the stirring rate that was changed from 250 to 500 and 750. We have already seen that in the presence of phosphoric acid the stirring rate from 250 to 750 rpm has poor influence on the ESBO concentration profile. This probably means that phosphoric acid strongly interacts with the oxygen of the oxirane ring through the hydrogen bonds so giving place to an adduct with surfactants properties that favor the formation of the oil–water emulsion with a high interface area also at low stirring rate. The parameters are, therefore, almost the same for all these three runs. Run 14, 16, and 17 have been made in the same conditions, changing only the H_3PO_4 amounts that were respectively 0.65 g, 1.3 g, and 0.79 g ($w = 80\%$). Surprisingly, the effect of phosphoric acid concentration on the ring opening reaction rate is poor and the parameters for the best fitting are practically the same. This behavior is probably due to the small difference in H^+ concentration in the mentioned runs changing from 0.0343 to 0.0455 mol/L and to the not negligible intervention of the mechanism of ring opening independent of the pH based on the nucleophilic attack instead of the protonic one.

Run 18 must be compared with run 14, because, it has been made in the same conditions with the exclusion of the formic acid amount that was 5.4 g ($w = 79\%$) for the run 14 and 10.76 g for the run 18. k_{10} would be the same in both cases, while, k_{11} resulted somewhat different, that is, for obtaining a satisfactory simulation of the run 18 k_{11} must be taken 2.875 greater than run 14. A possible explanation could be that at high HCOOH concentration the ring opening reaction consistently occurs also in the oil phase, but to demonstrate this assumption many other experiments are required. Runs 14, 19, and 20 have been made in the same conditions but changing the temperature respectively at 70, 60, and 80 °C. Both the parameters k_{10} and k_{11} increase with the temperature and the activation energies have been determined from the slopes of the Arrhenius plots related to k_{10} and k_{11} that both have given a good linear trend. Run 21 occurs in a full chemical regime, because, it requires a very high value of β to be correctly simulated.

At last by averaging the kinetic parameters found for all the performed runs we can write:

$$k_{10} = (1.62 \pm 0.11) \times 10^{-7} \exp\left[\left(\frac{-88,000 \pm 3930}{8.314}\right)\left(\frac{1}{T} - \frac{1}{343}\right)\right] (\text{L}^2 / (\text{Mol}^2 \text{ s})) \quad (50)$$

$$k_{11} = (4.24 \pm 0.35) \times 10^{-9} \exp\left[\left(\frac{-45,000 \pm 1980}{8.314}\right)\left(\frac{1}{T} - \frac{1}{333}\right)\right] (\text{L}^2 / (\text{Mol}^2 \text{ s})) \quad (51)$$

Simulation of the Runs Performed in the Absence of Mineral Acids

As it has been previously seen (Table 1 and Figure 11) three kinetic runs have been performed in the absence of mineral acid. In one run, run 23, all the usual reaction components ($HCOOH$, H_2O , H_2O_2), were added to the epoxidized soybean oil, while, in other two runs only $HCOOH$ and H_2O were added. Obviously, in the two last cases the formation and decomposition of $HCOOOH$ do not occur, the pH remains constant, and only the ring opening reaction occurs. These runs were also simulated and the parameters giving the best fitting are reported on Table 6.

Table 6. Kinetic parameters used for simulating the runs performed in the absence of mineral acids.

Run	$k_{10} (\times 10^7)$	$k_{11} (\times 10^9)$	$\beta (\times 10^4)$	$C_{H^+}^0$
22	1.61 ± 0.03	2.02 ± 0.04	1.01 ± 0.02	0.0558
23	1.81 ± 0.04	2.52 ± 0.04	2.02 ± 0.04	0.0188
24	1.51 ± 0.03	2.12 ± 0.04	1.72 ± 0.03	0.0180

In run 23, k_1 and k_2 and K_{eq} were imposed as in the previous cases. α_1 and γ_1 were imposed, too, while, k_{10} and k_{11} were determined by regression analysis on the experimental data taking into account, when necessary, also of the change of H^+ concentration occurring as a consequence of the $HCOOOH$ decomposition. The interpretation of run 22 and 24 required to change somewhat the program code,

because, in the absence of H_2O_2 the reactions of HCOOOH , formation and decomposition do not occur. These runs are important because they show the influence of HCOOH in the ring opening reaction without the interference of other occurring reactions. As it can be seen, the obtained parameters are in satisfactory agreement with both run 23 and the runs made in the presence of phosphoric acid. Very important is the result of run 22 that demonstrate the greatest nucleophilic power of HCOOH .

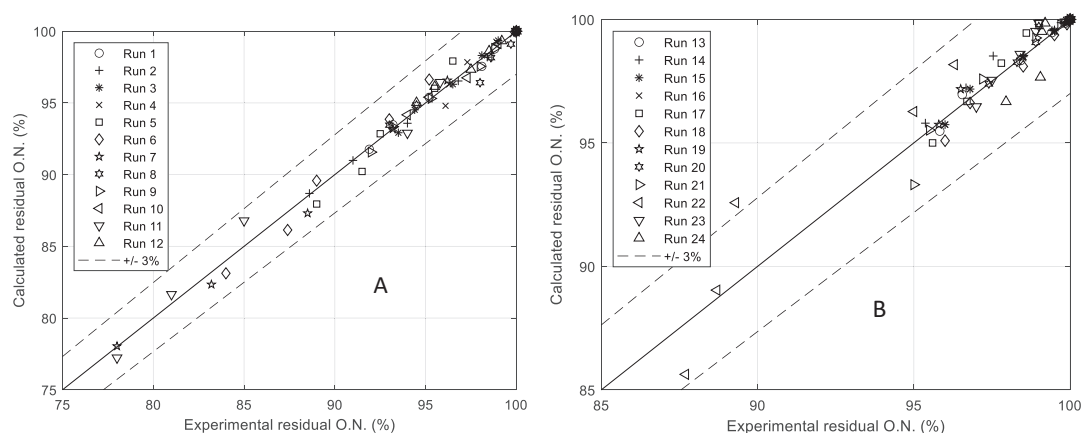


Figure 11. (A,B) A is the parity plot related to all the runs performed in the presence of H_2SO_4 (runs 1–12). B is the parity plot related to all the other performed runs (runs 13–24 of Table 1).

In conclusion, the developed model for interpreting the ring opening reaction rate, in different operative conditions, despite the difficulty of determining with precision all the parameters of the model, has given a satisfactory performance interpreting almost all the runs made. The obtained agreements in the simulation of the runs, characterized by the presence of a high HCOOH concentration, is poor requiring more experimental runs for a more correct interpretation.

Finally, in Figure 11A,B two parity plots compare all the experimental data with the calculated ones. As it can be seen the performance of the model is quite satisfactory giving place to an average error of less than 3%.

Finally, in Table 7, some statistical parameters are reported to better illustrate the quality of the overall fit for, respectively, the runs with sulfuric and phosphoric acid.

Table 7. Statistical parameters for the overall fit.

Parameter	Runs with Sulfuric Acid	Runs with Phosphoric Acid
R^2	0.9863	0.9203
R^2_{adj}	0.9861	0.9192
Mean error (%)	0.45	0.42

15. Conclusions

Many different kinetic runs have been made for studying the kinetics of the oxirane ring opening reaction in the presence of respectively sulfuric acid, phosphoric acid and in the absence of mineral acid starting, in all cases, from fully epoxidized soybean oil. The scope was to investigate about the role of acidity on the oxirane ring opening reaction rate or the eventual effect on the rate of the nucleophilic character of both reactants and products. It has been shown that the oxirane ring opening reaction, according to the operative conditions, can occur with two different reaction mechanism one characterized by the protonic attack to the epoxide oxygen, occurring at the liquid–liquid interface, and another one by an attack of a nucleophile to one of the two carbon atoms of the epoxide ring. Two different kinetic laws can be derived from the mentioned reaction mechanisms.

A biphasic kinetic model was developed for interpreting all the performed kinetic runs determining the related parameters by regression analysis on all the experimental data. In any case, also the contribution of the mass transfer was considered. This contribution is due to the migration of the bulky epoxide molecules from the oil bulk to the water–oil interface and is characterized by the mass transfer coefficient β and the epoxide gradients calculated for any single kinetic run. Despite the large number of imposed parameters recovered by previously published works the obtained agreements in simulating all the runs are satisfactory.

Author Contributions: E.S. coordinated all the aspect of the work, R.T. (Rosa Turco) has made the experimental runs, V.R. and R.T. (Riccardo Tesser) contributed in the elaboration of the kinetic model and calculations, M.D.S. helped in the coordination of all the aspects of the work. All authors have read and agreed to the published version of the manuscript.

Funding: Thanks are due to Desmet Ballestra Co. and Eurochem Engineering Ltd. for funding the research.

Conflicts of Interest: The authors declare no conflict of interest.

Glossary

List of symbols

c_i	Concentration identified by the subscript i (mol/l) in aqueous phase, (mol/cm ³ of oil) in oil phase
c_i^0	Initial concentration of i
c_e	Concentration of EPOX in the oil liquid bulk (mol/cm ³ of oil)
c_f	Concentration of EPOX at the liquid-liquid interface (mol/cm ³ of oil)
ΔE_1	Activation energy of performic acid formation (Joule/mol)
ΔE_2	Activation energy of performic acid decomposition (Joule/mol)
ΔH	Enthalpy change of the performic acid formation (Joule/mol)
k	Generic kinetic constant
k_{1-323}	Kinetic constant at 323 K of performic acid formation (l ² /mol ² s)
k_{2-323}	Kinetic constant at 323 K of performic acid decomposition (1/s)
K_{eq}	Equilibrium constant of performic formation
$K_{eq,ref}$	Equilibrium constant of performic formation at a reference temperature
K_1, K_2, K_3	Equilibrium constants of the three ionic dissociation of H ₃ PO ₄
K_{aFA}	Equilibrium constant of the ionic dissociation of formic acid
K_{1sulf}, K_{2sulf}	First and second ionic dissociation equilibrium constants of sulfuric acid
K_w	Ionic product of water
r	Generic reaction rate
r_1	Rate of performic acid formation (mol/l s). Volume referred to the aqueous solution
r_2	Rate of performic acid decomposition (mol/l s). Volume referred to the aqueous solution
r_{10}	Rate of epoxidation reaction promoted by acids (mol/(cm ³ s)). Volume referred to the oil solution
r_{11}	Rate of epoxidation reaction promoted by a nucleophile (mol/(cm ³ s)). Volume referred to the oil solution
r_g	Overall epoxidation rate (mol/(cm ³ s)). Volume referred to the oil solution
rpm	Stirring rate, Number of revolutions of the stirrer per minute
r_t	ESBO mass transfer rate (mol/(cm ³ s)). Volume referred to the oil solution
t	Time (s)
T	Temperature (K)

Greek Letters

α_N	Ring-opening parameters of nucleophilic power, $N = 1$ (FA), $N = 2$ (H ₂ O ₂), $N = 3$ (PFA), $N = 4$ (H ₂ O)
γ_N	Ring-opening parameters of nucleophilic power, $N = 1$ (FA), $N = 2$ (H ₂ O ₂), $N = 3$ (PFA), $N = 4$ (H ₂ O)
β	Liquid-liquid mass transfer coefficient, (1/s)

Subscripts defining concentrations

EPOX	Epoxide
EPOX ⁺	Protonated epoxide
Nu	Generic nucleophilic component
FA	Formic acid
PFA	Performic acid
H ₂ O	Water
H ₂ O ₂	Hydrogen peroxide
H ₂ SO ₄	Sulfuric acid
HSO ₄ ⁻	First dissociation sulfuric anion
SO ₄ ⁼	Second dissociation sulfuric anion
H ₃ PO ₄	Phosphoric acid
H ₂ PO ₄ ⁻	First dissociation phosphoric acid anion
HPO ₄ ⁼	Second dissociation phosphoric acid anion
PO ₄ ³⁻	Third dissociation phosphoric acid anion
HCOO ⁻	Dissociation of formic acid anion
OH ⁻	Hydroxyl
H ⁺	Proton

References

- Kirpluks, M.; Kalnbunde, D.; Walterova, Z.; Cabulis, U. Rapeseed Oil as Feedstock for High Functionality Polyol Synthesis. *J. Renew. Mater.* **2017**, *5*, 258–270. [[CrossRef](#)]
- Turco, R.; Tesser, R.; Vitiello, R.; Russo, V.; Andini, S.; Di Serio, M. Synthesis of Biolubricant Basestocks from Epoxidized Soybean Oil. *Catalysts* **2017**, *7*, 309. [[CrossRef](#)]
- Karadeniz, K.; Çalikoğlu, Y.; Sen, M.Y. A novel polyurethanes from epoxidized soybean oil synthesized by ring opening with bifunctional compounds. *Polym. Bull.* **2017**, *74*, 2819–2839. [[CrossRef](#)]
- Prileschajew, N. Oxydation ungesättigter Verbindungen mittels organischer Superoxyde. *Eur. J. Inorg. Chem.* **1909**, *42*, 4811–4815. [[CrossRef](#)]
- Santacesaria, E.; Tesser, R.; Di Serio, M.; Turco, R.; Russo, V.; Verde, D. A biphasic model describing soybean oil epoxidation with H₂O₂ in a fed-batch reactor. *Chem. Eng. J.* **2011**, *173*, 198–209. [[CrossRef](#)]
- Santacesaria, E.; Renken, A.; Russo, V.; Turco, R.; Tesser, R.; Di Serio, M. Biphasic Model Describing Soybean Oil Epoxidation with H₂O₂ in Continuous Reactors. *Ind. Eng. Chem. Res.* **2011**, *51*, 8760–8767. [[CrossRef](#)]
- Campanella, A.; Baltanás, M.A. Degradation of the oxirane ring of epoxidized vegetable oils in liquid-liquid systems: I. Hydrolysis and attack by H₂O₂. *Lat. Am. Appl. Res.* **2005**, *35*, 205–210.
- Campanella, A.; Baltanás, M.A. Degradation of the oxirane ring of epoxidized vegetable oils in liquid-liquid systems: II. Reactivity with solvated acetic and peracetic acid. *Lat. Am. Appl. Res.* **2005**, *35*, 211–216.
- Campanella, A.; Baltanás, M.A. Degradation of the oxirane ring of epoxidized vegetable oils in liquid-liquid heterogeneous reaction systems. *Chem. Eng. J.* **2006**, *118*, 141–152. [[CrossRef](#)]
- Campanella, A.; Fontanini, C.; Baltanás, M.A. High yield epoxidation of fatty acid methyl esters with performic acid generated in situ. *Chem. Eng. J.* **2008**, *144*, 466–475. [[CrossRef](#)]
- Gan, L.H.; Goh, S.H.; Ooi, K.S. Kinetic studies of epoxidation and oxirane cleavage of palm olein methyl esters. *J. Am. Oil Chem. Soc.* **1992**, *69*, 347–351. [[CrossRef](#)]
- Kousaalya, A.; Beyene, S.D.; Gopal, V.; Ayalew, B.; Pilla, S. Green epoxy synthesized from *Perilla frutescens*: A study on epoxidation and oxirane cleavage kinetics of high-linolenic oil. *Ind. Crop. Prod.* **2018**, *123*, 25–34. [[CrossRef](#)]
- Santacesaria, E.; Russo, V.; Tesser, R.; Turco, R.; Di Serio, M. Kinetics of Performic Acid Synthesis and Decomposition. *Ind. Eng. Chem. Res.* **2017**, *56*, 12940–12952. [[CrossRef](#)]
- Dearborn, E.C.; Fuoss, R.M.; Mackenzie, A.K.; Shepherd, R.G. Epoxy Resins from Bis-, Tris-, and Tetrakis-Glycidyl Ethers. *Ind. Eng. Chem.* **1953**, *45*, 2715–2721. [[CrossRef](#)]
- Paquot, C.; Hautfenne, A. Commission on Oils Fats and Derivatives. In *Standard Methods for the Analysis of Oils, Fats and Derivatives*; IUPAC, Applied Chemistry Division Blackwell Scientific Publications: London, UK, 1987.

16. D01 Committee. *Standard Test Methods for Epoxy Content of Epoxy Resins*; ASTM D1652–97; ASTM International: West Conshohocken, PA, USA, 1997.
17. Cai, X.; Zheng, J.L.; Aguilera, A.F.; Vernières-Hassimi, L.; Tolvanen, P.; Salmi, T.; Leveneur, S. Influence of ring-opening reactions on the kinetics of cottonseed oil epoxidation. *Int. J. Chem. Kinet.* **2018**, *50*, 726–741. [[CrossRef](#)]
18. International Association for the Properties of Water and Steam (IAPWS). 2020. Available online: <http://www.iapws.org/> (accessed on 10 September 2020).
19. Bandura, A. The Ionization Constant of Water over Wide Ranges of Temperature and Density. *J. Phys. Chem. Ref. Data* **2006**, *35*, 15. [[CrossRef](#)]
20. Lide, D.R. *CRC Handbook of Chemistry and Physics*, 70th ed.; CRC Press: Boca Raton, FL, USA, 1990.
21. Harned, H.S.; Embree, N.D. The ionization constant of formic acid from 0 °C to 60 °C. *J. Am. Chem. Soc.* **1934**, *56*, 1042–1044. [[CrossRef](#)]
22. Kim, M.H.; Kim, C.S.; Lee, H.W.; Kim, K. Temperature dependence of dissociation constants for formic acid and 2,6-dinitrophenol in aqueous solutions up to 175 °C. *J. Chem. Soc. Faraday Trans.* **1996**, *92*, 4951. [[CrossRef](#)]
23. Dickson, A.G.; Wesolowski, D.J.; Palmer, D.A.; Mesmer, R.E. Dissociation constant of bisulfate ion in aqueous sodium chloride solutions to 250 °C. *J. Phys. Chem.* **1990**, *94*, 7978–7985. [[CrossRef](#)]
24. Wu, Y.C.; Feng, D. The second dissociation constant of sulfuric acid at various temperatures by the conductometric method. *J. Solut. Chem.* **1995**, *24*, 133–144. [[CrossRef](#)]
25. Marshall, W.L.; Jones, E.V. Second dissociation constant of sulfuric acid from 25 to 350° evaluated from solubilities of calcium sulfate in sulfuric Acid. *J. Phys. Chem. A* **1966**, *70*, 4028–4040. [[CrossRef](#)]
26. Bates, R. First dissociation constant of phosphoric acid from 0-degrees-C to 60-degrees-C; Limitations of the electromotive force method for moderately strong acids. *J. Res. Natl. Inst. Stand. Technol.* **1951**, *47*, 126–134. [[CrossRef](#)]
27. Vega, C.A.; Romero, M.; Bates, R.G. First and second dissociation constants of phosphoric acid in 1 and 3 m sodium chloride solutions from 268.15 to 318.15 K. *J. Chem. Eng. Data* **1994**, *39*, 294–297. [[CrossRef](#)]



© 2020 by the authors. Licensee MDPI, Basel, Switzerland. This article is an open access article distributed under the terms and conditions of the Creative Commons Attribution (CC BY) license (<http://creativecommons.org/licenses/by/4.0/>).

Article

Design and Development of Novel Continuous Flow Stirred Multiphase Reactor: Liquid–Liquid–Liquid Phase Transfer Catalysed Synthesis of Guaiacol Glycidyl Ether

Nikhil H. Margi and Ganapati D. Yadav *

Department of Chemical Engineering, Institute of Chemical Technology, Nathalal Parekh Marg, Matunga, Mumbai 400019, India; nikhilmargi@gmail.com

* Correspondence: gd.yadav@ictmumbai.edu.in; Tel./Fax: +91-22-3361-2010

Received: 27 August 2020; Accepted: 30 September 2020; Published: 10 October 2020

Abstract: Phase transfer catalysed (PTC) reactions are used in several pharmaceutical and fine chemical industrial processes. We have developed a novel stirred tank reactor (Yadav reactor) to conduct batch and continuous liquid–liquid–liquid (L-L-L) PTC reactions. The reactor had a provision of using three independent stirrers for each phase, thereby having complete control over the rate of mass transfer across the two interfaces. In the continuous mode of operation, the top and bottom phases were continuously fed into the reactor while the middle phase was used as a batch. All three stirrers were used independently, thereby having independent control of mass transfer resistances. The reactor in a batch mode showed higher conversion and selectivity compared to a conventional batch reactor. L-L-L PTC reaction in the continuous mode was successfully performed without loss of the middle catalyst phase and with steady conversion and selectivity. The reaction of guaiacol with epichlorohydrin was conducted as a model reaction, with a 76% conversion of epichlorohydrin, 85% selectivity of guaiacol glycidyl ether, and the middle catalyst phase was stable throughout the process.

Keywords: continuous flow stirred tank reactor (CSTR); phase transfer catalysis (PTC); green chemistry; multiphase reactor; liquid–liquid–liquid reactions; guaiacol; epichlorohydrin; guaiacol glycidyl ether

1. Introduction

Liquid–liquid biphasic phase transfer catalysis (PTC) is a vital process in the fine chemical and pharmaceutical industries [1,2]. Primary PTC reactions include selective *O*-alkylation, *C*-alkylation, *N*-alkylation, etherification, oxidation, reduction, condensation, polymerisation, and addition reactions [3]. Most of the phase transfer catalysts used in the industry include toxic compounds like phosphonium salt, quaternary ammonium salts, and high molecular weight compounds like crown ether and polyethylene glycols (PEGs). However, due to recent strict environmental regulations, PTC reactions face the problem of catalyst separation and regeneration from the reaction mixture, and if not regenerated, this contributes to waste generation and expensive effluent treatment. In the liquid–liquid (L-L) PTC reaction, the separation of catalyst from the biphasic aqueous–organic mixture is difficult. Therefore, after the reaction, the catalyst is washed off from the organic phase and contributes to waste effluent. Since the catalyst is not reusable, it overall increases the cost of production [3,4].

To overcome the problem of catalyst separation and reuse, some researchers immobilised the phase transfer catalyst on a solid support which converts L-L PTC into a solid–liquid–liquid (S-L-L) PTC reaction system [5]. Although the catalyst is easy to separate, it reduces the rate of reaction due to mass transfer effects [3]. Another way is to convert the L-L PTC reaction into an L-L-L PTC reaction

system. This is a special type of multiphase PTC reaction which contains an organic phase in the upper layer, the catalyst-rich phase in the middle layer, and an aqueous phase in the lower layer. When the aqueous phase is supersaturated with salt, the catalyst is separated from the aqueous phase and forms the middle catalyst phase. A sharp increase in the rate of reaction is noticed as the middle catalyst phase is formed [6]. In the overall reaction, organic and aqueous phase reactants are transferred to the middle catalyst-rich phase, where the actual reaction occurs. The formation and stability of the middle catalyst phase is affected by the phase equilibrium, density differences in three phases, and temperature [7–10]. Compared to other types of PTC reactions, the L-L-L PTC reaction system increases the conversion and selectivity, permits catalyst reusability, and thus there is no need for solid support [11].

There are several reported L-L-L PTC systems, which include alkylation reactions like selective *O*-alkylation of phenol with benzyl chloride [12], 4-hydroxypropiophenone with benzyl chloride [13], reduction of *p*-chloronitrobenzene with sodium sulphide [11], selective oxidation of methyl mandelate [14], and etherification reaction for the synthesis of 2-((benzyloxy)methyl)furan [15]. Additionally, there are reactions like esterification of potassium 4-methoxyphenylacetate [16], sodium benzoate [17], synthesis of *n*-butyl salicylate by esterification of sodium salicylate [18], benzoylation of sodium 4-acetylphenoxide [19], 4-chloro-3-methylphenol sodium salt [20], synthesis of butyl salicylate [21], benzyl salicylate [22], and ultrasound-assisted synthesis of dialkyl peroxides [23]. Recently, the Horner–Wadsworth–Emmons (HWE) reaction was studied using an L-L-L PTC system [24–26].

Conventionally, a batch reactor with a single impeller stirrer is used for L-L-L PTC reactions [13]. In a batch reactor, catalyst separation from the reaction mixture is a complicated process which requires a complete shutdown of the operation. The higher speed of the stirring in one phase causes more fluid droplets to be carried over to the neighbouring phases, which results in the formation of a microemulsion [12,27]. In addition, to prepare L-L-L PTC systems, a large quantity of catalyst is needed, which increases the initial cost of operation [28]. To make L-L-L PTC systems economical, the continuous reuse and recirculation of the middle catalyst phase is required with a proper multiphase reaction.

To overcome the problems of batch reactor, Weng et al. [29] developed a continuous stirred tank reactor (CSTR) comprising five sections and a single stirrer with three impellers for agitation of each phase. Because of the high speed of the stirrer, the catalyst phase flows out from the reactor along with the organic and aqueous phases. Yang et al. [30,31] designed a continuous reactor with an ultrasound generator for a multiphase PTC reaction. In the reactor, the hydrophilic membrane was placed at the downside, and the hydrophobic membrane was placed in the upside reaction region. These membranes restricted the movement of the middle liquid phase out of the reactor. For efficient mixing, baffles were installed. However, because of the single stirrer, baffles, and countercurrent flow of aqueous and organic phases, the middle catalyst-rich phase was distributed in an organic and aqueous phase. This resulted in the catalyst phase flowing out of the reactor. In the above examples, conversion dropped down over a period as loss of catalyst occurred.

To overcome the problems of the batch and CSTR reactors in L-L-L PTC reactions, Yadav [32] designed a continuous flow stirred multiphase reactor in which the catalyst can be used continuously without the shutdown of the process. The present work mainly focused on carrying out a multiphase PTC reaction in continuous operation. Secondly, it focused on reusing the middle catalyst phase continuously without any post-recovery treatment and to keep all three phases steady.

2. Materials and Methods

2.1. Chemicals

Guaiacol, sodium hydroxide, epichlorohydrin, sodium chloride, and toluene (AR grade) were purchased from Thomas Baker, Mumbai. Tetra butyl ammonium bromide (TBAB) (AR grade) and *n*-decane (LR grade) were purchased from SD Fine Chem. Ltd., Mumbai, India.

2.2. Experimental Setup

The continuous flow stirred multiphase reactor was made up of the reactor vessel, pumping system, and feed vessels (see Figures 1 and 2). The reactor vessel (see Figures S1 and S2) was made up of glass. As shown in Figure 2, three concentric stirrers (11', 12', 13') with motors (11, 12, 13) were installed to agitate each phase independently with independent speeds of agitation. Thus, it was possible to have independent control over mass transfer rates. Flat (paddle) impellers were used. All stirrers were adjustable in height. The position of the upper organic phase stirrer (11') was such that it resided in the organic phase. The position of the lower aqueous phase stirrer (12') was such that it resided in the aqueous phase and middle phase stirrer (13') resided in the middle phase. No baffles were used in the reactor to maintain the steady-state phases. However, baffles can be used depending on the situation. Three separate motors (11, 12, 13) were used to control the agitation of each stirrer, and three pumps (21, 22, 23) were used to pump the three phases independently in the reactor. Independent inlet (15, 16, 17) and outlet nozzles (15', 16', 17') were provided for each phase. A jacketed heating system (18) was used for heating. Water was used in the jacket as the heating medium. To control the flow rate, metering valves (4, 5, 6) were installed at the outlet of each phase, and one metering valve (20) was installed at the inlet of the middle phase. The outlet of metering valves (1, 2, 3) was connected to collection vessels. A sampling valve (7) was installed to take an online sample of the organic phase for reaction monitoring and analysis. At the lower end of the reactor, a drain valve (19) was installed. Three feed vessels (24, 25, 26) were used to store each phase feed. Three single piston pumps (21, 22, 23) with pulse dampeners were used to pump each phase at the respective inlets. This arrangement (27) was made to circulate the middle phase continuously if needed. A thermowell with a thermocouple (9) was provided to monitor the temperature of the reaction mixture. The overflow tube (8) and an adjustable sampling tube with a feed system (10) was installed at the top (see Figure S3). The flow rate of the inlet and outlet and speed of agitation of stirrers were set so that it maintained steady three phases during the reaction. The material of construction of the reactor was glass and SS316. Additionally, the reactor was operated in batch and continuous modes [32].

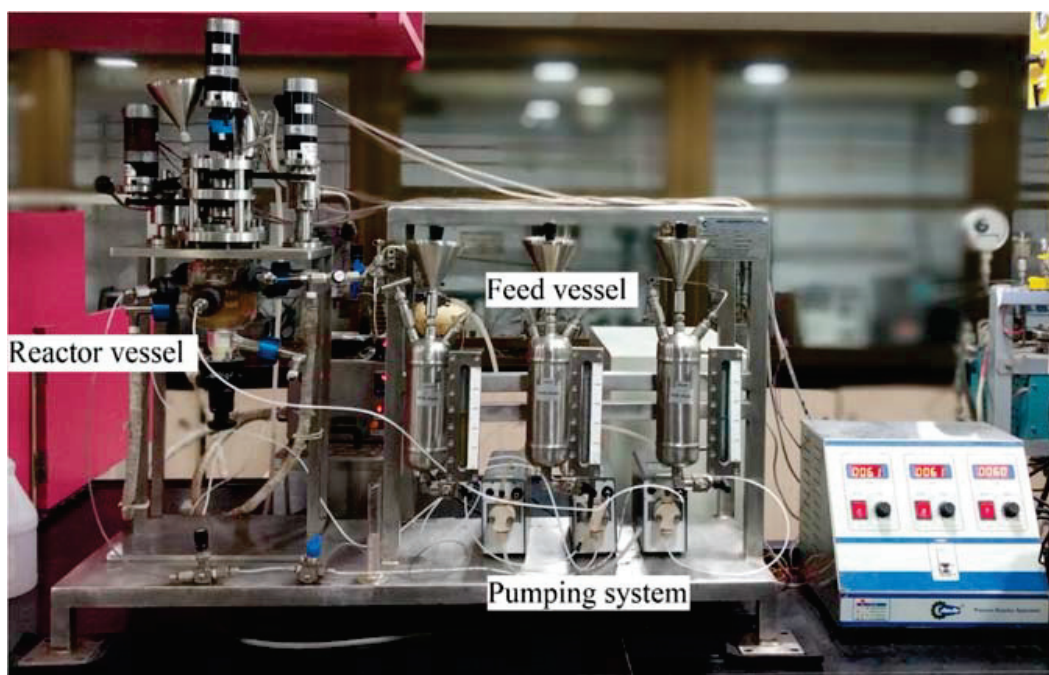


Figure 1. Front view of the actual continuous flow stirred multiphase reactor.

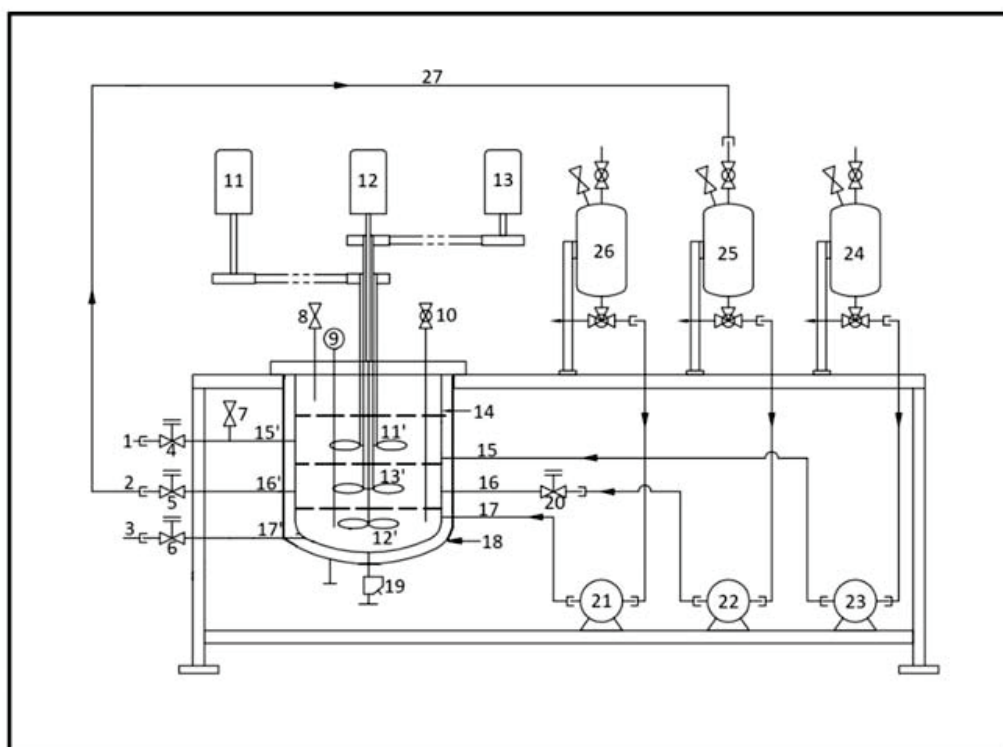


Figure 2. Schematic diagram of the continuous flow stirred multiphase reactor. 1—outlet for organic phase metering valve, 2—outlet for middle phase metering valve, 3—outlet for aqueous phase metering valve, 4—organic phase metering valve, 5—middle phase metering valve, 6—aqueous phase metering valve, 7—sampling valve for organic phase, 8—overflow tube, 9—thermowell with thermocouple, 10—adjustable sampling tube with feed system, 11—motor for organic phase, 12—motor for aqueous phase, 13—motor for middle phase, 11'—stirrer for organic phase, 12'—stirrer for aqueous phase, 13'—stirrer for middle phase, 14—reactor glass vessel, 15—inlet for organic phase, 16—inlet for middle phase, 17—inlet for aqueous phase, 15'—outlet for organic phase, 16'—outlet for middle phase, 17'—outlet for aqueous phase, 18—jacketed heating system, 19—drain valve, 20—metering valve at middle phase inlet, 21—aqueous phase pump, 22—middle phase pump, 23—organic phase pump, 24—organic phase feed vessel, 25—middle phase feed vessel, 26—aqueous phase feed vessel, 27—arrangement to circulate the middle phase continuously.

2.3. Reaction Procedure

The reaction was carried with guaiacol and epichlorohydrin using tetra-butyl ammonium bromide (TBAB) as a phase transfer catalyst, which formed guaiacol glycidyl ether as a product. The reaction mixture was prepared with 0.1 mol guaiacol, 0.2 mol sodium hydroxide, 0.14 mol tetra-n-butylammonium bromide, and 0.6 mol sodium chloride dissolved in water to make up the volume of the aqueous phase to 150 cm³ and 0.1 mol epichlorohydrin, and 0.03 mol n-decane as internal standards were dissolved in toluene to make up the volume of the organic phase to 150 cm³. The whole reaction mixture was stirred in the reactor, which formed three phases after settlement. For batch processing, the same reactor tank was used with three concentric stirrers to agitate each phase independently with independent speeds of agitation. The pump and metering valve did not operate during the batch operation.

For continuous reaction processing, feed solutions were prepared. The aqueous phase feed was prepared with 0.1 mol guaiacol, 0.2 mol sodium hydroxide, and 0.6 mol sodium chloride dissolved in water to make up the volume of the aqueous phase to 150 cm³. The organic phase feed was prepared with 0.1 mol epichlorohydrin and 0.03 mol n-decane as internal standards dissolved in toluene to make

up the volume of the organic phase to 150 cm³. Both aqueous and organic feeds were stored in the respective feed vessels.

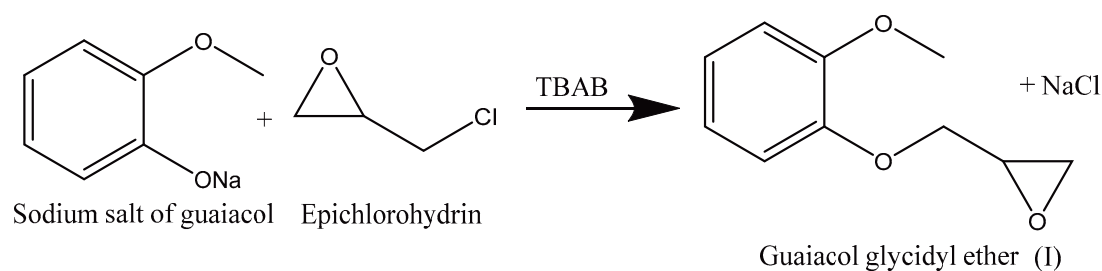
After preparing the reaction mixture in the reaction vessel, the organic and aqueous phases were pumped to the continuous flow stirred multiphase reactor through the separate inlet. The organic and aqueous phase flow rate was in the range of 0.5–1.3 mL/min, and a typical reaction was conducted at 40 °C. The metering valve was used to control the flow rate at the outlet of each phase. The samples of the organic phase were taken from the organic phase sampling valve for analysis until the steady state was reached. In all experiments, to study the stability of the steady state, the samples were also taken after a steady state was reached (till 6 h).

2.4. Method of Analysis

During the reaction, samples were periodically withdrawn from the organic phase and analysed using gas chromatography on a Thermo Trace GC1110 model equipped with a flame ionisation detector using a TG-MS 1 (30 m × 0.25 mm × 0.25 μm) column. The conversion was based on the disappearance of epichlorohydrin in the organic phase against n-decane as the internal standard. The product confirmation was done by Thermo Scientific Q Exactive Orbitrap GC-MS (HR-MS).

3. Results and Discussion

In the continuous flow stirred multiphase reactor, the reaction of guaiacol and epichlorohydrin with TBAB as a phase transfer catalyst was carried out, which formed guaiacol glycidyl ether as the product (Scheme 1) (Supplementary Materials Figures S4 and S5). Figure 3 shows how mass transfer occurs across the two interfaces and the reaction takes place in the middle phase. The aqueous phase reactant (anion) forms an ion pair with TBAB, which is then transferred to the middle catalyst phase because of the concentration gradient and favourable distribution in the middle phase. Similarly, the organic phase reactant (cation) diffuses to the middle catalyst phase, where the reaction takes place, and the product is formed. Because of the solubility of the product in the organic phase with favourable distribution and the concentration gradient, the product diffuses to the upper organic phase and is transferred through the organic phase outlet.



Scheme 1. Synthesis of guaiacol glycidyl ether.

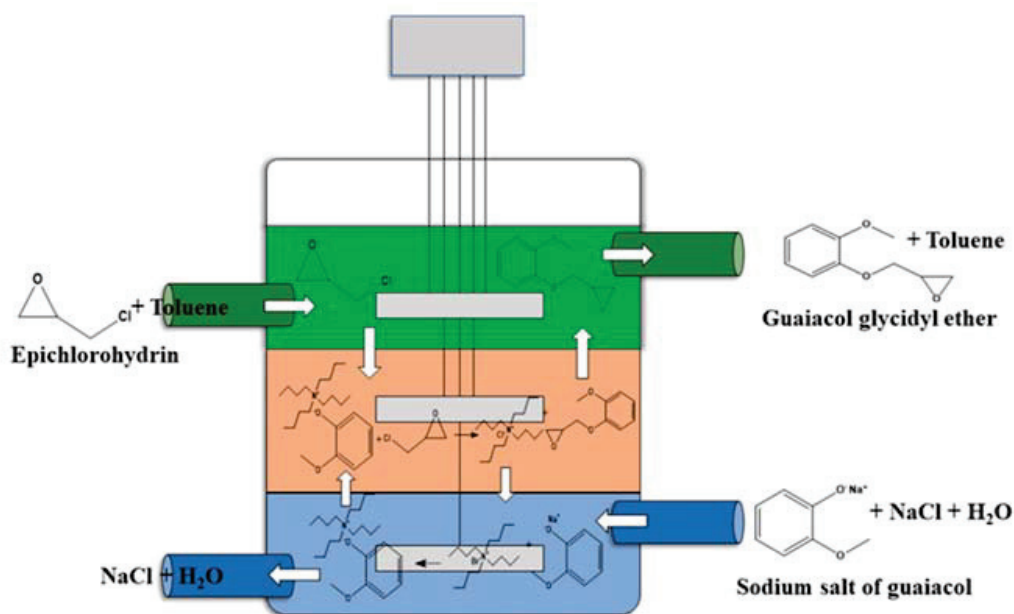


Figure 3. Liquid-liquid-liquid (L-L-L PTC) reaction in a continuous flow stirred multiphase reactor.

3.1. Batch Stirred Multiphase Reactor

The reactor was operated in batch mode, and different reaction parameters affecting conversion and selectivity were studied and optimised.

3.1.1. Effect of Speed of Agitation in a Batch Stirred Multiphase Reactor

In all experiments, the speed of agitation of all three stirrers was adjusted in such a way that all three phases maintained a steady state without mixing. From the experiments, it was observed that above 60 rpm, all phases started to ripple out because of increasing turbulence. Therefore, the experiment was carried out at 60 rpm. An 89% conversion of epichlorohydrin and 94% selectivity of guaiacol glycidyl ether were obtained at 60 rpm (see Figure 4).

To study the effect of the speed of agitation in each phase, different speeds of agitation were set for each phase. Here, the speed of agitation (in rpm) of the aqueous phase is denoted by A, the middle catalyst phase by M, and the organic phase by O. It was observed that at a lower aqueous phase speed and a higher middle phase speed, the conversion of epichlorohydrin was higher, but the selectivity of guaiacol glycidyl ether decreased by 10% (see Figure 4). As shown in Figure 4, the conversion was similar in the first three cases (89–91%). However, in the case of A-25, M-60, O-60, the conversion dropped by 5%. In this case, at the speeds of A-25 and M-60, the rate of transfer of the aqueous phase reactant (anion) to the middle phase catalyst was reduced, and therefore the conversion dropped by 5%. In the case of A-25, M-80, O-60, and A-25, M-60, O-80, the higher speed of agitation of the middle and the organic phase increased the mixing and increased mass transfer rates correspondingly; therefore, in the middle phase, where the reaction occurs, a larger number of product molecules reacted with guaiacol molecules present in the middle catalyst phase and hence formed the by-product, thereby reducing selectivity (see Scheme 2). In the case of A-60, M-60, O-60, the speed was the same; therefore, the rate of transfer of the aqueous and organic phase reactants was the same. Hence, the highest selectivity of 94% was obtained. The independent stirrer for each phase and the absence of baffles prevented mixing and helped to maintain the steady state of each phase without disturbing the two L-L interfaces.

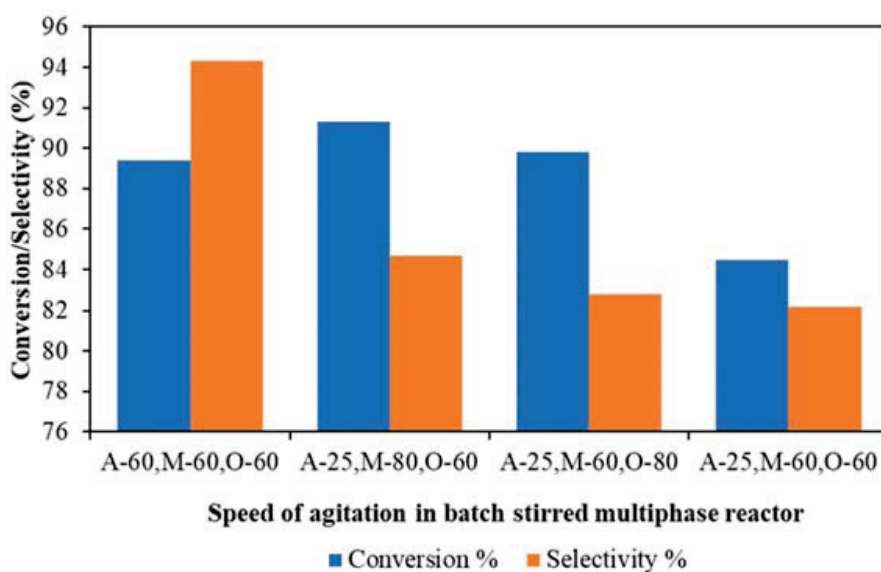
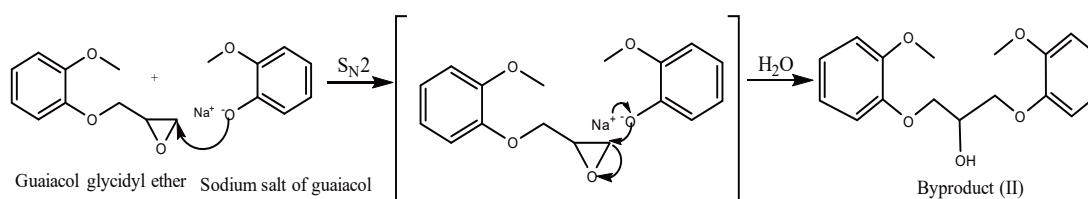


Figure 4. Effect of the speed of agitation in batch stirred multiphase reactor. Epichlorohydrin 0.1 mol, n-decane 0.03 mol, toluene 150 cm³, guaiacol 0.1 mol, sodium hydroxide 0.2 mol, sodium chloride 0.6 mol, tetra-n-butylammonium bromide 0.14 mol, and water 150 cm³. Temperature 40 °C, A—speed of agitation of lower aqueous phase, M—speed of agitation of middle catalyst phase, O—speed of agitation of upper organic phase, reaction time 6 h.

3.1.2. Effect of Mole Ratio of Guaiacol to Epichlorohydrin

To study the effect of the mole ratio of guaiacol to epichlorohydrin, different mole ratios of guaiacol to epichlorohydrin were studied (1:1, 2:1, and 1:2) under the same conditions with a constant mole ratio between guaiacol and sodium hydroxide (see Figure 5). As guaiacol concentration increases, the selectivity of guaiacol glycidyl ether decreases from 94% to 71%. At a 2:1 guaiacol to epichlorohydrin mole ratio, the excess of guaiacol attacks the ring carbon product via the S_N2 mechanism, forming a by-product (II) (see Schemes 1 and 2 and Supplementary Materials Figures S4 and S5) and reduces the selectivity of guaiacol glycidyl ether. An 89% conversion of epichlorohydrin and 94% selectivity of guaiacol glycidyl ether were the same for guaiacol to epichlorohydrin mole ratios of 1:1 and 1:2. Therefore, a 1:1 mole ratio was used for further experiments.



Scheme 2. By-product formation reaction.

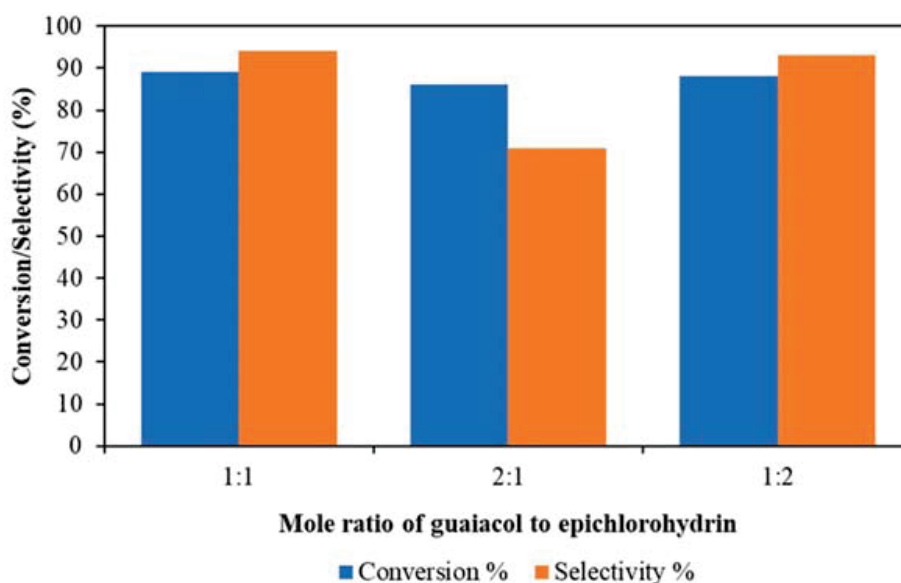


Figure 5. Effect of the mole ratio of guaiacol to epichlorohydrin. N-decane 0.03 mol, toluene 150 cm³, sodium chloride 0.6 mol, tetra-n-butylammonium bromide 0.14 mol, and water 150 cm³. Temperature 40 °C, speed of agitation 60 rpm for all three phases, and reaction time 6 h.

3.1.3. Effect of Mole Ratio of Guaiacol to Sodium Hydroxide

The effect of the mole ratio of guaiacol to sodium hydroxide was studied, from 1:1 to 1:2 (see Figure 6). At a lower concentration of sodium hydroxide, the conversion and selectivity decrease. This is because guaiacol (pKa 9.98) is a less acidic molecule compared to acetic acid (pKa 4.76) at room temperature [33]. Therefore, it needs a larger amount of sodium hydroxide to form a salt, which takes part in the reaction. The highest conversion (89%) of epichlorohydrin and the 94% selectivity of guaiacol glycidyl ether were obtained for a 1:2 mole ratio. Therefore, this was used for further experiments.

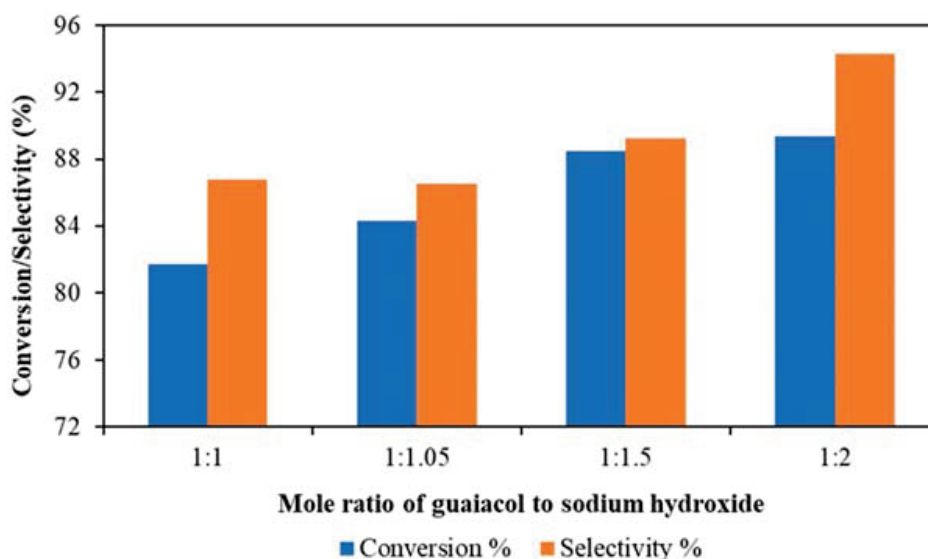


Figure 6. Effect of the mole ratio of guaiacol to sodium hydroxide. Epichlorohydrin 0.1 mol, n-decane 0.03 mol, toluene 150 cm³, sodium chloride 0.6 mol, tetra-n-butylammonium bromide 0.14 mol, and water 150 cm³. Temperature 40 °C, speed of agitation 60 rpm for all three phases, and reaction time 6 h.

3.1.4. Effect of Temperature

The effect of temperature on the reaction between guaiacol and epichlorohydrin was studied with optimised reaction parameters. The temperature was increased from 30 to 80 °C. At all temperatures, all three phases maintained a steady state without mixing. The conversion of epichlorohydrin was increased with an increase in the temperature, while selectivity considerably dropped with an increase in temperature. The conversion was increased due to an increase in temperature and the formation of by-product increased (see Scheme 2). An 89% conversion of epichlorohydrin and 94% selectivity of guaiacol glycidyl ether were obtained at 40 °C, and a 95% conversion of epichlorohydrin and 50% selectivity of guaiacol glycidyl ether were obtained at 80 °C. Therefore, 40 °C was considered as the optimum temperature for further experiments. The effect of temperature on the conversion and selectivity is given in Figures 7 and 8.

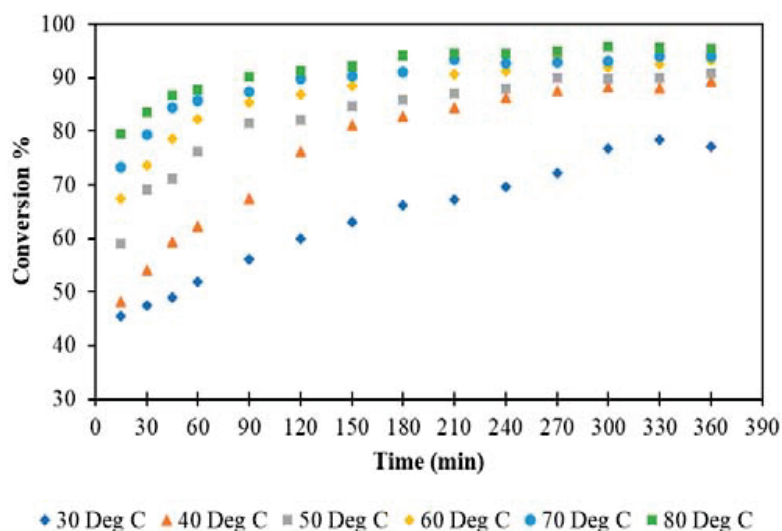


Figure 7. Effect of temperature on the conversion. Epichlorohydrin 0.1 mol, n-decane 0.03 mol, toluene 150 cm³, guaiacol 0.1 mol, sodium hydroxide 0.2 mol, sodium chloride 0.6 mol, tetra-n-butylammonium bromide 0.14 mol, and water 150 cm³. Speed of agitation 60 rpm for all three phases and reaction time 6 h.

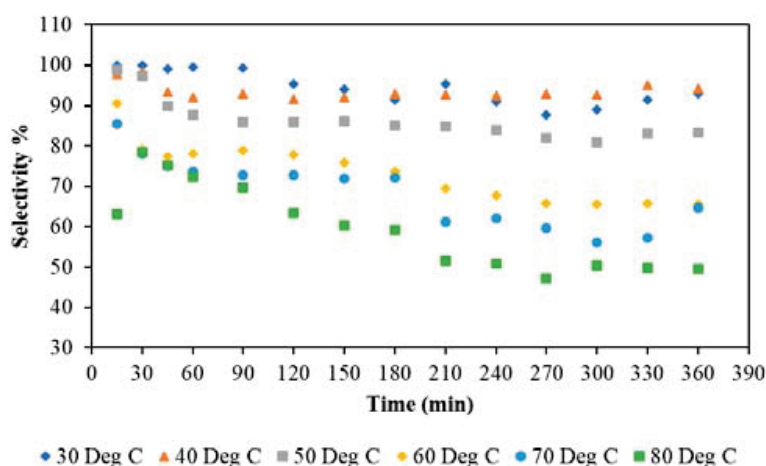


Figure 8. Effect of temperature on the selectivity. Epichlorohydrin 0.1 mol, n-decane 0.03 mol, toluene 150 cm³, guaiacol 0.1 mol, sodium hydroxide 0.2 mol, sodium chloride 0.6 mol, tetra-n-butylammonium bromide 0.14 mol, and water 150 cm³. Speed of agitation 60 rpm for all three phases and reaction time 6 h.

3.1.5. Comparison of Batch Stirred Multiphase Reactor with Conventional Single Stirrer PTC Batch Reactor

We compared our batch stirred multiphase reactor with a conventional single stirrer PTC batch reactor (see Figure 9). In our reactor, the agitation of each phase by the individual stirrer increased the mass transfer rate. Therefore, a 19% increase in the conversion of epichlorohydrin and a 4% increase in the selectivity of guaiacol glycidyl ether were observed compared to the conventional single stirrer PTC batch reactor.

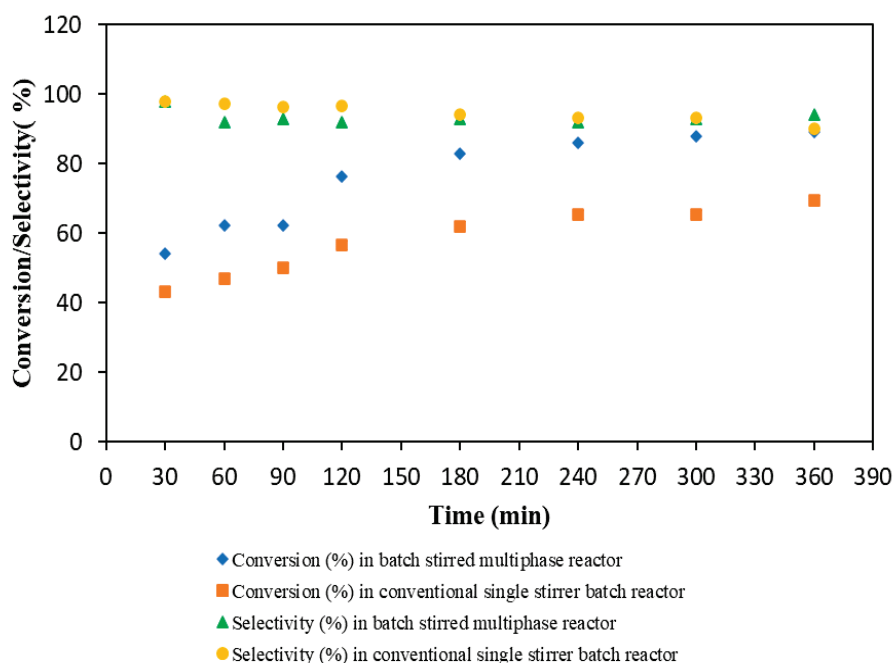


Figure 9. Comparison of batch stirred multiphase reactor with conventional single stirrer PTC batch reactor. Epichlorohydrin 0.1 mol, n-decane 0.03 mol, toluene 150 cm³, guaiacol 0.1 mol, sodium hydroxide 0.2 mol, sodium chloride 0.6 mol, tetra-n-butylammonium bromide 0.14 mol, and water 150 cm³. Temperature 40 °C, novel PTC reactor speed of agitation 60 rpm for all three phases, conventional PTC reactor speed of agitation 1200 rpm, and reaction time 6 h.

3.2. Continuous Flow Stirred Multiphase Reactor

The reactor was operated in continuous mode, and different reaction conditions affecting conversion and selectivity were studied and optimised.

3.2.1. The Effect of Speed of Agitation in a Continuous Flow Stirred Multiphase Reactor

The speed of agitation of all three stirrers was adjusted in such a way that all three phases maintained a steady state without mixing. It was observed that above 60 rpm, all phases started to ripple out. So, the reaction was carried out at 60 rpm. In the case of the same speed of agitation of each phase, the highest conversion (76%) of epichlorohydrin and 85% selectivity of guaiacol glycidyl ether were obtained. The experiments were also performed at a different speed of agitation for all three phases. It was found that the conversion of epichlorohydrin decreases slightly while the selectivity of guaiacol glycidyl ether decreases by 9–10% (see Figure 10).

In Figure 10, at A-60, M-60, O-60 rpm, the highest conversion and selectivity were achieved. In the case of the experiment with A-25, M-80, O-60 rpm, the speed of the aqueous phase was 25 rpm; therefore, the rate of transfer of the aqueous phase reactant (anion) to the middle phase catalyst was reduced, and conversion dropped by 8%. The speed of the middle phase was 80 rpm, which increased the mixing; therefore, a larger number of product molecules collided with guaiacol molecules present in

the middle catalyst phase and formed the by-product, thereby reducing selectivity by 8% (see Scheme 2). As the guaiacol molecules reacted with the product, a smaller number of molecules were available for epichlorohydrin to form the product, which also resulted in a drop in conversion. Similarly, in the case of experiments with A-40, M-80, O-60 rpm, the conversion dropped by 3%, and selectivity dropped by 9%. When the speed of the aqueous phase was 40 rpm, the conversion dropped by just 3%.

In previously reported continuous reactors, because of the high speed of the stirrer, the catalyst phase mixed with the organic and aqueous phases, and also the presence of baffles resulted in the mixing of three phases. This ultimately led to the catalyst phase flowing out of the reactor, along with the organic and aqueous phases. Thereby, the conversion dropped over a period as the loss of catalyst occurred [29–31]. In this reactor (named as “Yadav reactor [32]” after the inventor and corresponding author), to prevent vigorous mixing of the three phases, a separate stirrer for each phase was used, and the speed of agitation was maintained in such way that all three phases maintained a steady interface which prevented the catalyst phase from flowing out of the reactor and also gave the best conversion and selectivity. This reactor design also reduced the cost of membranes used in the previously reported reactor to separate the phases [30,31].

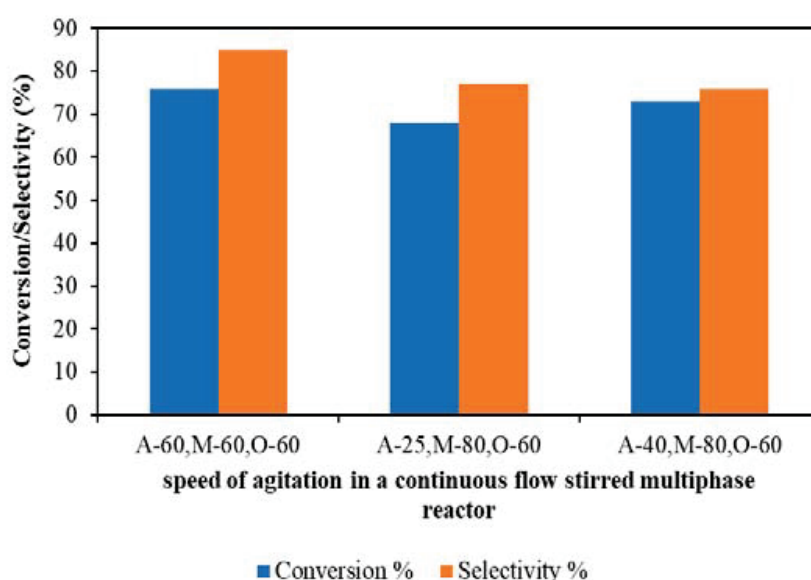


Figure 10. Effect of speed of agitation in a continuous flow stirred multiphase reactor. Epichlorohydrin 0.1 mol, n-decane 0.03 mol, toluene 150 cm³, guaiacol 0.1 mol, sodium hydroxide 0.2 mol, sodium chloride 0.6 mol, tetra-n-butylammonium bromide 0.14 mol, and water 150 cm³. Temperature 40 °C, flow rate for aqueous and organic phase 0.5 mL/min, A—speed of agitation of lower aqueous phase, M—speed of agitation of middle catalyst phase, O—speed of agitation of upper organic phase, and reaction time 6 h.

3.2.2. Effect of Flow Rate in a Continuous Flow Stirred Multiphase Reactor

The experiments were performed at the same speed of agitation for all three phases, i.e., 60 rpm, with three different flow rates of the aqueous and organic phase. It was found that at a lower flow rate, high conversion and selectivity were obtained. As the flow rates of both phases increased from 0.5 to 1.3 mL/min, the resident time decreased, which resulted in a drastic decrease in the conversion of epichlorohydrin, from 76% to 54%, and selectivity of guaiacol glycidyl ether, from 85% to 75% (see Figure 11).

Experiments were also performed at different speeds of agitation for all three phases. As the flow rate increased, the conversion of epichlorohydrin decreased from 68% to 56%, and the selectivity of guaiacol glycidyl ether decreased from 77% to 75% (see Figure 12).

In previously reported continuous reactors, the countercurrent flow of aqueous and organic phases distributed the middle catalyst-rich phase in an organic and aqueous phase, which resulted in the catalyst phase flowing out of the reactor along with the organic and aqueous phases [29–31]. In this reactor, to avoid the mixing of the three phases and to maintain a steady state of each phase, the countercurrent flow of the aqueous and organic phases was avoided. In addition, the speed of agitation was maintained, as described in Section 3.2.1. The organic and aqueous phases were introduced from the independent inlets. The organic phase inlet directly opens into the lower part of the organic phase layer, just above the middle catalyst phase layer, and the aqueous phase inlet directly opens into the upper part of the aqueous phase layer, just below the middle catalyst phase layer (see Figures 2 and 3 and Figures S1 and S2). This arrangement provides a fresh feed of reactants to the middle catalyst phase, where the actual reaction occurs. Because of the concentration gradient, only reactant ions are transferred across the two interfaces of the middle catalyst phase. In all experiments at each flow rate, the middle catalyst phase volume was retained with undisturbed interfaces, thereby leading to steady conversion and selectivity.

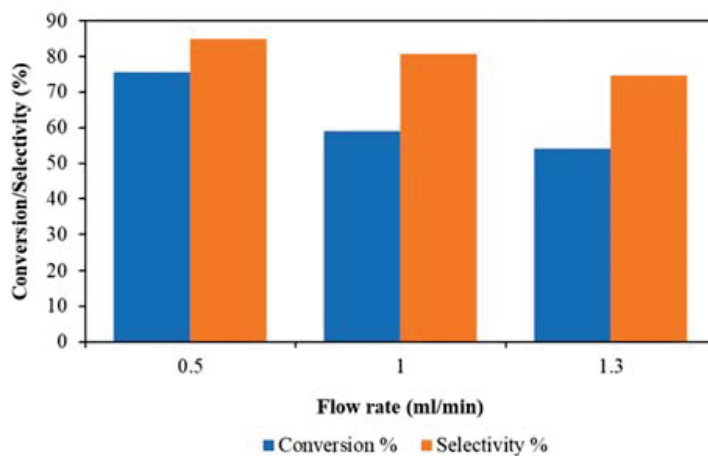


Figure 11. Effect of the flow rate at the same speed of agitation for three phases. Epichlorohydrin 0.1 mol, n-decane 0.03 mol, toluene 150 cm³, guaiacol 0.1 mol, sodium hydroxide 0.2 mol, sodium chloride 0.6 mol, tetra-n-butylammonium bromide 0.14 mol, and water 150 cm³. Temperature 40 °C, speed of agitation 60 rpm for all three phases, and reaction time 6 h.

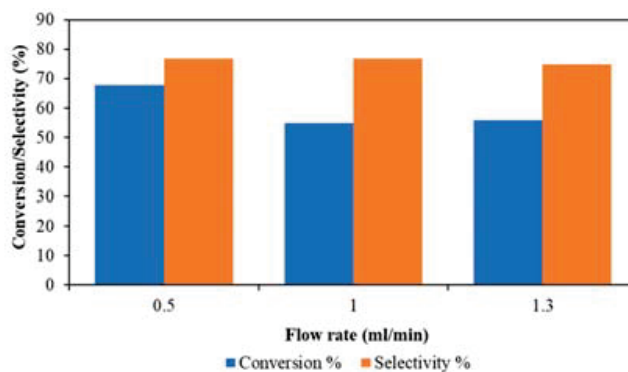


Figure 12. Effect of the flow rate at a different speed of agitation for three phases. Epichlorohydrin 0.1 mol, n-decane 0.03 mol, toluene 150 cm³, guaiacol 0.1 mol, sodium hydroxide 0.2 mol, sodium chloride 0.6 mol, tetra-n-butylammonium bromide 0.14 mol, and water 150 cm³, temperature 40 °C, speed of agitation of lower aqueous phase 25 rpm, speed of agitation of middle catalyst phase 80 rpm, speed of agitation of upper organic phase 60 rpm, and reaction time 6 h.

3.2.3. Effect of Middle Catalyst Phase Recirculation in a Continuous Flow Stirred Multiphase Reactor

The experiment was carried out with continuous circulation of the middle catalyst phase using the pump and metering valves; there was no loss of catalyst phase at the end of the reaction. The result was similar to that for the reaction where the steady middle catalyst phase was used. No significant increase in conversion of epichlorohydrin and selectivity of guaiacol glycidyl ether was observed. Therefore, for all further experiments, the middle catalyst phase was not recirculated; it was kept in a steady state.

3.2.4. Time on Stream Study in a Continuous Flow Stirred Multiphase Reactor

The time on stream (TOS) study was carried out for 18 h at 40 °C with 60 rpm as the speed of agitation for all three stirrers. The aqueous and organic phase flow rate was kept at 0.5 mL/min. Conversion of 76% of epichlorohydrin and 85% selectivity of guaiacol glycidyl ether were constant throughout the reaction (see Figure 13). There was no loss of the catalyst phase, even at the end of 18 h. In previously reported continuous reactors, the loss of the catalyst phase occurred, as it flowed out along with the other phases [29–31]. Here, in the Yadav reactor, to maintain the steady state of each phase, the parameters discussed in the above sections were used. The adjustable independent stirrer for each phase and flat (paddle) impellers and the absence of baffles prevented the mixing of phases, keeping the two interfaces steady. The use of pumps at the inlet and metering valves at the outlet maintained the steady inlet and outlet flows of aqueous and organic phases. Thereby, a constant volume of each phase was maintained. In the entire operation for a long period of time (time on stream, TOS), the catalyst phase retained its original volume, along with the chemical activity. The design of the reactor and reaction parameters successfully converted the batch L-L-L PTC reaction system into a continuous system.

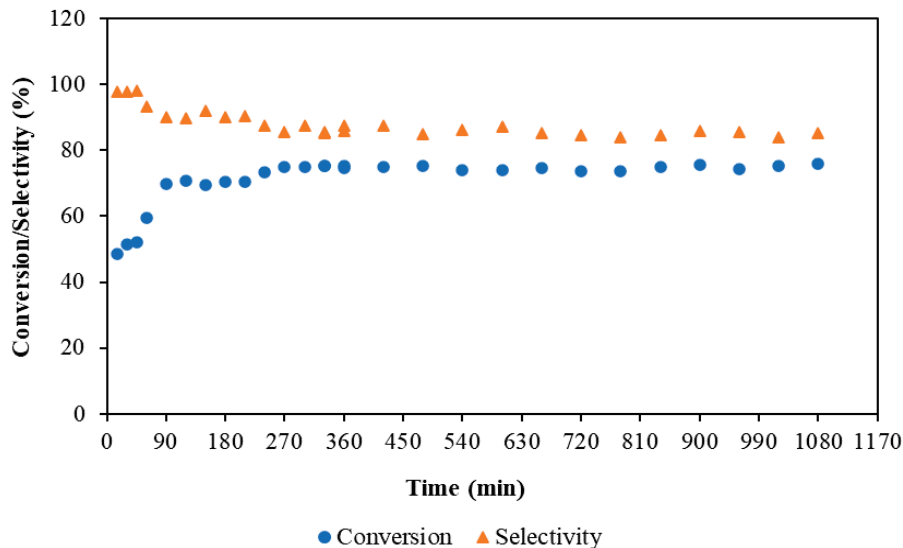


Figure 13. Time on stream study in a continuous flow stirred multiphase reactor. Epichlorohydrin 0.1 mol, n-decane 0.03 mol, toluene 150 cm³, guaiacol 0.1 mol, sodium hydroxide 0.2 mol, sodium chloride 0.6 mol, tetra-n-butylammonium bromide 0.14 mol, and water 150 cm³. Temperature 40 °C, speed of agitation of all three stirrers 60 rpm, and reaction time 18 h (1080 min).

4. Conclusions

The present work described a novel approach in the design of a multiphase reactor in a continuous operation mode for L-L-L PTC reactions. The catalyst phase was operated continuously, which gave the best activity with steady conversion and selectivity. The catalyst phase retained its volume as there was no physical loss of the catalyst phase from the reactor. In batch mode, using three concentric stirrers at

as low as 60 rpm gave the best conversion and selectivity compared to those of the conventional batch reactor. In the case of continuous mode, at 40 °C, the conversion of epichlorohydrin was 76% with a selectivity of guaiacol glycidyl ether of 85%. The time on stream study showed that the reaction could be carried out continuously without the shutdown of the process and with continuous reuse of the middle catalyst phase. Throughout the experiments, all three phases were steady without any change of conversion and selectivity. By using this process, industrially important guaiacol glycidyl ether was synthesised in continuous mode. The continuous flow stirred multiphase reactor can be used for various industrial L-L-L PTC reactions.

5. Patent

Yadav, G.D. An Improved Continuous Flow Stirred Multiphase Reactor. Patent PCT/IN2018/050535, 21 February 2019.

Supplementary Materials: The following are available online at <http://www.mdpi.com/2227-9717/8/10/1271/s1>, Figure S1: Schematic diagram of the front section the reactor vessel, Figure S2: Front view of the actual reactor vessel, Figure S3: Schematic diagram of a top view of the reactor vessel, Figure S4: GCMS spectra of (A) epichlorohydrin, (B) guaiacol glycidyl ether, (C) reaction by-product, and (D) n-decane, Figure S5: Typical GC chromatogram of reaction mass.

Author Contributions: N.H.M. contributed to the supervision of reactor fabrication at the fabricator site, conducting reactions in the continuous flow stirred multiphase reactor and analysed the reaction mixture with analytical instruments, and wrote the original draft. G.D.Y. contributed to the original idea of designing of the continuous flow stirred multiphase reactor, provided funds, provided research supervision and research infrastructure, and reviewed and edited the draft. All authors have read and agreed to the published version of the manuscript.

Funding: N.H.M. is grateful to the University Grants Commission (UGC) for a BSR Fellowship in Sciences for meritorious students under its Green Technology program. G.D.Y. received support from R. T. Mody Distinguished Professor Endowment and Tata Chemicals Darbari Seth Distinguished Professor of Leadership and Innovation Endowment, and the J. C. Bose National Fellowship of the Department of Science and Technology, Government of India.

Conflicts of Interest: The authors declare no conflict of interest.

References

1. Starks, C.M.; Liotta, C. *Phase Transfer Catalysis Principles and Techniques*; Academic Press: New York, NY, USA, 1978.
2. Makosza, M. Phase-transfer catalysis. A general green methodology in organic synthesis. *Pure Appl. Chem.* **2000**, *72*, 1399–1403. [[CrossRef](#)]
3. Naik, S.D.; Doraiswamy, L.K. Phase transfer catalysis: Chemistry and engineering. *AIChE J.* **1998**, *44*, 612–646. [[CrossRef](#)]
4. Yadav, G.D.; Sowbna, P.R. Process intensification and waste minimization in liquid–liquid–liquid phase transfer catalyzed selective synthesis of mandelic acid. *Chem. Eng. Res. Des.* **2012**, *90*, 1281–1291. [[CrossRef](#)]
5. Yadav, G.D. Insight into Green Phase Transfer Catalysis. *Top. Catal.* **2004**, *29*, 145–161. [[CrossRef](#)]
6. Wang, D.H.; Weng, H.S. Preliminary study on the role played by third liquid phase in phase transfer catalysis. *Chem. Eng. Sci.* **1988**, *43*, 2019–2024. [[CrossRef](#)]
7. Mason, D.; Magdassi, S.; Sasson, Y. Role of a third liquid phase in phase-transfer catalysis. *J. Org. Chem.* **1991**, *56*, 7229–7232. [[CrossRef](#)]
8. Wang, D.H.; Weng, H.S. Solvent and salt effects on the formation of third liquid phase and the reaction mechanisms in the phase transfer catalysis system—Reaction between N-butyl bromide and sodium phenolate. *Chem. Eng. Sci.* **1995**, *50*, 3477–3486. [[CrossRef](#)]
9. Hsiao, H.C.; Kao, S.M.; Weng, H.S. Synthesis of n-Butyl Phenyl Ether by Tri-Liquid-Phase Catalysis Using Poly(ethylene glycol)-600 as a Catalyst. 1. Analysis of Factors Affecting the Formation of a Third Liquid Phase. *Ind. Eng. Chem. Res.* **2000**, *39*, 2772–2778. [[CrossRef](#)]
10. Ohtani, N.; Ohta, T.; Hosoda, Y.; Yamashita, T. Phase Behavior and Phase-Transfer Catalysis of Tetrabutylammonium Salts. Interface-Mediated Catalysis. *Langmuir* **2004**, *20*, 409–415. [[CrossRef](#)]

11. Yadav, G.D.; Jadhav, Y.B.; Sengupta, S. Selectivity engineered phase transfer catalysis in the synthesis of fine chemicals: Reactions of p-chloronitrobenzene with sodium sulphide. *J. Mol. Catal. A Chem.* **2003**, *200*, 117–129. [[CrossRef](#)]
12. Yadav, G.D.; Badure, O.V. Role of Third Phase in Intensification of Reaction Rates and Selectivity: Phase-Transfer Catalyzed Synthesis of Benzyl Phenyl Ether. *Ind. Eng. Chem. Res.* **2007**, *46*, 8448–8458. [[CrossRef](#)]
13. Yadav, G.D.; Sowbna, P.R. Selectivity Engineering in Synthesis of 4-Benzyloxy Propiophenone Using Liquid–Liquid–Liquid Phase-Transfer Catalysis. *Ind. Eng. Chem. Res.* **2012**, *51*, 3256–3264. [[CrossRef](#)]
14. Yadav, G.D.; Motirale, B.G. Selective oxidation of methyl mandelate to methyl phenyl glyoxylate using liquid–liquid–liquid phase transfer catalysis. *Chem. Eng. J.* **2010**, *156*, 328–336. [[CrossRef](#)]
15. Katole, D.O.; Yadav, G.D. Process intensification and waste minimization using liquid-liquid-liquid tri-phase transfer catalysis for the synthesis of 2-((benzyloxy)methyl)furan. *Mol. Catal.* **2019**, *466*, 112–121. [[CrossRef](#)]
16. Yang, H.; Chen, Y. Ultrasound-assisted third-liquid phase-transfer catalyzed esterification of potassium 4-methoxyphenylacetate by dual-site phase-transfer catalyst. *J. Taiwan Inst. Chem. Eng.* **2012**, *43*, 897–903. [[CrossRef](#)]
17. Yang, H.M.; Lin, D.W. Third-liquid phase-transfer catalyzed esterification of sodium benzoate with novel dual-site phase-transfer catalyst under ultrasonic irradiation. *Catal. Commun.* **2011**, *14*, 101–106. [[CrossRef](#)]
18. Yang, H.M.; Chen, C.H. Catalytic esterification of sodium salicylate in third-liquid phase under ultrasound-assisted tri-liquid phase-transfer catalysis. *J. Mol. Catal. A Chem.* **2009**, *312*, 107–113. [[CrossRef](#)]
19. Huang, C.C.; Yang, H.M. Kinetics for benzylation of sodium 4-acetylphenoxide via third-liquid phase in the phase-transfer catalysis. *Appl. Catal. A Gen.* **2005**, *290*, 65–72. [[CrossRef](#)]
20. Yang, H.-M.; Huang, C.-C. Catalytic Benzylation of 4-Chloro-3-methylphenol Sodium Salt in Third-Liquid Phase under Conditions of Phase-Transfer Catalysis. *Ind. Eng. Chem. Res.* **2007**, *46*, 7915–7920. [[CrossRef](#)]
21. Yang, H.; Hung, Y.; Tu, C. Synthesis of butyl salicylate by phase-transfer catalysis with dual-site phase-transfer catalyst and ionic liquid in tri-liquid system. *J. Taiwan Inst. Chem. Eng.* **2014**, *45*, 1421–1427. [[CrossRef](#)]
22. Yang, H.M.; Li, C.C. Kinetics for synthesizing benzyl salicylate by third-liquid phase-transfer catalysis. *J. Mol. Catal. A Chem.* **2006**, *246*, 255–262. [[CrossRef](#)]
23. Kopeć, D.; Baj, S.; Siewniak, A. Ultrasound-Assisted Green Synthesis of Dialkyl Peroxides under Phase-Transfer Catalysis Conditions. *Molecules* **2020**, *25*, 118. [[CrossRef](#)] [[PubMed](#)]
24. Zhao, Q.; Sun, J.; Liu, B.; He, J. Novel kinetics model for third-liquid phase-transfer catalysis system of the “complex” carbanion: Competitive role between catalytic cycles. *Chem. Eng. J.* **2015**, *280*, 782–795. [[CrossRef](#)]
25. Zhao, Q.; Yang, L.; Shen, Y. Third-Liquid Phase Transfer Catalysis for Horner–Wadsworth–Emmons Reactions of “Moderately Acidic” and “Weakly Acidic” Phosphonates. *Ind. Eng. Chem. Res.* **2016**, *55*, 7604–7611. [[CrossRef](#)]
26. Zhao, Q.; Zhao, X.; Sun, J.; Yang, L.; Shen, Y. Catalytic Process for the Hydroxide-Initiated Reaction of the “Weakly Acidic” Substrate in the Third-Liquid Phase-Transfer Catalytic System. *Ind. Eng. Chem. Res.* **2018**, *57*, 13318–13326. [[CrossRef](#)]
27. Yadav, G.D.; Sowbna, P.R. Modeling of microwave irradiated liquid–liquid–liquid (MILLL) phase transfer catalyzed green synthesis of benzyl thiocyanate. *Chem. Eng. J.* **2012**, *179*, 221–230. [[CrossRef](#)]
28. Yadav, G.D.; Reddy, C.A. Kinetics of the n-Butoxylation of p-Chloronitrobenzene under Liquid–Liquid–Liquid Phase Transfer Catalysis. *Ind. Eng. Chem. Res.* **1999**, *38*, 2245–2253. [[CrossRef](#)]
29. Weng, H.S.; Wang, C.M.; Wang, D.H. A Preliminary Study on a Continuous Flow Stirred Vessel Reactor for Tri-Liquid-Phase Phase Transfer Catalysis. *Ind. Eng. Chem. Res.* **1997**, *36*, 3613–3618. [[CrossRef](#)]
30. Yang, H.M.; Peng, G.Y. Ultrasound-assisted third-liquid phase-transfer catalyzed esterification of sodium salicylate in a continuous two-phase-flow reactor. *Ultrason. Sonochem.* **2010**, *17*, 239–245. [[CrossRef](#)]
31. Yang, H.M.; Huang, Y.S. Green benzylation of sodium salicylate by phase-transfer catalysis with third-liquid phase in a continuous two-phase-flow reactor. *J. Taiwan Inst. Chem. Eng.* **2011**, *42*, 265–270. [[CrossRef](#)]

32. Yadav, G.D. An Improved Continuous Flow Stirred Multiphase Reactor. Patent PCT/IN2018/050535, 21 February 2019.
33. The Engineering ToolBox. Available online: https://www.engineeringtoolbox.com/paraffinic-benzoic-hydroxy-dioic-acids-structure-pka-carboxylic-dissociation-constant-alcohol-phenol-d_1948.html (accessed on 19 September 2020).



© 2020 by the authors. Licensee MDPI, Basel, Switzerland. This article is an open access article distributed under the terms and conditions of the Creative Commons Attribution (CC BY) license (<http://creativecommons.org/licenses/by/4.0/>).

Article

A Robust Method for the Estimation of Kinetic Parameters for Systems Including Slow and Rapid Reactions—From Differential-Algebraic Model to Differential Model

Tapio Salmi ^{1,*}, Esko Tirronen ¹, Johan Wärnä ¹, Jyri-Pekka Mikkola ^{1,2}, Dmitry Murzin ¹ and Valerie Eta ¹

¹ Laboratory of Industrial Chemistry and Reaction Engineering, Johan Gadolin Process Chemistry Centre, Åbo Akademi University, FI-20500 Turku, Finland; esko.tirronen@gmail.com (E.T.); johan.warna@abo.fi (J.W.); jpmikkol@abo.fi (J.-P.M.); dmitry.murzin@abo.fi (D.M.); valerie.eta@rebio.fi (V.E.)

² Department of Chemistry, Technical Chemistry, Chemical-Biological Center, Umeå University, SE-90187 Umeå, Sweden

* Correspondence: tapio.salmi@abo.fi

Received: 22 October 2020; Accepted: 23 November 2020; Published: 27 November 2020

Abstract: Reliable estimation of kinetic parameters in chemical systems comprising both slow and rapid reaction steps and rapidly reacting intermediate species is a difficult differential-algebraic problem. Consequently, any conventional approach easily leads to serious convergence and stability problems during the parameter estimation. A robust method is proposed to surmount this dilemma: the system of ordinary differential equations and nonlinear algebraic equations is converted to ordinary differential equations, which are solved in-situ during the parameter estimation. The approach was illustrated with two generic examples and an example from green chemistry: synthesis of dimethyl carbonate from carbon dioxide and methanol.

Keywords: kinetics; slow and rapid reactions; robust parameter estimation; dimethyl carbonate

1. Introduction

A reliable estimation of kinetic and thermodynamic parameters is one of the most important tasks in chemical reaction engineering. Only in few cases, like in the case of some homogeneous gas-phase reactions, is it possible to determine the kinetic constants a priori, exclusively from theoretical calculations. Consequently, in most cases, an extensive matrix of experimental work is needed. Particularly, in the presence of heterogeneous catalysts, small variations in the chemical composition and physical structure of the catalyst can change the reaction kinetics, and a new experimental program is inevitable. Typically, kinetic experiments are carried out in batch reactors or in continuous reactors with a well-established flow pattern, i.e., perfect back-mixing or plug flow. After that, the kinetic and thermodynamic parameters are determined by non-linear regression analysis. In the most recent 30 years, numerical methods and computing power have advanced tremendously. The development of solvers for stiff differential equations has enabled the treatment of difficult problems in chemical kinetics and simulation of large chemical systems appearing in combustion and atmospheric processes. However, even a superficially small problem can become a difficult one, as the system usually consists of a set of slow and rapid reaction steps. From a mathematical viewpoint, the system of ordinary differential equations describing the behavior of the components in a batch reactor becomes a system of differential-algebraic equations (DAE), for which solvers have been developed in recent years. In principle, the task could be solved by coupling a DAE solver to a parameter estimator (a nonlinear regression routine). However, if the parameters glide to an unrealistic regime in the

course of the parameter estimation, significant problems arise: the solutions of the algebraic equations induce problems, such as negative concentrations, which usually leads to the collapse of the whole computational process. Our experience with different case studies [1] has taught that a more robust approach is to convert the DAE problem to a set of ordinary differential equations (ODEs) and then solve these ODEs as a sub-problem in the parameter estimation. Here we illustrate the method with two generic examples and a highly relevant issue in chemical technology, namely the utilization of carbon dioxide as a raw material for the synthesis of green chemicals.

2. Development of a Robust Method

The tasks in the method are briefly summarized as follows:

- T1. Mass balances of all components in the batch reactor are written down (ODEs)
- T2. A quasi-steady-state hypothesis is applied to the intermediates—the ODEs become a system of DAEs is created
- T3. The DAE system is converted to a set of implicit ODEs by differentiation
- T4. The system of implicit ODEs is converted to a set of explicit ODEs
- T5. The system of explicit ODEs is implemented in a combined stiff ODE solver—parameter estimation software Modest.

2.1. Example: Consecutive Reactions with Slow and Rapid Steps

The following consecutive reaction scheme is considered in Figure 1. Step 1 is presumed to be slow whereas step 2 is rapid.



Figure 1. Consecutive reaction system.

The mass balances and rate equations of this consecutive reaction system can be written in the general case as follows,

$$\frac{dC_A}{dt} = -r_1 \quad (1)$$

$$\frac{dC_R}{dt} = r_1 - r_2 \quad (2)$$

$$\frac{dC_S}{dt} = r_2 \quad (3)$$

$$r_1 = k_1 \left(C_A - \frac{C_R}{K_1} \right) \quad (4)$$

$$r_2 = k_2 \left(C_R - \frac{C_S}{K_2} \right) \quad (5)$$

For the special case, where reaction step 1 is slow and step 2 is rapid, a reduced model can be derived:

$$\frac{C_S}{C_R} = K_2 \quad (6)$$

$$\frac{dC_S}{dt} = K_2 \frac{dC_R}{dt} \quad (7)$$

$$\frac{dC_A}{dt} + \frac{dC_R}{dt} + \frac{dC_S}{dt} = 0 \quad (8)$$

Substituting $\frac{dC_S}{dt}$ into Equation (8) yields

$$\frac{dC_A}{dt} + (1 + K_2) \frac{dC_R}{dt} = 0 \quad (9)$$

$$\frac{dC_R}{dt} = -\frac{1}{1 + K_2} \frac{dC_A}{dt} = +\frac{1}{1 + K_2} r_1 \quad (10)$$

$$\frac{dC_S}{dt} = +\frac{K_2}{1 + K_2} r_1 \quad (11)$$

As a summary we obtain for the special case of the consecutive reaction system, where step 1 is slow and step 2 is rapid:

$$\frac{dC_A}{dt} = -r_1$$

$$\frac{dC_A}{dt} = -r_1$$

$$\frac{dC_R}{dt} = \frac{1}{1 + K_2} r_1$$

$$\frac{dC_S}{dt} = \frac{K_2}{1 + K_2} r_1$$

$$r_1 = k_1 \left(C_A - \frac{C_R}{K_1} \right)$$

The general case was compared with the special case by increasing the value of the kinetic constant k_2 of the rapid reaction step 2 to find the value of k_2 by which the solution of the general case approaches that of the special case.

By setting $k_1 = 1$ and assuming arbitrary values for the equilibrium constants $K_1 = 10$ and $K_2 = 10$, the concentration profiles depicted in Figure 2 were obtained for the special case.

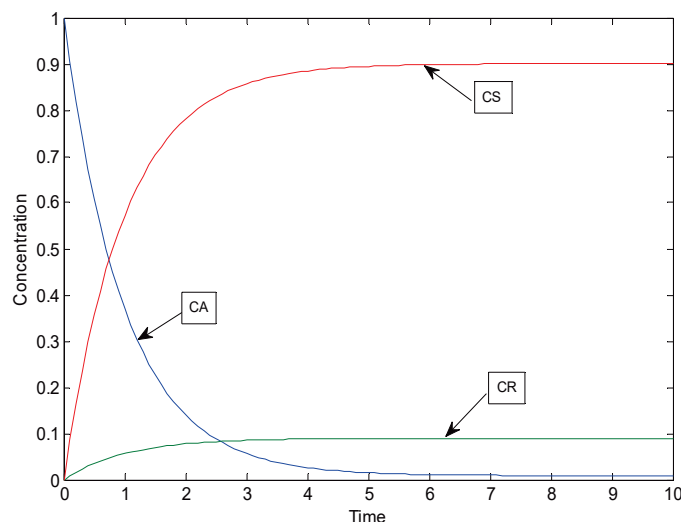


Figure 2. Concentration profiles of the special case of consecutive reactions with parameters: $k_1 = 1$, $K_1 = 10$ and $K_2 = 10$.

As revealed by Figure 2, the system behaves like a parallel reaction system, which is caused by the fact that as soon as R is formed, some part of it is immediately transformed to S.

The general case was simulated by increasing the value of the rate parameter k_2 of the rapid reaction step 2. Other parameters $k_1 = 1$, $K_1 = 10$ and $K_2 = 10$ were kept the same as in the special case. The sum of squared residuals was calculated for the difference between simulated data points of the

special case and the general case (number of simulated data points was 101 in the time frame of 0–10 in each case). Concentration profiles for the general case of consecutive reaction system corresponding to k_2 values of 1, 5, 10, 100 and 300 are depicted in Figure 3.

The sums of squared residuals of the general case simulations of consecutive reaction system with $k_1 = 1$, $k_2 = 1, 5, 10, 100$ and 300, $K_1 = 10$ and $K_2 = 10$ compared to the special case are presented in Table 1.

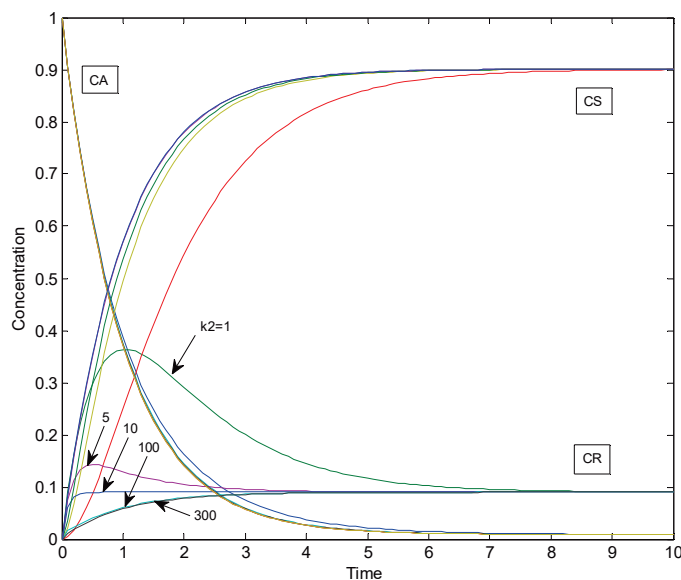


Figure 3. Concentration profiles of the general case of consecutive reactions with parameters: $k_1 = 1$, $k_2 = 1, 5, 10, 100$ and 300, $K_1 = 10$ and $K_2 = 10$.

The behavior of the sum of squared residuals as a function k_2 is displayed in Figure 4. The general case approaches the special case as the rate constant k_2 of the rapid reaction step 2 exceeds 100 i.e., 100 times the value of the rate parameter k_1 of the slow reaction step 1.

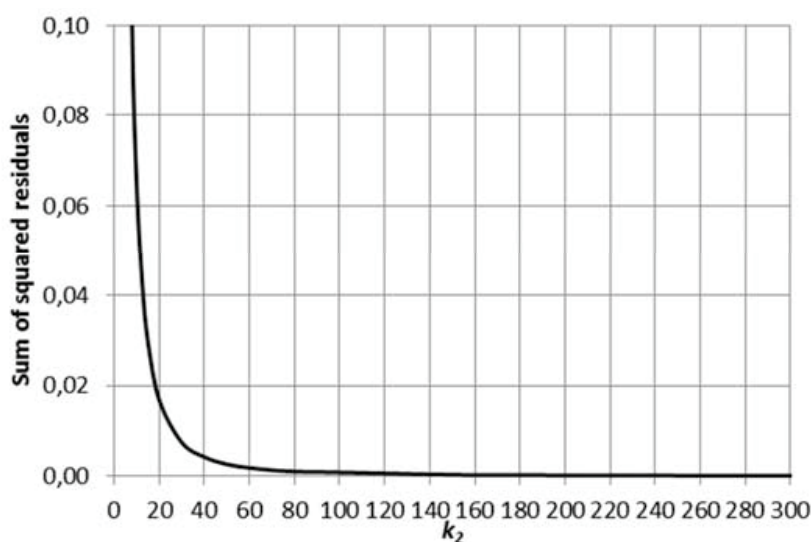


Figure 4. Sum of squared residuals as a function of the rate parameter k_2 of the rapid reaction step 2 in the general case of consecutive reaction system compared to the special case ($k_1 = 1$, $K_1 = 10$ and $K_2 = 10$).

Table 1. The sum of squared residuals of the general case simulations as compared to the special case ($k_1 = 1$, $K_1 = 10$ and $K_2 = 10$).

k_2	S
1	3.6113
5	0.2373
10	0.0644
100	0.006522
300	0.00071645

2.2. Parallel Reactions with Slow and Rapid Steps

The second example is the classical parallel reaction scheme displayed in Figure 5. Step 1 is presumed to be slow while step 2 is rapid.

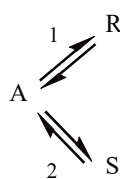


Figure 5. Parallel reaction system.

The mass balances and rate equations of this reaction system can be written in the general case as follows,

$$\frac{dC_A}{dt} = -r_1 - r_2 \quad (12)$$

$$\frac{dC_R}{dt} = r_1 \quad (13)$$

$$\frac{dC_S}{dt} = r_2 \quad (14)$$

$$r_1 = k_1 \left(C_A - \frac{C_R}{K_1} \right) \quad (15)$$

$$r_2 = k_2 \left(C_A - \frac{C_S}{K_2} \right) \quad (16)$$

For the special case, where reaction step 1 is slow and step 2 is rapid, a reduced model can be derived for the parallel reaction system:

$$\frac{dC_A}{dt} + \frac{dC_R}{dt} + \frac{dC_S}{dt} = 0 \quad (17)$$

$$\frac{C_S}{C_A} = K_2 \quad (18)$$

$$\frac{dC_S}{dt} = K_2 \frac{dC_A}{dt} \quad (19)$$

Substituting $\frac{dC_S}{dt}$ into Equation (17) yields:

$$(1 + K_2) \frac{dC_A}{dt} + \frac{dC_R}{dt} = 0 \quad (20)$$

$$\frac{dC_A}{dt} = -\frac{1}{1 + K_2} \frac{dC_R}{dt} = -\frac{1}{1 + K_2} r_1 \quad (21)$$

$$\frac{dC_S}{dt} = -\frac{K_2}{1 + K_2} r_1 \quad (22)$$

At time $t = 0$,

$$C_{R(0)} = 0 \quad (23)$$

$$\frac{C_{S(0)}}{C_{A(0)} - C_{S(0)}} = K_2 \quad (24)$$

$$C_{S(0)} = \frac{K_2 C_{0A}}{1 + K_2} \quad (25)$$

$$C_{A(0)} = \frac{C_{0A}}{1 + K_2} \quad (26)$$

The initial conditions (25) and (26) arise from the fact that some amounts of component S is formed immediately in the system, because step 2 progresses with an infinite rate. As a summary we obtain for the special case of the parallel reaction system, where step 1 is slow and step 2 is rapid:

$$\frac{dC_A}{dt} = -\frac{1}{1 + K_2} r_1$$

$$\frac{dC_R}{dt} = r_1$$

$$\frac{dC_S}{dt} = -\frac{K_2}{1 + K_2} r_1$$

$$r_1 = k_1 \left(C_A - \frac{C_R}{K_1} \right)$$

$$C_{A(0)} = \frac{C_{0A}}{1 + K_2}$$

$$C_{R(0)} = 0$$

$$C_{S(0)} = \frac{K_2 C_{0A}}{1 + K_2}$$

Initial values $C_A(0)$ and $C_S(0)$, $C_R(0) = 0$ as a function of equilibrium constant K_2 in the special case of a parallel reaction system are depicted in Figure 6.

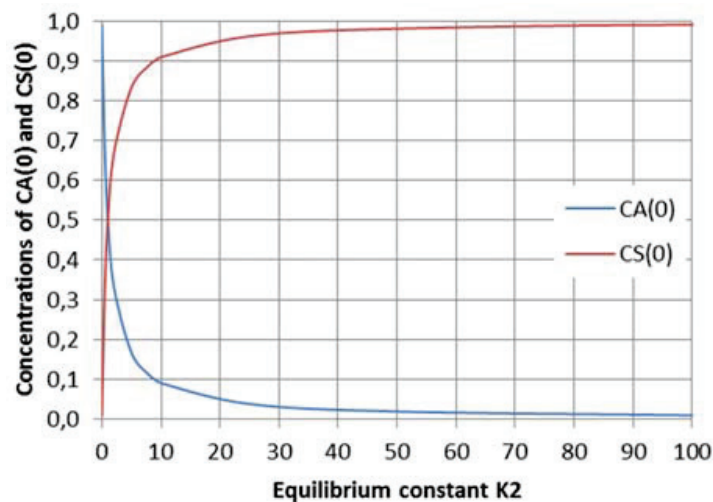


Figure 6. Initial values $C_A(0)$ and $C_S(0)$, $C_R(0) = 0$ as a function of equilibrium constant K_2 in the special case of a parallel reaction system, where step 1 is slow and step 2 is rapid.

Some concentration profiles as an example for the special case of a parallel reaction system with parameters $k_1 = 1$, $K_1 = 10$ and $K_2 = 2$ are displayed in Figure 7.

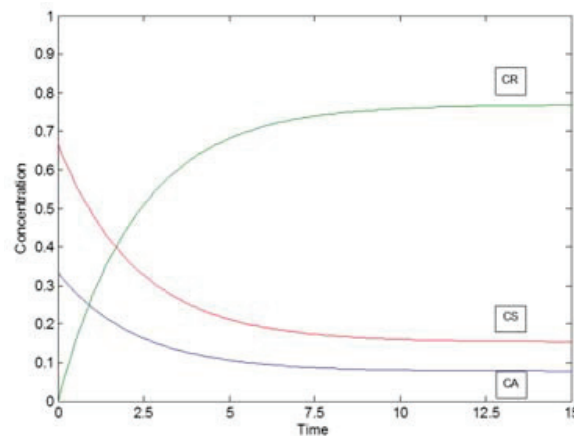


Figure 7. Concentration profiles of the special case of a parallel reaction system with parameters: $k_1 = 1$, $K_1 = 10$ and $K_2 = 2$.

The general case of a parallel reaction system was compared with the special case as in the previous example 2.1 by increasing the value of the rate parameter k_2 of the rapid reaction step 2 to find the value of k_2 by which the solution of the general case approaches that of the special case. Concentration profiles for the general case of parallel reactions corresponding to k_2 values of 2, 10 and 50 are depicted in Figure 8.

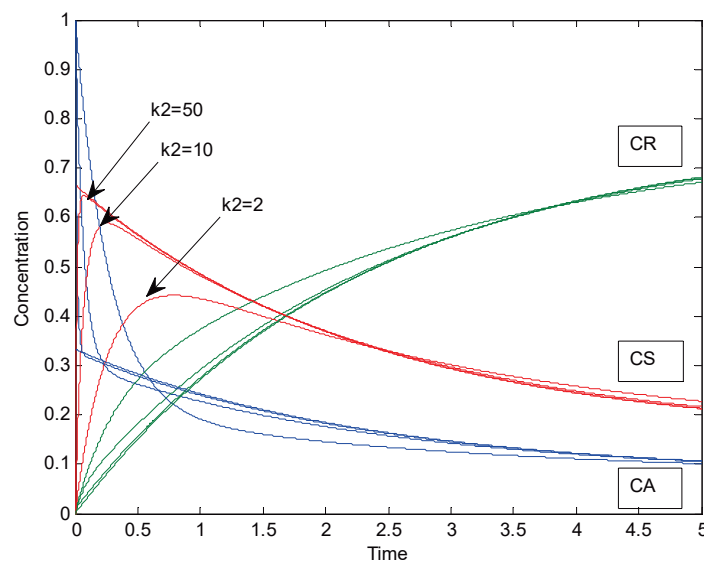


Figure 8. Concentration profiles of the general case of a parallel reaction system with parameters: $k_1 = 1$, $k_2 = 2, 10$ and 50 , $K_1 = 10$ and $K_2 = 2$.

The sum of squared residuals calculated as in the example 2.1 between simulated data points of the special case and the general case with different values of the rate parameter k_2 while $k_1 = 1$, $K_1 = 10$ and $K_2 = 2$, (the number of simulated data points was 301 in the time interval of 0–15) are shown in Table 2. The behavior of the sum of squared residuals as a function is displayed in Figure 9. The general case approaches the special case in this example when k_2 is >50 .

Table 2. The sum of squared residuals of the general case of parallel reaction system compared to the special case with different values of k_2 ($k_1 = 1$, $K_1 = 10$ and $K_2 = 2$).

k_2	S
2	3.31901
5	1.68380
10	1.14954
50	0.89085
100	0.88929
1000	0.88893
10,000	0.88889

This kind of parallel reaction system has been studied by Branco et al. [2], who developed a concept for the determination of the switching point between kinetic and thermodynamic control for cases when one of the reactions is very rapid, whereas the second one is thermodynamically favored. The same phenomenon can be seen in Figure 6: S is the kinetically favored product, with a rapidly increasing concentration in the beginning, but with an increasing reaction time the concentration of R becomes higher because it is favored by thermodynamics, i.e., its formation has a higher equilibrium constant.

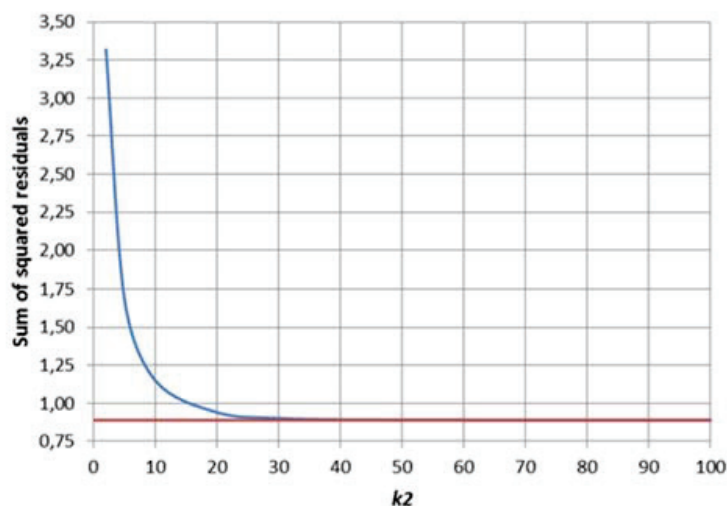


Figure 9. The sum of the squared residuals as a function of the rate parameter k_2 of the fast reaction step 2 in the general case of a parallel reaction system compared to the special case ($k_1 = 1$, $K_1 = 10$ and $K_2 = 2$).

2.3. Example: Synthesis of Dimethyl Carbonate from Methanol and Carbon Dioxide

Carbon dioxide reacts with methanol (MeOH) to yield dimethyl carbonate (DMC), which is a green alternative to methyl tert-butyl ether (MTBE) and can be used as a carbonylating and methylating agent [3,4]. The presence of a heterogeneous catalyst is required for the synthesis of DMC. We used zirconia-based catalysts (ZrO_2 -MgO) in an isothermal and isobaric laboratory-scale batch reactor [5]. The thermodynamics for this reaction is extremely unfavorable, so a way to shift the equilibrium is to include an additive to the reaction mixture; the role of the additive was to act as a chemical dehydration agent, i.e., to capture the water formed in the reaction. Butylene oxide (BO) was selected as the additive [5]. In this way, the process gains a more irreversible character and can be forced to the side of the products. Methylene butylate (MB) appears as an intermediate species, forming butylene glycol (BG) and thus preventing the water formation. The reaction scheme is displayed below in Figure 10, where * denotes a vacant site on the surface of the catalyst, and MeOH* denotes adsorbed methanol on the catalyst surface.

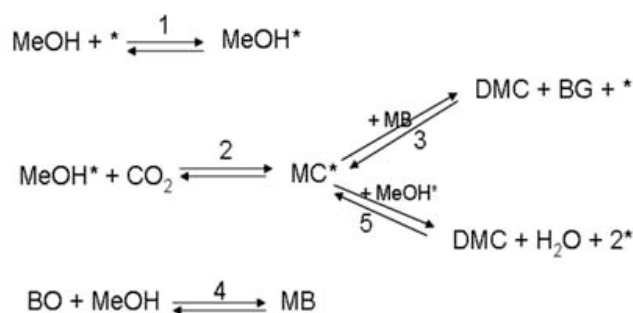


Figure 10. Reaction scheme for the synthesis of dimethyl carbonate (DMC).

Steps 1–3 and 5 take place on the catalyst surface, while step 4 proceeds as a homogeneous liquid-phase reaction. Reaction steps 2 and 4 in the scheme were assumed to be rate determining, whereas the adsorption step of methanol was presumed to be rapid. In addition, steps 3 and 5 were taken as rapid steps compared to steps 2 and 4. A constant-density system was assumed and the mass balance of carbon dioxide was not included, since CO_2 was constantly added to the system by keeping the pressure constant. Thus, the saturation concentration of CO_2 was presumed, and Henry's law was applied to relate the partial pressure of CO_2 and the concentration of dissolved CO_2 . A large excess of methanol was used. Based on the reaction mechanism displayed above, the rate equations for the rate determining steps were derived. The details of the derivation of the rate equations are given as supplementary material in Appendix A: Derivation of the Rate Equations.

2.3.1. Basic Mass Balances

The mass balances for bulk phase components in a batch reactor (assuming constant density) at a constant CO_2 concentration due to controlled pressure can be written as follows (ρ_B = mass of catalyst-to-liquid volume, i.e., the catalyst bulk density)

$$\frac{d[\text{DMC}]}{dt} = (r_3 + r_5)\rho_B \quad (27)$$

$$\frac{d[\text{BG}]}{dt} = r_3\rho_B \quad (28)$$

$$\frac{d[\text{H}_2\text{O}]}{dt} = r_5\rho_B \quad (29)$$

$$\frac{d[\text{MeOH}]}{dt} = -r_1\rho_B - r_4 \quad (30)$$

$$\frac{d[\text{BO}]}{dt} = -r_4 \quad (31)$$

$$\frac{d[\text{MB}]}{dt} = -r_3\rho_B + r_4 \quad (32)$$

Applying a quasi-steady state to MC^* and MeOH^* gives relations (33) and (34),

$$r_{\text{MC}^*} = r_2 - r_3 - r_5 \approx 0 \quad (33)$$

$$r_{\text{MeOH}^*} = r_1 - r_2 - r_5 \approx 0 \quad (34)$$

Substituting Equations (33) and (34) into Equations (27)–(32) results in the following relationships:

$$\frac{d[\text{DMC}]}{dt} = r_2\rho_B \quad (35)$$

$$\frac{d[BG]}{dt} = r_3\rho_B \quad (36)$$

$$\frac{d[H_2O]}{dt} = r_5\rho_B \quad (37)$$

$$\frac{d[MeOH]}{dt} = -(r_2 + r_5)\rho_B - r_4 \quad (38)$$

$$\frac{d[BO]}{dt} = -r_4 \quad (39)$$

$$\frac{d[MB]}{dt} = -r_3\rho_B + r_4 \quad (40)$$

2.3.2. Differential-Algebraic Problem

The addition of the mass balances further gives

$$\frac{d[MB]}{dt} + \frac{d[BG]}{dt} = r_4 \quad (41)$$

$$\frac{d[MB]}{dt} + \frac{d[MeOH]}{dt} = -2r_2\rho_B \quad (42)$$

$$\frac{d[H_2O]}{dt} + \frac{d[BG]}{dt} = r_2\rho_B \quad (43)$$

The ODEs (Equations (33) and (35)–(37)) give the stoichiometric relations

$$\int_0^{[DMC]} d[DMC] = \int_0^{[H_2O]} d[H_2O] + \int_0^{[BG]} d[BG] \quad (44)$$

$$[DMC] = [H_2O] + [BG]$$

Equations (36), (39) and (40) give

$$-\int_{[BO]_0}^{[BO]} d[BO] = \int_0^{[BG]} d[BG] + \int_0^{[MB]} d[MB] \quad (45)$$

$$[BO]_0 = [BO] + [BG] + [MB]$$

From Equations (27), (30) and (32)–(34) is obtained

$$-2 \int_0^{[DMC]} d[DMC] = \int_{[MeOH]_0}^{[MeOH]} d[MeOH] + \int_0^{[MB]} d[MB] \quad (46)$$

$$[MeOH]_0 = [MeOH] + 2[DMC] + [MB]$$

The following relationship between the concentrations was obtained by consideration of the reaction mechanism [6] ($\alpha = K_1K_5/K_3$),

$$\frac{[DMC]}{[BG]} = 1 + \alpha \frac{[MeOH]}{[MB]} \quad (47)$$

Equations (35), (39), (41)–(43) and (47) form a set of six differential-algebraic equations, with six unknowns: ([DMC], [BO], [BG], [H₂O], [MB], [MeOH]).

From Equation (47), the following expression can be obtained:

$$\frac{[BG]}{[DMC]} = \frac{1}{1 + \alpha \frac{[MeOH]}{[MB]}} = \frac{[MB]}{[MB] + \alpha[MeOH]} \quad (48)$$

From Equations (44) and (47), the following relationship is obtained:

$$\frac{[H_2O]}{[DMC]} = 1 - \frac{[BG]}{[DMC]} \quad (49)$$

$$\frac{[H_2O]}{[DMC]} = \frac{\alpha[MeOH]}{[MB] + \alpha[MeOH]} \quad (50)$$

Equations (45) and (48) give the following relation:

$$\frac{[MB][DMC]}{[MB] + \alpha[MeOH]} + [MB] = [BO]_O - [BO] = \omega \quad (51)$$

i.e.,

$$[MB][DMC] + [MB]^2 + \alpha[MeOH][MB] = \omega[MB] + \alpha[MeOH]\omega \quad (52)$$

i.e.,

$$[MB]^2 + ([DMC] - \omega)[MB] + (\alpha[MB] - \alpha\omega)([MeOH]_O - 2[DMC] - [MB]) = 0 \quad (53)$$

Rearranging of Equation (53) gives

$$(1 - \alpha)[MB]^2 + ([DMC] - \omega + \alpha\gamma + \alpha\omega)[MB] - \alpha\gamma\omega = 0 \quad (54)$$

where $\gamma = [MeOH]_O - 2[DMC]$. The solution of the second-degree Equation (54) becomes

$$[MB] = \frac{\beta \pm \sqrt{\beta^2 + 4(1 - \alpha)\alpha\gamma\omega}}{2(1 - \alpha)} \quad (55)$$

where $\beta = \omega - [DMC] - \alpha(\gamma + \omega)$. The sign + in the nominator gives the physically meaningful solution of Equation (55).

Equations (46), (48) and (50) give

$$[MeOH] = \gamma - [MB] \quad (56)$$

$$[BG] = \frac{[MB][DMC]}{[MB] + \alpha[MeOH]} \quad (57)$$

$$[H_2O] = \frac{\alpha[MeOH][DMC]}{[MB] + \alpha[MeOH]} \quad (58)$$

A system of two ODEs Equations (35) and (39) can be solved by employing Equations (55)–(58). Thus, the problem can in principle be solved as an ODE problem coupled to algebraic equations.

2.3.3. Transformation to ODEs

In order to obtain a more robust algorithm for parameter estimation, the differential-algebraic problem is transformed to ODEs as follows.

From Equation (48),

$$\frac{[BG]}{[DMC]} = \frac{\frac{MB}{MeOH}}{\frac{MB}{MeOH} + \alpha} \quad (59)$$

$$[BG] = \frac{y}{\alpha + y}[DMC] = f(y)[DMC] \quad (60)$$

where $y = \frac{[MB]}{[MeOH]}$.

The procedure is continued by differentiation as shown below,

$$\frac{df}{dt} = \frac{\frac{dy}{dt}(\alpha + y) - \frac{dy}{dt}(y)}{(\alpha + y)^2} = \frac{\alpha \frac{dy}{dt}}{(\alpha + y)^2} \quad (61)$$

$$\frac{d[BG]}{dt} = \frac{df}{dt}[DMC] + f \frac{d[DMC]}{dt} \quad (62)$$

$$\frac{d[BG]}{dt} = \frac{\alpha[DMC]}{(\alpha + y)^2} \frac{dy}{dt} + \frac{y}{\alpha + y} \frac{d[DMC]}{dt} \quad (63)$$

The definition y gives the relation

$$\frac{d[MB]}{dt} = \frac{dy}{dt}[MeOH] + y \frac{d[MeOH]}{dt} \quad (64)$$

$$\frac{dy}{dt} = \frac{\frac{d[MB]}{dt}}{[MeOH]} - y \frac{\frac{d[MeOH]}{dt}}{[MeOH]} \quad (65)$$

Equation (16) gives

$$\frac{d[MeOH]}{dt} = -\frac{d[MB]}{dt} - 2r_2\rho_B \quad (66)$$

A combination of Equations (65) and (66) gives

$$\frac{dy}{dt} = \frac{\frac{d[MB]}{dt}}{[MeOH]} + y \frac{\left(\frac{d[MB]}{dt} + 2r_2\rho_B\right)}{[MeOH]} \quad (67)$$

Equations (41) and (63) give

$$\begin{aligned} \frac{d[BG]}{dt} &= r_4 - \frac{d[MB]}{dt} \\ &= \frac{\alpha[DMC]}{(\alpha+y)^2} \frac{dy}{dt} + \frac{y}{\alpha+y} r_2\rho_B \end{aligned} \quad (68)$$

From Equation (68) dy/dt is solved:

$$\begin{aligned} \frac{dy}{dt} &= \frac{(\alpha+y)^2}{\alpha[DMC]} \\ &\left(r_4 - \frac{y}{\alpha+y} r_2\rho_B - \frac{d[MB]}{dt}\right) \end{aligned} \quad (69)$$

Equations (67) and (69) are equal, therefore,

$$\begin{aligned} &\frac{(1+y)}{[MeOH]} \frac{d[MB]}{dt} + 2r_2\rho_B \frac{y}{[MeOH]} \\ &= \frac{(\alpha+y)^2}{\alpha[DMC]} \left(r_4 - \frac{y}{\alpha+y} r_2\rho_B\right) - \frac{(\alpha+y)^2}{\alpha[DMC]} \frac{d[MB]}{dt} \end{aligned} \quad (70)$$

from which the time derivative is solved explicitly:

$$\begin{aligned} &\left[\frac{(1+y)[DMC]}{[MeOH]} + \frac{(\alpha+y)^2}{\alpha}\right] \frac{d[MB]}{dt} \\ &= -\left[\frac{(\alpha+y)y}{\alpha} - \frac{2y[DMC]}{[MeOH]}\right] r_2\rho_B + \frac{(\alpha+y)^2}{\alpha} r_4 \end{aligned} \quad (71)$$

$$\begin{aligned} &\left[\frac{\alpha(1+y)[DMC]}{(\alpha+y)^2[MeOH]} + 1\right] \frac{d[MB]}{dt} \\ &= r_4 - \frac{y}{\alpha+y} \left[1 - \frac{2\alpha}{\alpha+y} \frac{[DMC]}{[MeOH]}\right] r_2\rho_B \end{aligned} \quad (72)$$

The final forms of the mass balances for the liquid-phase components in the batch reactor thus become ($\alpha = \text{constant}$):

$$\frac{d[\text{DMC}]}{dt} = r_2 \rho_B \quad (73)$$

$$\frac{d[\text{BO}]}{dt} = -r_4 \quad (74)$$

$$\frac{d[\text{MB}]}{dt} = \omega^{-1} \left\{ r_4 - \left[\frac{y}{\alpha+y} \right] \left[1 - \frac{2\alpha}{\alpha+y} \frac{[\text{DMC}]}{[\text{MeOH}]} \right] r_2 \rho_B \right\}$$

$$\omega = \left[\frac{\alpha(1+y)[\text{DMC}]}{(\alpha+y)^2[\text{MeOH}]} + 1 \right] y = \frac{[\text{MB}]}{[\text{MeOH}]} \quad (75)$$

$$\frac{d[\text{BG}]}{dt} = r_4 - \frac{d[\text{MB}]}{dt} \quad (76)$$

$$\frac{d[\text{H}_2\text{O}]}{dt} = r_2 \rho_B - r_4 + \frac{d[\text{MB}]}{dt} \quad (77)$$

$$\frac{d[\text{MeOH}]}{dt} = -2r_2 \rho_B - \frac{d[\text{MB}]}{dt} \quad (78)$$

The rates of the rate-determining steps (r_2 and r_4) were obtained from the mechanism—these rates include only the concentrations of CO_2 , MeOH , DMC , MB , BO , BG and H_2O , respectively (Appendix A: Derivation of the Rate Equations). The rate equations are given below. The ODEs were solved with the backward difference method during the parameter estimation, which was performed with the Levenberg–Marquardt algorithm [7].

Rate equations:

$$r_2 = \frac{k_2 \left([\text{MeOH}] P_{\text{CO}_2} - \frac{1}{K} \frac{[\text{DMC}][\text{BG}]}{[\text{MB}]} \right)}{1 + K_1 [\text{MeOH}] + \frac{1}{K_3} \frac{[\text{DMC}][\text{BG}]}{[\text{MB}]}} \quad (79)$$

$$r_4 = k_4 [\text{BO}] [\text{MeOH}] \quad (80)$$

2.3.4. Parameter Estimation Results

Rate parameters k_2 and k_4 were estimated from isothermal experiments shown as Equations (79) and (80). The experimental temperature was 150 °C, and the pressure was 45 bar of CO_2 initially. Parameters K_1 and $1/K_3$ (Table 3, Equations (47) and (48)) turned out not to be significant and were approximated to zero in the rate expression r_2 . Parameter α was determined separately from the plot according to Equation (47); $\alpha = 1.3 \times 10^{-3}$. The thermodynamic equilibrium constant was estimated from theoretical calculations: $K = 0.08 \times 10^{-5}$, at 150 °C.

Table 3. Parameter estimation results.

Parameter	Value	Error/%
k_2	1.60×10^{-5}	6.8
k_4	1.12×10^{-2}	6.7
$K_1 = 0, 1/K_3 = 0, \alpha = 1.3 \times 10^{-3}, K = 0.08 \times 10^{-5}$, at 150 °C		

The solution of ODEs and parameter estimation progressed very smoothly and led to an excellent description of the experimental data. The errors of the kinetic parameters were clearly less than 10%. The performance of the procedure is illustrated in Figure 11. The numerical values of the estimated parameters are enlisted in Table 3. The overall degree of explanation was 99.98%.

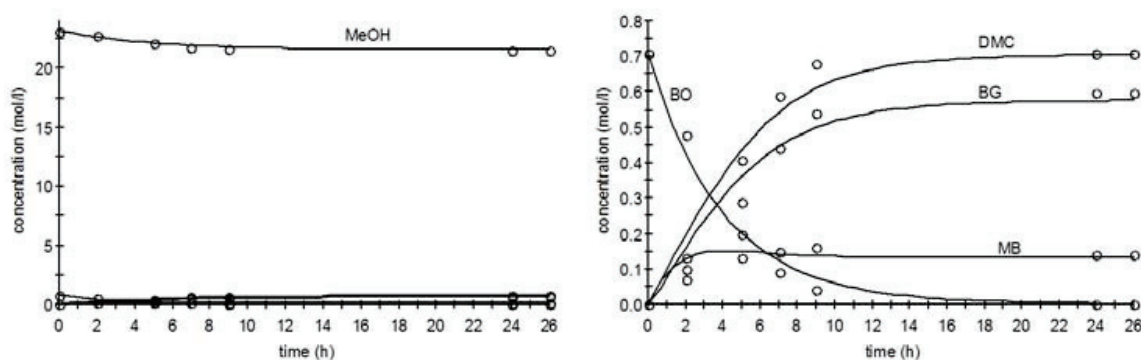


Figure 11. Performance of the solution of ordinary differential equations (ODEs) and parameter estimation method: synthesis of dimethyl carbonate (DMC) (150 °C, initial CO₂ pressure of 45 bar). The smaller concentrations in the left figure (butylene oxide (BO), DMC, butylene glycol (BG), methylene butylate (MB)) are magnified in the right figure.

3. Conclusions

Solution of a differential-algebraic problem in connection to both fast and slow reaction steps is a demanding task when coupled to a parameter estimation task. In order to surmount the numerical problems often appearing for DAE systems, we propose a robust procedure, which implies the transformation of the DAE system to a set of explicit ODEs that can be easily solved in-situ during the estimation of kinetic parameters. The success of the methodology was illustrated with two generic examples and a case study, synthesis of dimethyl carbonate (DMC) from methanol and carbon dioxide.

Author Contributions: J.-P.M. and V.E. conceived and designed the experiments; V.E. performed the experiments; T.S., J.W., D.M., J.-P.M. and V.E. analyzed the data; J.W. and E.T. performed the numerical simulations; T.S. and E.T. wrote the paper. All authors have read and agreed to the published version of the manuscript.

Funding: This research was funded by Academy of Finland (Academy professor's grant number 319002).

Conflicts of Interest: The authors declare no conflict of interest.

Notation

c	concentration
c^*	concentration of an intermediate
f	function
k	reaction rate constant
r	Rate
t	Time
y	concentration variable
α	parameter in rate equation
β	parameter in rate equation
γ	merged concentration
ρ_B	catalyst bulk density (mass of catalyst-to-liquid volume)
ω	merged parameter
$[]$	concentration

Appendix A. Derivation of the Rate Equations



This rapid step is in quasi-equilibrium giving

$$K_1 = \frac{[\text{MeOH}^*]}{[\text{MeOH}][*]} \quad (\text{A2})$$

from which the surface concentration is solved,

$$[MeOH^*] = K_1[MeOH] \quad (A3)$$

Analogously, for the rapid step



can be written

$$K_3 = \frac{[DMC][BG][*]}{[MC^*][MB]} \quad (A5)$$

and the surface concentration of MC is solved,

$$[MC^*] = \frac{[DMC][BG][*]}{K_3[MB]} \quad (A6)$$

The total balance of sites on the catalyst surface is (0^* is the total concentration of available sites on the surface)

$$[MeOH^*] + [MC^*] + [*] = [0^*] \quad (A7)$$

Equations (A3), (A6) and (A7) give the concentration of vacant sites,

$$[*] = \frac{[0^*]}{K_1[MeOH] + [DMC][BG]/(K_3[MB])} \quad (A8)$$

For the slow, rate determining step 2 is valid:

$$r_2 = k'_2[MeOH^*]P_{CO_2} - k'_{-2}[MC^*] \quad (A9)$$

$$r_2 = (k'_2K_1[MeOH]P_{CO_2} - k'_{-2}\frac{[DMC][BG]}{K_3[MB]})[*] \quad (A10)$$

The following merged constants are introduced

$$\begin{aligned} k'_2/k'_{-2} &= K_2, \\ K_1K_2K_3 &= K, \\ k'_2K_1[0^*] &= k_2 \end{aligned}$$

and introduced in Equation (A10). The final rate expression for step 2 becomes

$$r_2 = \frac{k_2([MeOH]P_{CO_2} - \frac{[DMC][BG]}{K[MB]})}{1 + K_1[MeOH] + \frac{[DMC][BG]}{K_3[MB]}} \quad (A11)$$

The slow step



takes place in the liquid bulk (not on the catalyst surface), and the rate is expressed in a straightforward way,

$$r_4 = k_4[BO][MeOH] \quad (A13)$$

References

1. Jogunola, O.; Salmi, T.; Wärnå, J.; Mikkola, J.-P.; Tirronen, E. Kinetics of methyl formate hydrolysis in the absence and presence of a complexing agent. *Ind. Eng. Chem. Res.* **2011**, *50*, 267–276. [\[CrossRef\]](#)
2. Branco, P.D.; Yablonsky, G.; Marin, G.B.; Constales, D. The switching point between kinetic and thermodynamic control. *Comp. Chem. Eng.* **2019**, *125*, 606–611. [\[CrossRef\]](#)
3. Ono, Y. DMC for environmentally benign reactions. *Catal. Today* **1997**, *35*, 15–25. [\[CrossRef\]](#)
4. Tundo, P. New developments in dimethyl carbonate chemistry. *Pure Appl. Chem.* **2001**, *73*, 1117–1124. [\[CrossRef\]](#)

5. Eta, V.; Mäki-Arvela, P.; Leino, E.; Kordás, K.; Salmi, T.; Murzin, D.; Mikkola, J.-P. Sustainable synthesis of dimethyl carbonate from methanol and carbon dioxide under dehydration- the effect of magnesium enhanced reactions. *Ind. Eng. Chem. Res.* **2010**, *49*, 9609–9617. [[CrossRef](#)]
6. Eta, V. Catalytic Synthesis of Dimethyl Carbonate from Carbon Dioxide and Methanol. Ph.D. Thesis, Åbo Akademi, Turku, Finland, 2011.
7. Haario, H. *Modest-User's Guide*; Profmath: Helsinki, Finland, 2007.

Publisher's Note: MDPI stays neutral with regard to jurisdictional claims in published maps and institutional affiliations.



© 2020 by the authors. Licensee MDPI, Basel, Switzerland. This article is an open access article distributed under the terms and conditions of the Creative Commons Attribution (CC BY) license (<http://creativecommons.org/licenses/by/4.0/>).

Review

Revisiting the Role of Mass and Heat Transfer in Gas–Solid Catalytic Reactions

Riccardo Tesser ¹ and Elio Santacesaria ^{2,*}

¹ NICTL—Naples Industrial Chemistry Laboratory, Department of Chemical Science, University of Naples Federico II, 80126 Naples, Italy; riccardo.tesser@unina.it

² CEO of Eurochem Engineering Ltd., 20139 Milan, Italy

* Correspondence: elio.santacesaria@eurochemengineering.com

Received: 14 October 2020; Accepted: 2 December 2020; Published: 4 December 2020

Abstract: The tremendous progress in the computing power of modern computers has in the last 20 years favored the use of numerical methods for solving complex problems in the field of chemical kinetics and of reactor simulations considering also the effect of mass and heat transfer. Many classical textbooks dealing with the topic have, therefore, become quite obsolete. The present work is a review of the role that heat and mass transfer have in the kinetic studies of gas–solid catalytic reactions. The scope was to collect in a relatively short document the necessary knowledge for a correct simulation of gas–solid catalytic reactors. The first part of the review deals with the most reliable approach to the description of the heat and mass transfer outside and inside a single catalytic particle. Some different examples of calculations allow for an easier understanding of the described methods. The second part of the review is related to the heat and mass transfer in packed bed reactors, considering the macroscopic gradients that derive from the solution of mass and energy balances on the whole reactor. Moreover, in this second part, some examples of calculations, applied to chemical reactions of industrial interest, are reported for a better understanding of the systems studied.

Keywords: gas–solid catalytic reactions; chemical kinetics; heat and mass transfer

1. Introduction

When a reaction occurs inside a catalytic particle, the reagents are consumed, giving rise to products and, in the meantime, heat is released or absorbed according to whether the enthalpy of the reaction is positive or negative. Inside and around the particles, gradients of respective concentration and temperature are generated as a consequence. Then, if the particles are put inside a tubular reactor (see Figure 1), macroscopic gradients (both in axial and radial directions) also arise as a consequence of the average rate of reaction in any single catalytic particle and the regime of mass and heat flow developed in the specific reactor. In Figure 1, all the possible gradients related to both temperature and concentration occurring in a tubular gas–solid catalytic reactor are illustrated.

These macroscopic (or “long-range”) gradients can be vanished by employing “gradientless” reactors that are isothermal CSTRs (continuous stirred tank reactors) normally used in laboratory kinetic studies (see Figure 2A,B).

Moreover, each particle inside a reactor has its own history, and microscopic gradients are developed in conditions at the particle surface that are generally different from the internal particle conditions.

At the industrial scale, gas–solid catalytic processes are usually carried out in very large capacity equipment represented by packed bed reactors with productivity of thousands of tons per year.

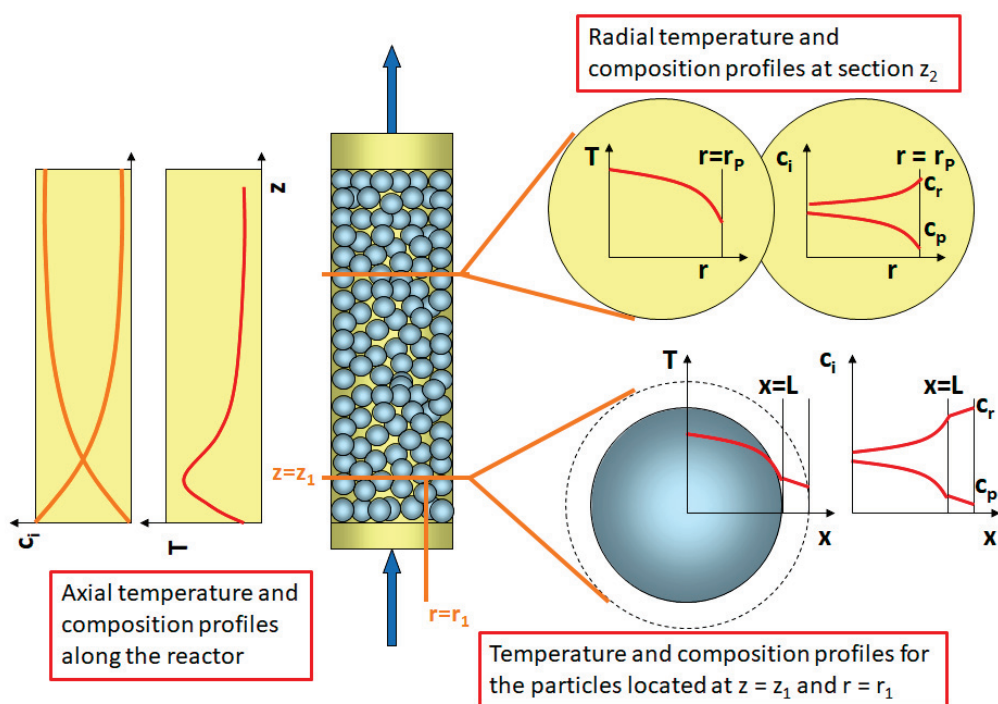


Figure 1. Overview of temperature and concentration macroscopic and microscopic gradients in packed bed reactor (taken and adapted from [1]). Reprinted with the permission of Springer, Copyright 2018.

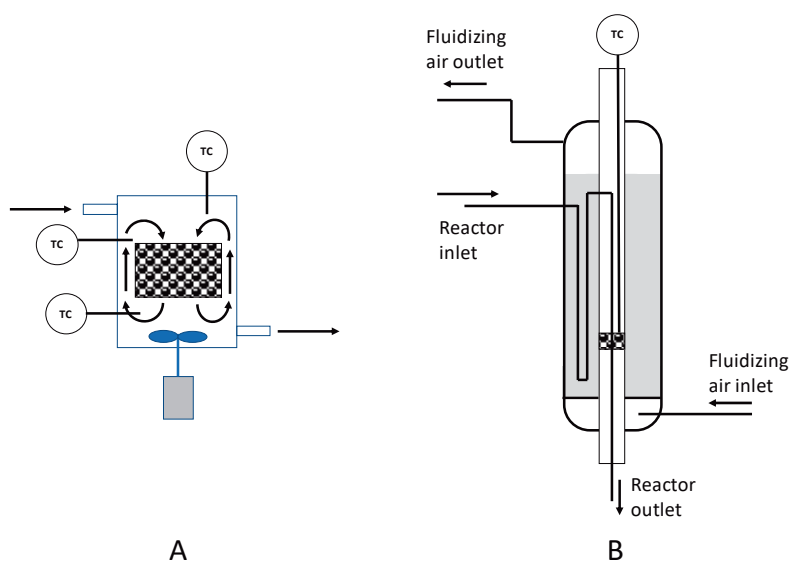
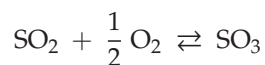


Figure 2. Examples of “gradientless” laboratory reactors. (A) Continuous stirred tank reactor (CSTR); (B) fixed-bed reactor.

Such reactors are arranged in a complex scheme also containing all the auxiliary equipment necessary for feeding, cooling, heating, or pressurizing operations. The necessity of supplying or removing heat according to the enthalpy of the reaction is the main reason for which reactors with multiple tubes (in many cases thousands of tubes) are preferred. The heat removal is obtained by circulating an opportune fluid externally to the tubes in order to limit the temperature rise (or drop) of the reactive mixture.

Normally, the goal is to obtain isothermal conditions, however, very frequently, these ideal conditions cannot be reached. On the contrary, when an equilibrium reaction is involved in the reaction scheme, such as for example:



a single reactor with large diameter, in which structurally different catalytic packed beds are contained and operating in adiabatic conditions, is preferred, because this type of reactor allows for the control of the overall conversion through the temperature of the outlet flow stream. The heat removal, in this case, is obtained by cooling the flow stream between two different catalytic stages of the reactor.

Two ideal limit conditions can be recognized, the isothermal and adiabatic, realized thanks to a more or less efficient system of heat exchange. However, a condition not isothermal and not adiabatic is more frequently encountered in practice. This implies the development of more complex models to describe the system in which the mentioned limit conditions are considered as particular cases.

Some other aspects are important in the design of fixed-bed reactors, such as pressure drop, safe operating protocol (to avoid runaway problems), temperature range, and catalyst packing modality.

From a general point of view, the design approach of catalytic fixed-bed reactors consists in correctly defining and then solving the mass and energy balance equations. Normally, the solution of such equations must be achieved only numerically, especially when the kinetic systems are characterized by a complex reaction scheme. The problem must to be solved simultaneously both at a microscopic local level, with the obtainment of the reagents and product concentration particle profiles, as well as of the effectiveness factor for all the occurring reactions, and at a macroscopic level, reproducing all the long-range concentration and temperature profiles. This specific situation requires an evaluation of the catalyst effectiveness factor in each position in the catalytic bed, considering the conditions we have at any instance in that point. This subject has been previously described in many books, papers, and reviews [1–17]. A modern and comprehensive approach to the problem, with many solved exercises, can be found in [1]. On the basis of all the examined literature, the scope of this review is to give, in a concise way, all the information necessary to the researchers to correctly face the study of the gas–solid reactions. In the following paragraphs, we consider, first of all, the mass and heat transfer occurring in a single catalytic particle, and then we will treat the macroscopic gradients related to the whole fixed-bed reactor.

2. Mass and Heat Transfer in a Single Catalytic Particle

When a reaction occurs inside a catalytic particle, the reagents are consumed for giving products and a certain amount of heat is consumed or released according to the thermal characteristic of the reaction (exothermic or endothermic). The concentration of the reagents decreases from the external geometric surface of the particles toward the center. The concentration of the products, on the contrary, increases. The temperature changes as a consequence of the heat consumed or released by the reaction, increasing or decreasing from the external surface to the center of the catalytic particle. In other words, the reaction is responsible of the concentration and temperature gradients originating inside the particle that act as driving forces for both the mass and heat transfer inside the catalyst particle. The faster the reaction, the steeper the gradients. In the case of high reaction rate, this effect is propagated toward the external part of the catalyst particle, generating other gradients of concentration and temperature between the catalyst surface and the bulk fluid. When the fluid flow regime is turbulent, as normally occurs in industrial reactors, the external gradients are confined to very thin layer, named the boundary layer, that surrounds the solid surface. The boundary layer is quiescent, and consequently mass and heat transfer occur through it, with a relatively slow process characterized by the molecular diffusion mechanism. The effects of reaction and diffusion rates are concentration and temperature profiles, respectively, such as the ones reported in Figure 3. External diffusion and chemical reaction are consecutive steps, and their contributions to the overall reaction rates can be considered separately. A similar approach cannot be adopted for the internal diffusion as it occurs simultaneously with the

chemical reaction. To describe the influence of internal diffusion on reaction rate requires solving the mass and heat balance equations related to any single particle for evaluating the concentration and temperature profiles inside the pellet.

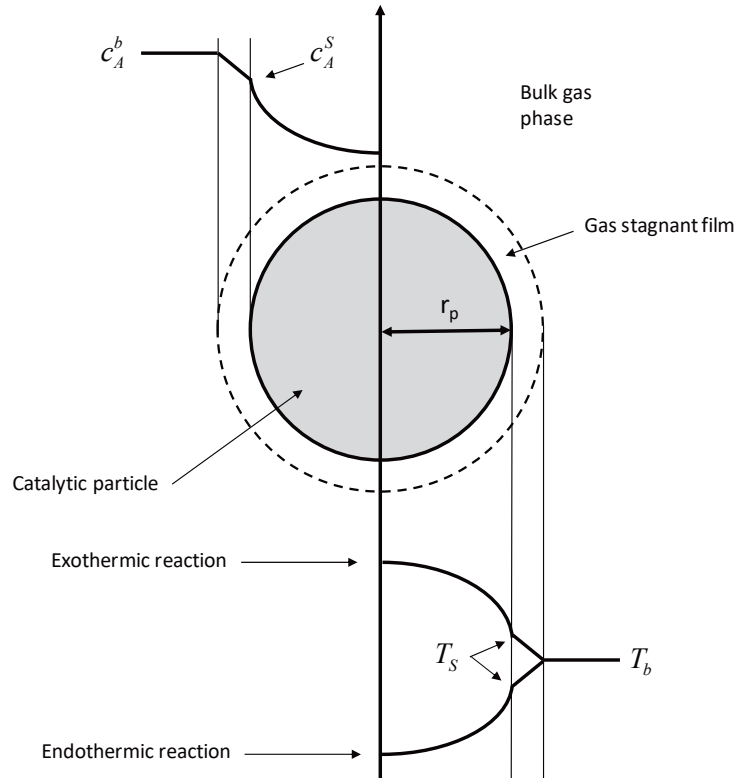


Figure 3. Profiles of concentration and temperature in a spherical catalytic particle.

2.1. Diffusion with Reaction in a Single Catalytic Particle: Mass and Heat Balance Equations

For a spherical particle, the mass balance can be written by considering the inlet, outlet, reaction, and accumulation terms related to a spherical shell of thickness dr and radius r (see Figure 4):

$$\left[\begin{array}{c} \text{diffusionrate} \\ \text{inward at } x = x + dx \end{array} \right] - \left[\begin{array}{c} \text{diffusionrate} \\ \text{outward at } x = x \end{array} \right] - \left[\begin{array}{c} \text{reactionrate} \\ \text{into the shell} \end{array} \right] = [\text{accumulation}] \quad (1)$$

Assuming steady state conditions, it results null the accumulation term and then

$$4\pi(x + dx)^2 N_{x+dx} - 4\pi x^2 N_x - 4\pi x^2 dx \cdot v_r = 0 \quad (2)$$

By introducing the Fick's law $N = D_{eff} \frac{dc}{dx}$ for the internal diffusive flux and a generic power law for the reaction rate $v = S_v k_S c^n$, related to a single reaction, and through rearranging we obtain

$$\frac{D_{eff}}{x^2} \frac{d}{dx} \left(x^2 \frac{dc}{dx} \right) - S_v k_S c^n = 0 \quad (3)$$

with the boundary conditions

$$\begin{aligned} \text{for } x = r_p &\rightarrow c = c_S \\ \text{for } x = 0 &\rightarrow \frac{dc}{dx} = 0 \end{aligned}$$

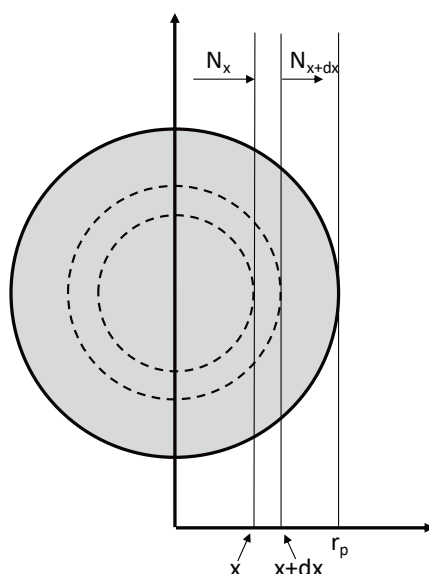


Figure 4. Reference scheme for mass and heat balance related to a catalyst particle.

For the heat balance, it is possible to follow a similar approach by introducing Fourier's law $q = -k_{eff} \frac{dT}{dx}$ instead of Fick's law, obtaining the following equation:

$$\frac{k_{eff}}{x^2} \frac{d}{dx} \left(x^2 \frac{dT}{dx} \right) - (-\Delta H) S_V k_S c^n = 0 \quad (4)$$

with boundary conditions

$$\begin{aligned} \text{for } x = r_p &\rightarrow T = T_S \\ \text{for } x = 0 &\rightarrow \frac{dT}{dx} = 0 \end{aligned}$$

Considering the common terms of Equations (3) and (4), it is possible to write

$$(T - T_S) = \frac{D_{eff}}{k_{eff}} (c - c_S) (-\Delta H) \quad (5)$$

From this equation, we can conclude that for any concentration profile, inside the particle, a corresponding profile of temperature can easily be determined by using Equation (5). Alternatively, a full energy balance on the particle must be solved. A maximum temperature gradient ΔT_{max} can be obtained when the concentration at the center of the particle can be assumed near to zero; in this case, $\Delta c \approx c_S$, and hence

$$\Delta T_{max} = \frac{D_{eff}}{k_{eff}} c_S (-\Delta H) \quad (6)$$

Referring ΔT_{max} to T_S , the temperature at the catalyst surface, the Prater's number is obtained, defined as $\beta = \Delta T_{max} / T_S$.

As the thermal conductivity of solid catalyst particles is normally much higher than those of the gaseous reaction mixture, in steady state conditions, internal temperature gradients are rarely important in practice.

The evaluation of the internal profiles of both concentration and temperature requires the solution of Equations (3) and (4). For this purpose, it is opportune to introduce some dimensionless terms such as

$$\varepsilon_{dr} = x/r_p \quad \gamma_{dr} = c/c_S \quad \psi_{dr} = v_r(c)/v_r(c_S) \quad \phi = r_p \sqrt{\frac{S_V k_S c_S^{n-1}}{D_{eff}}} \quad (7)$$

and Equation (3) for mass conservation becomes

$$\frac{1}{\varepsilon_{dr}^2} \frac{d}{d\varepsilon_{dr}} \left(\varepsilon_{dr}^2 \frac{d\gamma_{dr}}{d\varepsilon_{dr}} \right) = \phi^2 \psi_{dr} \quad (8)$$

where ϕ is called Thiele modulus [18]. It is interesting to observe that for $n = 1$, the Thiele modulus is independent of the concentration, and consequently Equation (3) or (8) can be solved analytically, while for different reaction orders or complex kinetics, an iterative numerical solution strategy must be adopted.

2.2. Definition and Evolution of the Effectiveness Factor

If the internal concentration profile of γ (dimensionless concentration) is known, it is possible to evaluate another dimensionless term η , named "effectiveness factor", defined as the ratio between the observed reaction rate, more or less affected by the internal diffusion, and the rate occurring in chemical regime, that is, not limited by internal diffusion. We can write

$$\eta = \frac{\text{effective reaction rate}}{\text{reaction rate from kinetic law}} \quad (9)$$

and can write accordingly

$$\eta = \frac{\int_0^{r_p} 4\pi x^2 v_r(c) dx}{\frac{4}{3}\pi r_p^3 v_r(c_S)} = 3 \int_0^1 \varepsilon_{dr}^2 \psi_{dr}(\gamma_{dr}) d\varepsilon_{dr} \quad (10)$$

Therefore, η is a dimensionless factor directly giving the effect of the internal diffusion on the reaction rate. For a reaction rate of a single reaction of n -th order, affected by internal diffusion, we can simply write

$$v_r = \eta k_S S_V c_S^n = \eta k_V c_S^n \quad (11)$$

The effectiveness factor η can also be determined by considering that, in steady state conditions, the overall reaction rate in a particle is equal to the rate of external mass transfer from bulk to the surface. Equation (10) can be rewritten as

$$\eta = \frac{-4\pi r_p^2 D_{eff} \left(\frac{dc}{dx} \right)_{r_p}}{\frac{4}{3}\pi r_p^3 v_r(c_S)} = \frac{-3D_{eff} \left(\frac{dc}{dx} \right)_{r_p}}{r_p k_S c_S} \quad (12)$$

As mentioned, for reaction order $n = 1$, the concentration profile can be analytically determined, and this can be done with Equation (13).

$$-\frac{dc}{dx} = \frac{c_S}{x} \left[\frac{\phi}{\tanh\phi} - \frac{1}{\phi} \right] \quad (13)$$

from which the following expression for the effectiveness factor can be derived by assuming a particle with spherical geometry:

$$\eta = \frac{3}{\phi} \left[\frac{1}{\tanh\phi} - \frac{1}{\phi} \right] \quad (14)$$

This equation changes with the shape of the catalyst particles, and the Thiele modulus ϕ changes too, as the quantity r_p in Equation (7) becomes a characteristic length given by the ratio between volume and external surface area of the catalytic pellet.

In some cases, the kinetic law is unknown, even if the data of the reaction rate are available. The evaluation of the Thiele modulus and of the effectiveness factor in these cases is not possible.

For this purpose, it is useful to define another dimensionless modulus, named the “Weisz modulus” [19], through the following relation:

$$M_W = \frac{r_p^2 v_r}{c_s D_{eff}} = \phi^2 \eta \quad (15)$$

The Weisz modulus allows for the evaluation of the effectiveness factor when experimental data of reaction rate are available.

Different plots of η , the “effectiveness factor”, as a function of ϕ or M_W can be drawn. Examples of these plots for spherical particles and first-order reactions are reported in Figure 5A,B. In these plots, we can recognize three different zones, the first, at low ϕ and M_W values, delimiting the chemical regime; the latter for high ϕ and M_W values, identifying the diffusional regime; and an intermediate zone corresponding to the gradual transition from chemical to diffusional regime. When the diffusional regime is operative, the effectiveness factor η can be calculated in an approximated way as $\eta = 1/\phi = 1/M_W$. This method of calculation can also be extended to the intermediate zone. This asymptotic approximation gives place to errors in η of less than 5%.

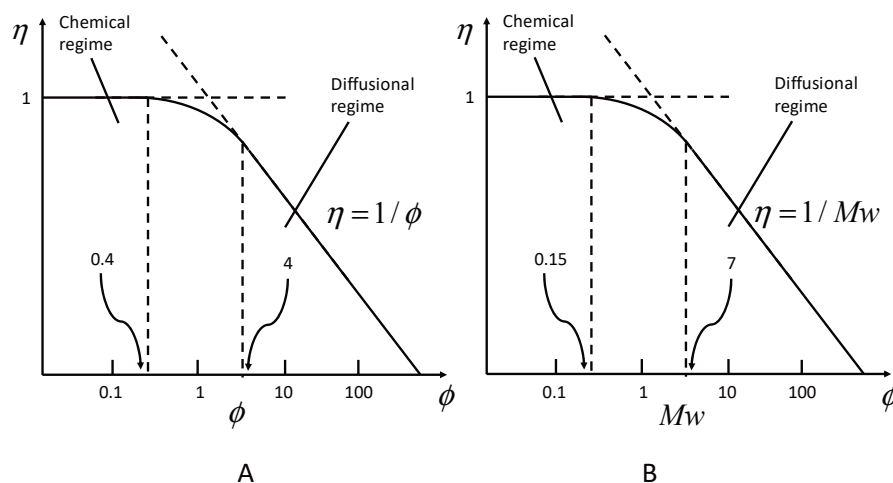


Figure 5. (A) Relationship between effectiveness factor and Thiele modulus; (B) relationship between effectiveness factor and Weisz modulus. Re-elaborated from Santacesaria [20] with the permission of Elsevier-Catalysis Today 1997.

The effect of the catalyst particle shape on $\eta = \eta(\phi)$ is quite small, while a larger influence has the reaction order, as can be appreciated in Figure 6.

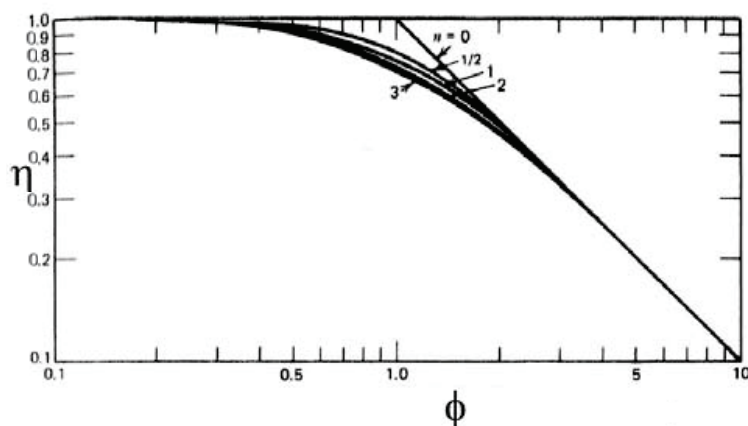


Figure 6. Effectiveness factor versus Thiele modulus for different order of reaction. Re-elaborated from Froment and Bischoff [21].

The effectiveness factor can also be evaluated experimentally by determining the reaction rate in the presence of catalyst pellets of different diameters and on finely powdered catalyst operating in chemical regime:

$$\eta = \frac{\text{rate observed for a given particle size}}{\text{rate observed in chemical regime on powdered catalyst}} \quad (16)$$

We have already seen that inside the catalyst particle, in correspondence to any concentration gradient, a temperature gradient is associated, determinable with Equations (5) or (6). The evolution of the effectiveness factor with the Thiele and Weisz moduli, reported in Figures 3 and 4, corresponds to isothermal conditions. When the reaction is exothermic or endothermic, the temperature inside the particle is, respectively, greater or lower than the external fluid. In these cases, the effectiveness factor can be affected by two other dimensionless factors:

(a) a heat generation parameter:

$$\beta = \frac{c_S(-\Delta H)D_{eff}}{k_{eff}T_S} = \frac{\Delta T_{max}}{T_S} = \text{Prater's number} \quad (17)$$

(b) the reaction rate exponential parameter:

$$\alpha_E = \frac{E}{RT_S} \quad (18)$$

For exothermic reactions $\beta > 0$ while for endothermic reactions $\beta < 0$; obviously, the isothermal condition can be identified when $\beta = 0$. For exothermic reactions, the effectiveness factor can be much greater than 1, while for endothermic reactions, this value is never reached. Examples of curves η - ϕ for different β values, at any given value of α_E , are reported in Figure 7.

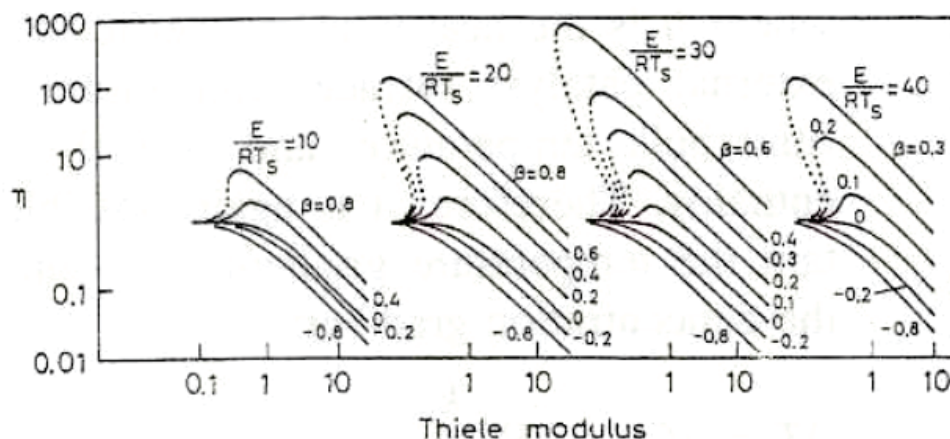


Figure 7. Effectiveness factors against the Thiele modulus in the case of both exothermic and endothermic reactions with an internal temperature gradient. Re-elaborated from Santacesaria [20] with the permission of Elsevier-Catalysis Today 1997.

2.3. Determination of the Effective Diffusional Coefficient D_{eff} and the Effective Thermal Conductivity k_{eff}

Effective diffusional coefficient depends on bulk diffusion coefficient D_{be} , the diffusion coefficient of the fluid in the macropores, and on the Knudsen diffusion coefficient D_{ke} , the diffusion coefficient in the micropores. We can write

$$\frac{1}{D_{eff}} = \frac{1}{D_{be}} + \frac{1}{D_{ke}} \quad (19)$$

where

$$D_{be} = \frac{D_{12}\theta}{\tau} \text{ and } D_{ke} = 1.94 \cdot 10^4 \frac{\theta^2}{\tau S_V \rho_p} \sqrt{\frac{T}{M}} \quad (20)$$

with θ being the porosity of the solid; τ being the tortuosity factor, an empirical parameter dependent on the characteristics of the pellets porosity texture with values falling in the range 0.3–10; S_V being the specific surface area; and ρ_p the catalyst particle density. D_{12} , which is normally considered equal to D_{21} , is the molecular diffusion coefficient for two components:

$$D_{12} = \frac{1.858 \cdot 10^{-3} \sqrt{\frac{T^3(M_1+M_2)}{M_1M_2}}}{P\sigma_{12}^2\Omega_D} \quad (21)$$

σ_{12} is the kinetic diameter for the molecules, while Ω_D , named “collision integral”, is a function of $k_B T/\varepsilon_{12}$; k_B is the Boltzmann constant, while ε is a molecular interaction parameter. Both σ_{12} and ε_{12} can be determined from the Lennard–Jones intermolecular potential equation (Equation (22)):

$$\phi_{LJ}(r) = 4\varepsilon_{ij} \left[\left(\frac{\sigma_{ij}}{\rho_d} \right)^{12} - \left(\frac{\sigma_{ij}}{\rho_d} \right)^6 \right] \quad (22)$$

$$\sigma_{ij} = (\sigma_i + \sigma_j)/2 \quad (23)$$

$$\varepsilon_{ij} = \sqrt{\varepsilon_i \varepsilon_j} \quad (24)$$

where ρ_d is the intermolecular distance, and σ_i and ε_i can be evaluated from critical temperature and volume of the molecules, that is, $\varepsilon_i/k_B = 0.75 T_c$ and $\sigma_i = 0.833 V_{ci}^{1/3}$.

When we have a mixture of more than two components, the calculation can be made by averaging the properties. Molecular diffusion coefficient D_{im} is, for example,

$$D_{im} = \frac{(1 - y_i)}{\sum_j y_j / D_{ij}} \quad (25)$$

Because of the uncertainty of the tortuosity factor τ , many experimental data have been determined for D_{eff} , generally in steady-state conditions by using an apparatus such as the one schematized in Figure 8. A single pellet is put in a device in which different gases are fed above and below the catalyst particle at the same pressure. Each gas slowly flows through the pellet and is determined at the outlet. The rate of gas diffusion through the pellet is related to D_{eff} because

$$N_A = -D_{eff} \frac{dc_A}{dr} = -\frac{P}{RT} D_{eff} \frac{dy_A}{dr} = -D_{eff} \frac{P}{RT} \frac{(y_A - y_A^0)}{\Delta r} \quad (26)$$

A dynamic method can also be used by employing a pulse of a diffusing component. The response pulse is related to the value of D_{eff} .

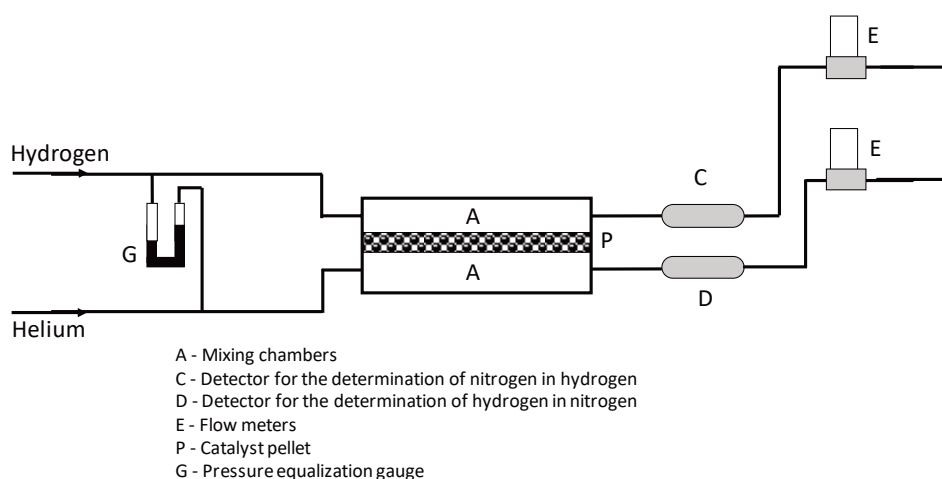


Figure 8. Scheme of the experimental device for the determination of effective diffusivity of a catalyst pellet.

The effective thermal conductivities of catalyst pellet could be surprisingly low for the numerous void spaces hindering the transport of energy. A simple but approximate approach for calculating k_{eff} has been given by Woodside and Messner [22]:

$$k_{eff} = k_{Sol} \left(\frac{k_f}{k_{Sol}} \right)^{1-\varepsilon_{Bs}} \quad (27)$$

where k_f and k_{Sol} are the thermal conductivities of the bulk fluid and of the solid phase, respectively, while ε_{Bs} is the void fraction of the solid.

Notwithstanding the difficulties in predicting k_{eff} , a reliable value can be estimated because it falls in a rather restricted range 0.1–0.4 Btu/(h ft °F) [1].

2.4. External Gradients

As before mentioned, external diffusion and reaction inside the catalytic particles can be considered as consecutive steps. Therefore, the corresponding rates can be expressed with different relationships. The external mass transfer rate expression derives from the first Fick's law and results in

$$v_{mt} = k_m a_m (c_b - c_s) \quad (28)$$

In steady state conditions, this expression must be equated to the one describing the rate of internal diffusion with reaction, that is,

$$v_r = \eta k c_s^n = k_m a_m (c_b - c_s) \quad (29)$$

For $n = 1$, after the elimination of c_s , it is possible to write

$$v_r = \frac{c_b}{\frac{1}{k_m a_m} + \frac{1}{\eta k}} \quad (30)$$

where the contribution of the resistance to the reaction rate, by external and internal mass transfer rate, clearly appears at the denominator of Equation (30). External diffusion strongly affects the kinetics, as the transport phenomena weakly depend on the temperature, and for a great contribution of the external diffusion on the reaction rate, the activation energy observed is about one-half of the true value observable in a chemical regime.

As mass transfer is originated by the reaction, it is always accompanied by heat transfer due to the heat absorbed or released by the reactions inside the particle. Therefore, for the rate of heat transfer, we can write

$$Q = k_m a_m (c_b - c_s)(-\Delta H) = h a_m (T_b - T_s) \quad (31)$$

Again, we can derive the temperature gradient from the corresponding concentration gradient

$$\Delta T = \Delta c(-\Delta H) \frac{k_m}{h} \quad (32)$$

that is, temperature and concentration gradients are strictly related, but the behavior of exothermic and endothermic reactions is quite different. It is useful to observe that both concentration and temperature gradients can fall between two limits:

$$\Delta c_{\min} \cong 0 \text{ when } c_b \cong c_s \text{ and } \Delta c_{\max} \cong c_b \text{ when } c_s \cong 0 \quad (33)$$

$$\Delta T_{\min} \cong 0 \text{ when } T_b \cong T_s \text{ and } \Delta T_{\max} \cong c_b(-\Delta H)k_m/h$$

It is possible to estimate mass and heat transfer coefficients from fluid dynamic correlations. As mentioned before, concentration and temperature gradients external to the particles are located in a thin layer (the boundary layer) surrounding the particle. The molar flow rate for each component will be

$$N_i = k_c (c_b - c_s) = k_g (p_b - p_s) \quad (34)$$

k_c and k_g are related to the molecular diffusion coefficient D_{12} , that is,

$$k_c = \frac{D_{12}}{\delta} \quad k_g = \frac{D_{12}}{\delta RT} \quad (35)$$

where δ is the thickness of the boundary layer. Similarly, the heat flow through the boundary layer will be

$$q = h(T_b - T_s) \text{ (heat/time} \times \text{surface area)} \quad (36)$$

Again, h is related to the thermal conductivity of the fluid, and k_f is a molecular property given by

$$k_f = 1.989 \times 10^{-4} \frac{\sqrt{T/M}}{\sigma^2 \Omega} \left(\frac{\text{cal}}{\text{cm s K}} \right) \quad (37)$$

and to the thickness of the boundary layer. This thickness depends on the fluid dynamic conditions adopted; consequently, the average transport coefficients (mass and energy) can be determined from the correlation between dimensionless groups such as Sherwood, Schmidt, and Reynolds numbers. Much experimental data have been correlated, and the following empirical relationship has been obtained for tubular reactors:

$$J_D = S_h \cdot S_c^{2/3} = \frac{\alpha_D}{\varepsilon_D} R_e^{-\beta_D} \quad (38)$$

$$S_h = \frac{k_c \rho}{G} \quad S_c = \frac{\mu}{D \rho} \quad R_e = \frac{G d_p}{\mu} \quad (39)$$

For $R_e > 10$, it results in $\alpha_D = 0.458$ and $\beta_D = 0.407$. For heat transfer coefficient, a quite similar approach is possible, giving place to

$$J_H = \frac{h}{C_p G} P_r^{2/3} = \frac{\alpha_H}{\varepsilon_H} R_e^{-\beta_H} \quad (40)$$

where $P_r = \mu C_p / k_t =$ number of Prandtl. A correlation exists between J_H and J_D , that is, $J_H \cong 1.08 J_D$. From these relations, it is possible to evaluate the heat and mass transfer coefficients. By putting in Equation (32) k_c and h derived from Equations (38) and (40), we obtain

$$\Delta T = \Delta c(-\Delta H) \frac{1}{\rho C_p} (L_e)^{2/3} \left(\frac{J_D}{J_H} \right) \quad (41)$$

$L_e =$ Lewis number $= \frac{C_p \mu / k}{\mu / \rho D} \cong 1$, being also $J_D / J_H \cong 1$, resulting in

$$\Delta T \cong \Delta c(-\Delta H) \frac{1}{\rho C_p} \quad (42)$$

Therefore, ΔT_{\max} can also be determined as

$$\Delta T_{\max} \cong c_b(-\Delta H) \frac{1}{\rho C_p} \quad (43)$$

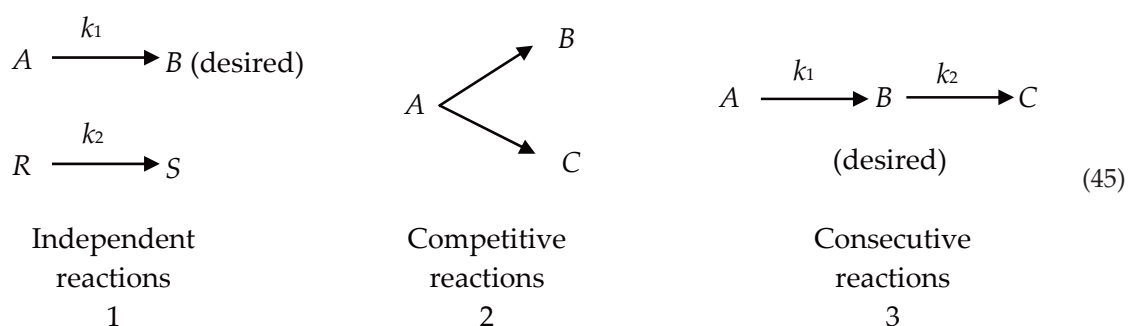
Equations (42) and (43) show that it is possible to have a significant temperature gradient even if the concentration gradient is very low as a consequence of the high value of ΔH . In conclusion, in steady state conditions, only two coupled equations are needed in order to quantitatively evaluate the effect of the external mass and heat transfer. These equations are

$$\begin{cases} k_m a_m (c_b - c_s) = \eta k c_s^n \\ h a_m (T_b - T_s) = \eta k c_s^n (-\Delta H) \end{cases} \quad (44)$$

In unsteady state conditions, four differential equations are needed, with these being different chemical and physical transport rates. The contribution of the external diffusion to reaction rate can then be estimated only on the basis of the fluid dynamic conditions in the system.

2.5. Diffusion and Selectivity

The selectivity of solid catalysts can be affected by diffusion in different ways according to the type of complex reactions involved. Consider as examples some very simple systems such as [3]



All the reactions are considered first-order reactions for simplicity.

First Case

By considering for each reaction both external and internal diffusion contribution, in the first case, we express the overall reaction rate as reported in Equation (30). The selectivity can be expressed as the ratio between r_1 and r_2 , that is,

$$S = \frac{r_1}{r_2} = \frac{[1/(k_m)_R a_m + 1/\eta_2 k_2] c_A}{[1/(k_m)_A a_m + 1/\eta_1 k_1] c_R} \quad (46)$$

In the case wherein the diffusion limitation is negligible, the selectivity becomes

$$S = \frac{k_1 c_A}{k_2 c_R} \quad (47)$$

By comparing Equations (46) and (47), we find a decrease of the selectivity to the desired product B for the effect of both external and internal mass transfer limitation. By considering predominantly the effect of internal diffusion and introducing the approximation (see Figure 5A) $\eta \cong 1/\phi$, we have

$$r_1 = \frac{1}{\phi_1} k_1 c_A = \frac{3}{r} \sqrt{\frac{k_1 (D_A)_{eff} c_A}{\rho_p}} \quad (48)$$

$$r_2 = \frac{1}{\phi_2} k_2 c_R = \frac{3}{r} \sqrt{\frac{k_2 (D_R)_{eff} c_R}{\rho_p}} \quad (49)$$

The selectivity becomes

$$S = \frac{r_1}{r_2} = \sqrt{\frac{k_1 c_A}{k_2 c_R}} \quad (50)$$

considering $(D_A)_{eff} \cong (D_R)_{eff}$. By comparing Equations (47) and (50), we find that internal diffusion reduces the selectivity to the square root of Equation (47).

Second Case

For competitive reactions, diffusion limitations have an effect on the selectivity only when the occurring reactions have different reaction orders. Otherwise, for reactions having the same reaction order, no effect on the selectivity can be observed.

Third Case

Considering the occurrence of consecutive reactions in a chemical regime, that is, without diffusion limitation, selectivity can be written as

$$S = \frac{B_{\text{production}}}{A_{\text{consumption}}} = \frac{k_1 c_A - k_2 c_B}{k_1 c_A} = 1 - \frac{k_2 c_B}{k_1 c_A} \quad (51)$$

When internal diffusion resistance is operative ($\eta < 0.2$), we have to calculate concentration profiles for both A and B. Assuming the effective diffusivities to be equal, selectivity results [3]

$$S = \frac{(k_1/k_2)^{1/2}}{1 + (k_1/k_2)^{1/2}} - (k_2/k_1)^{1/2} \frac{c_B}{c_A} \quad (52)$$

As can be seen, selectivity is also consistently lowered in this case for the influence of the internal diffusion.

2.6. Effectiveness Factor for a Complex Reaction Network

According to the general definition of effectiveness factor introduced in Section 2.2 and expressed by Equation (10), we can extend our treatment to a more general situation represented by N_r reactions with rate equations that are generic functions of temperature and composition, regardless of the form of these kinetic expressions. For such a system, an expression of the effectiveness factor related to reaction j can be written as

$$\eta_j = \frac{\int_0^{r_p} 4\pi x^2 v_{r,j}(c_i, T) dx}{\frac{4}{3}\pi r_p^3 v_{r,j}(c_i^S, T^S)} \quad (53)$$

Evaluating the integral in Equation (53) requires solving the mass and heat balance inside the particle in order to evaluate the internal profiles of both temperatures and concentration. The balance equations, for steady state conditions, can be written with the same criteria adopted for Equations (3) and (4), but considering multiple reactions and multicomponent systems characterized by N_c chemical species:

$$D_{eff_i} \left[\frac{\partial^2 c_i^P}{\partial x^2} + \frac{2}{x} \frac{\partial c_i^P}{\partial x} \right] = \rho_P \sum_{j=1}^{N_r} \gamma_{i,j} v_{r,j} \quad i = 1, 2, \dots, N_c \quad (54)$$

$$k_{eff} \left[\frac{\partial^2 T_P}{\partial x^2} + \frac{2}{x} \frac{\partial T_P}{\partial x} \right] = \rho_P \sum_{j=1}^{N_r} (-\Delta H_j) v_{r,j} \quad (55)$$

The simultaneous solution of this system of coupled partial differential equations (PDEs) must be accomplished using the following boundary conditions:

$$\begin{aligned} \frac{\partial c_i^P}{\partial x} = 0 \quad \frac{\partial T_P}{\partial x} = 0 \quad \text{at } x = 0 \\ c_i^P = c_i^S \quad T_P = T_S \quad \text{at } x = r_p \end{aligned} \quad (56)$$

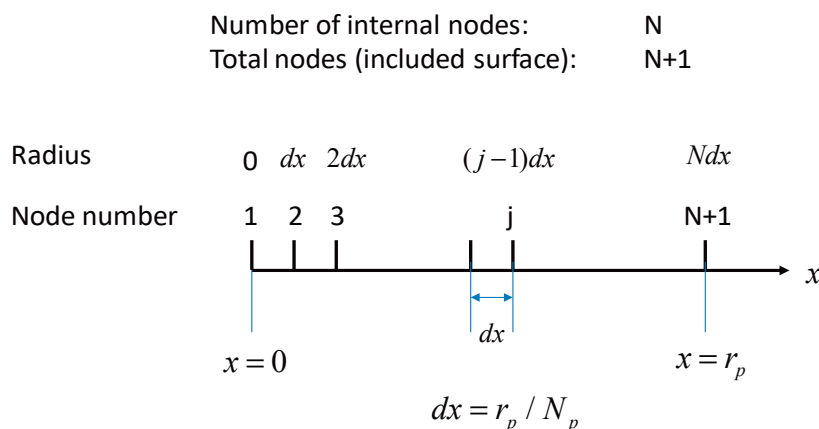
The described model is related to the simultaneous occurrence of both diffusion and chemical reactions inside a catalytic particle and consists of a system of coupled partial differential equations in one dimension with boundary values. The solution can be obtained numerically with different algorithms reported in the literature (finite differences, orthogonal collocation, method of lines, etc.).

The method of lines (MOL) [19] in particular consists in converting the system of partial differential equations—Equations (54) and (55)—in an ordinary differential equations system. The first step of this method consists in considering the transient version of Equations (54) and (55) represented by the following equations:

$$\varepsilon_P \frac{\partial c_i^P}{\partial t} = D_{eff_i} \left[\frac{\partial^2 c_i^P}{\partial x^2} + \frac{2}{x} \frac{\partial c_i^P}{\partial x} \right] - \rho_P \sum_{j=1}^{N_r} \gamma_{i,j} v_{r,j} \quad (57)$$

$$\varepsilon_P \rho_P C_P \frac{\partial T_P}{\partial t} = K_{eff} \left[\frac{\partial^2 T_P}{\partial x^2} + \frac{2}{x} \frac{\partial T_P}{\partial x} \right] - \rho_P \sum_{j=1}^{N_r} (-\Delta H_j) v_{r,j} \quad (58)$$

The successive step consists in a discretization of the particle radial coordinate in a series of equally spaced radial nodes from $r = 0$ to $r = R_p$. Then, the spatial derivatives in Equations (57) and (58) are replaced by their finite difference approximation. The discretization scheme is reported in Scheme 1.



Scheme 1. Scheme of discretization.

At each node along the radius, ordinary differential equation (ODE) equations can be written in replacement of PDEs (57) and (58). The resulting set of ordinary differential equations (ODEs) can be integrated with respect to time until stationary conditions are reached. The obtained values represent the steady-state solution of Equations (54) and (55). The method of lines is largely preferred through considering, first of all, the large availability of efficient and robust ODE solvers and also for the low numerical instability related to the transformed problem. A further advantage of the MOL method can be appreciated when the system of model ODEs is “stiff”, as in this case it can be treated with specifically developed ODE solvers such as, for example, GEAR and LSODE [23], or commercial solver included in MATLAB [24].

An alternative strategy to solve the particle balances for concentration and temperature internal profiles is the finite difference scheme [1] applied to Equations (54) and (55). The first step of this strategy consists, also in this case, of a nodal discretization along particle radius and then by replacing radial derivatives with a finite difference approximation formula. This method transforms the PDE system in a system of coupled nonlinear algebraic equations of the following form related to the mass balance of a generic component:

$$D_{eff} \left[\frac{2}{(i-1)\Delta x} \frac{c_A^{i+1} - c_A^{i-1}}{2\Delta x} + \frac{c_A^{i+1} + c_A^{i-1} - 2c_A^i}{(\Delta x)^2} \right] - (R_{ni}) = 0 \quad (59)$$

In this equation, the term R_{ni} represents the reaction rate evaluated at the location of nodal point i . In this way, the original second order PDE has been transformed into a system of nonlinear algebraic system with c_A^i as unknowns. It is worth noting that this approach is of general validity, as R_{ni} can represent any kinetic expression and can straightforwardly be extended to multiple chemical reactions by substituting the generation term with a sum of all reaction rates involving a specific component.

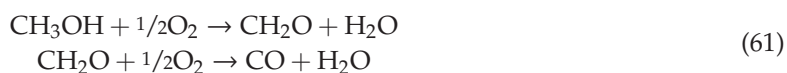
In the case of nonisothermal particles, heat balance must be taken into account, and the resulting finite difference nodal equation system is represented, in analogy to mass balance, by the following equation:

$$k_t \left[\frac{2}{(i-1)\Delta x} \frac{T^{i+1} - T^{i-1}}{2\Delta x} + \frac{T^{i+1} + T^{i-1} - 2T^i}{(\Delta x)^2} \right] + (-\Delta H)(R_{ni}) = 0 \quad (60)$$

From a numerical point of view, the two numerical approaches (method of lines and method of finite differences) are quite equivocal and are both able to treat virtually any type of kinetic in a solid catalytic particle.

2.7. An Example of Calculation of Effectiveness Factor Complex Reactions

We considered the conversion of methanol to formaldehyde catalyzed by iron–molybdenum oxide catalyst. Two consecutive reactions occur in the process [25]:



The conditions for the reactions, together with catalyst characteristics and other physical parameters [25] used in the calculations, are reported in Table 1.

Table 1. Physico-chemical data for the calculation.

$K_e = 2.72 \times 10^{-4}$	KJ/(s m K)	effective thermal conductivity
$D_e = 1.07 \times 10^{-5} \exp(-672/T)$	m ² /s	effective diffusivity
$\rho_p = 1180$	Kg/m ³	particle density
$C_p = 2.5$	KJ/(mole K)	particle specific heat
$P = 1.68$	atm	total pressure
$T_S = 539$	K	surface temperature
$d_p = 3.5 \times 10^{-3}$	m	particle diameter
Bulk gas composition	mol%	
CH ₃ OH	9.0	
O ₂	10.0	
CH ₂ O	0.5	
H ₂ O	2.0	
CO	1.0	
N ₂	77.5	

These reactions follow a redox mechanism, and the most reliable kinetics is the one suggested by Mars and Krevelen [26]:

$$v = \frac{k_1 k_2 P_m P_{O_2}^n}{k_1 P_m + k_2 P_{O_2}^n} \quad (62)$$

Different values of n have been suggested in the literature, generally considering $n = 1/2$ [27] or $n = 1$ [28]. The inhibition effect of water, formed in both the reactions, can also be introduced in the form of a Langmuir–Hinshelwood term [29], such as

$$v_r = \frac{k_1 k_2 P_m P_{O_2}^n}{k_1 P_m + k_2 P_{O_2}^n} \left(\frac{1}{1 + b_w P_w} \right) \quad (63)$$

Riggs [30] has proposed, on the contrary, pseudo Langmuir–Hinshelwood kinetic laws of the following type:

$$\begin{aligned} v_{r1} &= \frac{k_1 P_m}{1 + a_1 P_m + a_2 P_w} \\ v_{r2} &= \frac{k_2 P_f}{1 + b_1 P_m + b_2 P_w} \end{aligned} \quad (64)$$

where P_m , P_w , and P_f are, respectively, the partial pressures of methanol, water, and formaldehyde; k_1 , k_2 , a_1 , a_2 , b_1 , and b_2 are parameters whose values and dependence on temperature is reported Table 2.

Table 2. Kinetic parameters for the model.

$k_1 = 5.37 \times 10^2 \exp(-7055/T)$
$k_2 = 6.42 \times 10^{-5} \exp(-1293/T)$
$a_1 = 5.68 \times 10^2 \exp(-1126/T)$
$a_2 = 8.37 \times 10^{-5} \exp(7124/T)$
$b_1 = 6.45 \times 10^{-9} \exp(12,195/T)$
$b_2 = 2.84 \times 10^{-3} \exp(4803/T)$
$\Delta H_1 = 37,480$ cal/mole
$\Delta H_2 = 56,520$ cal/mole

The application of the model represented by Equations (57) and (58) to this example was performed with the following assumptions:

- Catalytic particle is spherical with uniform reactivity, density, and thermal conductivity.
- The heat of reactions does not change with the temperature.
- The external diffusion resistance is negligible, and therefore the surface concentration is equal to the one of the bulk.

- The effective diffusivity has been assumed equal for all the involved chemical species.

The numerical solution of this example was achieved by discretizing the particle radius with 20 internal nodes ($N_n = 20$). As the reactive mixture is constituted by six different components, we had globally $(N_c + 1) N_n = 140$ ODEs to be integrated to the stationary state. A further check demonstrated that by increasing the number of internal discretization points brings a negligible variation in the effectiveness factors. As result of this calculation, we obtained the concentration profile of each component inside the catalytic particle, as shown in Figure 9A. By examining this plot, it is clear that the concentration profiles of the reagents methanol and oxygen decreased from the external surface to the center of the pellet, while the opposite occurred for products.

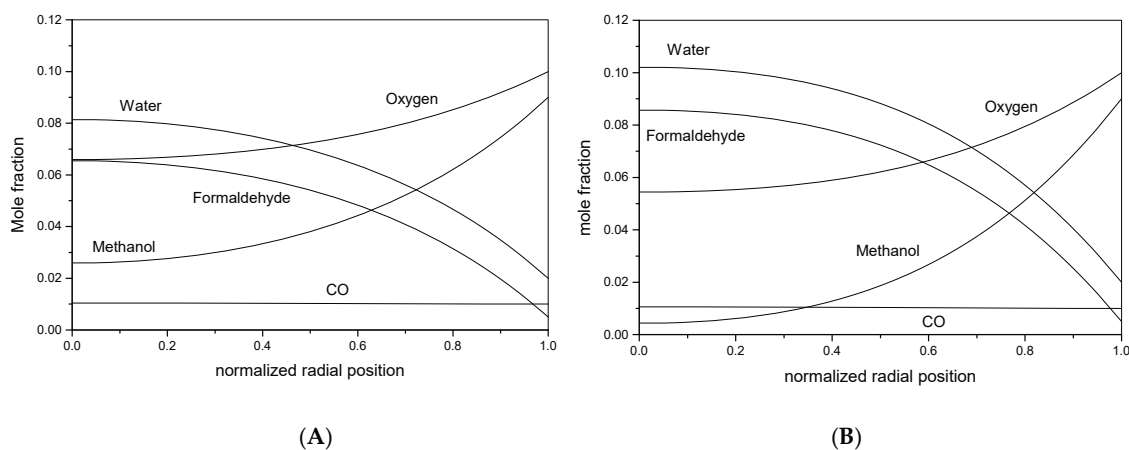


Figure 9. Mole fraction profiles inside a catalytic particle. (A) Kinetics of Riggs [30]; (B) kinetics of Dente et al. [28].

By employing Equation (53), it is possible from these profiles to evaluate the effectiveness factors for each reaction obtaining the following results: $\eta_1 = 0.778$, $\eta_2 = 8.672$.

The high effectiveness factor obtained for the second reaction was due to the low concentration of formaldehyde in the bulk gas, in comparison with the formaldehyde concentration accumulated inside the particle, which was significantly higher.

A further result of this example is related to the temperature profile reported in Figure 10. With the reactions being very exothermic, the temperature increased, as expected, from the external surface toward the center, and the overall ΔT was about 3.5 °C. In Figure 10, reported for comparison, are also the same calculations made by adopting the Mars–Krevelen model with the parameters taken from Dente et. al. [28] and Riggs [30].

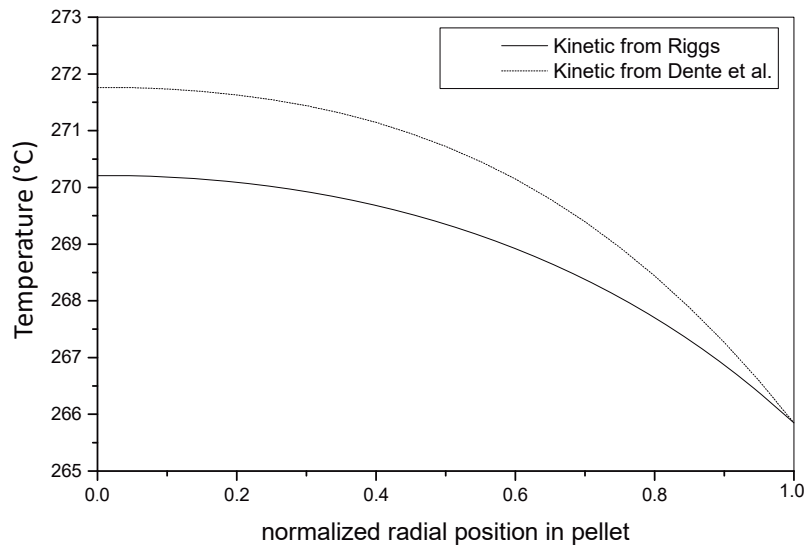


Figure 10. Internal temperature profile for a catalytic particle obtained with different kinetic models.

3. Mass and Heat Transfer in Packed Bed Reactors: Long Range Gradients

3.1. Conservation Equations for Fixed-Bed Reactors: Mass and Energy Balances

The generic mass conservation equation for a system of N_c components involved in a reaction network of N_r chemical reactions, related to the i 'th component, can be written as in the following equation [16]:

$$\frac{\partial c_i}{\partial t} = -\nabla(c_i u + J_i) + \sum_{j=1}^{N_r} \gamma_{i,j} v_{r,j} \quad (65)$$

where u is the fluid velocity component along various dimensions, c_i is the concentration of a generic component, $\gamma_{i,j}$ is the stoichiometric coefficient of chemical species i in reaction j , and $v_{r,j}$ is the j -th rate of reaction based on fluid volume. The quantity J_i represents the molar flux of the i -th component originated by the concentration gradients, temperature gradients, and pressure gradients. The molar flux is in relation with the effective diffusion coefficient D_i by Fick's law, represented by the following equation:

$$J_i = -D_i \nabla c_i \quad (66)$$

Equation (65) is valid in both steady and unsteady state conditions and also contains the accumulation term resulting from the unbalanced difference between input, output, and chemical reactions terms. The overall balance is referred to a suitable control volume.

In the case of a fixed-bed reactor, the control volume assumes the shape of an annulus in a cylindrical coordinate system. By applying the conservation concepts expressed by Equation (65), assuming that only the velocity in the direction of flow ($u_z = v$) is dominant with respect to other directions and as represented in Figure 11, the general Equations (65) and (66) can be combined to give

$$\varepsilon_B \frac{\partial c_i}{\partial t} = -\frac{\partial}{\partial z}(u c_i) + \frac{\partial}{\partial z} \left[D_{ai} \frac{\partial c_i}{\partial z} \right] + \frac{1}{r} \frac{\partial}{\partial r} \left[D_{ri} \frac{\partial c_i}{\partial r} \right] + (1 - \varepsilon_B) \sum_{j=1}^{N_{re}} \gamma_{i,j} v_{r,j}^G \quad (67)$$

where D_{ai} and D_{ri} are the effective dispersion coefficients (diffusivities), in axial and radial directions, for the i -th component. These quantities are referred to the total cross-sectional area perpendicular to the diffusion direction; u is the linear velocity in the catalyst bed and ε_B is the void fraction of the catalyst bed. The overall reaction rate $v_{r,j}^G$ is then multiplied by the factor $(1 - \varepsilon_B)$ as the reaction rate is based on the catalyst particle volume.

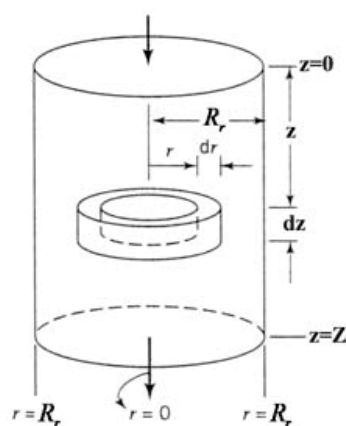


Figure 11. Scheme of the coordinate system and control volume for the fixed-bed conservation equations.

A simplification can be introduced in Equation (3) by assuming a constant linear velocity in z -direction (reactor axis) and also constant diffusivities along both z and r . Under these assumptions, Equation (67) can be reformulated as follows:

$$\varepsilon_B \frac{\partial c_i}{\partial t} + u \frac{\partial c_i}{\partial z} - D_{a_i} \frac{\partial^2 c_i}{\partial z^2} - D_{r_i} \left[\frac{\partial^2 c_i}{\partial r^2} + \frac{1}{r} \frac{\partial c_i}{\partial r} \right] = +(1 - \varepsilon_B) \sum_{j=1}^{N_{re}} \gamma_{i,j} v_{r,j}^G \quad (68)$$

A similar approach can be adopted for the energy balance by replacing in Equation (68) the following quantities: the term $\rho C_p T$ instead of concentration of chemical species C_i , the effective thermal conductivities K instead of diffusivities D , and reaction enthalpy term $(-\Delta H_j) R_{Gj}$ instead of reaction rate R_{Gj} :

$$\varepsilon_B \frac{\partial T}{\partial t} + u \frac{\partial T}{\partial z} - K_a \frac{\partial^2 T}{\partial z^2} - K_r \left[\frac{\partial^2 T}{\partial r^2} + \frac{1}{r} \frac{\partial T}{\partial r} \right] = \frac{(1 - \varepsilon_B)}{\rho C_p} \sum_{j=1}^{N_{re}} (-\Delta H_j) v_{r,j}^G \quad (69)$$

where ρ and C_p are the density and specific heat (average values) referred to the gas mixture, respectively.

Considering a fixed-bed reactor, bulk phase concentration and temperature can be regarded, in general, as functions of both r and z coordinates:

$$\begin{aligned} c_i^B &= f(z, r) \\ T_b &= g(z, r) \end{aligned} \quad (70)$$

In the assumptions above, the general mass and energy balance equations for the fixed-bed reactor in which N_r chemical reactions and N_c components are involved are

$$\varepsilon_B \frac{\partial c_i^B}{\partial t} + u \frac{\partial c_i^B}{\partial z} - D_{a_i} \frac{\partial^2 c_i^B}{\partial z^2} - D_{r_i} \left[\frac{\partial^2 c_i^B}{\partial r^2} + \frac{1}{r} \frac{\partial c_i^B}{\partial r} \right] = (1 - \varepsilon_B) \sum_{j=1}^{N_R} \gamma_{i,j} v_{r,j}^G \quad (71)$$

$$i = 1, 2, \dots, N_c$$

$$\varepsilon_B \frac{\partial T_B}{\partial t} + u \frac{\partial T_B}{\partial z} - K_a \frac{\partial^2 T_B}{\partial z^2} - K_r \left[\frac{\partial^2 T_B}{\partial r^2} + \frac{1}{r} \frac{\partial T_B}{\partial r} \right] = \frac{(1 - \varepsilon_B)}{\rho C_p} \sum_{j=1}^{N_R} (-\Delta H_j) v_{r,j}^G \quad (72)$$

Equations (71) and (72) represent a system of PDEs (partial differential equations) for which a solution can be obtained by imposing some suitable boundary conditions related to both variables

(temperature and concentration) and their derivatives with respect to z and r . Usual boundary conditions can be written as follows:

$$\frac{\partial T_B}{\partial r} = \frac{\partial c_i^B}{\partial r} = 0 \text{ at the centerline of the reactor } (r = 0) \text{ for all } z \quad (73)$$

$$\frac{\partial c_i^B}{\partial r} = 0; h_w(T_B - T_C) = -\rho C_p K_r \frac{\partial T_B}{\partial r} \text{ at the wall of reactor } (r = R) \text{ for all } z \quad (74)$$

The first boundary condition (Equation (73)) can be written by considering the symmetry around the axis of the tubular reactor, while the second condition (Equation (74)) expresses the constraint that no mass transfer occurs across the reactor wall. The second part of Equation (74) expresses the zero-accumulation of energy and is related to the heat transfer boundary condition according to which the heat transferred to the cooling fluid, at a temperature T_C , is equal to the heat conducted at the wall.

The axial boundary conditions, written at the reactor inlet, consists of the following equations:

$$\begin{aligned} (uc_i^B)_{in} &= (uc_i^B - D_{a_i} \frac{\partial c_i^B}{\partial z})_{z=0} \\ (uT_B)_{in} &= (uT_B - K_a \frac{\partial T_B}{\partial z})_{z=0} \end{aligned} \quad \text{at } z = 0 \quad (75)$$

While at the outlet

$$\frac{\partial c_i^B}{\partial z} = \frac{\partial T_B}{\partial z} = 0 \text{ at } z = Z \quad (76)$$

The boundary conditions (Equations (75) and (76)) are based on the flux continuity (both mass and heat) across a boundary, represented by the catalytic bed inlet and outlet.

3.2. External Transport Resistance and Particle Gradients

The link between macroscopical ("long-range"), concentration, and temperature gradients, described by the conservation equations for the entire reactor, and the microscopic situation locally developed around catalytic particles and inside it, is represented by a relation between the overall rate of reaction and the intrinsic kinetic. At a macroscopical level, the observed reaction rate, R_{Gi} , represents the rate of mass transfer across an interface between fluid and solid phase, which is ultimately related to the flux at the catalyst particle surface:

$$\sum_{j=1}^{N_r} \gamma_{i,j} v_{r,j}^G = \frac{k_g}{L} (c_i^B - c_i^S) = \frac{D_{ei}}{L} \frac{\partial c_i^P}{\partial x} \Big|_{x=L} = \sum_{j=1}^{N_{re}} \gamma_{i,j} \eta_j v_{r,j} \quad j = 1, 2, \dots, N_r \quad (77)$$

with the following mean of the symbols:

- k_g —gas-solid mass transfer coefficient (film);
- L —characteristic length of particle (radius for spherical pellets);
- c_i^S —surface concentration of component i ;
- c_i^P —particle internal concentration of component i ;
- D_{ei} —effective diffusivity of component i into the particle;
- x —particle radial coordinate;
- η_j —effectiveness factor for reaction j ;
- $v_{r,j}$ —intrinsic rate of reaction j .

In a similar way, we can write a relation for the thermal flux:

$$\sum_{j=1}^{N_r} (-\Delta H_j) v_{r,j}^G = \frac{h}{L} (T_S - T_b) = -\frac{K_{eff}}{L} \frac{\partial T_P}{\partial x} \Big|_{x=L} \quad (78)$$

where

- h —film heat transfer coefficient;
- T_S —temperature at the surface of the pellet;
- T_P —temperature inside the pellet;
- K_{eff} —effective thermal conductivity of the catalytic particle.

By considering Equation (77), the relationship between the rate of reaction at a macroscopic level and the intrinsic reaction rate is expressed for each chemical reaction by the effectiveness factor η or, in an equivalent way, by means of the concentration gradients measured at the particle surface. This consideration evidences the necessity to solve mass and energy balance equations related to catalytic particles to calculate local (microscopic) concentration and temperature profile. This calculation must be replicated, in principle, in each position along the reactor.

Conservation equations for the particles can be written as in the following equations (Equations (79) and (80)):

$$\varepsilon_P \frac{\partial c_i^P}{\partial t} = D_{e_i} \left[\frac{\partial^2 c_i^P}{\partial x^2} + \frac{2}{x} \frac{\partial c_i^P}{\partial x} \right] - \rho_P \sum_{j=1}^{N_r} \gamma_{i,j} r_{c_j} \quad i = 1, 2, \dots, N_c \quad (79)$$

$$\varepsilon_P \rho_P C_P^P \frac{\partial T_P}{\partial t} = K_e \left[\frac{\partial^2 T_P}{\partial x^2} + \frac{2}{x} \frac{\partial T_P}{\partial x} \right] - \rho_P \sum_{j=1}^{N_r} (-\Delta H_j) r_{c_j} \quad (80)$$

with the following meanings of the symbols:

- ε_P —catalytic particle void fraction;
- ρ_P —catalytic particle density;
- C_P^P —catalytic particle specific heat.

The simultaneous solution of PDE system represented by Equations (79) and (80) can be obtained by imposing some boundary conditions that are valid at the center and at the external surface of the catalyst particle respectively. These boundary conditions can be derived from symmetry consideration and from continuity related to both concentration and temperature:

$$\begin{aligned} \frac{\partial c_i^P}{\partial x} &= 0 \quad \frac{\partial T_P}{\partial x} = 0 \quad \text{at } r = 0 \text{ (center)} \\ c_i^P &= c_i^S \quad T_P = T_S \quad \text{at } r = L \text{ (surface)} \end{aligned} \quad (81)$$

As it was defined, the problem consists in a set of non-linear partial differential equations (PDEs) that must be solved at two levels: the first is a local level, related to a single catalytic particle, and the second is a long-range scale for the entire reactor. The solution of the problem in the full form, expressed by the Equations (72) to (79), is a complex task, even by adopting sophisticated numerical solution algorithms, while an analytical exact solution is impossible for the mostly practical cases. In the following part of this review, an overview of the possible simplifications is presented and some simplified equations are reported in association with problems much easier to solve.

3.3. Conservation Equations in Dimensionless Form and Possible Simplification

A convenient way to introduce the mentioned simplifications is in rewriting mass and energy balances for the reactor in a dimensionless form. This strategy has both the scope to emphasize some parameters of the reactor and the ability to implement a more robust procedure for the numerical solution.

We can pose

$$n_d = \frac{Z}{d_p} \quad m_d = \frac{R}{d_p} \quad A_d = \frac{Z}{R} \quad \theta_d = \frac{Z}{u} \quad \bar{c}_i = \frac{c_i^B}{c_i^{B(in)}} \quad (82)$$

$$\bar{T} = \frac{T_B}{T_{B(in)}} \quad \bar{r} = \frac{r}{R_r} \quad \bar{z} = \frac{z}{Z} \quad \bar{t} = \frac{t}{\theta_d}$$

with

- d_p —particle diameter;
- R —fixed-bed reactor radius;
- Z —fixed-bed reactor length;
- $c_i^{B(in)}$ —reactor inlet concentration;
- $T_{B(in)}$ —reactor inlet temperature.

Within these assumptions, the reactor conservation equations become

$$\varepsilon_B \frac{\partial \bar{c}_i}{\partial \bar{t}} + \frac{\partial \bar{c}_i}{\partial \bar{z}} - \frac{1}{n_d P_{ma}} \frac{\partial^2 \bar{c}_i}{\partial \bar{z}^2} - \frac{1}{m_d P_{mr}} \left[\frac{\partial^2 \bar{c}_i}{\partial \bar{r}^2} + \frac{1}{\bar{r}} \frac{\partial \bar{c}_i}{\partial \bar{r}} \right] = \frac{(1 - \varepsilon_B) \theta_d}{c_i^{B(in)}} \sum_{j=1}^{N_{re}} \gamma_{i,j} v_{r,j}^G \quad i = 1, 2, \dots, N_c \quad (83)$$

$$\varepsilon_B \frac{\partial \bar{T}}{\partial \bar{t}} + \frac{\partial \bar{T}}{\partial \bar{z}} - \frac{1}{n_d P_{ha}} \frac{\partial^2 \bar{T}}{\partial \bar{z}^2} - \frac{A_d}{m_d P_{hr}} \left[\frac{\partial^2 \bar{T}}{\partial \bar{r}^2} + \frac{1}{\bar{r}} \frac{\partial \bar{T}}{\partial \bar{r}} \right] = \frac{(1 - \varepsilon_B) \theta_d}{\rho C_p T_{B(in)}} \sum_{j=1}^{N_{re}} (-\Delta H_j) v_{r,j}^G \quad (84)$$

In the Equations (83) and (84), we can recognize some fundamentals dimensionless groups that are related to mass dispersion, which is related to axial and radial directions, represented by Peclet's numbers expressed by the following equations:

$$P_{ma} = \frac{d_p u}{D_a} \quad (\text{axial}) \quad P_{mr} = \frac{d_p u}{D_r} \quad (\text{radial}) \quad (85)$$

and analogously for heat dispersion we have

$$P_{ha} = \frac{d_p u}{k_a} \quad (\text{axial}) \quad P_{hr} = \frac{d_p u}{k_r} \quad (\text{radial}) \quad (86)$$

The quantitative criteria that can be adopted to determine if the dispersion phenomena affect the overall reactor performances are Peclet's numbers and reactor-to-particle size ratios (n , m , and A). Moreover, these criteria can give indications to decide whether or not some simplifications are allowed. The operative conditions adopted and chemical reaction characteristics can suggest further simplifications according to which mass and energy conservation equations can be solved in a simplified form. The first and more common simplification is represented by the steady state, allowing the elimination of time variable and all its derivatives, in the left-hand sides of Equations (71), (72), (79), and (80). From an energetic point of view, the reaction enthalpy also plays a very important role. When the reaction heat is negligible or very low, the reactor can be run isothermally, and then, with the temperature being a constant, the heat balance equation can be eliminated. If the reactor is thermally insulated from the environment, it is operated in adiabatic conditions, as many reactors are in practice. In this case, radial gradients could be negligible, and therefore only a one-dimensional model is sufficient for the description of the reactor behavior. An intermediate situation, comprising these two limit cases described, is represented by a reactor working in conditions that cannot be considered isothermal nor adiabatic. This is the case of very exothermal reactions for which an external cooling system is required in order to guarantee the safety of the reactor and to preserve the catalyst durability. In this case, a numerical solution of conservation equations in full form appears to be the only feasible strategy. However, the conservation equations can still be applied in a simplified form, even if the problem remains complex to solve and is more difficult with respect to the two limit cases (isotherm and

adiabatic) cited previously. Normally, for an extremely exothermic chemical reaction, the packed beds with small diameter are used for promoting the heat removal, and in this case the radial temperature profile can be neglected. The problem is again mono-dimensional in this case. In general, according to Carberry [31], the gradients along the reactor radius, for practical purposes, can be neglected when the radial aspect ratio $m = R/d_p$ is less than 3 or 4. Further guidelines can be gained by examining the values of Peclet's numbers and the reactor aspect ratios; as an example, the axial aspect ratio $n=Z/d_p$ is usually very large, and considering that P_{ma} is about 2 for gases flowing through a catalytic bed for Reynold's number (based on particle diameter) greater than 10, then the term nP_{ma} is also large, revealing that axial mass dispersion can be almost completely neglected. Table 3 [32] summarizes the general guidelines to introduce principal simplifications in the mass balance for a packed-bed reactor operating under stationary conditions; the two limit cases are also reported with concern to the isothermal and adiabatic reactor together with the intermediate situation in which the reactor cannot be considered isothermal nor adiabatic.

Table 3. Guidelines for simplifications in the left-hand side of conservation equations, with reference to stationary conditions.

Reactor Conditions	Aspect Ratio Criteria	Left-Hand Side of Equations (71) and (72)
Isothermal		$u \frac{\partial c_B^i}{\partial z}$
Adiabatic	$\left(\frac{Z}{d_p}\right)\left(\frac{d_p}{D_a}\right) > 300 \quad Re > 10$	$u \frac{\partial c_B^i}{\partial z}$ $\rho C_p u \frac{\partial T_B}{\partial z}$
	$\left(\frac{Z}{d_p}\right)\left(\frac{d_p}{D_a}\right) < 300 \quad Re > 10$	$u \frac{\partial c_B^i}{\partial z}$ $\left\{ \begin{array}{l} \rho C_p u \frac{\partial T_B}{\partial z} \\ \rho C_p u \frac{\partial T_B}{\partial z} - K_a \frac{\partial^2 T_B}{\partial z^2} \end{array} \right.$ or, if necessary
Non-isothermal and non-adiabatic	$\frac{R_r}{d_p} > 4$	$u \frac{\partial c_B^i}{\partial z} - D_r \left(\frac{\partial^2 c_B^i}{\partial r^2} + \frac{1}{r} \frac{\partial c_B^i}{\partial r} \right)$ $\rho C_p u \frac{\partial T_B}{\partial z} - K_r \left(\frac{\partial^2 T_B}{\partial r^2} + \frac{1}{r} \frac{\partial T_B}{\partial r} \right)$
	$\frac{R_r}{d_p} \leq 4 \quad Re > 30$	$u \frac{\partial c_B^i}{\partial z}$ $\rho C_p u \frac{\partial T_B}{\partial z}$

3.4. Examples of Applications

In the following sections, we examine some examples concerning fixed-bed reactors operating in the various possible thermal regimes.

3.4.1. Isothermal Conditions

Isothermal conditions are seldom obtained in industrial packed bed reactors and are only for systems with a very low heat of reaction, whereas they are most commonly encountered in slurry reactors because liquid phase has a high thermal conductivity. Therefore, in these cases, we can have only internal, and sometimes external, diffusion limitation to the reaction.

3.4.2. Adiabatic Conditions

If the reactor is operated so that heat transfer to the surrounding is negligible, the system could be considered in adiabatic conditions. For simplicity, we can consider a system of a single reaction, $A \rightarrow P$, in steady state adiabatic conditions, and then the material energy balances for a tubular reactor with no axial and radial dispersion could be derived from Equations (69) and (70), resulting in the following expressions:

$$\begin{aligned} \frac{dF_A}{dz} &= \rho_B A \bar{R}_1 \\ \frac{dT}{dz} &= \frac{\rho_B}{GC_p} (-\Delta H_1) \bar{R}_1 \end{aligned} \quad (87)$$

where

- G —mass velocity;
- cross section of the reactor tube;
- F_A, F_A^0 component molar flow rate;
- \bar{R}_j —reaction rate for reaction j based on catalyst mass.

In the above equations, it is convenient to introduce the fractional conversion, X_A , obtaining the following equations:

$$\begin{aligned} \frac{dX_A}{dz} &= -\frac{\rho_B^A}{F_A^0} \bar{R}_1 \\ \frac{dT}{dz} &= \frac{\rho_B}{GC_p} (-\Delta H_1) \bar{R}_1 \end{aligned} \quad (88)$$

Dividing Equations (87) and (88) term by term, we obtain an expression relating the conversion and the temperature:

$$\frac{dX_A}{dT} = -\frac{AGC_p}{F_A^0} (-\Delta H_1) \quad \text{or in integrated form: } X_A = \alpha_A + \beta_A T \quad (89)$$

with α_A and β_A as constants. The main result expressed by the previous equation is that a linear relationship exists between the temperature and the conversion for an adiabatic reactor.

Adiabatic reactors are frequently employed in industrial practice, especially in the case of equilibrium reactions for which the desired conversion is achieved through assembling the reactor in a series of adiabatic catalytic beds provided with intermediate heat removal or supplying system in accordance with the reaction being exothermic or endothermic. Figures 12 and 13 report a schematic reactor configuration for an exothermic and an endothermic reaction, respectively, together with temperature-conversion diagrams that show conversion equilibrium curves and straight lines resulting from balance Equation (89) and cooling or heating. With such an arrangement, it is possible to achieve good control over the final conversion of reversible reactions by controlling the temperature at the outlet of each catalytic bed. In the diagrams reported in Figures 12 and 13, dashed lines represent cooling or heating operations.

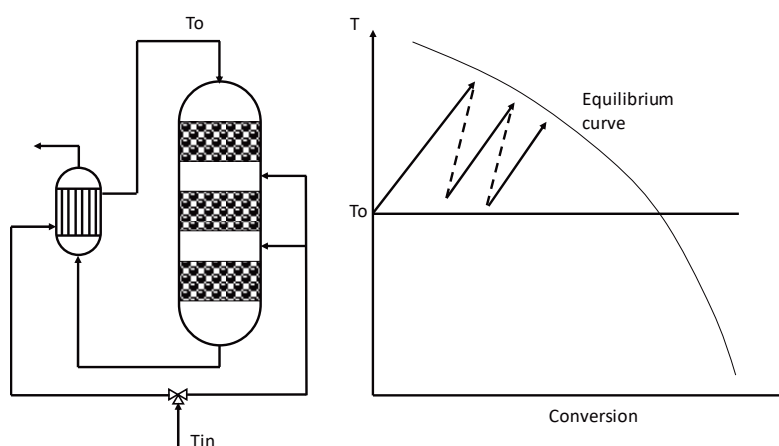


Figure 12. Scheme of a multistage adiabatic reactor (exothermic reaction). (left) reactor setup; (right) temperature profile.

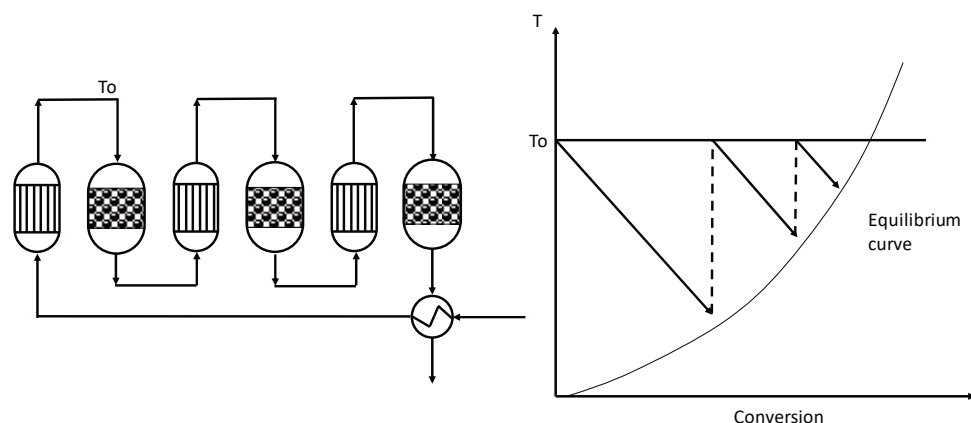
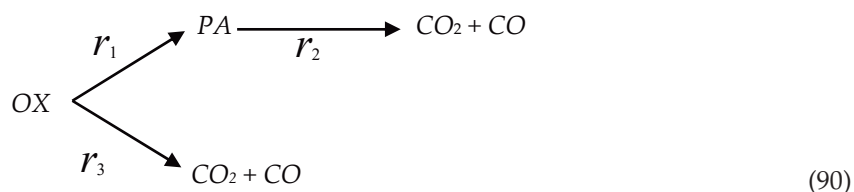


Figure 13. Scheme of a multistage adiabatic reactor (endothermic reaction). **(left)** reactor setup; **(right)** temperature profile.

4. Non-Isothermic and Non-Adiabatic Conditions

4.1. Conversion of *o*-Xylene to Phthalic Anhydride

Let us consider, first of all, a reaction that is performed in a packed-bed tubular reactor, operated in an modality non-isothermal and non-adiabatic that consists in the synthesis of phthalic anhydride (PA) obtained by oxidation of *o*-xylene (OX) with oxygen (O). A simplified scheme for this oxidation reaction can be expressed as follows:



The reaction is catalyzed by vanadium pentoxide supported on α -alumina and has a high exothermic character. From Equation (90), it is evident that the reaction can lead to CO_2 and CO production, if not properly thermally controlled, giving a low yield in PA. For the reactor simulation, therefore, thermal effect must be taken into account for both the reaction and the heat exchanged with the cooling medium. The kinetic equations and related parameters for the reactions (Equation (90)) are reported in Table 4, together with the characteristics of the reactor and of the catalytic particles used in the simulations [33].

A specific characteristic of this reactor is the catalyst dilution with an inert material in the first part of the reactor (0.75 m) that is realized at the purpose of an improved temperature control.

For the model development, some basic assumptions should be stated, as in the following points:

- No axial and radial dispersion;
- No radial temperature and concentration gradients in the reactor body;
- Plug flow behavior of the reactor;
- No limitation related to internal diffusion in catalytic particles.

Table 4. Kinetic data for the conversion of o-xylene to phthalic anhydride.

$r_1 = k_1 P_{OX} P_O$ (Kmol/Kg-cat h)	$\ln k_1 = -27,000/RT + 19.837$
$r_2 = k_2 P_{PA} P_O$ (Kmol/Kg-cat h)	$\ln k_2 = -31,000/RT + 20.860$
$r_3 = k_3 P_{OX} P_O$ (Kmol/Kg-cat h)	$\ln k_3 = -28,600/RT + 18.970$
$\Delta H_1 = -307$ Kcal/mol	
$\Delta H_2 = -783$ Kcal/mol	
$\Delta H_3 = -1090$ Kcal/mol	
$U = 82.7$ Kcal/ m ² h °C	overall heat transfer coefficient
$D = 0.025$ m	reactor diameter
$Z = 3$ m	reactor length
$d_p = 0.003$ m	particle diameter
$C_p = 0.25$ Kcal/Kg °C	average specific heat
$\rho_B = 1300$ Kg/m ³	bulk density of the bed
Feed composition:	$y_{OX} = 0.0093$ $y_O = 0.208$
Feed molar flow rate	$F = 0.779$ moles/h
Inert dilution of the catalyst	$m_I = 0.5$ for the first quarter
Inlet temperature	$T_0 = 370$ °C

The assumptions related to radial profiles can be supported by the criteria expressed in Table 3 for radial aspect ratio $m=R/d_p$ that can be estimated as $m = 4.1$ and then slightly above the limit. By considering the assumptions and simplifications applied to this system, we can write a material balance equation directly from Equation (69) considered in the stationary state:

$$\frac{dF_i}{dz} = F \frac{dy_i}{dz} = \rho_B \frac{\pi D_r^2}{4} \sum_{j=1}^{N_r} \gamma_{i,j} \frac{\bar{R}_j}{(1 + m_I)} \quad i = 1, 2, \dots, N_c \quad (91)$$

assuming a constant molar flow rate F , and with the following substitution:

$$u = \frac{Q}{A} \quad Q_{c_i} = F_i \quad A = \frac{\pi D_r^2}{4} \quad F_i = y_i F \quad (92)$$

where:

- Q —volumetric overall flow rate;
- A —cross section of the reactor tube;
- D_r —reactor diameter;
- F_i —component molar flow rate;
- y_i —mole fraction of component i ;
- m_I —mass of inert per unit mass of catalyst (dilution ratio);
- \bar{R}_j —reaction rate for reaction j based on catalyst mass.

The heat is constituted by Equation (72) and can be modified in a way similar to that adopted for mass balance and according to the absence of radial profiles and to the heat exchange of external cooling fluid in the reactor jacket. The thermal exchange with the surrounding (thermal fluid into the jacket) cannot be considered only as a boundary condition but as a separate term in the energy balance equation. A behavior similar to that of a double pipe heat exchanger (see Figure 14) can be adopted for the reactor and then, referring to a unit of reactor volume, the heat transferred across the external surface is defined as

$$q = \frac{U(T_C - T)\pi D_r dz}{Adz} = \frac{U(T_C - T)\pi D_r}{A} = \frac{4U(T_C - T)}{D_r} \quad (93)$$

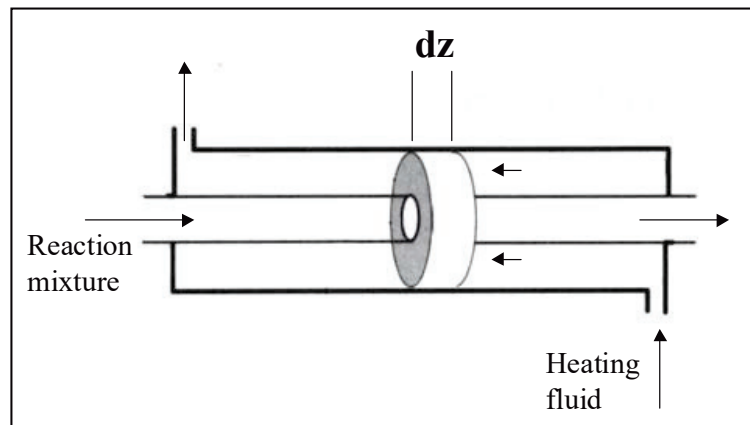


Figure 14. Double-pipe countercurrent reactor.

Equation (93) represents an additional term in the energy balance, and must be added to the heat associated with the reaction, resulting in the following overall differential equation for temperature evolution along the reactor axis:

$$\frac{dT}{dz} = \frac{\rho_B}{GC_P} \sum_{j=1}^{N_r} (-\Delta H_j) \frac{\bar{R}_j}{(1 + m_I)} + \frac{4U}{DGC_P} (T_C - T) \quad (94)$$

with $G = \frac{F \cdot M_F}{A}$, with the following meanings for the symbols:

- G —mass velocity;
- M_F —average molecular weight of mixture.

The system of differential Equations (91) and (94) can be integrated in axial direction, z , for the calculation of temperature and composition profiles. The temperature profile resulting from this mono-dimensional model (axial coordinate) is reported in Figure 15 [33], with this diagram also reporting, as a comparison, the result of a more complex bi-dimensional model in which profiles in a radial direction are also taken into account.

As was shown before, the bi-dimensional model involves the solution of partial differential equations. In the considered example is the numerical strategy of finite differences method (FDM). The two models (one and two dimensions) give comparable results for what concerns axial temperature profiles. A conclusion is that the one-dimensional model can be considered sufficiently accurate for many practical purposes. The bi-dimensional model, however, foresees a slightly higher conversion to CO and CO₂, due to the higher temperature along the reactor.

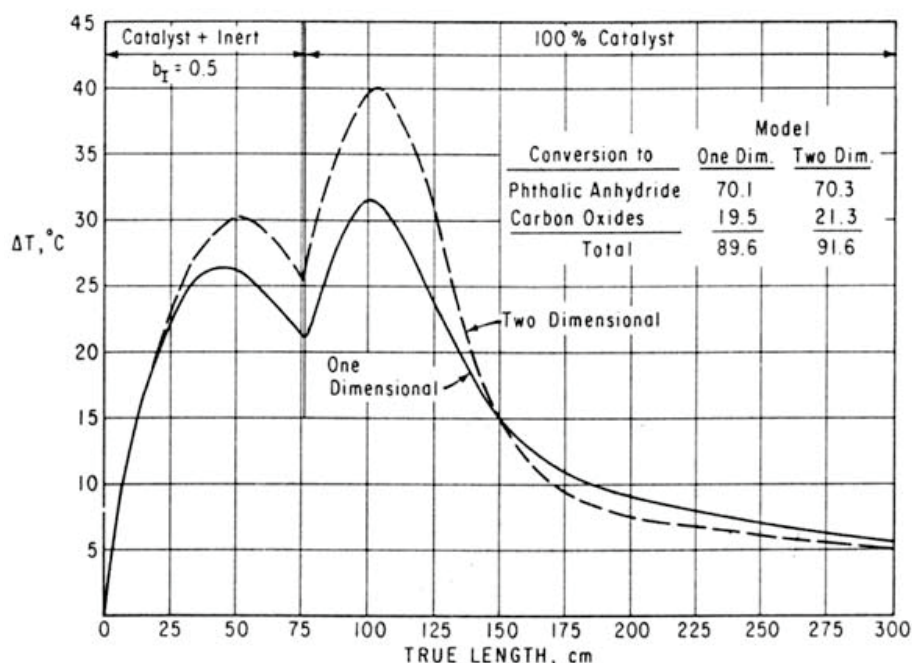


Figure 15. Comparison of the results of the one- and bi-dimensional models for reactor simulation (elaborated from data reported by Froment [33], see also [1]).

4.2. Conversion of Methanol to Formaldehyde

As a further example of a system that cannot be considered isothermal nor adiabatic, we chose the same reaction previously adopted in Section 2.7 for the evaluation of the effectiveness factor in a non-isothermal pellet, that is, the catalytic conversion of methanol to formaldehyde. Two reactions occurred as seen previously (Equation (61)).

These reactions were performed in a tubular reactor packed with catalyst and equipped with a jacket in which a heat transfer fluid is circulated with the purpose to a better temperature control. Table 5 reports the reactor operating conditions and other characteristics. A simulation was performed by using these conditions and the kinetic data from Riggs [29] (details were reported in [25]), obtaining composition and temperature profiles along the reactor axis. In this case study, a further aspect was introduced into the model, consisting in the calculation of the catalyst effectiveness factor along the reactor, considering diffusional limitations inside the particles.

Table 5. Reactor characteristic and operating conditions.

Inlet temperature	539 K
Total pressure	1.68 atm
Bulk density of the bed	0.88 Kg/m ³
Overall heat transfer coefficient U	0.171 KJ/(m ² s K)
Heating medium temperature	544 K
Reactor diameter	2.54 × 10 ⁻² m
Particles diameter	3.5 × 10 ⁻³ m
Reactor length	0.35 m
Gas inlet composition	mol %
CH ₃ OH	9
O ₂	10
CH ₂ O	0.5
H ₂ O	2
CO	1
N ₂	77.5

Some simplifying assumptions were introduced in the present case for the model development in a way similar to that of the example reported in the previous section:

- Negligible dispersion in axial and radial directions;
- Absence of concentration and temperature profiles along the reactor radius;
- Plug flow reactor behavior.

By applying the criteria of Table 3, radial profiles can be considered negligible as the aspect ratio in radial direction was $m = R/d_p = 3.6$, which was well below the limit value of 4. Under these assumptions, the resulting model is mono-dimensional because it only considers axial reactor profiles. At each location along the reactor axis, an effectiveness factor calculation was performed to obtain the value of the reaction rate that is related to that point, determining, in this way, an effectiveness factor axial profile. On the basis of the described assumptions and introducing molar flow rates relative to each chemical component, we can express material balance equations by the following model:

$$\frac{dF_i}{dz} = \rho_B \frac{\pi D_r^2}{4} \sum_{j=1}^{N_r} \gamma_{i,j} \bar{R}_j \quad i = 1, 2, \dots, N_c \quad (95)$$

$$u = \frac{Q}{A} \quad Qc_i = F_i \quad A = \frac{\pi D_r^2}{4} \quad (96)$$

that can be derived upon the following substitution in Equation (71):

The energy balance, represented by Equation (72), can also be simplified, as done for the mass balance, according to the assumed absence of radial profiles and to the presence of reactor jacket with cooling fluid, as reported, for example, in Session 4.1. The heat exchanged per unit of reactor volume between the reactor and the cooling jacket can be defined as follows:

$$q = \frac{U(T_C - T)\pi D_r dz}{Adz} \quad (97)$$

This term must be added algebraically to the reaction enthalpy term in the heat balance equation, yielding the following expression:

$$\left(\sum_{i=1}^{N_c} F_i C_{p_i} \right) \frac{dT}{dz} = \frac{\pi D_r^2}{4} \rho_B \sum_{j=1}^{N_r} (-\Delta H_j) \bar{R}_j + \pi D_r U (T_C - T) \quad (98)$$

Equations (95) and (98) represent a system of N_c+1 coupled ordinary differential equations that must be integrated along the z axial direction to calculate the desired profiles of composition and temperature. At each integration step along z , a calculation of the effectiveness factor for each chemical reaction must be performed according to the procedure described in Session 2.6. A suitable integration algorithm must be adopted with a variable z step size, inversely proportional to the axial derivative dT/dz , so that a smaller step size is used when a steep temperature increase is detected in correspondence to a steeper profile. Figure 16 reports the axial temperature profile as a result of this simulation. This figure shows that the reaction mixture fed to the reactor undergoes a steep increase in gas temperature due to the strong exothermic character of this reactive system.

As methanol conversion proceeds (see composition profile reported in Figure 17), the main reaction rate also decreases, and the same trend can be appreciated for the temperature. Finally, in Figure 18, the profiles of the effectiveness factors for the two reactions is reported. It is interesting to observe that the main reaction is characterized, in the first part of the reactor, by an effectiveness factor much higher than unity, with this indicating that catalytic particles are not isothermal and a temperature profile is developed inside them.

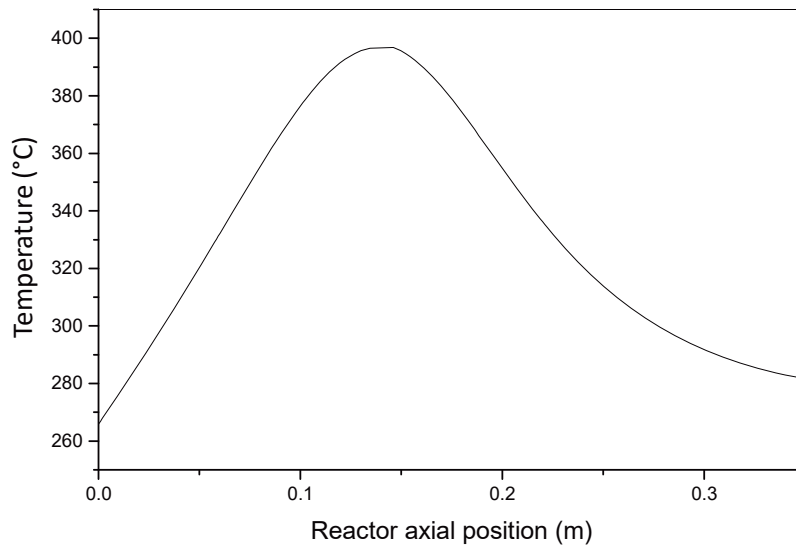


Figure 16. Axial temperature profile.

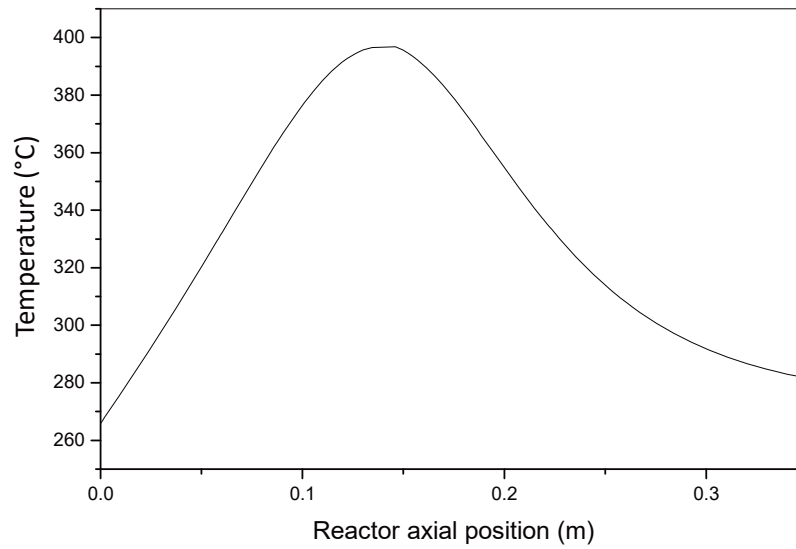


Figure 17. Axial profiles for component mole fractions.

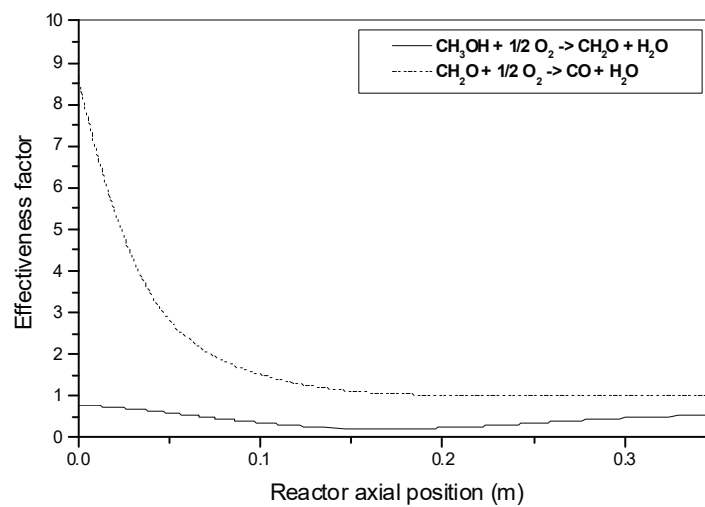


Figure 18. Axial profiles for the effectiveness factor for the two reactions.

5. Conclusions

The role of heat and mass transfer in affecting the kinetic studies in gas–solid tubular reactors was discussed in detail by surveying the abundant literature published on the subject. All the occurring phenomena were described and the equations for their interpretation were given.

Considering the enormous progress of electronic computers, many problems that were intractable in the past for their mathematical complexity can today be easily and rigorously solved with numerical approaches. For more clarity, some examples of mathematical solutions were reported.

Author Contributions: E.S. wrote the first part of the work related to the heat and mass transfer in the single pellet. R.T. wrote the second part related to the long-range gradients in packed bed reactors. All authors have read and agreed to the published version of the manuscript.

Funding: Thanks are due to Eurochem Engineering Ltd for funding the work.

Conflicts of Interest: The authors declare no conflict of interest.

Glossary

List of Symbols

a_m	Specific surface area
A	Reactor cross section
b_w	Water adsorption equilibrium constant
c	Generic concentration
c_i	Concentration of component i
c_i°	Initial i concentration
c_b	Generic concentration of a component in the bulk
c_i^B	Concentration of i in the bulk
c_i^P	Concentration of i inside a catalytic particle
c_S	Generic concentration at the catalytic surface
c_i^S	Concentration of i at the surface
C_p	Average gas specific heat
C_p^P	Particle specific heat
Δc	Concentration gradient
Δc_{\min}	Minimum concentration gradient
D	Reactor diameter
d_p	Particle diameter
D	Generic molecular diffusivity
D_i	Molecular diffusivity of component i
$D_{i,j}$	Mutual binary diffusion coefficient
D_{12}	Mutual binary diffusion coefficient
D_{im}	Diffusion coefficient of i in a mixture m
D_{eff}	Effective molecular diffusivity
$(D_i)_{\text{eff}}$	Effective molecular diffusivity of component i
D_{be}	Bulk diffusion coefficient
D_{ke}	Knudsen diffusion coefficient
D_{ei}	Effective diffusivity inside particle
D_{ai}	Axial diffusivity of component i
D_{ri}	Radial diffusivity of component i
F_i	Molar flow rate of component i
F	Overall molar flow rate
G	Mass velocity
h	Film heat transfer coefficient
h_w	Wall heat transfer coefficient
ΔH	Generic reaction enthalpy
ΔH_j	Enthalpy of reaction j

J_i	Molar flux of component i
J_D, J_H	Terms for mass and heat transfer analogy
k, k_i	Generic kinetic constant
k_B	Boltzmann's constant
k_T	Generic thermal conductivity of the fluid
k_f	Thermal conductivity of the bulk
k_{eff}	Effective thermal conductivity
k_{Sol}	Thermal conductivity of the solid
K_a	Axial thermal conductivity
K_r	Radial thermal conductivity
K_e	Particle thermal conductivity
k_S	Kinetic constant
k_c	Film mass transfer coefficients (concentration gradient)
k_g	Film mass transfer coefficients (pressure gradient)
k_m	Mass transfer coefficient
L	Characteristic length
L_e	Lewis's number
m	Radial aspect ratio
m_I	Inert dilution ratio
M, M_i	Molecular weight
M_F	Average molecular weight of the mixture
M_{iw}	Weisz modulus
N_C	Number of components
N_{re}	Number of reactions
N_r	Molar flux
$N_{i,r}, N_A$	Molar flux
N	Number of nodes
n	Reaction order
P	Total pressure
P_m	Methanol partial pressure
P_f	Formaldehyde partial pressure
P_w	Water partial pressure
P_{O_2}	Oxygen partial pressure
P_{ma}	Axial Peclet's number for mass
P_{mr}	Radial Peclet's number for mass
P_{ha}	Axial Peclet's number for heat
P_{hr}	Radial Peclet's number for heat
P_r	Prandtl's number
Q	Rate of heat transfer
Q_v	Overall volumetric flow rate
q	Heat flux
r	Reactor radial coordinate
r_p	Particle spherical radius
R	Gas constant
R_r	Reactor radius
R_{ni}	Reaction rate at node i
R_j	Reaction rate (fluid volume)
\bar{R}_j	Reaction rate (catalyst mass)
r_{cj}	Intrinsic reaction rate
Re	Reynold's number
S_v	Specific surface area
S_h	Sherwood's number
S_c	Schmidt's number
S	Selectivity
S_g	Specific surface area

T	Generic temperature
T_S	Temperature at particle surface
T_P	Temperature inside the particle
T_b	Bulk temperature
T_c	Cooling fluid temperature
ΔT_{\max}	Maximum temperature difference
t	Time
u	Velocity
u_z	Velocity in z direction
U	Overall heat transfer coefficient
v_r	Reaction rate
$v_{r,i}$	Reaction rate, reaction i-th
$v_{r,j}^G$	Reaction rate (pellet volume)
V_{ci}	Critical volume of component i
x	Particle radial coordinate
X_i	Fractional conversion
y_i	Gas phase mole fraction component i
z	Axial reactor coordinate
Z	Reactor length

Greek Letters

α_A	Constant in Equation (89)
α_B	Constant in Equation (89)
α_E	Reaction rate exponential parameter
α_J	Constant in Equation (38)
α_H	Constant in Equation (40)
β	Prater's number
β_J	Constant in Equation (38)
β_H	Constant in Equation (40)
γ_{dr}	Dimensionless concentration
γ_{ij}	Stoichiometric coefficient
δ	Thickness of boundary layer
ε_{dr}	Dimensionless radius
ε_B	Bed void fraction
ε_{Bs}	Bed void fraction of the solid
ε_J	Constant in Equation (38)
ε_H	Constant in Equation (40)
ε_{ij}	Interaction parameter
ε_p	Particle void fraction
η, η_j	Effectiveness factor
μ	Viscosity
θ	Porosity of the solid
ρ	Average gas density
ρ_p	Particle density
ρ_d	Intermolecular distance
σ_{ij}	Kinetic diameter
τ	Tortuosity factor
ϕ	Thiele modulus
ϕ_{LJ}	Lennard-Jones potential
y_{dr}	Dimensionless reaction rate
Ω_D	Collision integral
∇	Nabla operator

References

1. Santacesaria, E.; Tesser, R. *The Chemical Reactor from Laboratory to Industrial Plant*; Springer: Berlin, Germany, 2018.
2. Froment, G.F. The kinetics of complex catalytic reactions. *Chem. Eng. Sci.* **1987**, *42*, 1073–1087. [[CrossRef](#)]
3. Smith, J.M. *Chemical Engineering Kinetics*; McGraw-Hill: New York, NY, USA, 1981.
4. Fogler, H.S. *Elements of Chemical Reaction Engineering*; Prentice-Hall International: Upper Saddle River, NJ, USA, 1986.
5. Horak, J.; Pasek, J. *Design of Industrial Chemical Reactors from Laboratory Data*; Hayden Publishing: London, UK, 1978.
6. Satterfield, C.N.; Sherwood, T.K. *The Role of Diffusion in Catalysis*; Addison-Wesley Publishing: Boston, MA, USA, 1963.
7. Levenspiel, O. *The Chemical Reactor Omnibook*; OSU Book Store: Corvallis, OR, USA, 1984.
8. Satterfield, C.N. *Heterogeneous Catalysis in Practice*; Addison-Wesley Publishing: Boston, MA, USA, 1972.
9. Holland, C.D.; Anthony, R.G. *Fundamentals of Chemical Reaction Engineering*; Prentice-Hall: London, UK, 1979.
10. Westerterp, K.R.; van Swaaij, W.P.M.; Beenackers, A.A.C.M. *Chemical Reactor Design and Operation*; John Wiley & Sons: New York, NY, USA, 1984.
11. Davis, M.E.; Davis, R.J. *Fundamentals of Chemical Reaction Engineering*; Dover Publications, Inc.: New York, NY, USA, 2003.
12. Vogel, G.H. *Process Development Wiely—VCH*; John Wiley & Sons: Weinheim, Germany, 2005.
13. Winterbottom, J.M.; King, M.B. *Reactor Design for Chemical Engineers*; Stanley Thornes Ltd.: Cheltenham Glos, UK, 1999.
14. Wheeler, A. Reaction rates and selectivity in catalyst pores. In *Advances in Catalysis*; Academic Press: Cambridge, MA, USA, 1951; Volume 3.
15. Bird, R.B.; Stewart, W.E.; Lightfoot, E.N. *Fenomeni di Trasporto*; Casa Editrice Ambrosiana: Milan, Italy, 1970.
16. Missen, R.W.; Mims, C.A.; Saville, B.A. *Chemical Reaction Engineering and Kinetics*; John Wiley & Sons: New York, NY, USA, 1999.
17. Carberry, J.J. Physico chemical aspects of mass and heat transfer in heterogeneous catalysis. In *Catalysis*; Springer: Berlin/Heidelberg, Germany, 1987; pp. 131–171.
18. Thiele, E.W. Relation between catalytic activity and size of particle. In *Industrial and Engineering Chemistry*; ACS Publications: Washington, DC, USA, 1939; Volume 31, pp. 916–920.
19. Weisz, P.B.; Prater, C.D. Interpretation of measurements in experimental catalysis. In *Advances in Catalysis*; Academic Press: New York, NY, USA, 1954; Volume 6, pp. 143–196. [[CrossRef](#)]
20. Santacesaria, E. Catalysis and transport phenomena in heterogeneous gas-solid and gas-liquid-solid systems. In *Catalysis Today*; Elsevier Science: Amsterdam, The Netherlands, 1997; Volume 34, pp. 411–420.
21. Froment, G.F.; Bishoff, K.B. *Chemical Reaction Analysis and Design*; John Wiley & Sons: New York, NY, USA, 1990.
22. Woodside, W.W.; Messner, J.H. Thermal conductivity of porous media. *J. Appl. Phys.* **1961**, *32*, 1688. [[CrossRef](#)]
23. Hindmarsh, A.C. LSODE and LSODI, two initial value ordinary differential equation solvers. *ACM Signum* **1980**, *15*, 10–11. [[CrossRef](#)]
24. Palm, W.J. *Introduction to MATLAB for Engineers*; Mc Graw-Hill: New York, NY, USA, 2011.
25. Tesser, R.; Santacesaria, E. Catalytic oxidation of methanol to formaldehyde: An example of kinetics with transport phenomena in a packed -bed reactor. *Catal. Today* **2003**, *77*, 325–333. [[CrossRef](#)]
26. Mars, J.; Krevelen, D.W. Oxidations carried out by means of vanadium oxide catalysts. *Chem. Eng. Sci.* **1954**, *3*, 41. [[CrossRef](#)]
27. Santacesaria, E.; Morbidelli, M.; Carrà, S. Kinetics of the catalytic oxidation of methanol to formaldehyde. *Chem. Eng. Sci.* **1981**, *36*, 909–918. [[CrossRef](#)]
28. Dente, M.; Collina, A.; Pasquon, I. Verifica di un reattore tubolare per l'ossidazione del metanolo a formaldeide. *La Chimica Industria* **1966**, *48*, 581–588.
29. Riggs, J.B. *Introduction to Numerical Methods for Chemical Engineers*; Texas Tech University Press: Lubbock, TX, USA, 1988.

30. Carrà, S.; Forzatti, P. Engineering aspects of selective hydrocarbons oxidation. *Catal. Rev. Sci. Eng.* **1977**, *15*, 1–52. [[CrossRef](#)]
31. Carberry, J.J. *Chemical and Catalytic Reaction Engineering*; McGraw-Hill: New York, NY, USA, 1976.
32. Lee, H.H. *Heterogeneous Reactors Design*; Butterwoth Publisher: Oxford, UK, 1984.
33. Froment, G.F. Fixed bed catalytic reactors—Current design status. *Ind. Eng. Chem.* **1967**, *59*, 18–27. [[CrossRef](#)]

Publisher’s Note: MDPI stays neutral with regard to jurisdictional claims in published maps and institutional affiliations.



© 2020 by the authors. Licensee MDPI, Basel, Switzerland. This article is an open access article distributed under the terms and conditions of the Creative Commons Attribution (CC BY) license (<http://creativecommons.org/licenses/by/4.0/>).

Article

Numerical Study on Bubble Rising in Complex Channels Saturated with Liquid Using a Phase-Field Lattice-Boltzmann Method

Kang Yu ^{1,2}, Yumei Yong ^{1,*} and Chao Yang ^{1,2,3,*}

¹ CAS Key Laboratory of Green Process and Engineering, Institute of Process Engineering, Chinese Academy of Sciences, Beijing 100190, China; kyu@ipe.ac.cn

² School of Chemical Engineering, University of Chinese Academy of Sciences, Beijing 100049, China

³ Dalian National Laboratory for Clean Energy, Dalian 116023, China

* Correspondence: ymyong@ipe.ac.cn (Y.Y.); chaoyang@ipe.ac.cn (C.Y.)

Received: 16 November 2020; Accepted: 4 December 2020; Published: 7 December 2020

Abstract: Packed bed reactors have been widely applied in industrial production, such as for catalytic hydrogenation. Numerical simulations are essential for the design and scale-up of packed beds, especially direct numerical simulation (DNS) methods, such as the lattice-Boltzmann method (LBM), which are the focus of future researches. However, the large density difference between gas and liquid in packed beds often leads to numerical instability near phase interface when using LBM. In this paper, a lattice-Boltzmann (LB) model based on diffuse-interface phase-field is employed to simulate bubble rising in complex channels saturated with liquid, while the numerical problems caused by large liquid-to-gas density ratio are solved. Among them, the channel boundaries are constructed with regularly arranged circles and semicircles, and the bubbles pass through the channels accompanied by deformation, breakup, and coalescence behaviors. The phase-field LB model is found to exhibit good numerical stability and accuracy in handling the problem of the bubbles rising through the high-density liquid. The effects of channel structures, gas-liquid physical properties, and operating conditions on bubble deformation, motion velocity, and drag coefficient are simulated in detail. Moreover, different flow patterns are distinguished according to bubble behavior and are found to be associated with channel structure parameters, gravity Reynolds number (Re_{Gr}), and Eötvös number (Eu).

Keywords: packed bed reactor; multiphase system; phase-field LB model; complex channel; flow pattern; bubble evolution

1. Introduction

Packed bed reactors have the advantages of simple structure, convenient operation, low operating cost, good heat, and mass transfer performance, and have thus been widely used in industrial processes such as catalytic hydrogenation [1], oxidation reaction [2], nitrification reaction [3], and wastewater treatment [4], among others. For gas-liquid-solid three-phase packed bed reactors, the dynamic behaviors of the dispersed phase directly affect the mixing, mass transfer, and reaction efficiency between gas and liquid, which are extremely important for the design, optimization, and scale-up of the packed beds. However, the detailed dynamics of the dispersed phase and the complicated topological evolution of the gas-liquid interface are difficult to fully understand through experiments or numerical simulations on the reactor scale. The direct numerical simulation (DNS) provides us with a promising solution, in which the lattice-Boltzmann method (LBM) has attracted more and more attention due to its simple computation and clear physical background. At present, LBM has realized the precise tracking of the gas-liquid interface and the accurate prediction of the bubble (dispersed phase) dynamics from the mesoscopic scale [5]. However, the density ratios of liquid to gas in the

actual packed beds are often as high as 1000, which tends to cause numerical instability at the gas-liquid interface in the simulations using LBM.

In recent decades, various lattice-Boltzmann (LB) models have been proposed for multiphase flows. Based on the approaches of describing the interactions between fluids, these models can be divided into four categories, including the color model [6], the pseudo-potential model [7], the free-energy model [8], and the kinetic model [9]. Undesirably, the original forms of these models are all accompanied by numerical instability defects when applied to multiphase systems with large density ratios in the range of 500–1000. In order to remedy the limitation, Inamuro et al. [10] developed an LB model that satisfies Galileo invariance for incompressible two-phase flows with density ratios of 50–1000 based on the free-energy model, but the implementation of this method requires high computational costs for solving the introduced pressure-Poisson equation, which destroys the simplicity of LBM. Lee et al. [11,12] successively proposed innovative LB models with three-step algorithms and second-order mixed difference schemes based on the Cahn-Hilliard model [13], achieving numerical stability at large density ratios up to 1000. In addition to the complicated and inefficient algorithms, some researchers [14,15] pointed out that the models of the Lee's group [11,12] lacked accurate mass conservation due to the inconsistent invocations of central and biased finite differences. Zheng et al. [16] claimed to develop an LB model for multiphase systems with large density ratios by improving the free-energy model, but Fakhari and Rahimian [17] thought that their model was restricted to density-matched binary fluids, and incapable of modeling actual multiphase flows with large density ratios.

Over the past ten years, Fakhari and his group [17–24] have been dedicated to the LBM studies of multiphase systems with large density ratios, and have proposed various improved LB models and made a series of research progress. In particular, a phase-field LB model suitable for large density ratios has been constantly modified and optimized, which already has the characteristics of exact mass conservation, superior accuracy, and stability [19,20]. Until 2019, this LBM was used to solve various numerical problems such as bubble rising [17,19,21,24], droplet falling [17,19,20,22], von Kármán vortex street flows [18,20], and gas-liquid flows in porous media [23]. However, due to the complicated topological evolutions of the gas-liquid interface, including the bubble deformation, splitting, coalescence, and interplay with obstacles, no researchers have studied the bubble rising in the packed bed by this method so far. In order to save computing resources, the packed bed is simplified and replaced by two complex channels in our work, the bubble rising problem in the channels saturated with liquid will be investigated using the phase-field LB model.

In this paper, the phase-field LB model is tested by several benchmark problems and proved to indeed be a numerical method with high numerical stability and accuracy. Subsequently, this model is employed to simulate bubble rising in complex channels saturated with liquid at large density ratios, in which the problem of specifying the contact angle is also taken into account. The numerical results reveal the effects of channel structures, gas-liquid physical properties, and operating conditions on bubble deformation, motion velocity, and drag coefficient. Additionally, different flow patterns are recognized and found being dependent of channel structure parameters, gravity Reynolds number (Re_{Gr}), and Eötvös number (EO). In the following, the specific numerical algorithm of phase-field LB model and its implementation details are presented in Section 2. Several verification examples used to test the phase-field LB model are listed in Section 3. Then, detailed numerical results and the discussions are given in Section 4. Finally, a summary and conclusions for the whole article are given in Section 5.

2. Numerical Method

In this paper, a phase-field LB model [20] is employed to solve the problem of bubble rising in complex channels saturated with liquid. This model is characterized by good accuracy and strict mass conservation, and has smaller spurious velocities and performs better in handling multiphase flows with large density and viscosity ratios than color and pseudo-potential models. In addition, the method also takes into account the three-phase contact line dynamics.

2.1. Phase-Field LB Model

The phase-field LB model we currently use is proposed by Fakhari et al. [20], in which the lattice-Boltzmann equations (LBE) combine a modified interface tracking equation and improved hydrodynamic evolution equations to achieve numerical computations of isothermal incompressible multiphase fluid systems.

2.1.1. Macroscopic Governing Equations

In the phase-field LB model, a phase-field variable ϕ is defined and its value is zero in the light fluid (gas bubbles) while one in the heavy fluid (liquid), which changes smoothly across the phase interface between two different fluids. Unlike those phase-field models based on the Cahn-Hilliard equation [13,17,25], a so-called conservative phase-field equation is used in the current model for interface tracking [26]:

$$\frac{\partial \phi}{\partial t} + \nabla \cdot (\phi \mathbf{u}) = \nabla \cdot \left[M \left(\nabla \phi - \frac{4}{\xi} \phi (1 - \phi) \hat{\mathbf{n}} \right) \right] \quad (1)$$

where t is the time, \mathbf{u} is the macroscopic velocity vector, M is the mobility, ξ is the interface thickness, and $\hat{\mathbf{n}}$ represents the unit vector normal to the gas-liquid interface, whose direction is away from the liquid side and points to the gas bubble side, that is

$$\hat{\mathbf{n}} = \frac{\nabla \phi}{|\nabla \phi|} \quad (2)$$

The isothermal incompressible multiphase flows are governed by Navier-Stokes equations, including the continuity equation:

$$\frac{\partial \rho}{\partial t} + \nabla \cdot \rho \mathbf{u} = 0 \quad (3)$$

and the momentum conservation equation,

$$\rho \left(\frac{\partial \mathbf{u}}{\partial t} + \mathbf{u} \cdot \nabla \mathbf{u} \right) = -\nabla p + \nabla \cdot \left(\mu \left[\nabla \mathbf{u} + (\nabla \mathbf{u})^T \right] \right) + \mathbf{F}_s + \mathbf{F}_b \quad (4)$$

where ρ and μ represent the fluid density and viscosity respectively, p is the macroscopic pressure, \mathbf{F}_b is the body force, and \mathbf{F}_s is the surface tension force due to the presence of interface, which can be calculated by [27]:

$$\mathbf{F}_s = \mu_\phi \nabla \phi \quad (5)$$

in which μ_ϕ is the chemical potential of the binary-fluid system, which is defined by the derivative of the volumetric free energy E_f with respect to the phase field ϕ :

$$\mu_\phi = \frac{\delta E_f}{\delta \phi} = 4\beta\phi(\phi - 1)(\phi - 1/2) - \kappa \nabla^2 \phi \quad (6)$$

where the volumetric free energy is given by [27,28]:

$$E_f = \oint \left(\beta \Psi(\phi) + \frac{1}{2} \kappa |\nabla \phi|^2 \right) dV \quad (7)$$

in which the coefficients $\beta = 12\sigma/\xi$ and $\kappa = 3\sigma\xi/2$ are related to the surface tension σ and the interface thickness ξ , and $\Psi(\phi)$ is the bulk free energy and expressed as:

$$\Psi(\phi) = \phi^2(1 - \phi)^2 \quad (8)$$

It should be noted that in the above equations, the gradient and Laplacian of the phase field ϕ are computed using a second-order isotropic central difference scheme. This scheme avoids the occurrence

of a fourth-order derivative when solving the Laplacian in Equation (6) [13,25], and the combination of central and biased differences that was employed in previous studies [11,12], which weakens the numerical dispersion and maintains the conservation of mass and momentum. Therefore, the phase-field LB model is prone to numerical stability at large density ratios.

2.1.2. LBE for Interface Tracking

The following LBE has been recovered into Equation (1) by Geier et al. [29], which can be used to track the gas-liquid interface:

$$h_\alpha(\mathbf{x} + \mathbf{e}_\alpha \delta t, t + \delta t) = h_\alpha(\mathbf{x}, t) - \frac{h_\alpha(\mathbf{x}, t) - h_\alpha^{\text{eq}}(\mathbf{x}, t)}{\tau_\phi + 1/2} \quad (9)$$

where h_α is the phase-field distribution function, τ_ϕ is the phase-field relaxation time, \mathbf{e}_α represents the lattice-related mesoscopic velocity set. For the lattice of D2Q9 model, \mathbf{e}_α is given by [30]:

$$\mathbf{e}_\alpha = c \begin{cases} (0, 0), & \alpha = 0 \\ (\cos \theta_\alpha, \sin \theta_\alpha), & \theta_\alpha = (\alpha - 1)\pi/2, \quad \alpha = 1 \sim 4 \\ (\cos \theta_\alpha, \sin \theta_\alpha) \sqrt{2}, & \theta_\alpha = (2\alpha - 9)\pi/4, \quad \alpha = 5 \sim 8 \end{cases} \quad (10)$$

where $c = \delta x / \delta t = 1$, δx and δt represent the unit lattice length and unit time, respectively, and both δx and δt are set to one in uniform grids. h_α^{eq} is the equilibrium phase-field distribution function, which is expressed as:

$$h_\alpha^{\text{eq}} = \phi \Gamma_\alpha + w_\alpha \frac{M}{c_s^2} \left[\frac{4}{\xi} \phi (1 - \phi) \right] (\mathbf{e}_\alpha \cdot \hat{\mathbf{n}}) \quad (11)$$

in which

$$\Gamma_\alpha = w_\alpha \left[1 + \frac{\mathbf{e}_\alpha \cdot \mathbf{u}}{c_s^2} + \frac{(\mathbf{e}_\alpha \cdot \mathbf{u})^2}{2c_s^4} - \frac{\mathbf{u} \cdot \mathbf{u}}{2c_s^2} \right] \quad (12)$$

In Equations (11) and (12), c_s is the lattice sound speed and $c_s = c / \sqrt{3}$, and w_α represents the lattice-related weight coefficient set [30], where $w_0 = 4/9$, $w_{1-4} = 1/9$, $w_{5-8} = 1/36$. Mobility M is positively correlated with the phase-field relaxation time τ_ϕ as:

$$M = \tau_\phi c_s^2 \delta t \quad (13)$$

After the calculation of a two-step collision-streaming sequence, the phase field is updated by taking the zeroth moment of the phase-field distribution function:

$$\phi = \sum_\alpha h_\alpha \quad (14)$$

and subsequently the density ρ can be obtained by linear interpolation:

$$\rho = \rho_g + \phi(\rho_l - \rho_g) \quad (15)$$

where ρ_g and ρ_l represent the densities of the gas and liquid, respectively.

2.1.3. LBE for Hydrodynamics

An improved hydrodynamic LBE based on HCZ model [9] was developed by Fakhari et al. [17] to update pressure and velocity fields in nearly incompressible multiphase flows:

$$\bar{g}_\alpha(\mathbf{x} + \mathbf{e}_\alpha \delta t, t + \delta t) = \bar{g}_\alpha(\mathbf{x}, t) + \Omega_\alpha(\mathbf{x}, t) + F_\alpha(\mathbf{x}, t) \quad (16)$$

where \bar{g}_α is called the modified hydrodynamic distribution function, and F_α is the forcing term, which is calculated by [20]:

$$F_\alpha(\mathbf{x}, t) = \delta t [(\Gamma_\alpha - w_\alpha)(\rho_l - \rho_g)c_s^2 + \Gamma_\alpha \mu_\phi] (\mathbf{e}_\alpha - \mathbf{u}) \cdot \nabla \phi + \delta t \Gamma_\alpha (\mathbf{e}_\alpha - \mathbf{u}) \cdot \mathbf{F}_b \quad (17)$$

Ω_α is the collision operator, here the collision operator with a multiple-relaxation-time (MRT) model [31] is employed because its performance is more stable in the implementation than the Bhatnagar-Gross-Krook (BGK) model:

$$\Omega_\alpha(\mathbf{x}, t) = -\mathbf{M}^{-1} \hat{\mathbf{S}} \mathbf{M} (\bar{g}_\alpha - \bar{g}_\alpha^{\text{eq}}) \quad (18)$$

where $\bar{g}_\alpha^{\text{eq}}$ is called the modified equilibrium distribution function and is given by:

$$\bar{g}_\alpha^{\text{eq}} = g_\alpha^{\text{eq}} - \frac{1}{2} F_\alpha \quad (19)$$

in which the equilibrium distribution function g_α^{eq} is defined as:

$$g_\alpha^{\text{eq}} = p w_\alpha + \rho c_s^2 (\Gamma_\alpha - w_\alpha) \quad (20)$$

\mathbf{M} is an orthogonal transformation matrix to transform the distribution functions from physical space into moment space [31] and \mathbf{M}^{-1} is its inverse matrix, and $\hat{\mathbf{S}}$ is a diagonal relaxation matrix. For the D2Q9 lattice, $\hat{\mathbf{S}}$ can be selected as:

$$\hat{\mathbf{S}} = \text{diag}(1, 1, 1, 1, 1, 1, 1, s_v, s_v) \quad (21)$$

in which

$$s_v = \frac{1}{\tau + 1/2} \quad (22)$$

where τ is the hydrodynamic relaxation time, which is calculated according to the dynamic viscosity derived by linear interpolation:

$$\mu = \mu_g + \phi(\mu_l - \mu_g) \quad (23)$$

and

$$\tau = \frac{\mu}{\rho c_s^2} \quad (24)$$

Among them, μ_g and μ_l represent the dynamic viscosities of the gas and liquid, respectively.

After solving the modified hydrodynamic distribution function according to the two-step calculation sequence of collision-streaming, the hydrodynamic properties are obtained by:

$$\mathbf{u} = \frac{1}{\rho c_s^2} \sum_\alpha \bar{g}_\alpha \mathbf{e}_\alpha + \frac{\delta t}{2\rho} (\mathbf{F}_s + \mathbf{F}_b) \quad (25)$$

$$p = \sum_\alpha \bar{g}_\alpha + \frac{\delta t}{2} (\rho_l - \rho_g) c_s^2 \mathbf{u} \cdot \nabla \phi \quad (26)$$

Note that the calculation of pressure p requires the updated velocity \mathbf{u} , so the update sequence of velocity must precede the pressure.

2.2. Numerical Implementation

2.2.1. Discretization

As described in Section 2.1, a second-order isotropic central difference scheme for the phase field is adopted in the phase-field LB model, which is conducive to stable implementation while retaining

the second-order accuracy. In detail, the gradient terms used in Equations (5), (17), and (26) and the Laplacian term in Equation (6) are computed according to the following discrete schemes:

$$\nabla\phi = \frac{1}{2c_s^2\delta t} \sum_{\alpha=1}^8 \mathbf{e}_\alpha w_\alpha [\phi(\mathbf{x} + \mathbf{e}_\alpha\delta t) - \phi(\mathbf{x} - \mathbf{e}_\alpha\delta t)] \quad (27)$$

$$\nabla^2\phi = \frac{1}{c_s^2\delta t^2} \sum_{\alpha=1}^8 w_\alpha [\phi(\mathbf{x} + \mathbf{e}_\alpha\delta t) - 2\phi(\mathbf{x}) + \phi(\mathbf{x} - \mathbf{e}_\alpha\delta t)] \quad (28)$$

2.2.2. Curved Boundary Treatment

If the solid walls are set in the computational domain, the interaction between the fluids and the solid walls can be described by imposing a specified contact angle at the solid boundary [28]:

$$\hat{\mathbf{n}}_w \cdot \nabla\phi|_{x_w} = \Theta\phi_w(1 - \phi_w) \quad (29)$$

where x_w is the position of a point on the solid boundary, $\hat{\mathbf{n}}_w$ is a unit vector normal to the solid boundary, with its direction pointing away from the solid wall, and ϕ_w is the phase field value of the point on the solid boundary. Θ is related to the equilibrium contact angle θ and is written as:

$$\Theta = -\sqrt{\frac{2\beta}{\kappa}} \cos\theta \quad (30)$$

As shown in Figure 1, the solid (black dots) is presented with a curved solid boundary (black solid line); then Equation (29) is modified to [20]:

$$\hat{\mathbf{n}}_w \cdot \nabla\phi|_{x_w} = \frac{\partial\phi}{\partial\mathbf{n}_w}|_{x_w} = \frac{\phi_m - \phi_{i,j}}{2h} = \Theta\phi_w(1 - \phi_w) \quad (31)$$

where ϕ_m is the phase field value of the interpolated point in the fluid (blue dots), and $h = |x_m - x_w|$ is the distance from the interpolated point to the solid boundary. ϕ_w is estimated by interpolation:

$$\phi_w = \frac{\phi_m + \phi_{i,j}}{2} \quad (32)$$

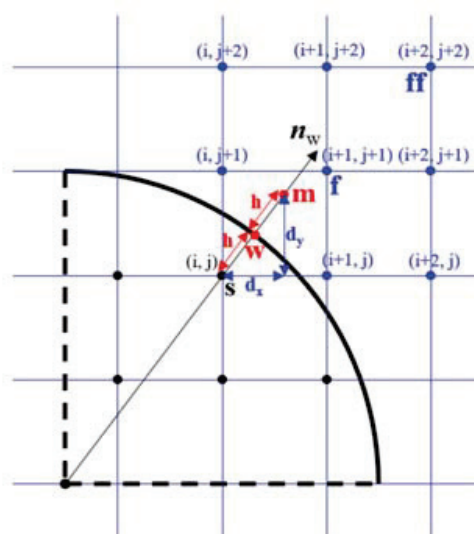


Figure 1. Schematic of curved boundary treatment.

Equation (31) can be solved by replacing ϕ_w with Equation (32):

$$\phi_{i,j} = \frac{1}{a} \left(1 + a - \sqrt{(1+a)^2 - 4a\phi_m} \right) - \phi_m \quad (33)$$

where

$$a = h\Theta = -h \sqrt{\frac{2\beta}{\kappa}} \cos \theta \neq 0 (\theta \neq 90^\circ) \quad (34)$$

As for the neutral wetting conditions ($\theta = 90^\circ$), Equation (31) has a trivial solution $\phi_{i,j} = \phi_m$. To find $\phi_{i,j}$ and impose the contact angle conditions on the solid boundary, ϕ_m is the only unknown parameter, which can be obtained by the bidirectional interpolation scheme by utilizing the phase field values of four nearby nodes, and the coordinate positions of nearby nodes are depicted in Figure 1. If the unknown $\phi_{i,j}$ is required for interpolation, it is replaced by the $\phi_{i,j}$ from the previous time step.

After specifying the wetting boundary conditions, the unknown incoming distribution functions from the solid boundary nodes towards the fluid nodes can be determined by referring to the model of Yu et al. [32]:

$$h_{\alpha^-}^*(\mathbf{x}_s) = h_{\alpha}^*(\mathbf{x}_f) \quad (35)$$

$$\bar{g}_{\alpha^-}^*(\mathbf{x}_s) = \frac{\Delta}{1+\Delta} [\bar{g}_{\alpha^-}^*(\mathbf{x}_f) + \bar{g}_{\alpha}^*(\mathbf{x}_f)] + \frac{1-\Delta}{1+\Delta} \bar{g}_{\alpha}^*(\mathbf{x}_{ff}) \quad (36)$$

where

$$\Delta = \frac{|\mathbf{x}_f - \mathbf{x}_w|}{|\mathbf{x}_f - \mathbf{x}_s|} \quad (37)$$

The subscript α^- denotes the incoming distribution functions, such that $e_{\alpha^-} = -e_{\alpha}$, and the superscript asterisk denotes the pre-streaming or post-collision state of the distribution functions.

3. Numerical Validation

3.1. Laplace Law

Laplace law states that the pressure difference between the inside and outside of a stationary bubble is proportional to the surface tension and inversely proportional to the bubble radius, which is often used to verify the numerical accuracy of the multiphase LB model [8,11,16,17]. The Laplace law for a two-dimensional bubble is written as:

$$\Delta p = p_{in} - p_{out} = \frac{\sigma}{R_b} \quad (38)$$

where R_b is the radius of the bubble. The computational domain of this verification is a square domain with 201×201 grids, and periodic boundary conditions are applied at its four boundaries. At the initial moment of the simulation, the center of the single bubble is located at (101,101), and the bubble is immersed in the liquid phase without any external force. The physical properties of the liquid and bubble are fixed as $\rho_l/\rho_g = 1000$ and $\mu_l/\mu_g = 100$. Zheng et al. [16] found that the simulation results were in better agreement with the analytical solutions and the spurious current was smaller when the interface thickness was greater than 4.5 lattice units (lu). Thus, the interface thickness is fixed to 6 lu in this Laplace-law test, and the bubble radius and surface tension are adjusted in the range of 10–50 lu and 0.01–0.1, respectively.

Figure 2a,b show the phase field contour of a bubble that has reached a stable state and the distribution curve of the phase field in the radial direction through the bubble, respectively. The analytical curve of the phase field distribution in Figure 2b is derived from the equilibrium phase field profile of diffuse-interface models:

$$\phi(\mathbf{x}) = \frac{1}{2} \left[1 - \tanh \left(\frac{|\mathbf{x} - \mathbf{x}_0|}{\xi/2} \right) \right] \quad (39)$$

where x_0 is the location of the bubble interface. By comparison, it can be seen that the numerical results are almost the same as the analytical solutions.

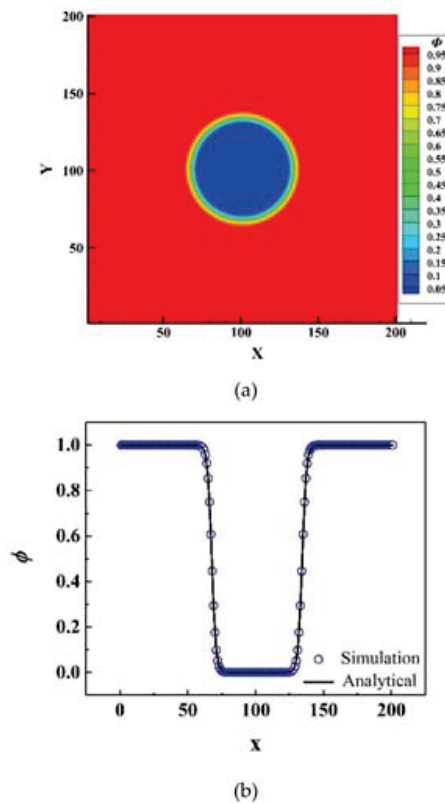


Figure 2. Phase field distribution contour (a) of the stable bubble and phase field distribution comparison in the radial direction (b) through the bubble.

The relationship between pressure difference, surface tension, and radius of the bubble is plotted in Figure 3, which is found to be highly consistent with Laplace law with deviations less than 3% and proves the accuracy of the current phase-field LB model quantitatively.

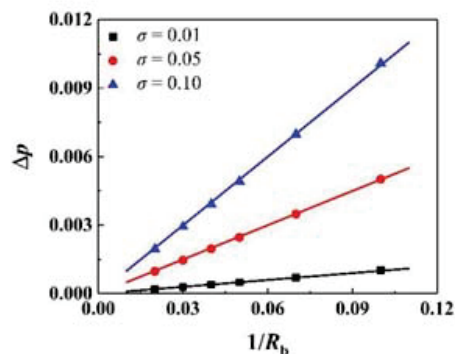


Figure 3. Relationship between pressure difference, surface tension, and radius of the bubble.

3.2. Bubble Deformation

The rising process of a single bubble under buoyancy action in a rectangular liquid-filled channel is often studied and used to test numerical models [33–36]. The single bubble will reach a relatively stable state with a constant rising velocity and terminal shape after rising for some time. In our simulations, a static circular bubble with a diameter $D_b = N_x/5$ is initially placed at $(N_x/2, N_y/4)$ in a

rectangular computational domain discretized with $N_x \times N_y = 512 \times 1536$ grid cells. A volumetric buoyancy force $F_b = (\rho - \rho_l)G_y\hat{y}$, where G_y is the magnitude of the gravitational acceleration and \hat{y} is a unit vector with a vertical downward direction, is continuously imposed on the bubble. The periodic boundary conditions are used at the left and right boundaries of the computational domain, while the bounce-back boundary schemes are applied at the top and bottom boundaries. The density and viscosity ratios of the liquid and bubble are fixed as $\rho_l/\rho_g = 1000$ and $\mu_l/\mu_g = 100$. Besides, there are several dimensionless parameters for characterizing bubble dynamics:

- (1) The gravity Reynolds number (Re_{Gr}),

$$Re_{Gr} = \frac{\sqrt{G_y \rho_l (\rho_l - \rho_g) D_b^3}}{\mu_l} \quad (40)$$

- (2) The Eötvös number (Eo),

$$Eo = \frac{G_y (\rho_l - \rho_g) D_b^2}{\sigma} \quad (41)$$





















- (3) The Morton number (Mo),

$$Mo = \frac{G_y (\rho_l - \rho_g) \mu_l^4}{\sigma^3 \rho_l^2} \quad (42)$$

- (4) The above three are not independent, since $Mo = Eo^3 / Re_{Gr}^4$.

Table 1 lists the terminal bubble shapes under different Re_{Gr} and Eo obtained by present LBM and other experimental or numerical methods [33–37]. By comparison, the terminal bubble shapes in our simulations can be observed to be highly similar to other research results, which achieves numerical stability under large liquid-to-gas density ratio conditions and demonstrates the qualitative accuracy of the current LB model.

Table 1. Comparison of terminal bubble shapes observed in experiments and predicted by front tracking method, previous and present LBMs.

Case	Re_{Gr}	Eo	Experiments (Bhaga and Weber, 1981) [37]	Front Tracking Method (Hua and Lou, 2007) [33]	LBM (Liang et al., 2019) [36]	Present LBM
A1	1.67	17.7				
A2	79.88	32.2				
A3	134.63	115				
A4	30.83	339				
A5	49.72	641				

During the bubble rising, the Reynolds number of the bubble $Re = u_g D_b \rho_l / \mu_l$ is continuously recorded. The comparison between the Re obtained from the present LBM and the experimental results is listed in Table 2. The acceptable relative errors further confirm the numerical accuracy of the phase-field LB model.

Table 2. Comparison of Re obtained from the present LBM and the experimental results.

Case	Re of Experiments [37]	Re of Present LBM	Relative Error (%)
A1	0.232	0.211	9.05
A2	55.3	47.8	13.56
A3	94.0	87.5	6.91
A4	18.3	16.4	10.38
A5	30.3	27.5	9.24

4. Numerical Results and Discussion

4.1. Channel Construction and Numerical Initialization

Figure 4 shows the schematics of two computational domains in 2D Cartesian systems for the bubble rising problem in complex channels, in which the lateral boundaries are set as periodic boundaries, while the bounce-back boundary schemes are adopted at the top and bottom. Among them, the blue circular areas represent the gas bubbles, the red areas are the liquid that fills the channels and surrounds the bubbles, and the white circular and semicircular areas are the artificially constructed bounce-back domains, which are referred to as solid particles and not involved in the iterative computations of phase field and hydrodynamic properties.

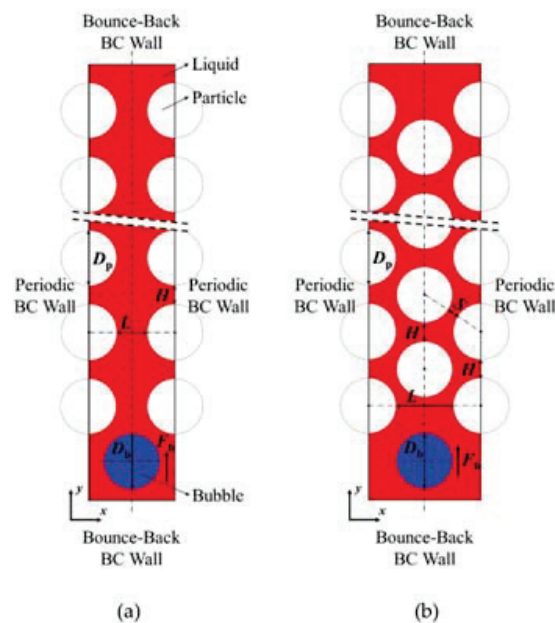


Figure 4. Schematics of wavy vertical channel (a) and S-shaped curved channel (b).

As depicted in Figure 4, two types of symmetric channels are formed by arranging the solid particles in rectangular and triangular matrices, and they are named wavy vertical channel and S-shaped curved channel, respectively. D_b and D_p marked in the figures are the bubble and particle diameters, the horizontal spacing L of the particles refers to the shortest distance between two horizontally adjacent particles and similarly the vertical spacing H is the shortest distance between two vertically adjacent particles, and S represents the shortest distance between two diagonally adjacent particles. Hereinafter we use the particle spacing normalized by the bubble diameter to characterize the channel width.

Initially, a static and stable circular bubble is placed in the middle of the channel and submerged in the liquid with a diameter D_b and a volumetric buoyancy force $F_b = (\rho - \rho_l)G_y \hat{y}$. The phase field in the solid particles is fixed to 0, and in other computational domains the phase field is initialized by the following hyperbolic tangent profile:

$$\phi(x) = \frac{1}{2} \left[1 + \tanh \left(\frac{R(x) - R_0}{\xi/2} \right) \right] \quad (43)$$

where R_0 is the initial bubble radius and represents the position of the gas-liquid interface in the radial direction of the bubble, and $R(x)$ is the distance from any position x in the flow domains to the center of the bubble. Unless otherwise specified, in the following simulations, the initial bubble diameter and particle diameter are set as $D_b = D_p = 51$ lu. The density and viscosity ratios of the liquid and gas are fixed to $\rho_l/\rho_g = 1000$ and $\mu_l/\mu_g = 100$, respectively. Taking into account the balance of numerical stability and accuracy at large density ratios [22], the mobility and interface thickness are taken as $M = 0.03$ and $\xi = 5$ lu in the present simulations, respectively. As for the wetting properties, the contact angle of gas-liquid interface on particle surfaces is specified as 40° .

After initialization, the bubble rises through the channel under the action of buoyancy, and simultaneously undergoes a series of evolutions such as deformation, fragmentation, and coalescence. During these processes, as an important dimensionless parameter related to the bubble dynamics, the drag coefficient (C_D) is constantly monitored:

$$C_D = \frac{4G_y(\rho_l - \rho_g)D_b}{3\rho_l u_g^2} \quad (44)$$

where u_g is the average velocity of bubbles rising, which is obtained by averaging the instantaneous y -direction velocities over all gas-phase nodes ($\rho < (\rho_l + \rho_g)/2$).

4.2. Grid Independence

The channel structure and the effect of the channel on the bubble are greatly affected by the grid, so the case of the bubble rising in a rectangular channel without particles at $Re_{Gr} = 100$ and $EO = 20$ is selected for testing the grid independence. Five different grids with $N_x \times N_y = 96 \times 1536$, 128×1536 , 176×1536 , 256×1536 and 512×1536 grid cells are applied in the bubble rising problem, respectively. The number of grid cells in the y -direction is sufficiently large and constant because its influence on the bubble steady velocity is negligible. The rising velocity variation of the bubble with $D_b = N_x/5$ over the dimensionless time is present in Figure 5, and the gravity-based dimensionless time is defined as $t^* = t \sqrt{G_y/D_b}$. It can be observed that when the grid cells are less than 176×1536 , the bubble terminal velocity is unstable, and the calculation deviation is unacceptable. Thus, the minimum number of grid cells used in the following simulations is set to 176×1536 .

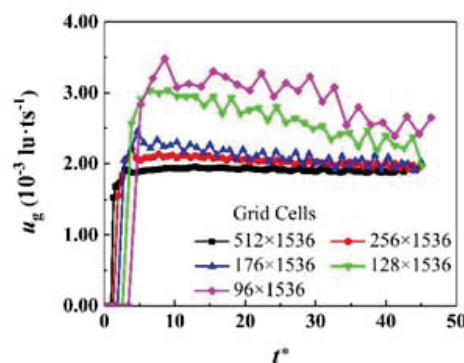


Figure 5. Variations of the bubble rising velocity with dimensionless time using five different grids.

According to the grid independence test results, considering that the channel width is one of the investigated variables affecting the bubble movement, the two computational domains of wavy and S-shaped channels are discretized using 176×1536 to 512×1536 and 192×1536 to 512×1536 grid cells, respectively.

4.3. Mass Conservation

In order to verify the mass conservation of the current model, the evolution of the total system mass versus the dimensionless time is recorded in Figure 6 during a numerical simulation of bubble rising in a wavy vertical channel with $L/D_b = 0.719$ and $H/D_b = 0.875$ at $Re_{Gr} = 100$ and $Eu = 20$. It is observed that the variation of the normalized total system mass M/M_0 is much less than 10^{-6} over a long period of time, indicating that the mass of the gas-liquid two-phase system is conserved well using current phase-field LB model.

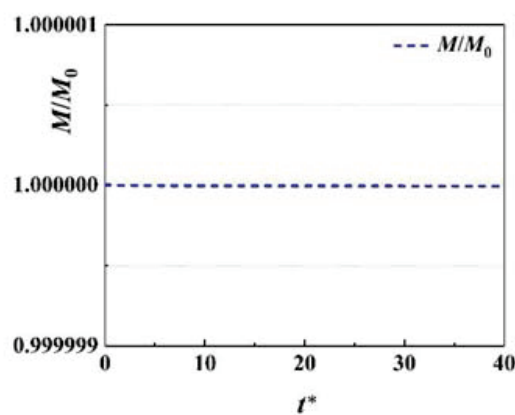


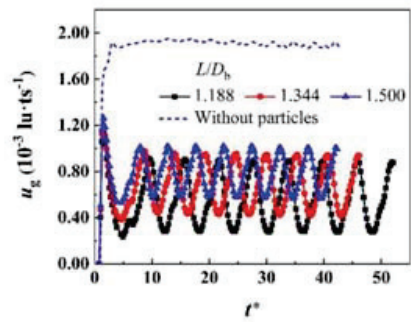
Figure 6. Variation of the normalized total system mass with dimensionless time.

4.4. Channel Width Effect

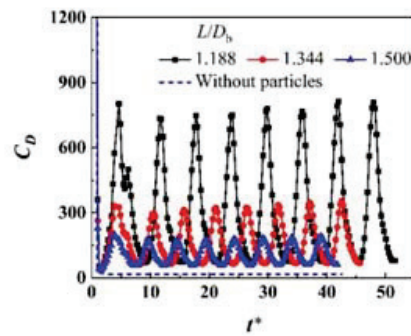
Undoubtedly, one of the variables that has the most obvious impact on bubble movement in the aforementioned channels is the channel width.

Figure 7 shows the evolution curves of bubbles rising velocity and drag coefficient versus the dimensionless time at $Re_{Gr} = 100$ and $Eu = 20$. In the wavy vertical channel, the bubble is prone to a stabilized state with a periodically fluctuating terminal velocity, along with C_D fluctuating within the certain ranges. In Figure 7, compared with the channel without particles, the rising velocity of the bubble is lower, and the drag coefficient is larger in the channel when the particles are arranged, which indicates that the presence of particles has a significant hindrance to the movement of the bubble.

u_g and C_D under different channel widths are given in Figure 8, which are calculated by averaging the regularly fluctuating u_g and C_D over a certain period of time in Figure 7. C_D is found to be lower as the channel width becomes wider, and the bubble rises faster. The same results are observed by Patel et al. [38] in the studies on the effects of the amplitude of the sinusoidal channel walls on bubble dynamics. In addition, the horizontal spacing between particles has a more severe impact on the bubble movement than the vertical spacing of the particles. Because the horizontal spacing of the particles directly affects the interaction between the bubble and the particles, and determines the difficulty for the bubble to pass through each gap, while the vertical spacing affects the fluctuation frequency of the bubble drag force, which can only indirectly act on the drag force. In view of this, unless otherwise stated, the following numerical results are obtained from the simulations in the channels with $H/D_b = 0.875$.

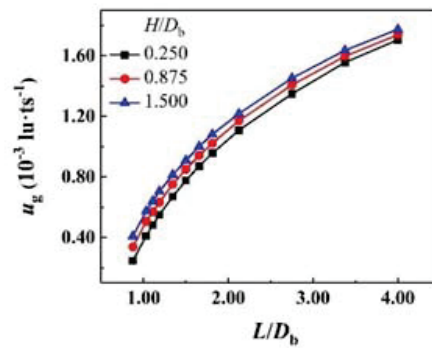


(a)

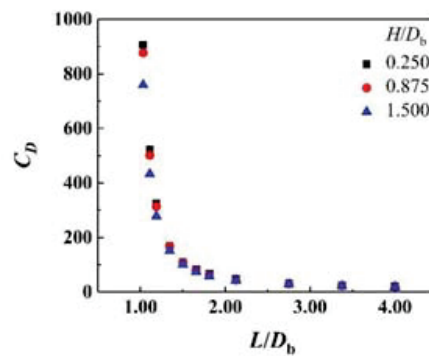


(b)

Figure 7. Variations of u_g (a) and C_D (b) with dimensionless time at $Re_{Gr} = 100$ and $Eo = 20$.



(a)



(b)

Figure 8. Variations of u_g (a) and C_D (b) with channel width at $Re_{Gr} = 100$ and $Eo = 20$.

4.5. Surface Tension Effect

Surface tension is an important parameter to characterize the deformation properties of the gas-liquid interface. As for the bubble, a large surface tension means that the bubble is not easy to deform and break. In our study, since the total bubble mass is well conserved, we count the ratio of the total length of the gas-liquid interface to the area occupied by the bubble to measure the deformation rate of the bubble. As shown in Figure 9, the bubble deformation rate is proved to reduce with the increase of surface tension, which confirms that the bubble with large surface tension tends to maintain its original shape and resist deformation.

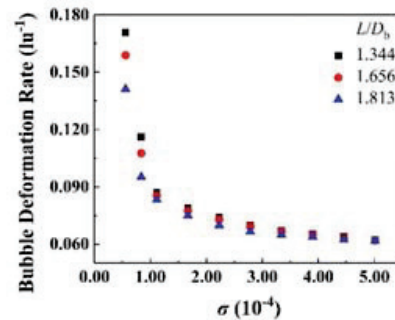


Figure 9. Variation of bubble deformation rate with surface tension at $Re_{Gr} = 100$ and $Eo = 20$.

Furthermore, the declining u_g and ascending C_D are observed in Figure 10 when the surface tension is gradually increasing. This is because the bubble resists deformation more strongly when colliding with the particles, which restricts the bubble rising velocity. In contrast, the bubble with smaller surface tension is more likely to pass through the narrow gaps in the channel by deforming or even breaking. This phenomenon is consistent with the numerical results of Patel et al. [38], and similar to the studies on the effect of surface tension on liquid penetration by Shi et al. [39].

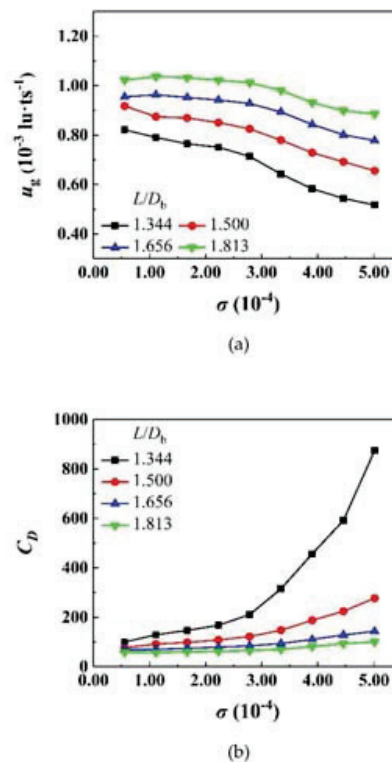


Figure 10. Variations of u_g (a) and C_D (b) with surface tension at $Re_{Gr} = 100$ and $Eo = 20$.

4.6. Bubble Diameter Effect

The effects of bubble diameter on bubble dynamics are depicted in Figure 11. The bubble diameter in this part is not equivalent to the particle diameter; it varies in the range of 25–204 μm , but the particle diameter is still fixed at 51 μm . Figure 11a indicates that it is more difficult for a bubble with larger diameter to pass through the channel due to the greater blocking effects of the particles, so the bubble rising velocity is slowed down, resulting in the ascent of drag coefficient, as demonstrated in Figure 11b.

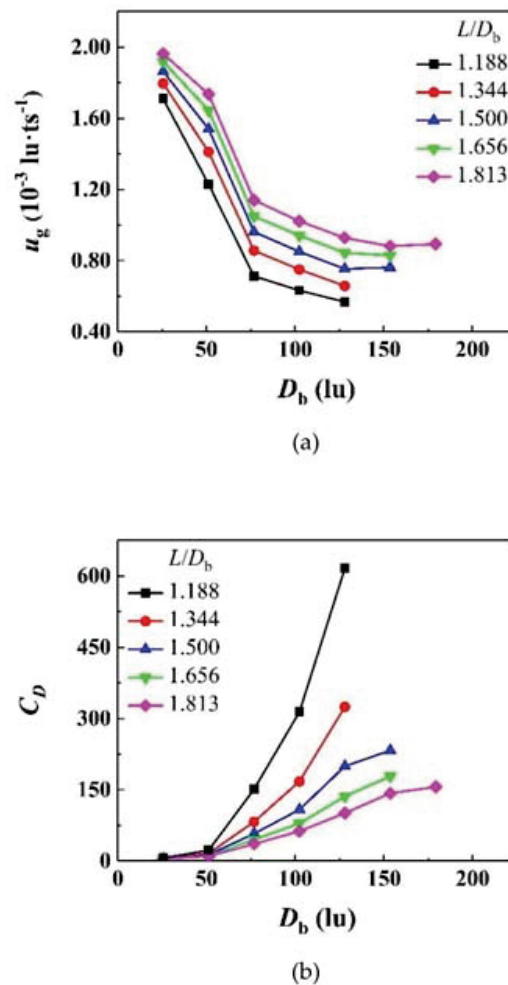


Figure 11. Variations of u_g (a) and C_D (b) with bubble diameter at $Re_{Gr} = 100$ and $Eo = 20$.

4.7. Driving Force Effect

An additional driving force source term F_d can be added to the right side of the governing Equation (4) to simulate the changes in the pressure difference of the packed bed in the actual industry. Here we use the dimensionless ratio $F_d/(G_y \cdot \rho_l)$ to measure the magnitude of the driving force.

As illustrated in Figure 12, when the incremental additional driving forces are imposed on the bubble based on the presence of buoyancy force, u_g increases linearly while C_D decreases rapidly. Because the additional driving force pushes the bubble to pass through the channel faster and more smoothly, the rising velocity is significantly increased, so that u_g increases and C_D decreases.

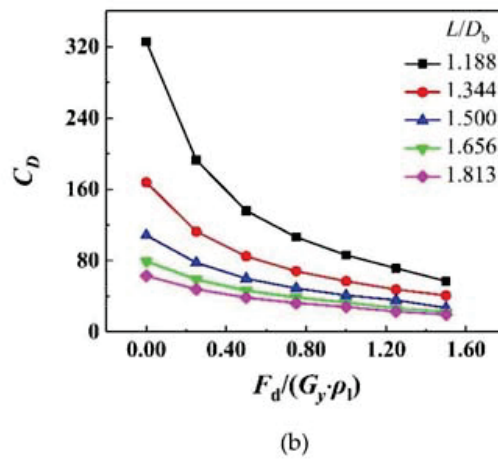
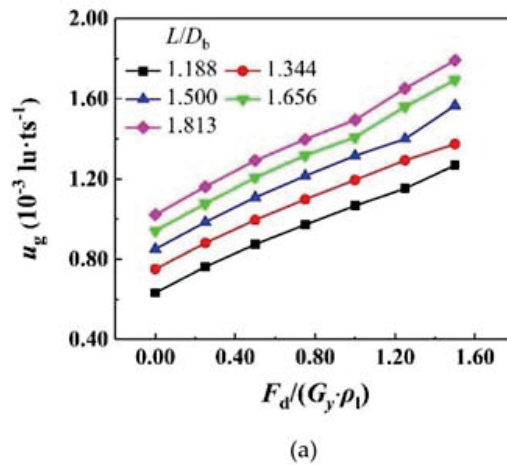


Figure 12. Variations of u_g (a) and C_D (b) with additional driving force at $Re_{Gr} = 100$ and $Eo = 20$.

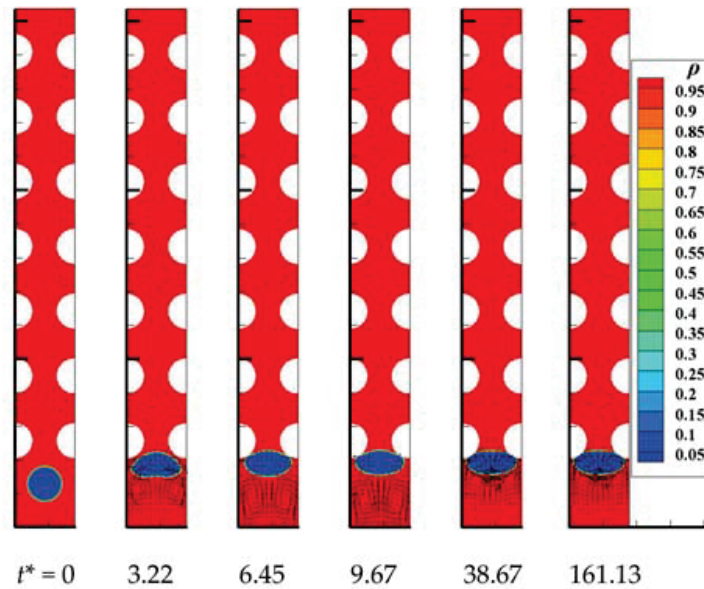
4.8. Bubble Flow Pattern

During the numerical simulations, we found that the fluid properties and operating conditions set in the numerical initializations have significant impacts on the evolutions of the bubble. In order to classify the different bubble evolution processes, the gravity Reynolds number and Eötvös number that include fluid property and operating condition parameters are used as the classification criteria.

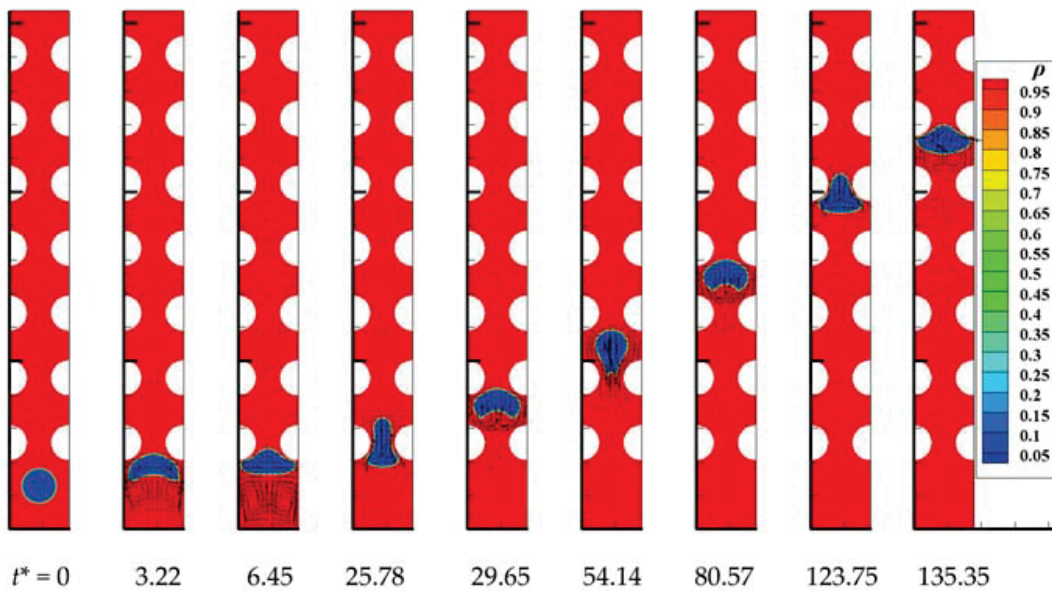
For the wavy vertical channel, mainly four types of bubble flow patterns are identified, and their detailed bubble evolution diagrams are listed in Figure 13. The four flow patterns are named Aw, Bw, Cw, and Dw, respectively; their subscript “w” represents the wavy vertical channel, and the capital letters are used to distinguish different flow patterns.

By observing Figure 13, the flow pattern Aw describes that the bubble is completely blocked by the two particles at the entrance of the channel, and even cannot enter the channel. It is inferred from the small Eo that the bubble surface tension in this flow pattern is relatively large, which makes it difficult for the bubble to enter the channel through deformation when encountering obstacles. In contrast, the bubble in the flow pattern Bw will become elongated when it flows into the narrow gaps thanks to the reduced surface tension, thus passing through the channel integrally. In flow pattern Cw, whenever the bubble crosses the gaps and collides with the particles, some secondary bubbles are split from the tail of the parent bubble. Then these secondary bubbles will gradually merge and expand following the parent bubble, and the coalesced secondary bubble with smaller rising resistance will catch up with and merge into the parent bubble finally. As for the flow pattern Dw, compared to

the flow pattern Cw, more secondary bubbles are generated after the parent bubble interacts with the particles due to the extremely small surface tension, and the parent bubble will eventually be split into multiple secondary bubbles and dispersed in the liquid. As a summary, a lower Eo leads to a steady rise of the bubble, while a higher Eo instigates the dynamics instability and causes a multiple breakup in the form of secondary bubbles, which is in good agreement with the numerical results of Patel et al. [38] on bubble dynamics in sinusoidal channels using the level set method.



(a) Flow pattern Aw ($Re_{Cr} = 100, Eo = 10$)



(b) Flow pattern Bw ($Re_{Cr} = 100, Eo = 20$)

Figure 13. Cont.

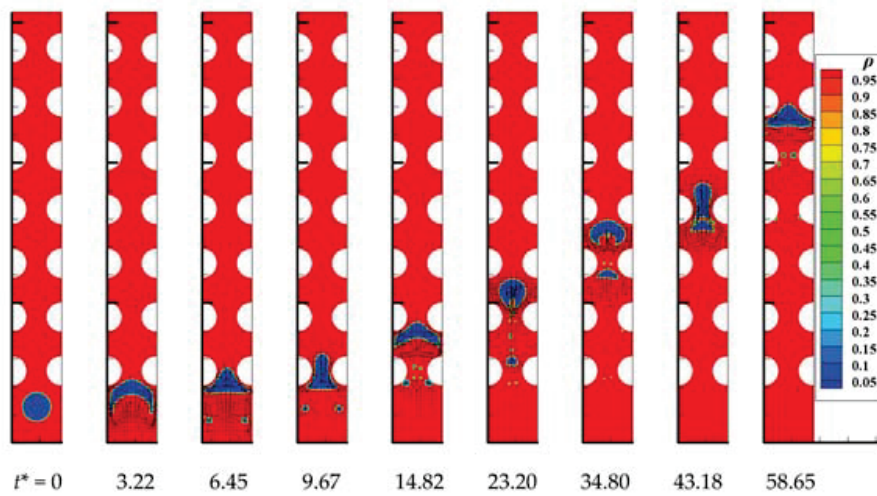
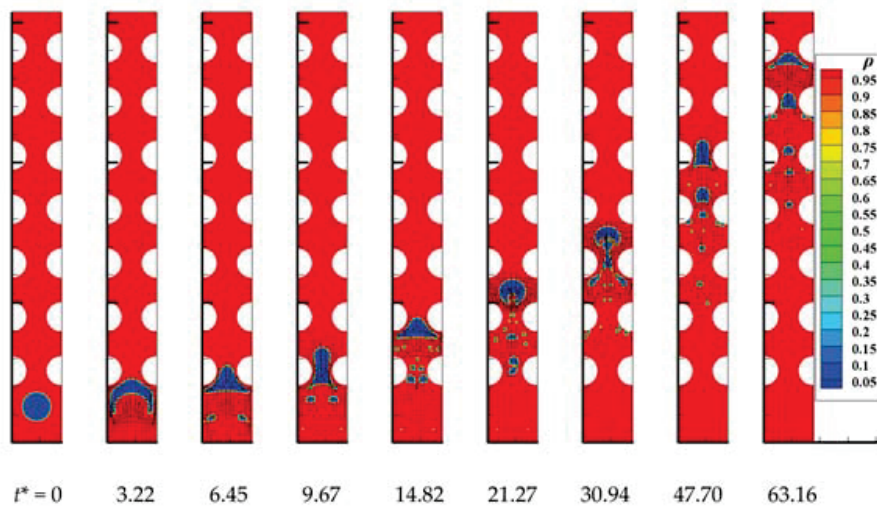
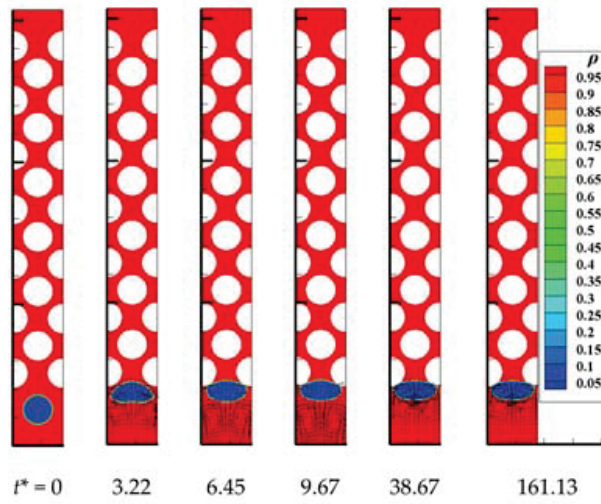
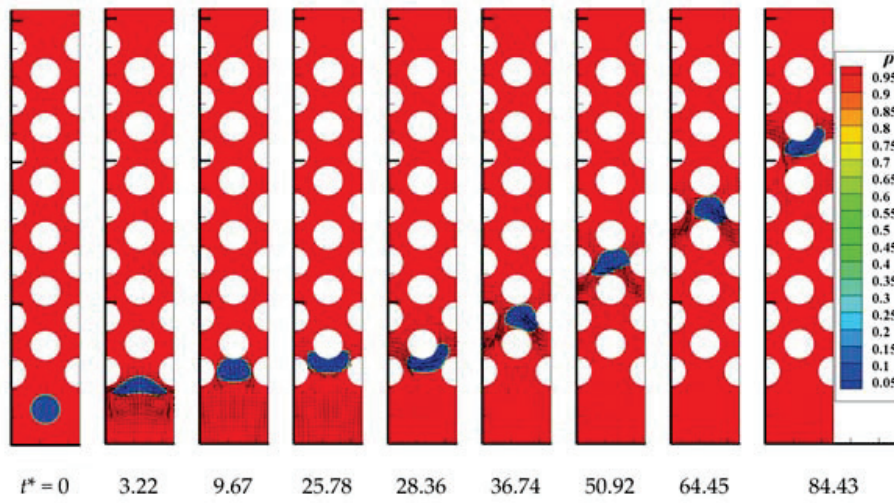
(c) Flow pattern Cw ($Re_{Gr} = 100$, $Eo = 60$)(d) Flow pattern Dw ($Re_{Gr} = 100$, $Eo = 120$)

Figure 13. Bubble evolution diagrams of flow patterns Aw (a), Bw (b), Cw (c), and Dw (d) in the wavy vertical channel with $L/D_b = 0.719$.

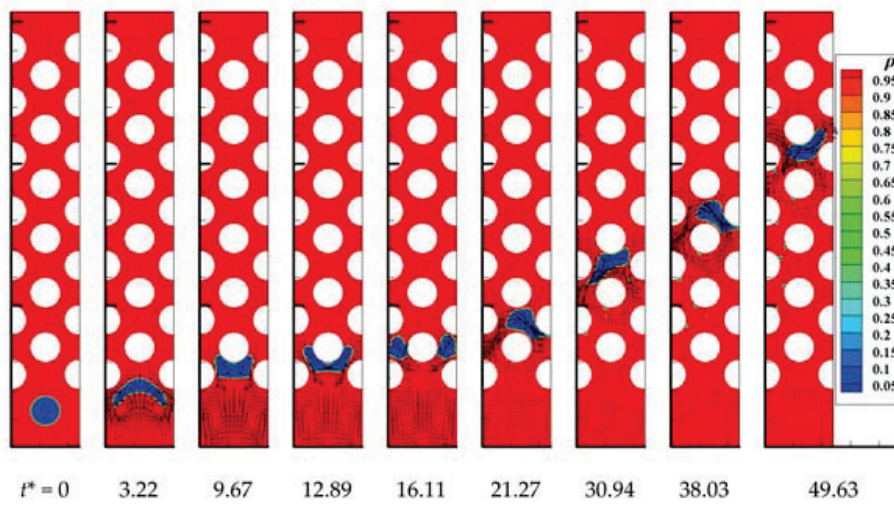
For the S-shaped curved channel, according to different bubble evolutions, five flow patterns As, Bs, Cs, Ds, and Es are distinguished, as illustrated in Figure 14. Among them, flow pattern As is described as the bubble cannot enter and pass through the channel due to the obstruction of the narrow channel. In flow pattern Bs, the bubble enters the channel by being squeezed and elongated, and it shuttles left and right to rise through the channel. For flow patterns As and Bs, the bubbles retain good integrity because of the higher surface tension. As for the flow pattern Cs, the bubble first splits into two after colliding with the particle, and then the two secondary bubbles will coalesce under their interaction. In another case, the two separated secondary bubbles will rise simultaneously with negligible mutual interference due to their far distance, which is named flow pattern Es. Similar to the flow pattern Dw, the bubble in flow pattern Ds is gradually broken into multiple small secondary bubbles and they are dispersed in the liquid phase, continuously breaking and coalescing. It is worth mentioning that the bubbles in the flow patterns Dw and Ds have better dispersibility and higher specific surface area, which are more conducive to gas-liquid mixing and mass transfer in actual industrial production.



(a) Flow pattern As ($Re_{Cr} = 100$, $Eo = 10$, $L/D_b = 0.719$)



(b) Flow pattern Bs ($Re_{Cr} = 120$, $Eo = 10$, $L/D_b = 1.344$)



(c) Flow pattern Cs ($Re_{Cr} = 140$, $Eo = 30$, $L/D_b = 1.344$)

Figure 14. Cont.

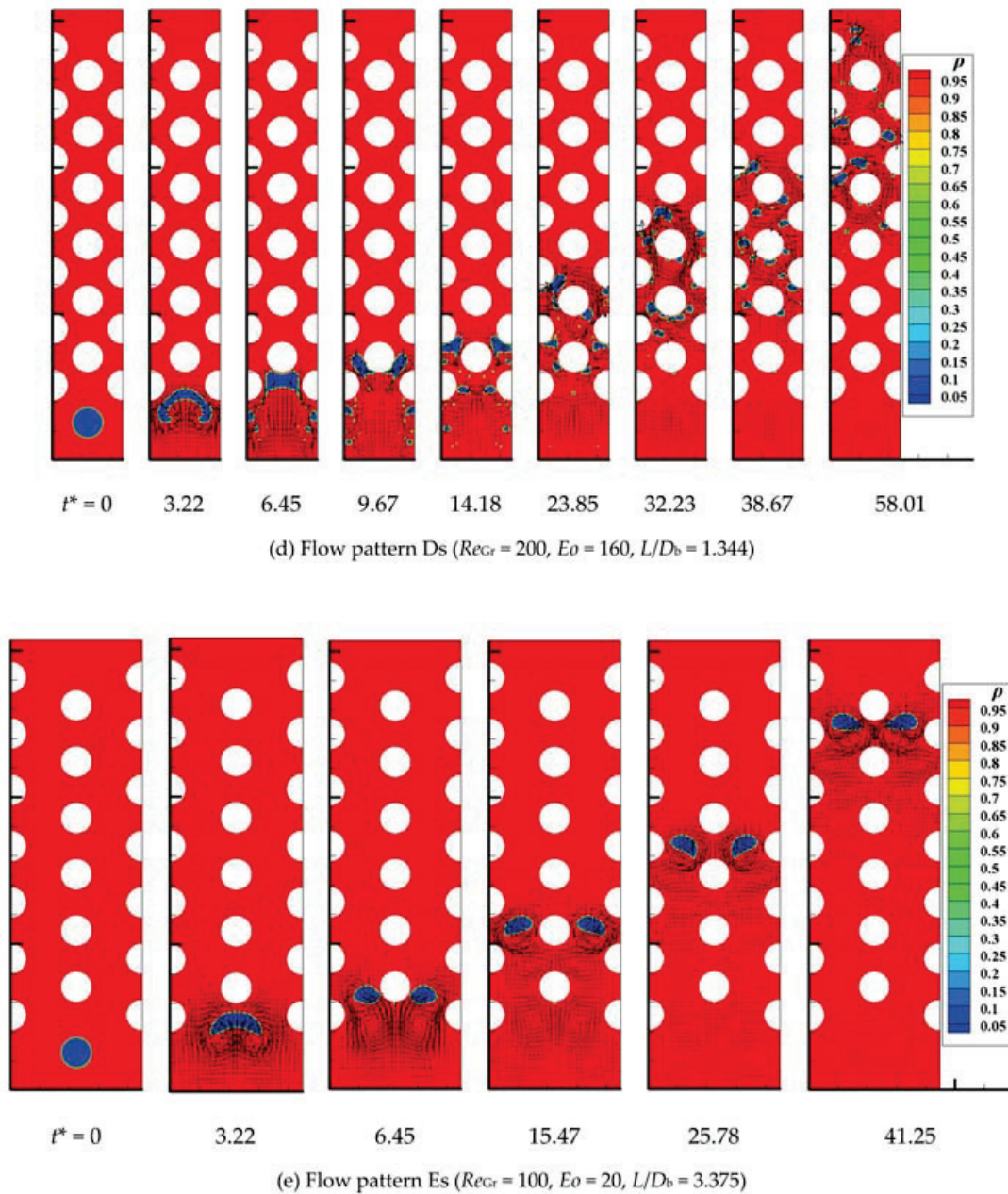


Figure 14. Bubble evolution diagrams of flow patterns As (a), Bs (b), Cs (c), Ds (d), and Es (e) in the S-shaped curved channel.

In our studies, multiple sets of simulations have been executed within the Re_{Gr} range of 0–350 and Eo range of 0–250. Figure 15 depicts the divisions of flow patterns while changing Re_{Gr} and Eo with fixed channel widths $L/D_b = 0.719$ and $H/D_b = 0.875$ in the wavy vertical channel and $L/D_b = 1.344$ and $H/D_b = 0.875$ in the S-shaped curved channel. Eo is found to have more significant effects on the flow patterns compared to Re_{Gr} , and lower Eo numbers often correspond to the bubbles with higher integrity because the surface tension that is related to Eo number plays a leading role in bubble deformation. In the S-shaped channel, the flow pattern Ds occupies a wider range than the flow pattern Dw in the wavy channel, indicating that the bubbles are more likely to reach the state of fragmentation and dispersion because of more frequent collisions with particles.

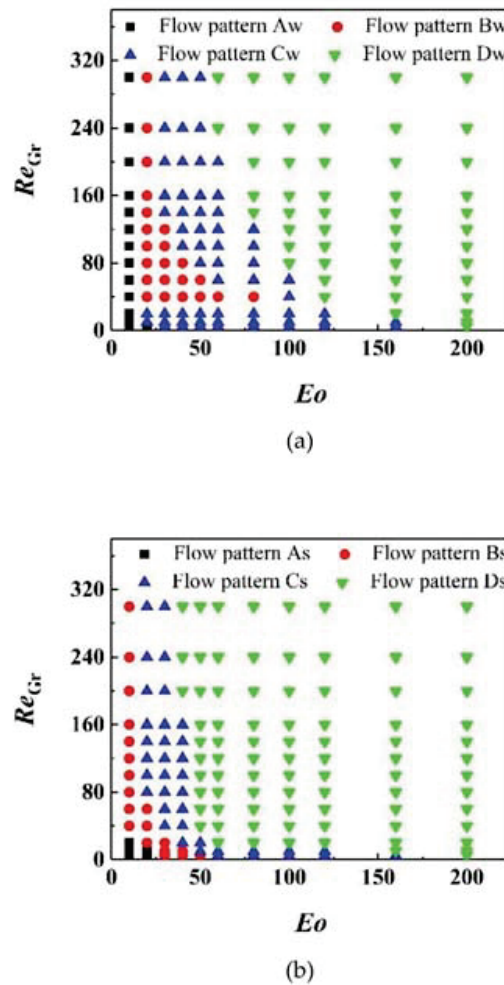


Figure 15. Flow pattern divisions according to Re_{Gr} and Eo in the wavy vertical channel (a) and S-shaped curved channel (b).

It is worth reminding that the trend of the boundaries between different flow patterns in an S-shaped curved channel is similar to the shape regime curve of the single bubble under gravitational motion in the work of Clift et al. [40].

It can be qualitatively summarized from Figure 15 that the bubble becomes more broken and dispersed as Re_{Gr} and Eo increase, and this is attributed to the changes in liquid viscosity and bubble surface tension that have significant impacts on the gas-liquid interface. The increase of Re_{Gr} and Eo leads to the reduction of liquid viscosity and surface tension, respectively. The reduced liquid viscosity causes the weakening of the viscous effects, which results in the increase of bubble wobbling [38], and the lowered surface tension further promotes bubble deformation and breakup.

In addition to the Re_{Gr} and Eo , channel width also has an important influence on the bubble flow patterns. The flow pattern divisions according to the channel widths of two types of channels are demonstrated in Figure 16. The horizontal spacing between particles is found to have more obvious impacts on the flow of bubbles compared to the vertical spacing. The horizontal spacing of the particles directly affects the interaction between the bubble and the particles, thereby affecting the bubble shapes and flow patterns.

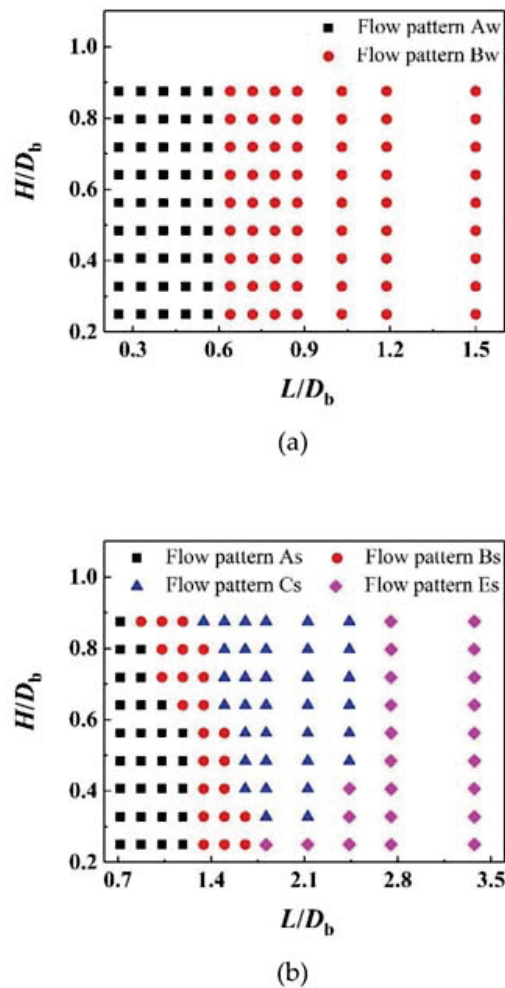


Figure 16. Flow pattern divisions according to the channel widths of the wavy vertical channel (a) and S-shaped curved channel (b) at $Re_{Gr} = 100$ and $Eo = 20$.

On the other hand, in the wavy channel, the changes in channel width do not contribute much to the transitions of bubble flow patterns while maintaining the same Re_{Gr} and Eo . Conversely, in the relatively complex S-shaped channel, the transitions of the flow patterns are more sensitive to the variations of channel width; four different flow patterns are revealed by changing the channel width. Under this Re_{Gr} and Eo condition, the flow pattern Cs is more conducive to the even distribution of the dispersed phase in practice because too-small channel width is not prone to the disintegration and flow of the dispersed phase, and too large channel width reduces the contact between the dispersed phase and the particles.

5. Conclusions

In this paper, the numerical studies on two-dimensional bubble rising in complex channels saturated with liquid at large density ratios within a wide range of gravity Reynolds numbers and Eötvös numbers have been implemented using phase-field LB model. The main research conclusions of this work are as follows:

- (1) The present LB model is tested through three aspects of Laplace law, bubble deformation, and mass conservation, and it has been proven to have good stability, accuracy, and conservation from both qualitative and quantitative perspectives.

- (2) In the simulations of bubble rising in complex channels, the effects of channel width, surface tension, bubble diameter and additional driving force on bubble motion are investigated in detail. The larger channel width and additional driving force as well as smaller bubble diameter and surface tension lead to lower drag coefficients, which are conducive to smooth passage through the channels for the bubble.
- (3) Four and five types of bubble flow patterns are divided according to different bubble evolution processes under different Re_{Gr} , Eo and channel structures conditions in the wavy vertical channel and S-shaped curved channel, respectively. The detailed flow pattern diagrams are drawn for flow pattern recognition. To some extent, this study has some guiding significance for the regulation of bubble flow patterns in the industrial packed beds.

Author Contributions: Conceptualization, Y.Y.; methodology, K.Y.; program execution, K.Y.; validation, K.Y.; investigation, K.Y. and Y.Y.; data curation, K.Y. and Y.Y.; writing—original draft preparation, K.Y.; writing—review and editing, K.Y., Y.Y. and C.Y.; visualization, K.Y.; supervision, Y.Y. and C.Y.; funding acquisition, C.Y. All authors have read and agreed to the published version of the manuscript.

Funding: This work was supported by the National Key Research and Development Program (2019YFC1904204), National Natural Science Foundation of China (21776283, 91934301, 21961160745), External Cooperation Program of BIC, Chinese Academy of Sciences (122111KYSB20190032), and DNL Cooperation Fund, CAS (DNL201902).

Conflicts of Interest: The authors declare no conflict of interest.

Abbreviations

Symbols

c_s	Lattice sound speed
C_D	Drag coefficient
D_b	Bubble diameter
D_p	Particle diameter
e_α	Lattice-related mesoscopic velocity set
E_f	Volumetric free energy
Eo	Eötvös number
F_α	Forcing term of the hydrodynamic LBE
F_b	Body force
F_d	Additional driving force
F_s	Surface tension force
$\bar{g}_\alpha^{\text{eq}}$	Equilibrium hydrodynamic distribution function
\bar{g}_α	Modified hydrodynamic distribution function
$\bar{g}_\alpha^{\text{eq}}$	Modified equilibrium hydrodynamic distribution function
G_y	Gravitational acceleration
h_α	Phase-field distribution function
h_α^{eq}	Equilibrium phase-field distribution function
H	Vertical spacing between two vertically adjacent particles
L	Horizontal spacing between two horizontally adjacent particles
M	Mobility
\mathbf{M}	Orthogonal transformation matrix
M	Total mass of the gas-liquid system
M_0	Initial total mass of the gas-liquid system
Mo	Morton number
\hat{n}	Unit vector normal to the gas-liquid interface
\hat{n}_w	Unit vector normal to the solid boundary
p	Macroscopic pressure
Δp	Pressure difference between inside and outside the bubble
R_b	Bubble radius

Re	Reynolds number of the rising bubble
Re_{Gr}	Gravity Reynolds number
S	Shortest spacing between two diagonally adjacent particles
\hat{S}	Diagonal relaxation matrix
t	Time
t^*	Gravity-based dimensionless time
u	Macroscopic velocity vector
u_g	Bubble rising velocity
w_α	Lattice-related weight coefficient set
x	Coordinates of the lattice nodes
x_w	Position of the point on the solid boundary
\hat{y}	Unit vector with a vertical downward direction
δt	Unit time
δx	Unit lattice length
ξ	Interface thickness
μ	Fluid mixed viscosity
μ_g	Gas viscosity
μ_l	Liquid viscosity
μ_ϕ	Chemical potential
ϕ	Phase-field variable
ϕ_m	Phase field value of the interpolated point
ϕ_w	Phase field value of the point on the solid boundary
ρ	Fluid mixed density
ρ_g	Gas density
ρ_l	Liquid density
σ	Surface tension
τ	Hydrodynamic relaxation time
τ_ϕ	Phase-field relaxation time
θ	Contact angle
Ω_α	Collision operator of the hydrodynamic LBE
$\Psi(\phi)$	Bulk free energy

References

1. Tailleur, R.G.; Hernandez, J.; Rojas, A. Selective hydrogenation of olefins with mass transfer control in a structured packed bed reactor. *Fuel* **2008**, *87*, 3694–3705. [[CrossRef](#)]
2. Yuan, R.; He, Z.; Zhang, Y.; Wang, W.; Chen, C.; Wu, H.; Zhan, Z. Partial oxidation of methane to syngas in a packed bed catalyst membrane reactor. *AIChE J.* **2016**, *62*, 2170–2176. [[CrossRef](#)]
3. Miladinovic, N.; Weatherley, L.R. Intensification of ammonia removal in a combined ion-exchange and nitrification column. *Chem. Eng. J.* **2008**, *135*, 15–24. [[CrossRef](#)]
4. Huggins, T.M.; Haeger, A.; Biffinger, J.C.; Ren, Z.J. Granular biochar compared with activated carbon for wastewater treatment and resource recovery. *Water Res.* **2016**, *94*, 225–232. [[CrossRef](#)]
5. Li, Q.; Luo, K.H.; Kang, Q.J.; He, Y.L.; Chen, Q.; Liu, Q. Lattice Boltzmann methods for multiphase flow and phase-change heat transfer. *Prog. Energy Combust. Sci.* **2016**, *52*, 62–105. [[CrossRef](#)]
6. Gunstensen, A.K.; Rothman, D.H.; Zaleski, S.; Zanetti, G. Lattice Boltzmann model of immiscible fluids. *Phys. Rev. A* **1991**, *43*, 4320–4327. [[CrossRef](#)] [[PubMed](#)]
7. Shan, X.; Chen, H. Lattice Boltzmann model for simulating flows with multiple phases and components. *Phys. Rev. E* **1993**, *47*, 1815–1819. [[CrossRef](#)]
8. Swift, M.R.; Osborn, W.R.; Yeomans, J.M. Lattice Boltzmann simulation of nonideal fluids. *Phys. Rev. Lett.* **1995**, *75*, 830–833. [[CrossRef](#)]
9. He, X.; Chen, S.; Zhang, R. A lattice Boltzmann scheme for incompressible multiphase flow and its application in simulation of Rayleigh-Taylor instability. *J. Comput. Phys.* **1999**, *152*, 642–663. [[CrossRef](#)]
10. Inamuro, T.; Ogata, T.; Tajima, S.; Konishi, N. A lattice Boltzmann method for incompressible two-phase flows with large density differences. *J. Comput. Phys.* **2004**, *198*, 628–644. [[CrossRef](#)]

11. Lee, T.; Lin, C.L. A stable discretization of the lattice Boltzmann equation for simulation of incompressible two-phase flows at high density ratio. *J. Comput. Phys.* **2005**, *206*, 16–47. [[CrossRef](#)]
12. Lee, T.; Liu, L. Lattice Boltzmann simulations of micron-scale drop impact on dry surfaces. *J. Comput. Phys.* **2010**, *229*, 8045–8063. [[CrossRef](#)]
13. Cahn, J.W.; Hilliard, J.E. Free energy of a nonuniform system. I. Interfacial free energy. *J. Chem. Phys.* **1958**, *28*, 258–267.
14. Chiappini, D.; Bella, G.; Succi, S.; Toschi, F.; Ubertini, S. Improved lattice Boltzmann without parasitic currents for Rayleigh–Taylor instability. *Commun. Comput. Phys.* **2010**, *7*, 423–444. [[CrossRef](#)]
15. Guo, Z.; Zheng, C.; Shi, B. Force imbalance in lattice Boltzmann equation for two-phase flows. *Phys. Rev. E* **2011**, *83*, 036707. [[CrossRef](#)]
16. Zheng, H.W.; Shu, C.; Chew, Y.T. A lattice Boltzmann model for multiphase flows with large density ratio. *J. Comput. Phys.* **2006**, *218*, 353–371. [[CrossRef](#)]
17. Fakhari, A.; Rahimian, M.H. Phase-field modeling by the method of lattice Boltzmann equations. *Phys. Rev. E* **2010**, *81*, 036707. [[CrossRef](#)]
18. Fakhari, A.; Lee, T. Finite-difference lattice Boltzmann method with a block-structured adaptive-mesh-refinement technique. *Phys. Rev. E* **2014**, *89*, 033310. [[CrossRef](#)]
19. Fakhari, A.; Geier, M.; Lee, T. A mass-conserving lattice Boltzmann method with dynamic grid refinement for immiscible two-phase flows. *J. Comput. Phys.* **2016**, *315*, 434–457. [[CrossRef](#)]
20. Fakhari, A.; Bolster, D. Diffuse interface modeling of three-phase contact line dynamics on curved boundaries: A lattice Boltzmann model for large density and viscosity ratios. *J. Comput. Phys.* **2017**, *334*, 620–638. [[CrossRef](#)]
21. Fakhari, A.; Mitchell, T.; Leonardi, C.; Bolster, D. Improved locality of the phase-field lattice-Boltzmann model for immiscible fluids at high density ratios. *Phys. Rev. E* **2017**, *96*, 053301. [[CrossRef](#)] [[PubMed](#)]
22. Fakhari, A.; Bolster, D.; Luo, L.S. A weighted multiple-relaxation-time lattice Boltzmann method for multiphase flows and its application to partial coalescence cascades. *J. Comput. Phys.* **2017**, *341*, 22–43. [[CrossRef](#)]
23. Fakhari, A.; Li, Y.; Bolster, D.; Christensen, K.T. A phase-field lattice Boltzmann model for simulating multiphase flows in porous media: Application and comparison to experiments of CO₂ sequestration at pore scale. *Adv. Water Resour.* **2018**, *114*, 119–134. [[CrossRef](#)]
24. Mitchell, T.; Leonardi, C.; Fakhari, A. Development of a three-dimensional phase-field lattice Boltzmann method for the study of immiscible fluids at high density ratios. *Int. J. Multiph. Flow* **2018**, *107*, 1–15. [[CrossRef](#)]
25. Magaletti, F.; Picano, F.; Chinappi, M.; Marino, L.; Casciola, C.M. The sharp-interface limit of the Cahn–Hilliard/Navier–Stokes model for binary fluids. *J. Fluid Mech.* **2013**, *714*, 95–126. [[CrossRef](#)]
26. Chiu, P.H.; Lin, Y.T. A conservative phase field method for solving incompressible two-phase flows. *J. Comput. Phys.* **2011**, *230*, 185–204. [[CrossRef](#)]
27. Jacqmin, D. Calculation of two-phase Navier–Stokes flows using phase-field modeling. *J. Comput. Phys.* **1999**, *155*, 96–127. [[CrossRef](#)]
28. Jacqmin, D. Contact-line dynamics of a diffuse fluid interface. *J. Fluid Mech.* **2000**, *402*, 57–88. [[CrossRef](#)]
29. Geier, M.; Fakhari, A.; Lee, T. Conservative phase-field lattice Boltzmann model for interface tracking equation. *Phys. Rev. E* **2015**, *91*, 063309. [[CrossRef](#)]
30. He, X.; Luo, L.S. Theory of the lattice Boltzmann method: From the Boltzmann equation to the lattice Boltzmann equation. *Phys. Rev. E* **1997**, *56*, 6811–6817. [[CrossRef](#)]
31. Lallemand, P.; Luo, L.S. Theory of the lattice Boltzmann method: Dispersion, dissipation, isotropy, Galilean invariance, and stability. *Phys. Rev. E* **2000**, *61*, 6546–6562. [[CrossRef](#)]
32. Yu, D.; Mei, R.; Shyy, W. A unified boundary treatment in lattice Boltzmann method. *AIAA J.* **2003**. [[CrossRef](#)]
33. Hua, J.; Lou, J. Numerical simulation of bubble rising in viscous liquid. *J. Comput. Phys.* **2007**, *222*, 769–795. [[CrossRef](#)]
34. Fakhari, A.; Rahimian, M.H. Simulation of an axisymmetric rising bubble by a multiple relaxation time lattice Boltzmann method. *Int. J. Mod. Phys. B* **2009**, *23*, 4907–4932. [[CrossRef](#)]
35. Huang, H.; Huang, J.J.; Lu, X.Y. A mass-conserving axisymmetric multiphase lattice Boltzmann method and its application in simulation of bubble rising. *J. Comput. Phys.* **2014**, *269*, 386–402. [[CrossRef](#)]

36. Liang, H.; Li, Y.; Chen, J.; Xu, J. Axisymmetric lattice Boltzmann model for multiphase flows with large density ratio. *Int. J. Heat Mass Transf.* **2019**, *130*, 1189–1205. [[CrossRef](#)]
37. Bhaga, D.; Weber, M.E. Bubbles in viscous liquids: Shapes, wakes and velocities. *J. Fluid Mech.* **1981**, *105*, 61–85. [[CrossRef](#)]
38. Patel, T.; Patel, D.; Thakkar, N.; Lakdawala, A. A numerical study on bubble dynamics in sinusoidal channels. *Phys. Fluids* **2019**, *31*, 052103. [[CrossRef](#)]
39. Shi, Y.; Tang, G.H.; Lin, H.F.; Zhao, P.X.; Cheng, L.H. Dynamics of droplet and liquid layer penetration in three-dimensional porous media: A lattice Boltzmann study. *Phys. Fluids* **2019**, *31*, 042106. [[CrossRef](#)]
40. Clift, R.; Grace, J.R.; Weber, M.E. *Bubbles, Drops, and Particles*; Academic Press: New York, NY, USA, 1978.

Publisher’s Note: MDPI stays neutral with regard to jurisdictional claims in published maps and institutional affiliations.



© 2020 by the authors. Licensee MDPI, Basel, Switzerland. This article is an open access article distributed under the terms and conditions of the Creative Commons Attribution (CC BY) license (<http://creativecommons.org/licenses/by/4.0/>).

Article

Study of Deactivation in Suzuki Reaction of Polymer-Stabilized Pd Nanocatalysts

Linda Nikoshvili ^{1,*}, Elena S. Bakhvalova ², Alexey V. Bykov ¹, Alexander I. Sidorov ¹, Alexander L. Vasiliev ³, Valentina G. Matveeva ^{1,2}, Mikhail G. Sulman ¹, Valentin N. Sapunov ⁴ and Lioubov Kiwi-Minsker ^{2,5,*}

¹ Department of Biotechnology, Chemistry and Standardization, Tver State Technical University, A. Nikitina str., 22, 170026 Tver, Russia; bykovav@yandex.ru (A.V.B.); sidorov@science.tver.ru (A.I.S.); matveeva@science.tver.ru (V.G.M.); sulmanmikhail@yandex.ru (M.G.S.)

² Regional Technological Centre, Tver State University, Zhelyabova str., 33, 170100 Tver, Russia; bakhvalova.es@mail.ru

³ National Research Centre “Kurchatov Institute”, 123182 Moscow, Russia; a.vasiliev56@gmail.com

⁴ Department of Chemical Technology of Basic Organic and Petrochemical Synthesis, D. Mendeleev University of Chemical Technology of Russia, Miusskaya pl., 9, 125047 Moscow, Russia; sapunovvals@gmail.com

⁵ Ecole Polytechnique Fédérale de Lausanne, GGRC-ISIC-EPFL, CH-1015 Lausanne, Switzerland

* Correspondence: nlinda@science.tver.ru (L.N.); lioubov.kiwi-minsker@epfl.ch (L.K.-M.); Tel.: +7-904-005-7791 (L.N.); +41-21-693-3182 (L.K.-M.)

Received: 1 December 2020; Accepted: 14 December 2020; Published: 15 December 2020

Abstract: This work is addressed to the phenomenon of catalyst deactivation taking place during the repeated uses in the reaction of Suzuki-Miyaura (S-M) cross-coupling, which is widely applied in industry for C-C bond formation. Ligandless catalysts based on Pd(0) NPs supported on hyper-cross-linked polystyrene (HPS) of two types (non-functionalized and bearing tertiary amino groups) were studied in a model S-M reaction between 4-bromoanisole and phenylboronic acid. Synthesized catalysts were shown to be highly active under mild reaction conditions. HPS allows stabilization of Pd(0) NPs and prevents their agglomeration and detectable Pd leaching. However, the loss of catalytic activity was observed during recycling. The deactivation issue was assigned to the hydrophobic nature of non-functionalized HPS, which allowed a strong adsorption of cross-coupling product during the catalyst separation procedure. A thorough washing of Pd/HPS catalyst by hydrophobic solvent was found to improve to the big extent the observed catalytic activity, while the replacement of non-functionalized HPS by a one containing amino groups increased the catalyst stability at the expense of their activity.

Keywords: Suzuki cross-coupling; hyper-cross-linked polystyrene; palladium nanoparticles; catalyst stability

1. Introduction

The reaction of Suzuki-Miyaura (S-M) cross-coupling between aryl halides and arylboronic acids is one of the most common and effective methods for the synthesis of biaryls, which are important intermediates in the synthesis of pharmaceuticals, ligands, and polymers [1,2]. It is known that this reaction is a palladium-catalyzed condensation reaction, which proceeds via a Pd(0)/Pd(II) cycle involving the oxidative addition of the starting components and the reductive elimination of the resulting reaction products. The loss of the catalyst activity is an important issue of all the cross-coupling reactions. Various processes (e.g., aggregation, dissociation, leaching, etc.) can contribute to changes of the catalyst nature and, as a result, its activity and selectivity [3–5]. Aryl halides cause very low

palladium dissolution, while arylboronic acids, on the contrary, causes significant palladium leaching accompanied by its reduction and formation of palladium black. However, in the presence of both substrates, Pd(0) formed in the solution with participation of arylboronic acid is converted by aryl halide without precipitation of nanoparticles (NPs) [6].

This work addresses the catalytic behavior of palladium NPs stabilized within hyper-cross-linked polystyrene (HPS) support during the repeated reaction runs. HPS of two types was used, non-functionalized (MN270) and bearing tertiary amino groups (MN100), both relate to so-called “Davankov-type” resins [7,8]. In our previous works we have shown that Pd/HPS catalysts are highly active and selective in S-M reaction between phenylboronic acid (PBA) and 4-bromoanisole (BrAn) as model compounds [9–11]. However, due to the complex homo-heterogeneous mechanism [12] of this reaction, especially in the case of so-called “cocktail” type catalysts (containing metal NPs as reservoirs for catalytically active species [4,13]), the question about deactivation during the reaction course and the reasons for such behavior remains open. The term “cocktail” catalyst was proposed by Ananikov and coworkers [3,4] for cross-coupling processes and describes catalytic systems containing more than one form of palladium including Pd(0) NPs, where the latter serve as pre-catalysts generating active species during the reaction. For such catalysts it was established that virtually any form of Pd (small clusters, NPs, inorganic salts, complexes containing palladium ions or atoms) might start catalytic cycle. General scheme of catalytic cycle of S-M cross-coupling is presented in Figure 1.

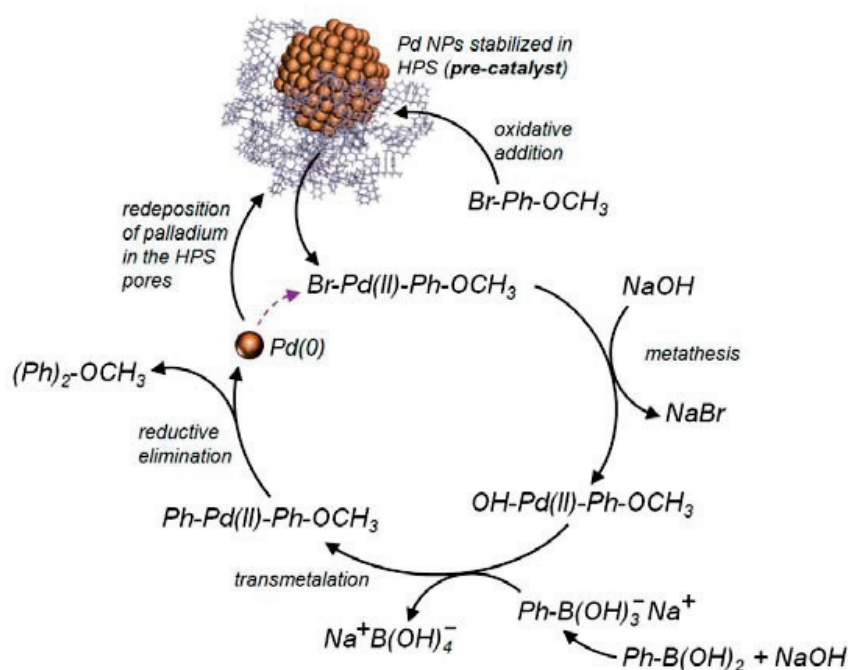


Figure 1. Simplified scheme of proposed catalytic cycle taking place while using Pd/HPS in S-M cross-coupling between BrAn (designated here as Br-Ph-OCH₃) and PBA (Ph-B(OH)₂) resulting in formation of 4-methoxybiphenyl (designated here as (Ph)₂-OCH₃).

In many works [4,6,14–16], the leaching of Pd and the formation of inert Pd(0)NPs are considered as the main reasons hampering catalyst reuse. There are two main ways to study catalyst deactivation and the nature (homogeneous vs. heterogeneous) of the active species: (i) hot filtration test and (ii) mercury test [16]. Each of them has certain disadvantages when working with a complex “cocktail” type catalyst with high porosity support. The pores of polymeric support can play a role of nanoreactors, in which Pd NPs can undergo dissolution, migration, reprecipitation and aggregation during the reaction course; hence actually the reaction location may shift to the polymer volume rather than being catalyzed by soluble Pd species in the reaction mixture. In this study, we chose the hot filtration test. We carried it out with the samples of Pd/HPS preliminarily reduced in hydrogen to form Pd(0)

NPs, in order to see if any loss of Pd species takes place. However, the nature of deactivation was completely different and didn't rely on Pd leaching but was due to a strong adsorption of the target product 4-methoxybiphenyl (MBP) on hydrophobic HPS support. Therefore, catalyst reuse is possible and is just a matter of suitable regeneration between the cycles.

2. Results and Discussion

The catalyst Pd/MN270, synthesized by the impregnation of non-functionalized HPS with Pd(OAc)₂ and containing small Pd NPs formed during the reduction in hydrogen flow, allows nearly complete conversion of aryl halide in the reaction between BrAn and PBA for 60 min at mild conditions (70 °C, NaOH as a base, EtOH-water mixture as a solvent). By the end of the reaction the share of the target cross-coupling product, MBP, among possible products (MBP and biphenyl (BP)—the result of PBA homocoupling) was relatively high—96.3%. At the same time, during the repeated reaction runs we observed a considerable catalyst deactivation from cycle to cycle with the decrease of not only the initial transformation rate, R_0 (from 411 $\mu\text{mol}(\text{BrAn})/\text{min}$ to 291 $\mu\text{mol}(\text{BrAn})/\text{min}$ after the first run and to 75 $\mu\text{mol}(\text{BrAn})/\text{min}$ after the second run), but also the achieved BrAn conversion: from 99.7% to 54.8% and 14.1% for the first, second and third cycle, respectively (see Figure 2a). The decrease of catalytic activity was supposed to be due to the loss of catalytically active species. However, it was found (Figure 2b) that after filtration of the reaction mixture (separation of the solid catalyst) the S-M reaction stopped, which indicated the absence of any active Pd species in filtrate.

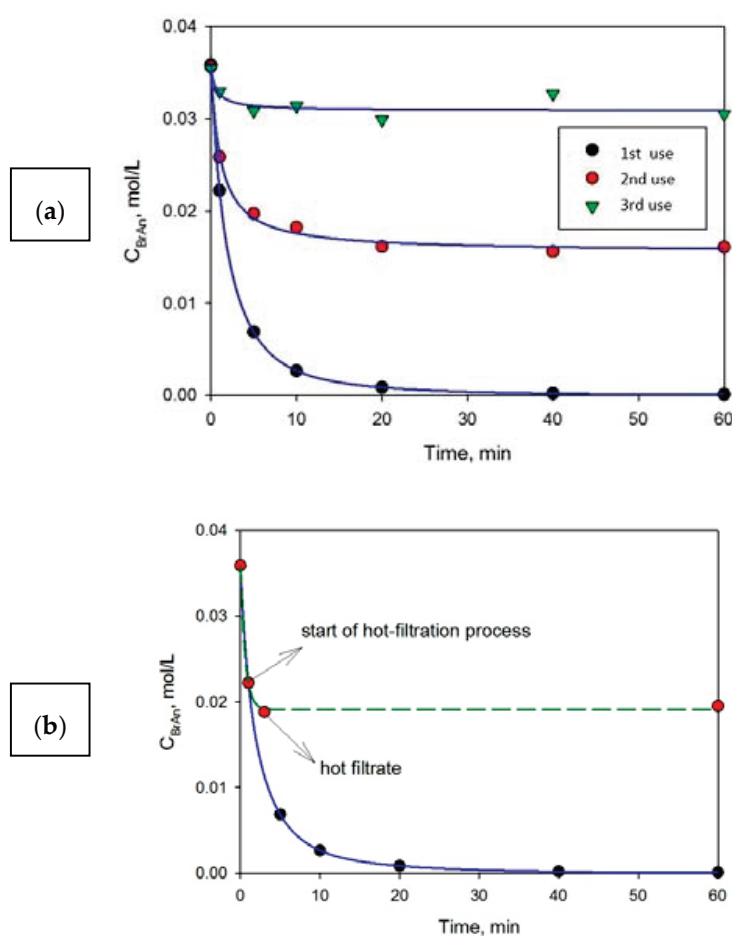


Figure 2. The activity of Pd/MN270 at repeated uses (a) and the hot-filtration test (b).

By the XFA method it was shown that Pd content in the catalyst remains the same (2.5 wt%) after the catalytic reaction. Thus, the loss of catalytic activity can't be associated with a detectable loss of palladium. Other reasons could be either aggregation of Pd NPs or clogging of HPS pores making active Pd-species inaccessible for reactants.

S/TEM studies showed (Figure 3) that for Pd/MN270 taken after the first use in the S-M reaction, Pd NPs decreased in size ($D_m = 6.8 \pm 2.9$ nm) and formed grape-type clusters (Figure 3c,d). The original fresh sample (see Figure 2a,b) contained Pd NPs with an average diameter of 8.2 ± 2.4 nm. Thus, we came to the conclusion that NPs aggregation, which is mentioned as an important factor in catalyst deactivation [17], cannot lead to the observed loss of Pd/MN270 activity upon repeated use.

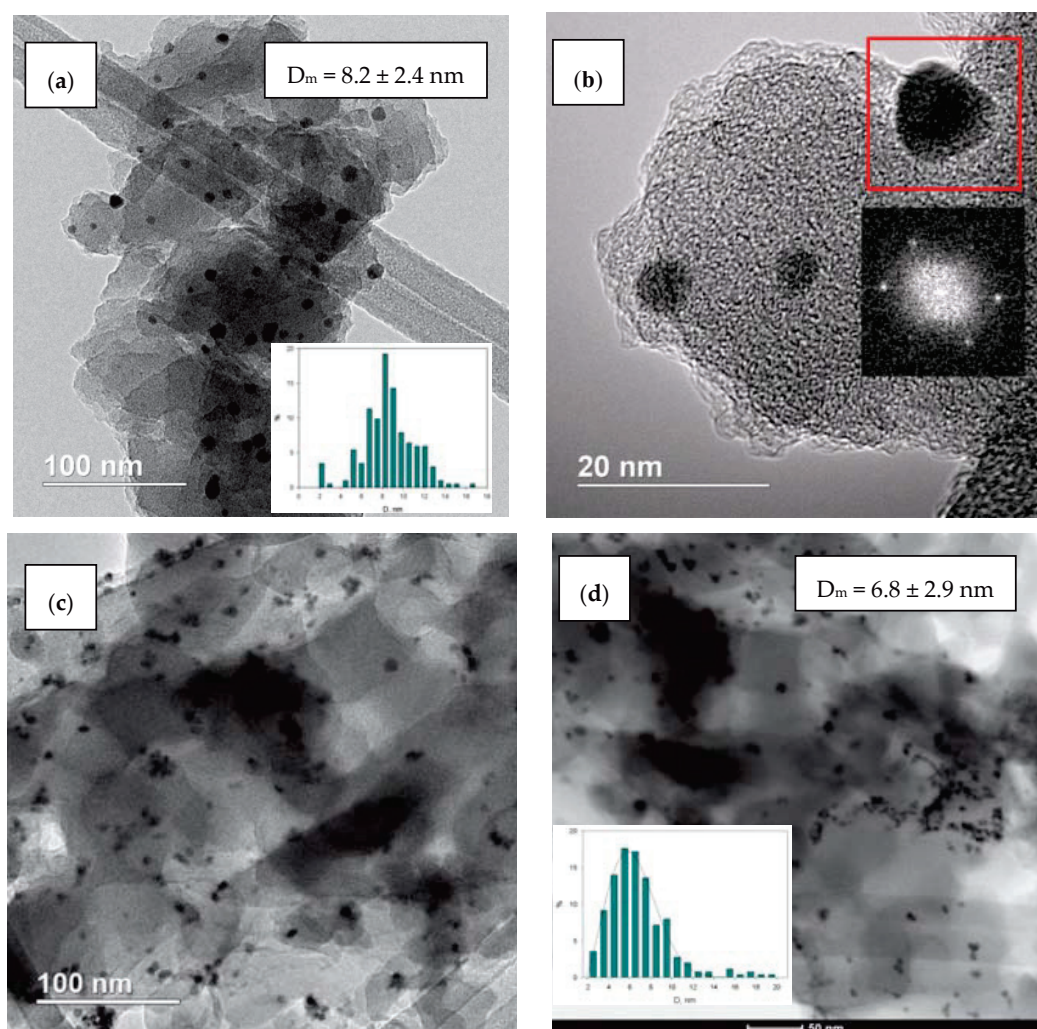


Figure 3. TEM (a) and HRTEM (b) images of the initial Pd/MN270 and also TEM image (c) and bright-field STEM image (d) of Pd/MN270 taken after the first run in S-M reaction.

Low-temperature physisorption of nitrogen showed that all catalyst samples have a predominant microporosity (Figure 4a). It is noteworthy that after the formation of NPs in the hydrogen flow, the SSA of the sample Pd(OAc)₂ decreased (Table 1, Figure 4b) from 1084 m²/g to 842 m²/g, mainly due to a decrease in microporosity (SSA of micropores decreased from 945 m²/g to 623 m²/g). However, after the first use in S-M reaction SSA of Pd/MN270 increased up to 977 m²/g (BET model) due to the increase of the share of both micro- and meso-pores, which in turn can be due to the NPs reprecipitation inside the HPS pores and is in good agreement with the results of S/TEM, obviously showing that no pore blockage took place during the use of Pd/MN270 in S-M cross-coupling.

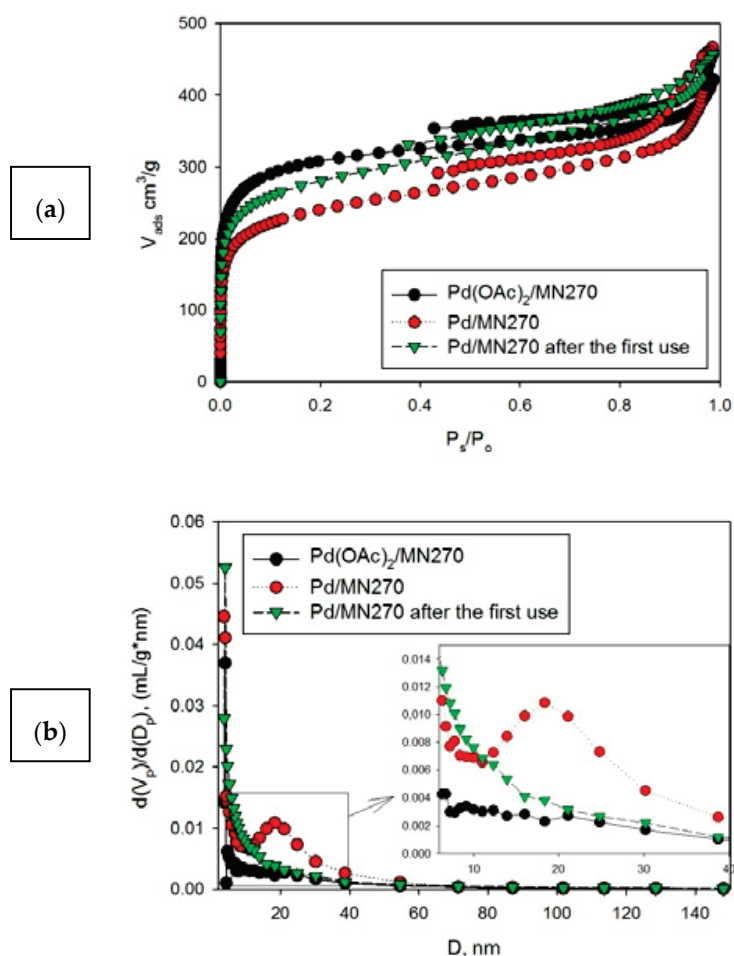


Figure 4. Adsorption-desorption isotherms (a) and pore volume distribution (b) for samples: initial Pd(OAc)₂/MN270 (black circles), reduced Pd/MN270 (red circles), and Pd/MN270 taken after the S-M reaction (green triangles).

Table 1. Data of low-temperature nitrogen physisorption for Pd/MN270 samples.

Sample	BET SSA, m^2/g	SSA According to t -Plot Model, m^2/g	Specific Pore Volume, mL/g	
			Total	Micropores
Pd(OAc) ₂ /MN270	1084	135 ^a ; 945 ^b	0.66	0.43
Pd/MN270	842	219 ^a ; 623 ^b	0.74	0.28
Pd/MN270 after the first use	977	264 ^a ; 742 ^b	0.71	0.33

^a external SSA; ^b SSA of micropores.

At the same time, after the second use of Pd/MN270 in S-M reaction between BrAn and BPA we observed unusual behavior of the catalyst on the membrane filter: there was a tendency to form aggregates during washing of the catalyst suspension with polar solvents. It is noteworthy that initial suspension in the reactor was without any aggregates. This tendency was typical not only for the catalyst (Figure 5a), but also for initial MN270, which was sustained in the MBP solution (Figure 5b). Taking into account the aromatic nature of HPS, we considered the adsorption of MBP, which may increase hydrophobicity of the surface leading to the aggregation.

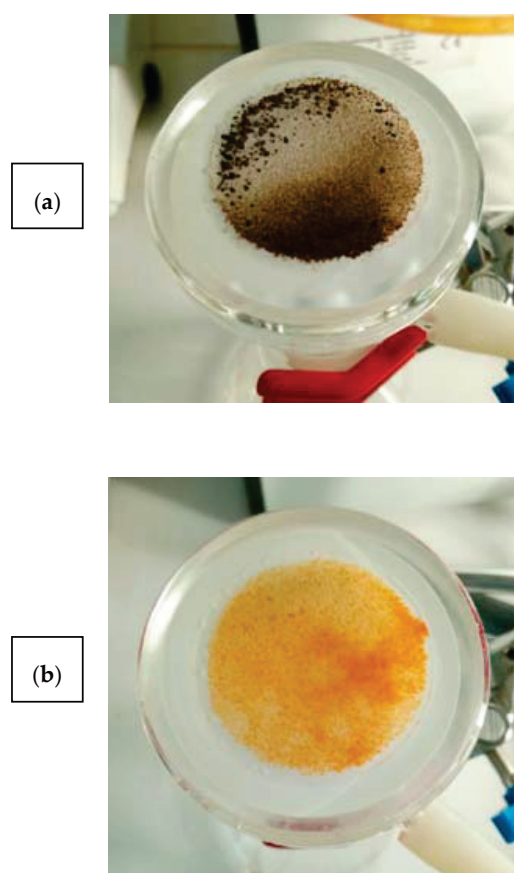


Figure 5. Pd/MN270 taken immediately after the second use in S-M cross-coupling (a) and initial MN270 after 3 h in the EtOH-water mixture containing 1 mmol of MBP (b).

Although different reactants can potentially adsorb on the catalyst surface during the S-M reaction, we supposed that MBP is responsible for the observed deactivation due to the following reasons:

- bromine and boron were not detected on the surface of Pd/MN270 neither after the first run nor after the second run, which exclude strong adsorption of BrAn and PBA;
- sodium was found on the Pd/MN270 surface in trace amounts (less than 0.2 at.%), so, sodium-containing compounds can not be considered as the main adsorbed species;
- high selectivity of the catalyst with respect to MBP (share of MBP among the reaction products is higher than 96%) excludes the strong influence of BP;
- sharp increase of oxygen content was found after the repeated reaction runs, and this oxygen does not belong to the oxygen of polymeric matrix itself (see below).

The adsorption of MBP was confirmed by the XPS (Figure 6). On the surface of Pd/MN270 taken after the first use in S-M reaction all the Pd was belonging to partially oxidized metallic Pd NPs (Figure 6a). While oxygen included two components (Figure 6b): (i) oxygen belonging to HPS matrix and (ii) oxygen of the ether bond (-O-CH₃). Oxygen of PdO was not considered in O 1s deconvolution because of relatively low signal of Pd.

DRIFT study confirmed the above assumption. Normalized FTIR spectra of Pd/MN270 (Figure S1) clearly show that after the second use in S-M reaction, the intensity of adsorption bands belonging to C-H of alkanes ($\nu_{\text{C-H}} = 2857 \text{ cm}^{-1}$, $\delta_{\text{C-H}} = 1452$ and 1418 cm^{-1}) and benzene rings ($\nu_{\text{C-H}} = 3019 \text{ cm}^{-1}$, in-plane vibrations $\delta_{\text{C-H}}$ in the range of $1250\text{--}950 \text{ cm}^{-1}$, out-of-plane vibrations $\delta_{\text{C-H}}$ in the range of $900\text{--}650 \text{ cm}^{-1}$) increased. Moreover, noticeable increase of the intensity of the adsorption band belonging to C-O bond ($\nu_{\text{C-O}} = 1294 \text{ cm}^{-1}$) occurred.

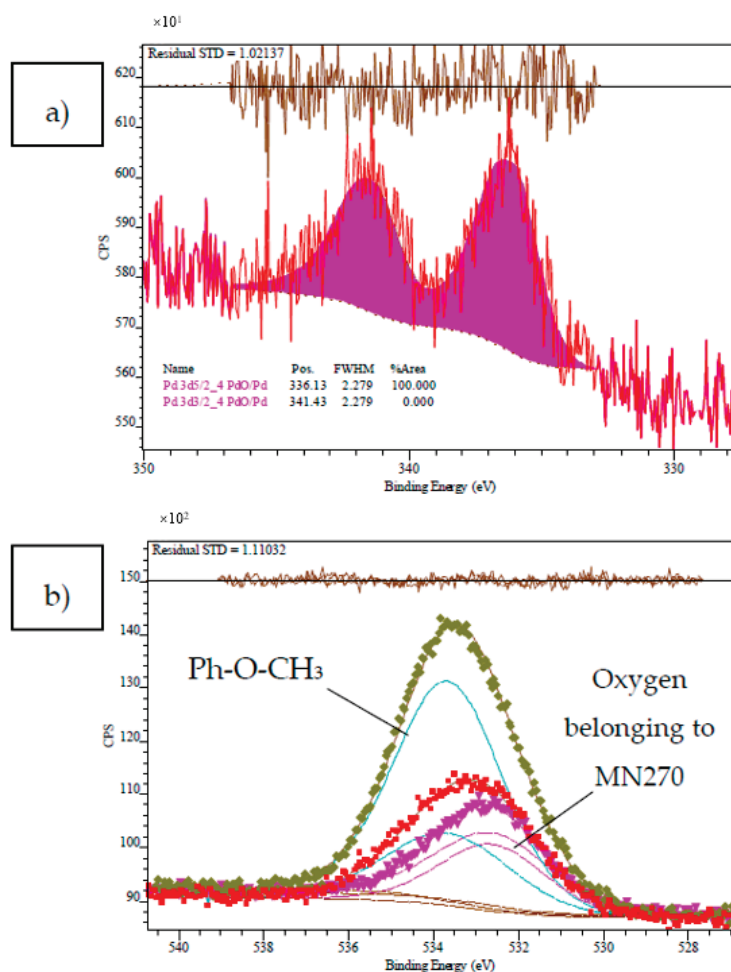


Figure 6. High resolution photoelectron spectrum of Pd 3d for Pd/MN270 taken after the first use in S-M reaction (a) and comparison of high resolution photoelectron spectra of O 1s (b) for initial Pd/MN270 (pink triangles), and Pd/MN270 taken after the first use (red squares) as well as after the second use (green rhombs).

In order to prove the loss of catalytic activity due to the MBP adsorption, the sample Pd/MN270 taken after the first use in S-M reaction was washed additionally with chloroform for 5 h at room temperature and intensive stirring. After that, washed sample was tested again (see Figure 7), and the catalytic activity was almost fully recovered.

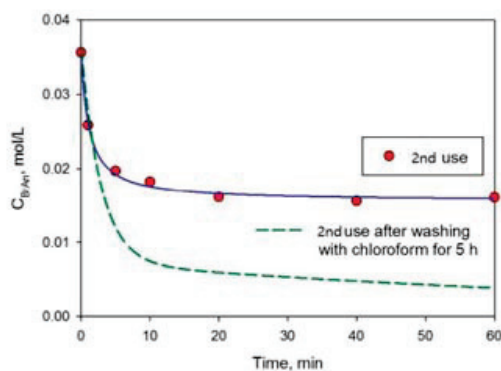


Figure 7. Influence of washing with chloroform on the activity of Pd/MN270 taken after the first use in S-M reaction.

As the further step of investigation, we compared stability of two catalysts, Pd/MN270 and Pd/MN100 under equal reaction conditions, in order to find if there is any deactivation during the repeated use in the case of MN100 containing tertiary amino groups, which make this polymer relatively more hydrophilic than MN270 (non-functionalized). As it can be seen in Figure 8a, Pd/MN100 can be recycled without noticeable loss of catalytic activity. At the same time the oxygen belonging to the ether bond (-O-CH₃) increases after the second use only slightly (Figure 8b) in comparison with the sample Pd/MN270 (see Figure 6b). It is noteworthy that Pd/MN100 did not undergo additional washing procedure between the catalytic cycles.

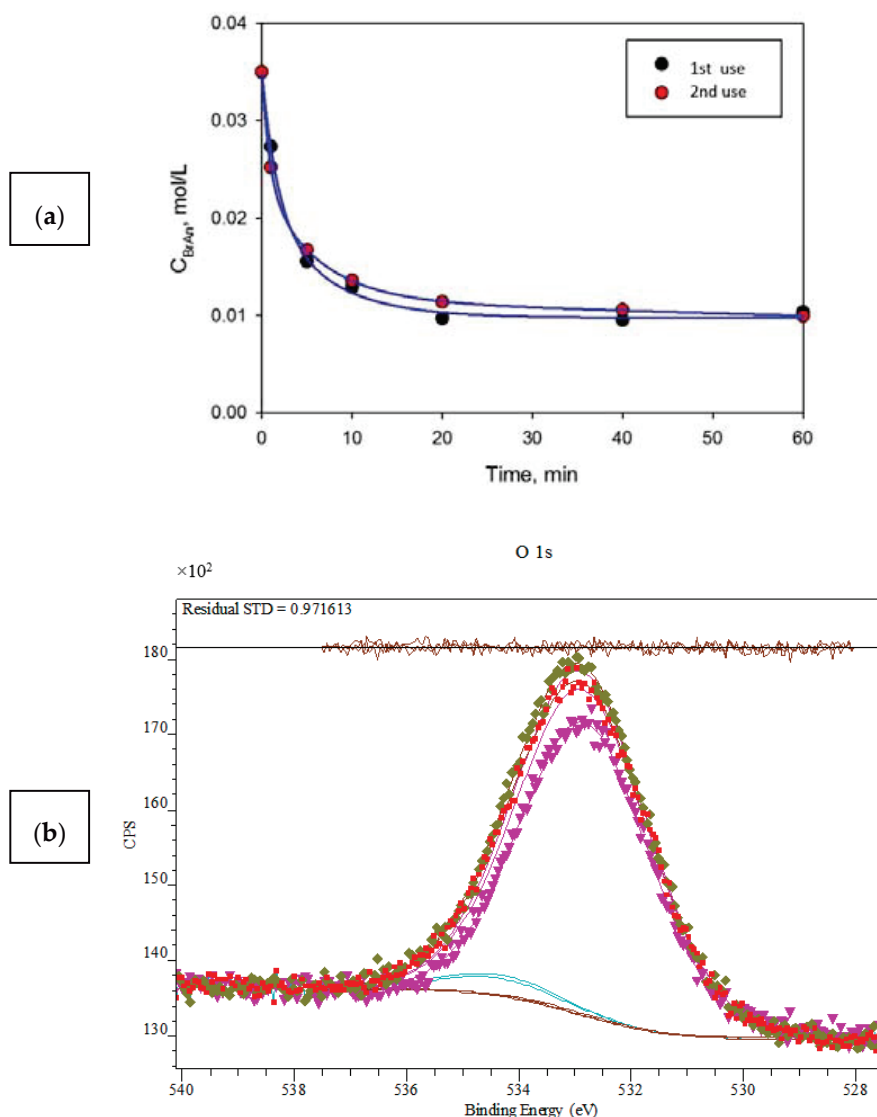


Figure 8. Influence of repeated uses on the activity of Pd/MN100 (a) and comparison of high resolution photoelectron spectra of O 1s (b) for initial Pd/MN100 (pink triangles), and Pd/MN100 taken after the first use (red squares) as well as after the second use (green rhombs).

It should be also mentioned that the observed “plateau” on the kinetic curves (Figure 8a) is due to the lack of PBA and corresponding NaOH, as monometallic catalysts of S-M cross-coupling based on MN100 typically possesses lower selectivity (the share of MBP is about 94% at complete conversion of BrAn) and requires higher excess of PBA with respect to BrAn in the reaction mixture. In this particular case, if PBA will be taken in 2.5-fold excess with respect to BrAn (at 3.0 mmol of NaOH), more than

95% of BrAn conversion will be achieved by 20 min of the reaction. The necessity to use high excess of PBA can be likely due to the side reactions, e.g., PBA deboronation, which might take place in the presence of water [18] in case of more hydrophilic polymer.

3. Materials and Methods

3.1. Materials

HPS (Purolite Int., Llantrisant, UK) used as catalyst support was of two types: hyper-cross-linked non-functionalized polystyrene, Macronet MN270, and HPS containing tertiary amino groups, MN100. Both supports were washed with distilled water and acetone and then dried under vacuum as described elsewhere [19]. 4-Bromoanisole (BrAn, $\geq 98\%$) was purchased from Merck KGaA. 4-Methoxybiphenyl (MBP, $>99\%$) was purchased from Tokyo Chemical Industry Co. Ltd. Phenylboronic acid (PBA, 95%), diphenylamine (99%), biphenyl (BP, 99.5%), tetrahydrofuran (THF, $\geq 99.9\%$), ethanol (EtOH, $\geq 99.8\%$), isopropanol (*i*-PrOH, $\geq 99.5\%$), chloroform (CHCl_3 , $\geq 99\%$, anhydrous, containing 0.5% EtOH as a stabilizer), sodium hydroxide (NaOH, $\geq 98\%$) were obtained from Sigma-Aldrich. Palladium acetate ($\text{Pd}(\text{CH}_3\text{COO})_2$, Pd content 47.68%) was purchased from JSC "Aurat" (Moscow, Russia). All chemicals were used as received. Distilled water was purified with an Elsi-Aqua water purification system.

3.2. Catalyst Synthesis

HPS MN270-based catalyst containing Pd was synthesized via wet-impregnation method. In a typical experiment, 1 g of pretreated, dried and crushed ($<63 \mu\text{m}$) granules of MN270 were impregnated with 2.8 mL of the THF solution of precursor ($\text{Pd}(\text{CH}_3\text{COO})_2$) of a certain concentration. The sample was dried at 70°C until the constant weight. Thus the catalyst $\text{Pd}(\text{OAc})_2/\text{MN270}$ was synthesized containing 2.5 wt% of Pd (confirmed by the XFA). This catalyst was also reduced in a hydrogen flow (100 mL/min) at 300°C for 3 h (the catalysts was designated as Pd/MN270).

By the same method, the catalyst based on HPS MN100 was synthesized ($\text{Pd}(\text{OAc})_2/\text{MN100}$, with 1.0 wt% of Pd as confirmed by the XFA) and after reduction in a hydrogen flow was designated as Pd/MN100.

To confirm the state of Pd, the synthesized samples were analyzed by the X-Ray Photoelectron Spectroscopy (XPS). The XPS data revealed (see Figure 9) that both Pd/MN270 (Figure 9a) and Pd/MN100 (Figure 9b) contain palladium in the form of partly oxidized NPs (E_b is 335.0 eV for metallic Pd and 336.3 for PdO/Pd [20]) and PdO ($E_b = 337.2 \text{ eV}$ [20]) on their surfaces. For simplification of discussion we suppose that predominant form of palladium is metallic form, Pd(0), in the case of the reduced catalysts (Pd/HPS).

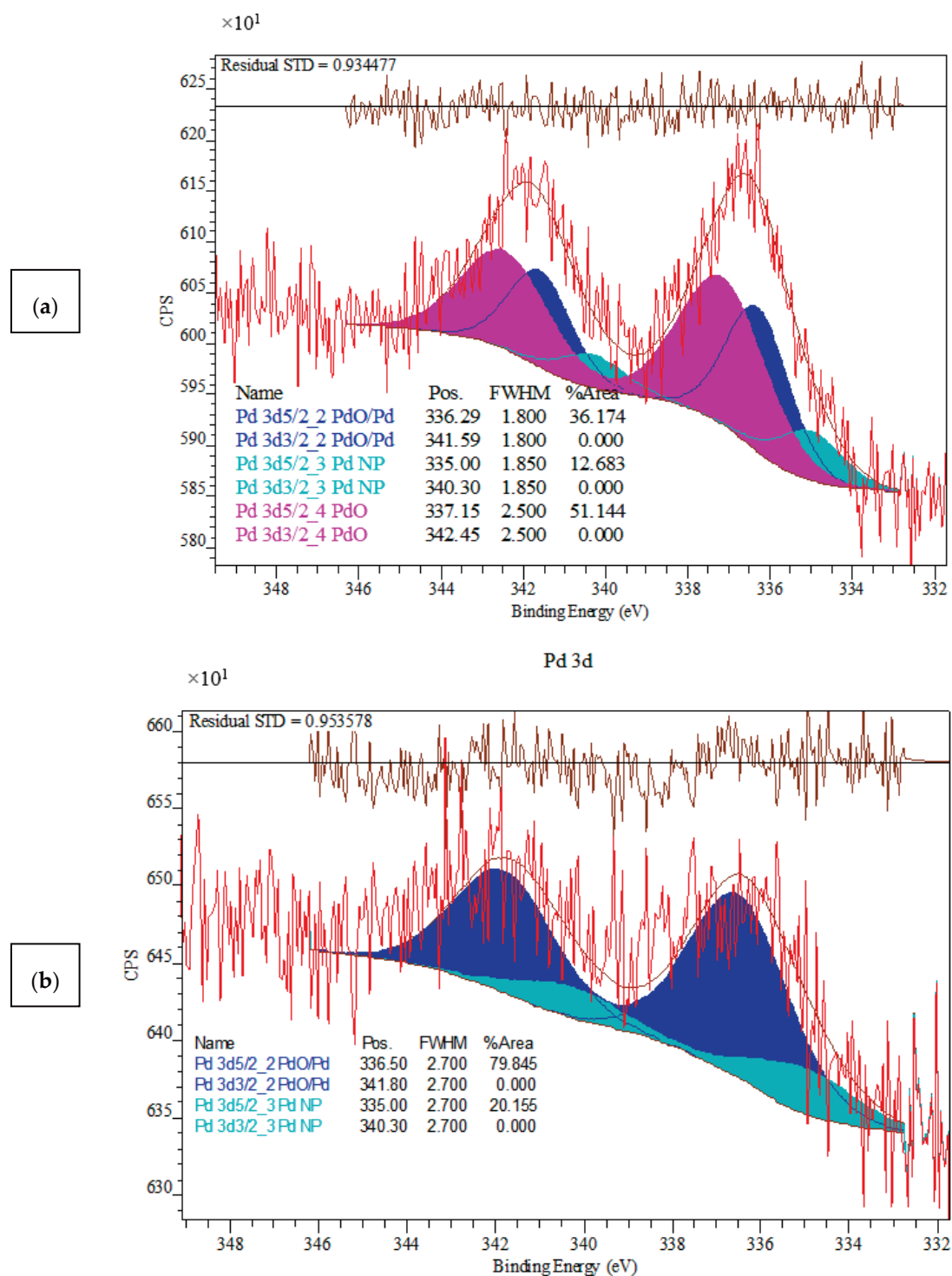


Figure 9. High resolution XPS of Pd 3d in Pd/MN270 (a) and Pd/MN100 (b).

3.3. Reaction Procedure and Analysis of Reaction Mixture

The Suzuki-Miyaura (S-M) cross-coupling was carried in a temperature controlled shaker-type glass batch reactor at following reaction parameters: Pd concentration 0.157 mmol/L (which is equal to 0.47 mol% with respect to BrAn), PBA amount 1.5 mmol, NaOH amount 2.0 mmol, BrAn amount 1.0 mmol, stirring intensity 800 two-sided shaking per minute, reaction temperature 70 °C, EtOH-to-H₂O volumetric ratio 5:1 (total volume of liquid phase 30 mL), and nitrogen as gas phase. Preliminary

experiments showed that the reaction of BrAn and PBA at chosen conditions when using Pd/MN270 as a catalyst proceeds almost quantitatively (97–99 mol%); the formation of BP does not exceed 2% molar, and the formation of σ,σ' -dianisoles is not detected.

The excess of PBA with respect to BrAn was used due to the possible non-selective catalyst behavior as a result of PBA homocoupling with the formation of BP. It is noteworthy that before the catalyst addition in the reactor, in each experiment the blank test (duration of 60 min) was carried out in order to ensure that there is no reaction without catalyst.

The choice of EtOH/water mixture as a solvent was, from one hand, due to the environmentally benign nature of these solvents, and from the other hand, by the no need of phase-transfer agents, since the system remained all time homogeneous in the range of selected concentrations of reactants (BrAn, PBA and NaOH) and the products formed (MBP and BP). Moreover, it is known that addition of water to an organic solvent avoids the formation of inactive trimers of boronic acid [21].

Regarding the inert gas atmosphere, it should be noted that Pd/HPS catalysts can be used in air, but the rate of BrAn transformation is lower (Figure 10) and the share of target MBP in the reaction products also decreased from 98.4% to 95.9% at 94% of BrAn conversion due to the increase of BP accumulation. Adrio et al., also reported accelerated PBA homocoupling in the presence of air [22]. The role of oxygen is presumably in partial oxidation of palladium as it was shown by McGlacken et al. [23], while Pd(II) is able to react with PBA prior to BrAn. In our opinion, the interaction of oxygen in the aqueous medium with Pd(0) leads to formation of tightly bound ligands in Pd(OH)₂, blocking “hot” atoms of the Pd and reducing its activity.

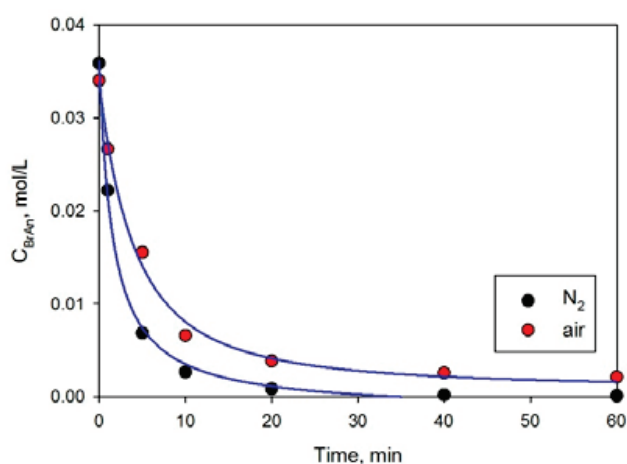


Figure 10. Influence of gas phase on the activity of Pd/MN270.

In each catalytic experiment, samples of reaction mixture were periodically taken and analyzed via GC-MS (Shimadzu GCMS-QP2010S) equipped with a capillary column HP-1MS (100 m × 0.25 mm i.d., 0.25 μm film thickness). Helium was used as a carrier gas at pressure of 74.8 kPa and linear velocity of 36.3 cm/s. Oven temperature was programmed: 120 °C (0 min) → 10 °C/min (160 °C) → 25 °C/min (300 °C) → 300 °C (2.4 min). Temperature of injector, interface and ion source was at 260 °C, range from 10 up to 500 *m/z*. The concentrations of the reaction mixture components were calculated using the internal standard calibration method (diphenylamine was used as an internal standard). It is noteworthy that during the GC-MS analysis, PBA underwent dehydration and trimerization, which negatively affected the signal intensity. Due to the low level of confidence in the quantitative analysis of PBA content, its consumption was not studied.

Catalytic activity was characterized by the initial transformation rate, (R_0) and defined as a tangent of slope of the initial linear part on kinetic curves of BrAn consumption: $R_0 = (N_{BrAn,0} - N_{BrAn,i}) \times \tau_i^{-1}$, where N_{BrAn} is number of moles of BrAn (μmol); and τ is the reaction time (min).

Conversion ($X, \%$) of BrAn was defined as $X = (N_{BrAn,0} - N_{BrAn,i}) \times N_{BrAn,0}^{-1} \times 100$.

3.4. Isolation of the Catalysts from the Reaction Mixture for Reuse

After the completion of the S-M reaction, the catalysts were filtered under vacuum using membrane filter (cellulose acetate, 0.45 μm pore size, 50 mm diameter) and sequentially washed with EtOH (30 mL), i-PrOH (30 mL), water (500 mL), i-PrOH (30 mL) and chloroform (50 mL). Then they were dried till constant weight at 70 $^{\circ}\text{C}$. It is noteworthy that for the repeated use, several (at least 4) catalyst samples were collected from previous runs and averaged catalyst sample was taken for further run. In this way all the reaction conditions remained unchanged including the catalyst weight.

3.5. Procedure of Hot-Filtration of the Reaction Mixture

The S-M reaction was started as usual according to the procedure described in Section 3.3. After 1 min, 10 mL of the reaction mixture was separated (start of hot-filtration) using syringe equipped with membrane (0.22 μm pore size) and promptly transferred to the second glass batch reactor (end of hot-filtration process), which was preliminarily thermostated and sealed. After that the filtrate was kept under the reaction conditions for 60 min with periodic sampling and analysis.

3.6. Catalyst Characterization

Pd/HPS catalysts were characterized by liquid nitrogen physisorption, X-ray Fluorescence Analysis (XFA), X-ray Photoelectron Spectroscopy (XPS), Diffuse Reflectance Infrared Fourier Transform Spectroscopy (DRIFTS) and Scanning Transmission Electron Microscopy (STEM).

Liquid nitrogen physisorption was carried out using Beckman Coulter SA 3100 (Coulter Corporation, USA). Prior to the analysis, each sample was placed in a quartz cell installed in the Beckman Coulter SA-PREP. The samples were pretreated over 60 min under nitrogen at 120 $^{\circ}\text{C}$. Once the pretreatment was complete, the cell was cooled and weighed, and then transferred to the analytical port. Analysis was performed at -196°C and a relative pressure of 0.9814 (for pores less than 100 nm in diameter) to obtain a PSD (ADS) profile.

XFA was carried out to determine the Pd content. It was performed with a Zeiss Jena VRA-30 spectrometer (Mo anode, LiF crystal analyzer and SZ detector). Analyses were based on the Co $K\alpha$ line and a series of standards prepared by mixing 1 g of polystyrene with 10–20 mg of standard compounds. The time of data acquisition was constant at 10 s.

XPS data were obtained using Mg $K\alpha$ ($h\nu = 1253.6$ eV) radiation with ES-2403 spectrometer (Institute for Analytic Instrumentation of RAS, St. Petersburg, Russia) equipped with energy analyzer PHOIBOS 100-MCD5 (SPECS, Berlin, Germany) and X-ray source XR-50 (SPECS, Berlin, Germany). All the data were acquired at X-ray power of 250 W. Survey spectra were recorded at an energy step of 0.5 eV with an analyzer pass energy 40 eV, and high resolution spectra were recorded at an energy step of 0.05 eV with an analyzer pass energy 7 eV. Samples were outgassed for 180 min before analysis and were stable during the examination. The data analysis was performed via CasaXPS.

DRIFTS was carried out using an IRPrestige-21 FTIR spectrometer (Shimadzu, Kyoto, Japan) equipped with a DRS-8000 diffuse reflectance accessory (Shimadzu, Kyoto, Japan). The background sample was a mirror of the material of the optical system of the DRS-8000 accessory. All spectra were recorded in the range of 4000–500 cm^{-1} wave numbers with the resolution of 4 cm^{-1} .

STEM characterization was carried out using FEI Tecnai Osiris instrument (Thermo Fisher Scientific, Waltham, MA, USA) operating at an accelerating voltage of 200 kV, equipped with high-angle annular dark field (HAADF) detector (Fischione, Export, PA, USA) and energy-dispersive X-ray (EDX) microanalysis spectrometer (EDAX, Mahwah, NJ, USA). Samples were prepared by embedding the catalyst in epoxy resin with following microtoming (*ca.* 50 nm thick) at ambient temperature. For the image processing Digital Micrograph (Gatan, Pleasanton, CA, USA) software and TIA (Thermo Fisher Scientific, Waltham, MA, USA) were used. Holey carbon/Cu grid was used as a sample support.

4. Conclusions

In summary, we have synthesized highly active Pd-nanocatalysts for Suzuki-Miyaura cross-coupling using hyper-cross-linked non-fictionalized polystyrene, MN270 as a support. For the first time it was shown that aromatic polymeric matrix allows stabilization of Pd nanoparticles during repeated reaction runs. However, in spite of the absence of nanoparticles agglomeration and detectable Pd leaching in the reaction media, loss of catalytic activity was observed during recycling. The deactivation issue was assigned to the hydrophobic nature of the HPS support, which allowed a strong adsorption of target cross-coupling product. This assumption was confirmed by using more hydrophilic hyper-cross-linked polystyrene, containing tertiary amino groups. A thorough washing of Pd/MN270 catalyst by hydrophobic solvent between reaction runs was found to improve to the big extent the stability of the catalytic system developed.

Supplementary Materials: The following are available online at <http://www.mdpi.com/2227-9717/8/12/1653/s1>, Figure S1. Normalized FTIR spectra for Pd/MN270: initial (black solid line), after the first use (red dash line) and after the second use (green dash-dot line) in Suzuki reaction.

Author Contributions: Conceptualization, V.N.S.; methodology, L.N.; XPS and DRIFTS, A.V.B.; validation, L.K.-M., V.N.S. and V.G.M.; investigation, E.S.B. and L.N.; low-temperature nitrogen physisorption, A.I.S.; electron microscopy, A.L.V.; resources, M.G.S.; writing—original draft preparation, L.N.; writing—review and editing, V.N.S. and L.K.-M.; visualization, A.V.B., A.L.V. and L.N.; supervision, V.G.M., L.K.-M. and L.N.; project administration, L.K.-M.; funding acquisition, M.G.S. and L.K.-M. All authors have read and agreed to the published version of the manuscript.

Funding: The work was supported by the Russian Science Foundation (project 20-19-00386).

Acknowledgments: The authors highly appreciate the work of Irina Yu. Tiamina on the catalysts preparation.

Conflicts of Interest: The authors declare no competing financial interest.

Abbreviations

S-M: Suzuki-Miyaura; NPs: nanoparticles; HPS: hyper-cross-linked polystyrene; BrAn: 4-bromoanisole; MBP: 4-methoxybiphenyl; BP: biphenyl; PBA: phenylboronic acid.

References

1. Suzuki, A. Organoboron compounds in new synthetic reaction. *Pure Appl. Chem.* **1985**, *57*, 1749–1758. [[CrossRef](#)]
2. Buskes, M.J.; Blanco, M.-J. Impact of cross-coupling reactions in drug discovery and development. *Molecules* **2020**, *25*, 3493. [[CrossRef](#)] [[PubMed](#)]
3. Kashin, A.S.; Ananikov, V.P. Catalytic C-C and C-heteroatom bond formation reactions: *In situ* generated or preformed catalysts? Complicated mechanistic picture behind well-known experimental Procedures. *J. Org. Chem.* **2013**, *78*, 11117–11125. [[CrossRef](#)] [[PubMed](#)]
4. Eremin, D.B.; Ananikov, V.P. Understanding active species in catalytic transformations: From molecular catalysis to nanoparticles, leaching, “cocktails” of catalysts and dynamic systems. *Coord. Chem. Rev.* **2017**, *346*, 2–19. [[CrossRef](#)]
5. Reay, A.J.; Fairlamb, I.J.S. Catalytic C–H bond functionalisation chemistry: The case for quasi-heterogeneous catalysis. *Chem. Commun.* **2015**, *51*, 16289–16307. [[CrossRef](#)] [[PubMed](#)]
6. Soomro, S.S.; Ansari, F.L.; Chatziapostolou, K.; Köhler, K. Palladium leaching dependent on reaction parameters in Suzuki-Miyaura coupling reactions catalyzed by palladium supported on alumina under mild reaction conditions. *J. Catal.* **2010**, *273*, 138–146. [[CrossRef](#)]
7. Tsyurupa, M.P.; Davankov, V.A. Porous structure of hypercrosslinked polystyrene: State-of-the-art mini-review. *React. Funct. Polym.* **2006**, *66*, 768–779. [[CrossRef](#)]
8. Tan, L.; Tan, B. Hypercrosslinked porous polymer materials: Design, synthesis, and applications. *Chem. Soc. Rev.* **2017**, *46*, 322–3356.
9. Nikoshvili, L.Z.; Nemygina, N.A.; Khudyakova, T.E.; Tiamina, I.Y.; Bykov, A.V.; Stein, B.D.; Sulman, E.M.; Kiwi-Minsker, L. Pd nanoparticles stabilized by hypercrosslinked polystyrene catalyze selective triple C-C bond hydrogenation and Suzuki cross-coupling. *J. Nanomater.* **2019**, *2019*, 6262176. [[CrossRef](#)]

10. Nemygina, N.; Nikoshvili, L.; Bykov, A.; Sidorov, A.; Molchanov, V.; Sulman, M.; Tiamina, I.; Stein, B.; Matveeva, V.; Sulman, E.; et al. Catalysts of Suzuki cross-coupling based on functionalized hyper-cross-linked polystyrene: Influence of precursor nature. *Org. Process Res. Dev.* **2016**, *20*, 1453–1460. [[CrossRef](#)]
11. Nemygina, N.A.; Nikoshvili, L.Z.; Matveeva, V.G.; Sulman, M.G.; Sulman, E.M.; Kiwi-Minsker, L. Pd-nanoparticles confined within hollow polymeric framework as effective catalysts for the synthesis of fine chemicals. *Top. Catal.* **2016**, *59*, 1185–1195. [[CrossRef](#)]
12. Nemygina, N.; Nikoshvili, L.; Tiamina, I.; Bykov, A.; Smirnov, I.; LaGrange, T.; Kaszkur, Z.; Matveeva, V.; Sulman, E.; Kiwi-Minsker, L. Au (core)/Pd (shell) bimetallic nanoparticles immobilized within hyper-crosslinked polystyrene for mechanistical study of Suzuki cross-coupling: Homogeneous or heterogeneous catalysis? *Org. Process Res. Dev.* **2018**, *22*, 1606–1613. [[CrossRef](#)]
13. Balanta, A.; Godard, C.; Claver, C. Pd nanoparticles for C–C coupling reactions. *Chem. Soc. Rev.* **2011**, *40*, 4973–4985. [[CrossRef](#)] [[PubMed](#)]
14. Chen, J.-S.; Vasiliev, A.N.; Panarello, A.P.; Khinast, J.G. Pd-leaching and Pd-removal in Pd/C-catalyzed Suzuki couplings. *Appl. Catal. A Gen.* **2007**, *325*, 76–86. [[CrossRef](#)]
15. Molnár, A. Efficient, selective, and recyclable palladium catalysts in carbon-carbon coupling reactions. *Chem. Rev.* **2011**, *111*, 2251–2320. [[CrossRef](#)] [[PubMed](#)]
16. Chernyshev, V.M.; Astakhov, A.V.; Chikunov, I.E.; Tyurin, R.V.; Eremin, D.B.; Ranny, G.S.; Khrustalev, V.N.; Ananikov, V.P. Pd and Pt catalyst poisoning in the study of reaction mechanisms: What does the mercury test mean for catalysis? *ACS Catal.* **2019**, *9*, 2984–2995. [[CrossRef](#)]
17. Larina, E.V.; Kurokhtina, A.A.; Schmidt, A.F. Approach to the determination of kinetic order of catalyst deactivation: Observation of unusual kinetics in the Suzuki-Miyaura reaction. *Mendeleev Commun.* **2014**, *24*, 96–97. [[CrossRef](#)]
18. Lima, C.F.R.A.C.; Rodrigues, A.S.M.C.; Silva, V.L.M.; Silva, A.M.S.; Santos, L.M.N.B.F. Role of the base and control of selectivity in the Suzuki-Miyaura cross-coupling reaction. *Chem. Cat. Chem.* **2014**, *6*, 1291–1302.
19. Sulman, E.M.; Nikoshvili, L.Z.; Matveeva, V.G.; Tyamina, I.Y.; Sidorov, A.I.; Bykov, A.V.; Demidenko, G.N.; Stein, B.D.; Bronstein, L.M. Palladium containing catalysts based on hypercrosslinked polystyrene for selective hydrogenation of acetylene alcohols. *Top. Catal.* **2012**, *55*, 492–497. [[CrossRef](#)]
20. (National Institute of Standards and Technology, Gaithersburg, 2012) NIST. X-Ray Photoelectron Spectroscopy Database, Version 4.1. Available online: <http://srdata.nist.gov/xps/> (accessed on 21 November 2020).
21. Lennox, A.J.J.; Lloyd-Jones, G.C. Selection of boron reagents for Suzuki-Miyaura coupling. *Chem. Soc. Rev.* **2014**, *43*, 412–443. [[CrossRef](#)]
22. Adrio, L.A.; Nguyen, B.N.; Guilera, G.; Livingston, A.G.; Hii, K.K.M. Speciation of Pd(OAc)₂ in ligandless Suzuki-Miyaura reactions. *Catal. Sci. Technol.* **2012**, *2*, 316–323. [[CrossRef](#)]
23. Collins, G.; Schmidt, M.; O'Dwyer, C.; Holmes, J.D.; McGlacken, G.P. The origin of shape sensitivity in palladium-catalyzed Suzuki-miyaura cross coupling reactions. *Angew. Chem. Int. Ed.* **2014**, *53*, 4142–4145. [[CrossRef](#)] [[PubMed](#)]

Publisher's Note: MDPI stays neutral with regard to jurisdictional claims in published maps and institutional affiliations.



© 2020 by the authors. Licensee MDPI, Basel, Switzerland. This article is an open access article distributed under the terms and conditions of the Creative Commons Attribution (CC BY) license (<http://creativecommons.org/licenses/by/4.0/>).

Article

Development of Carbonization and a Relatively High-Temperature Halogenation Process for the Removal of Radionuclides from Spent Ion Exchange Resins

Hee-Chul Yang ^{1,*}, Hyeon-Oh Park ², Kyu-Tae Park ², Sung-Jun Kim ^{1,3}, Hyung-Ju Kim ¹, Hee-Chul Eun ¹ and Keunyoung Lee ¹

¹ Korea Atomic Energy Research Institute, Daedukdaero 989-111, Yuseong-gu, Daejeon 34057, Korea; kimsj93@kaeri.re.kr (S.-J.K.); hyungjukim@kaeri.re.kr (H.-J.K.); ehc2004@kaeri.re.kr (H.-C.E.); lky@kaeri.re.kr (K.L.)

² Sunkwang T&S Co. Ltd., Sunkyung Officetel 20F, Gongwon-ro, Guro-gu, Seoul 08298, Korea; pho1428@daum.net (H.-O.P.); paradoxno1@hanmail.net (K.-T.P.)

³ Department of Chemical and Biological Engineering, Korea University, 145 Anam-ro, Seongbuk-gu, Seoul 02841, Korea

* Correspondence: nhcyang@kaeri.re.kr; Tel.: +82-42-868-2575

Abstract: This study investigated a two-step thermochemical treatment process consisting of carbonization and halogenation for the removal of radionuclides from spent cation-exchange resin (CER). Based on a thermal analysis of cation-exchange resins, we propose a two-step thermochemical treatment process involving the conversion of spent CER into pyrocarbon and then the removal of radioactive elements from the carbonized CER by converting them volatile halides at very high temperatures. The proposed process mainly consists of a carbonization and halogenation reactor, a UHC (unburned hydrocarbon) combustor, and wet scrubber. A step-by-step experimental and numerical optimization study was conducted with the carbonization and halogenation reactor and the UHC combustor. The optimum operating conditions could be established based on the results of a thermal analysis of the CER, a nonisothermal kinetic analysis, a numerical modeling study of a plug flow reactor (PFR)-type combustor, and a thermodynamic equilibrium analysis of a system consisting of a mix of carbonized CER and halogenation gas. The results of this study present detailed design of a novel multifunctional reactor and operating conditions of a bench-scale carbonization and halogenation process. Basic performance tests using CER doped with nonradioactive Co and Cs, indicated as Cs-137/134 and Co-60/58, were conducted under the optimized conditions. The results of these tests showed that the novel thermochemical process proposed in this study is a viable process that effectively removes radioactive elements from spent CER.

Citation: Yang, H.-C.; Park, H.-O.; Park, K.-T.; Kim, S.-J.; Kim, H.-J.; Eun, H.-C.; Lee, K. Development of Carbonization and a Relatively High-Temperature Halogenation Process for the Removal of Radionuclides from Spent Ion Exchange Resins. *Processes* **2021**, *9*, 96. <https://doi.org/10.3390/pr9010096>

Received: 30 November 2020

Accepted: 30 December 2020

Published: 5 January 2021

Publisher's Note: MDPI stays neutral with regard to jurisdictional claims in published maps and institutional affiliations.



Copyright: © 2021 by the authors. Licensee MDPI, Basel, Switzerland. This article is an open access article distributed under the terms and conditions of the Creative Commons Attribution (CC BY) license (<https://creativecommons.org/licenses/by/4.0/>).

Keywords: carbonization; halogenation; spent resin; kinetic analysis; thermodynamic analysis; numerical optimization

1. Introduction

Ion-exchange (IE) polymer is an insoluble solid resin that acts as a medium for the ion exchange process. When it comes into contact with a liquid that contains ions in a solution, it exchanges some of its constitutive ions with other ions [1,2]. IE resins are widely used in various separation, purification, and decontamination processes. Both chemical (coal and gas) and nuclear power plants utilize organic IE resins to polish condensate materials within water stream circuits [3]. Over time, these IE resins must be regenerated or replaced. When this happens, the spent IE resins must be disposed of and, as such, spent IE resins are a major fraction of the hazardous organic waste from power plants [4].

Spent IE resins, a type of combustible organic waste, cannot be readily disposed due to problems associated with the emissions of toxic gases and volatile radioactive elements [5,6]. Despite such difficulties, the organic fraction of spent IE resins should be

properly decomposed, and the decomposition residue should then be immobilized for safe disposal in a radwaste repository. There have therefore been many studies of the low-temperature pyrolysis of spent IE resins in the nuclear industry. Brähler and Slametschka (2012) studied low-temperature pyrolysis of spent ion-exchange resins in a pebble bed at approximately 500 °C with keeping radioactive cesium species in the solid pyrolysis residue [7,8]. An earlier study by Peterson and Kemmler (1984) involved the drying of wet spent resins and the pyrolysis of dried powder-type resins at 300–350 °C with keeping radioactive elements in the pyrolysis residue, which in that case was mostly composed of ash and carbon [9]. Matsuda et al. (1987) investigated the influence of functional sulfonic acid group on the pyrolysis characteristics for cation exchange resins [10]. These studies focused on the pyrolysis conditions that allow the retention of radioactive elements in a pyrolysis residue. However, pyrolysis residues bearing radioactive and hazardous elements should be further treated and transformed into a high-integrity waste form that can be safely disposed of in a radwaste repository. These processes result in a significant increase in the volume of the final waste form.

The portion of inorganics, including ion-exchanged radioactive elements and dirt, is at most approximately 2% of dried spent IE resins [11]. Conventional thermal treatment technologies such as incineration and other similar thermal treatment processes, i.e., high-temperature plasma and pyrolysis processes, which combust or gasify most organic constituents in IE resins, have led to valuable reductions in waste volumes. Instead, however, a very large volume of off-gas bearing UHCs (unburned hydrocarbons), acid gases, and toxic and radioactive elements are generated. The emission of these hazardous constituents in the off-gas can be effectively controlled using currently well-developed APCDs (air pollution control devices). However, the use of a very sizable off-gas treatment system, which must become radioactive decommissioning waste itself at the end of its service life, is unavoidable. Generally, this overly significant flaw means such devices cannot be readily commercialized as a radioactive facility.

This work proposes a novel thermochemical decontamination process for spent IE resins conducting a two-stage process of the carbonization of organic constituents and the halogenation removal of radionuclides from carbonized IE resins. The proposed process initially converts the organic constituents of spent IE resins into pyrocarbon. The radionuclides in the carbonized spent resins are then readily removed by converting them into volatile halides in a halogenation atmosphere at higher temperatures. Three key unit processes are carbonization, the combustion of pyrolysis gas during carbonization, and the halogenation removal of radioactive elements in the carbonized resins.

A step-by-step experimental and numerical optimization study for these key unit processes was conducted in this study. An appropriate operation condition for a carbonization reactor was initially determined through a kinetic analysis of the carbonization of cation-exchange resin (CER). The generation of UHCs during the carbonization process was then experimentally investigated. The carbonization of CER generates various aromatic hydrocarbons, such as styrene, toluene, and benzene. Fortunately, these UHCs are key components of commercial liquid fuels such as benzene and toluene; thus, an extensive range of experimental data on the kinetics of combustion reactions for these UHCs is available in the literature [12]. Parametric modeling studies could therefore be conducted to determine an appropriate condition for UHC combustion for the substantial burnout of the UHCs generated during the course of carbonization.

The behavior of radionuclides in the waste thermal treatment process was investigated in a thermodynamic equilibrium modeling study. This was done because a detailed accounting of all possible reactions for inorganic compounds at high temperatures is not available, unlike in the case of the gas-phase combustion mechanisms of organic constituents. Ho et al., investigated the behavior of uranium and plutonium during a thermal treatment of waste under oxidizing and reducing conditions [13]. The behaviors of various radionuclides in irradiated graphite during combustion and hydrothermal oxidation were also investigated by a thermodynamic modelling approach [14]. These equilibrium mod-

elling studies were done in an effort to establish a thermal treatment condition that avoids the emission of radionuclides by volatilization. The present study also used a thermodynamic equilibrium modelling study of the behavior of radionuclides under halogenation treatment conditions. On the other hand, however, the present study established the range of the reactor operating condition for the volatilization-related removal of radionuclides by means of thermodynamic modelling.

A bench-scale carbonization and halogenation process was designed and installed based on the results of the experimental and modeling studies of these key unit processes. The capability of this process with regard to the removal of radionuclides from spent resins was demonstrated using non-radioactive surrogates under experimentally and numerically determined appropriate carbonization and halogenation process conditions.

2. Principle of Carbonization/Halogenation Treatment

2.1. Characteristics of a Target Waste Stream

The target waste stream in this study is spent CER (cation-exchange resin) of the type generated in the nuclear industry. The principal applications of ion exchange processes in nuclear facilities are the removal of contaminants from wastewater effluents and the demineralization of process water streams. A granular type of mixed IE resin with a 1.2:1 cation-to-anion ratio is generally used in nuclear power plants. CER is denser than AER (anion exchange resin). The spent mixed resin bed is conventionally separated by passing water up through the resin bed for fluidization, therefore allowing the denser CER to settle first [11]. It is crucial for the most appropriate method to be applied for each separated spent resin stream after separation. Spent CER bearing metallic radionuclides such as Cs-137 and Co-60 is the target waste type in this study. The chemical structure of the strong acidic CE resins used in this study is shown in Figure 1. The ion-exchange mechanisms of two typical ions, a one-valence-count ion (Cs^+) and a two-valence-count ion (Co^{2+}), as examples, are also described in Figure 1.

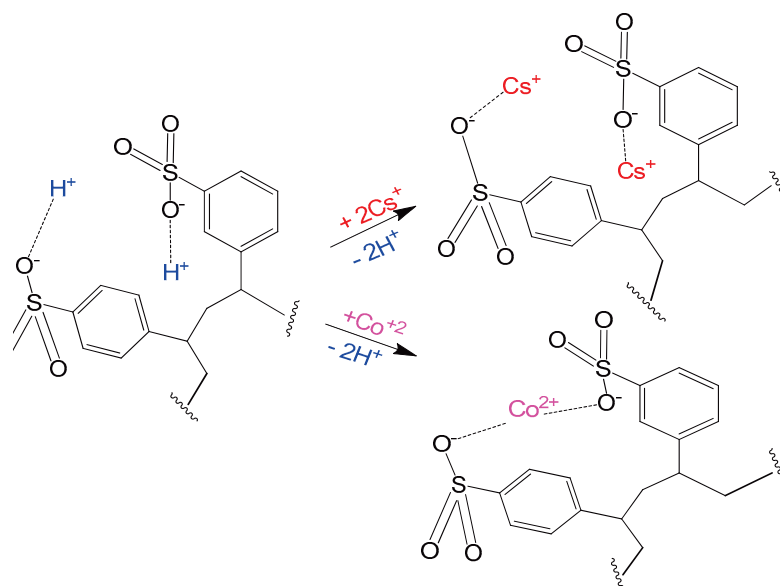


Figure 1. Chemical structure of the strong acidic cationic ion exchange (IE) resins with functional groups of $-\text{SO}_3\text{H}^+$ and ion-exchange mechanisms of two typical ions of a one-valence-count ion (Cs^+) and a two-valence-count ion (Co^{2+}).

2.2. Principle of the Proposed Process

The principle of the carbonization and halogenation process for the removal of radionuclides from spent CER is shown in Figure 2. Carbon materials are stable, even at very high temperatures, in the absence of oxygen. If we convert spent CER into carbon

materials after removing moisture and volatiles, we can then treat them with halogen gases at very high temperatures. The first step of the proposed process is low-temperature pyrolysis followed by carbonization. During the course of the low-temperature pyrolysis step, moisture and volatiles are removed and the remaining carbon-bearing organics are then converted into pyrocarbon at higher temperatures. During this pyrolysis and carbonization step, captured radioactive metal species such as Cs and Co in the spent CER, as depicted in Figure 1, are converted into their corresponding sulfates or sulfides [15]. The next step is the halogenation treatment of the carbonized spent CER to convert radioactive elements into volatile chlorides. Spent CER contains various types of radionuclides of different origins, including nuclear fuel fission products such as Cs-134, Cs-137, and Sr-90 and activation products such as Fe-59, Co-58, Co-60, Mn-54, Zn-65, and Zr-95. All of these metallic radioactive species remaining in carbonized resins can be removed by converting them into their respective volatile halides by halogenation gases at high temperatures.

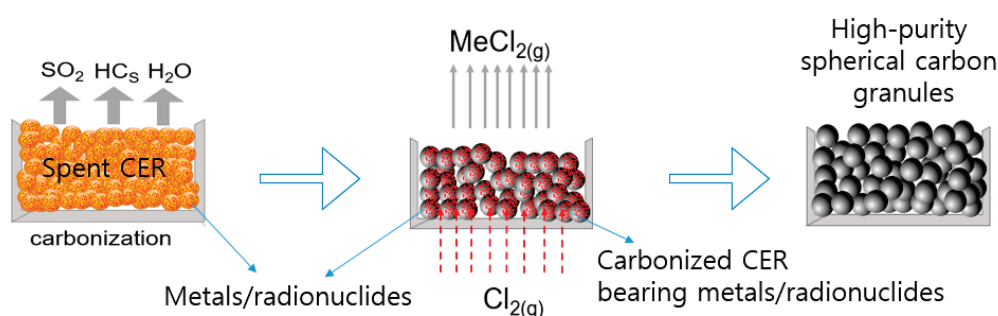


Figure 2. Principle of the carbonization and halogenation treatment process for the removal of radionuclides from spent ion-exchange resins.

The granular form of carbonized CER is stable at very high temperatures under a halogenating gaseous condition, such as chlorine and fluorine. However, metals and radionuclides in any other chemical form are converted into their respective volatile halides at high temperatures. If we use chlorine as a halogenating gas, as shown in Figure 2, the sulfate or sulfide forms of radionuclides are converted into their corresponding chlorides. Chlorides of metals and radionuclides have high vapor pressures at high temperatures, and they vaporize into a gaseous stream.

The gas effusion process, the diffusion into micropores of carbon materials, speeds up considerably at higher temperatures. Halogenating gases such as chlorine and fluorine readily diffuse into micropores in the spherical form of carbonized resin and then convert inorganic species into volatile halides. During this process, the major element carbon, C, in the carbonized resins facilitates the halogenation process by taking over oxygen from inorganic compounds. Using the proposed two-step thermochemical process, consisting of carbonization and halogenation, we can readily separate radioactive metal species from spent CER.

3. Experimental and Numerical Optimization Study for Key Processes

3.1. Procedure of Experimental and Numerical Modeling Study

The key process units in the proposed process to be optimized to design a bench-scale process for trial tests are a carbonization/halogenation reactor for spent CER and an oxidizer for the UHCs (unburned hydrocarbons) generated during the course of the carbonization of CER. The purpose of this experimental and modeling study was to establish design conditions and the appropriate range of operating conditions of these two key process units. Step-by-step numerical determination of the operating conditions for these two process units were carried out, and these results were used to design of the bench-scale process for trial tests. The establishment of the carbonization condition of spent CER was initially conducted by means of a kinetic analysis and through a prediction

of the carbonization reaction of the CER. Establishment of the operating condition of the UHC combustor for the burnout of the UHCs generated during the carbonization of CER under the optimized condition was then established by a numerical modeling study of a PFR (plug flow reactor) type of combustor. As a final step, an optimum range of the halogenation process conditions for carbonized spent resins was determined.

3.2. Establishment of the Carbonization Reactor Condition

3.2.1. Analysis of Pyrolysis and Carbonization Steps

A TGA (thermogravimetric analysis) system (SETSYS-Evolution, SETARAM, Lyon, France) was used to investigate the carbonization characteristics of CER. A commercially used form of CER, Amberlite IRN-77 (Rohm and Haas, Philadelphia, PA, USA), with the chemical structure shown in Figure 1, was used in this study. Nonisothermal TGAs with a heating rate of 1 K/min for the CER dried in an oven at 100 °C for 24 h were conducted under an inert atmosphere (>99.999% Ar). The changes in the sample weight and the derivative of the sample weight at elevated temperatures are plotted in Figure 3. Three pyrolysis steps, denoted as R1, R2, and R3, are clearly discriminated by dTG (derivatives of TG, dW/dt) plot. The approximate temperature ranges of R1, R2, and R3 were 50–250 °C, 250–450 °C, and 450–800 °C, respectively.

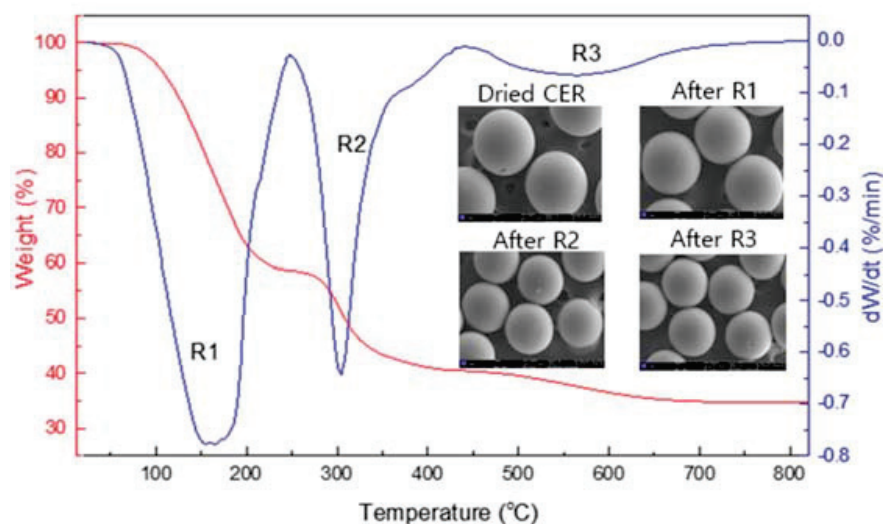


Figure 3. Changes of the sample weight (TG) and derivative of the samples weight (dTG) at elevated temperatures, and SEM image of dried sample and those after the R1, R2, and R3 reaction steps.

The SEM images of the CER granules, which were pyrolyzed to approximate ending temperatures of R1, R2, and R3 (250 °C, 450 °C, and 800 °C, respectively), are also shown in Figure 3. The first weight loss reaction R1, corresponding to approximately 40% of the initial CER weight, is mainly due to the thermal dissociation of SO₂ from polystyrene sulfonate and the vaporization of moisture in the dried CER [15]. The second reaction step R2, corresponding to approximately 20% of the initial CER weight, may be due to the partial decomposition of polystyrene granules. The size of the granules was reduced significantly by shrinkage during the R2 reaction step due to the pyrolysis of polystyrene copolymer upon the emitting of volatile hydrocarbons. No significant reduction in the size of granules was found for the R3 reaction step. This suggests that the third reaction step is the carbonization step. The R3 reaction step continued to approximately 800 °C. Weight loss of approximating 5% was found as a result of this step, although it started at 450 °C and continued for 350 min when ramping up the temperature of the samples from 450 °C to 800 °C. No further weight loss was noted at elevated temperatures exceeding 800 °C. This confirms the R3 reaction step as the carbonization step.

A nonisothermal kinetic analysis and a prediction of the carbonization reaction step, indicated as R3 in Figure 3, were conducted to establish an appropriate carbonization reactor condition. In a nonisothermal system, reaction rates are given as a function of two time-dependent variables: The temperature (T) and the reaction progress (α). This is expressed as

$$\frac{d\alpha}{dt} = A \exp\left(\frac{-E}{RT}\right) f(\alpha), \quad (1)$$

where α is the weight reduction fraction, A is the pre-exponential (frequency) factor, E is the activation energy, T is the absolute temperature, R is the gas constant, and $f(\alpha)$ is the reaction model [16]. For the TGA study, α is defined as

$$\alpha = (m_0 - m_t) / (m_0 - m_f), \quad (2)$$

where m_0 , m_t , and m_f are the initial weight, the weight at processing time t , and the final weight, respectively. In a nonisothermal heating system with a constant heating rate ($dT/dt = B$), the reaction rate is given by the following Equation (3):

$$\frac{d\alpha}{dT} = \frac{A}{B} \exp\left(\frac{-E}{RT}\right) f(\alpha) \quad (3)$$

Multiple chemical reactions occur during reaction step R3; thus, precise knowledge of reaction model $f(\alpha)$ is not available. Therefore, a differential isoconversional method, which does not require an explicit assumption of the form of $f(\alpha)$, and constancy of A and E , were used during the kinetic analysis of the nonisothermal TGA data [16]. The differential isoconversional method by Friedman [17] was used in this study. This method is based on the logarithm shown in Equation (3). The values of the kinetic triplets A_α , E_α , and $f(\alpha)$, which change with the reaction progress α , can be obtained as a function of α by the following Equation (4):

$$\ln \left[B \left(\frac{d\alpha}{dT} \right) \right] = \ln [A_\alpha f(\alpha)] - \frac{E_\alpha}{RT} \quad (4)$$

The results of the nonisothermal TGAs of the CER with heating rates of 0.5, 1, 1.5, and 2 under an inert atmosphere (>99.999% Ar) are shown in Figure 4a. The reaction rates at different heating rates determined by the nonisothermal TGA data are plotted in Figure 4b. A detailed kinetic study of reaction step R3, which is considered as the carbonization reaction step, was done using the reaction rate data in the temperature range of 400–800 °C.

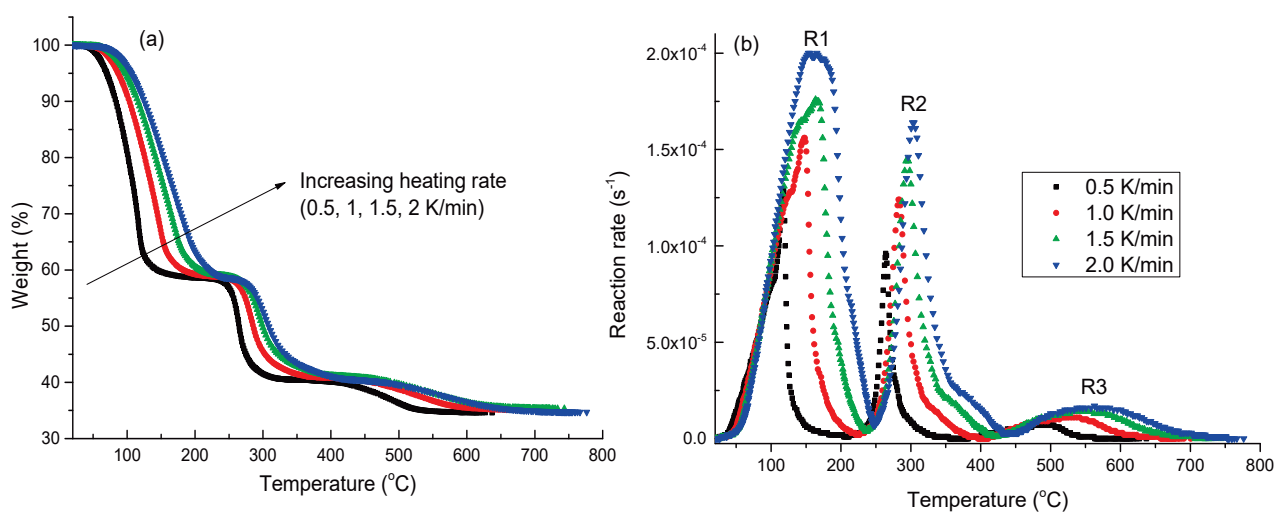


Figure 4. Weight changes of cation-exchange resin (CER) (a) and the reaction rates (b) determined by the nonisothermal TGAs with different heating rates of 0.5, 1.0, 1.5 and 2.0 K/min.

Plots for the determination of the activation energy E_α and modified pre-exponential factor $A'(\alpha)$ ($=A_\alpha f(\alpha)$) for reaction step R3 were constructed using Equation (4); these are shown in Figure 5a. The values of E_α and $A'(\alpha)$ determined by the slopes and intercepts of straight lines in Figure 5a are shown in Figure 5b.

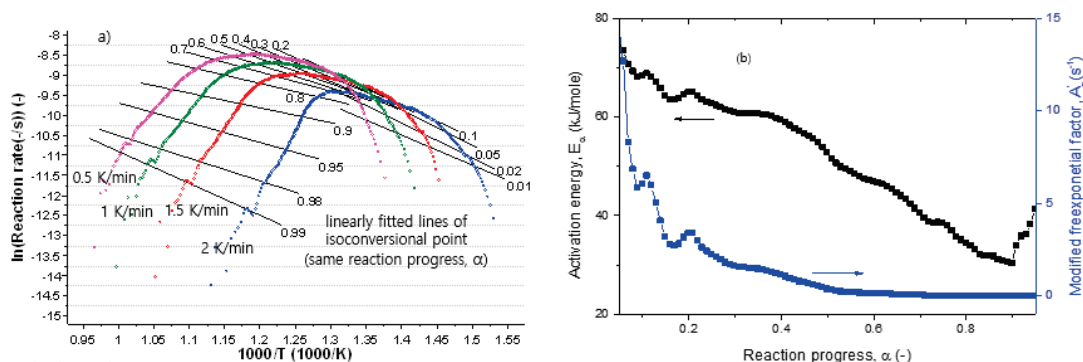


Figure 5. Plots for the determination of the activation energy E_α (a) and the determined modified pre-exponential factor $A'(\alpha)$ ($=A_\alpha f(\alpha)$) for reaction step R3 (b).

3.2.2. Establishment of the Carbonization Reactor Condition

An accurate interpretation of the kinetic model is not possible when multiple reactions simultaneously occur because E_α and $A'(\alpha)$ vary with the reaction progress α , as shown in Figure 5b. However, a kinetic prediction for the determination of the time and temperature profile of a reactor to obtain the target reaction progress α when treating the material is possible by applying the determined values of the kinetic triplets (E_α and $A'(\alpha)$ ($=A_\alpha f(\alpha)$)) of any reaction progress α to Equation (5) below.

$$t_\alpha = \int_0^{t_\alpha} dt = \int_0^\alpha \frac{d\alpha}{A_\alpha f(\alpha) \exp\left(-\frac{E_\alpha}{RT}\right)} \quad (5)$$

A set consisting of the reactor temperature and processing time required to complete the progress of carbonization reaction R3 can be established using Equation (5). The progress of carbonization step (reaction step R3) for several different pyrolysis temperature profiles was calculated based on the values of the kinetic triplets shown in Figure 4b using AKTS-Thermokinetics software [18,19]. An example of the optimized pyrolysis condition is shown in Figure 6. If the reactor is heated to 800 °C and sustained for 40 min at 800 °C, carbonization of CER will be completed. Additionally, the progress of the R1 and R2 reactions steps must also be completed during the course of elevating the temperature of the carbonization reactor up to 800 °C. An optimized carbonization condition is the slow heating of the spent CER to 800 °C from 300 °C at a heating rate of 10 K/min to avoid the sudden generation of a large amount of UHCs, and then holding the temperature at 800 °C for 40 min.

3.3. Determination of Operating Condition of the UHC Combustor

3.3.1. UHCs Generated by the Carbonization of CER

The carbonization process generates a significant amount of UHCs, which should be properly decomposed and oxidized into H₂O and CO₂. The characteristics of the UHCs generated during the carbonization of CER were investigated using a Py(pyrolysis)-GC/MS (pyrolysis-gas chromatography and mass spectrometer). The instruments used were a portable pyrolyzer (JCI-21) and the HP6890N GC/MS system. The Py-GC/MS result using a pyro-foil at the Curie point temperature of 764 °C are shown in Figure 7. Various types of aromatic hydrocarbons were generated during result pyrolysis of CER. The major UHCs generated were aromatic hydrocarbons. These were C₆H₆, C₆H₅CH₃,

$C_6H_5CH_2CH_3$, and $C_6H_5CH=CH_2$, and their molar compositions based on the peak areas of the GC chromatogram were 7.21%, 15.08%, 12.21%, and 49.08, respectively.

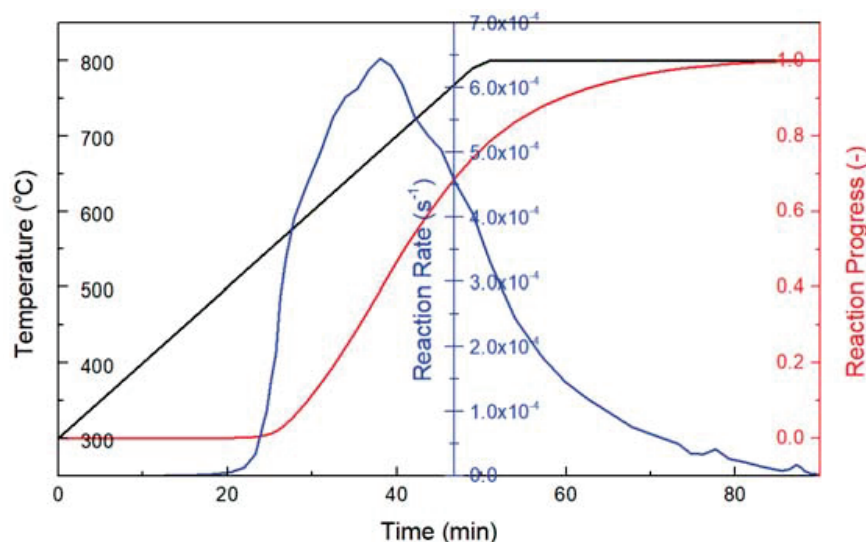


Figure 6. Optimized carbonization reactor heating condition for the completion of carbonization reaction step (R3) with a slow ramping rate to 800 °C to avoid the sudden generation of a large amount of UHCs.

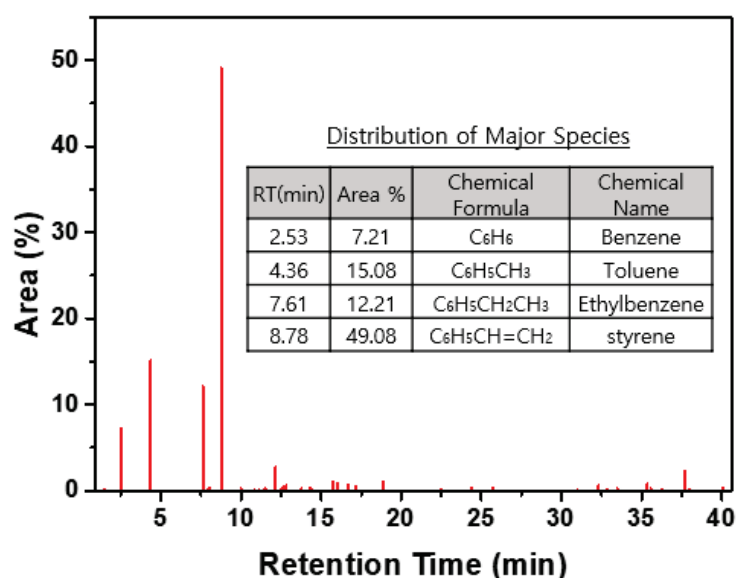


Figure 7. Py-GC/MS result when using a pyro-foil at the Curie point temperature of 764 °C and distribution of the major species of UHCs.

3.3.2. Numerical Determination of the UHC Combustor Operating Condition

A numerical modeling study of the UHC combustor was conducted to design a bench-scale process with a capacity of 5 kg/batch. The simulated conditions for the determination of the UHC combustor operating condition are shown in Figure 8. A cylindrical UHC combustor with a 5 cm inner diameter was assumed as an ideal PFR, in which there is no mixing in the axial direction but perfect mixing in the traverse direction. Parametric model studies of the UHC combustor were performed with ANSYS Chemkin Pro [20]. Chemical kinetic reaction mechanisms for n-alkane hydrocarbons developed by Westbrook et al. [21] were used. The mechanisms were used for the simulation of the combustion of

the normalized composition of generated aromatic hydrocarbons (C_6H_6 : 8.6%, $C_6H_5CH_3$: 18.1%, $C_6H_5CHCH_2$: 58.7%, and $C_6H_5CH_2CH_3$: 14.6%). It was assumed that SO_2 is not involved in the combustion reactions of the UHCs. Based on a treatment rate of 1 kg spent CER/h and a mass loss fraction of the R1 and R2 steps determined by the TGA, as shown in Figure 2, the program input feed rate of gaseous species to the UHC combustor was 0.3 kg/h. The parameters varied for the UHC combustor simulation were the heating temperature, PFR length with a diameter of 5 cm, and equivalence ratio ϕ (the actual air–UHC ratio to the stoichiometric air–UHC ratio for combustion), as shown in Figure 8.

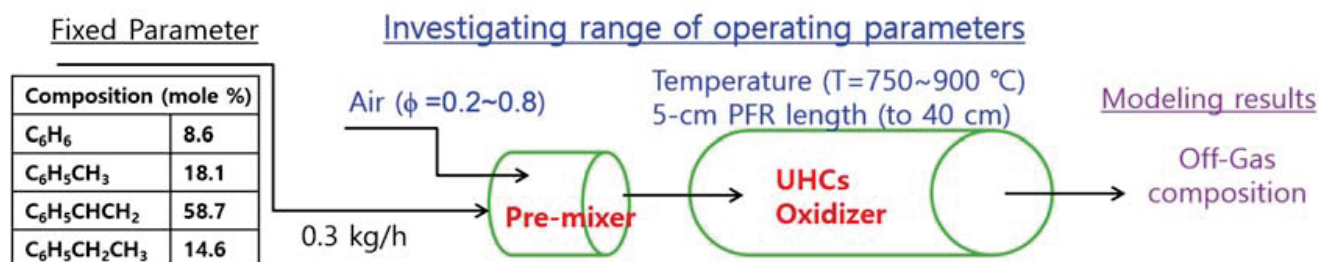


Figure 8. Simulated conditions for the determination of the unburned hydrocarbon (UHC) combustor operating condition.

The concentrations of the fed UHCs at a ϕ value of 0.2 and temperature of 750 °C as a function of the reactor distance are shown in Figure 9a. The reactor length of 16 cm is a critical distance for the substantial destruction of fed UHCs under this condition. Figure 9b shows that various types of other aromatic hydrocarbons were newly formed during the thermal decomposition of the fed UHCs. These were also substantially decomposed just before the reactor length of 16 cm. A significant amount of a product of incomplete combustion (PIC), carbon monoxide (CO), however, remained after the reactor length of 16 cm. The carbon monoxide was nearly completely oxidized at the length of ≥ 20 , as shown in Figure 9b.

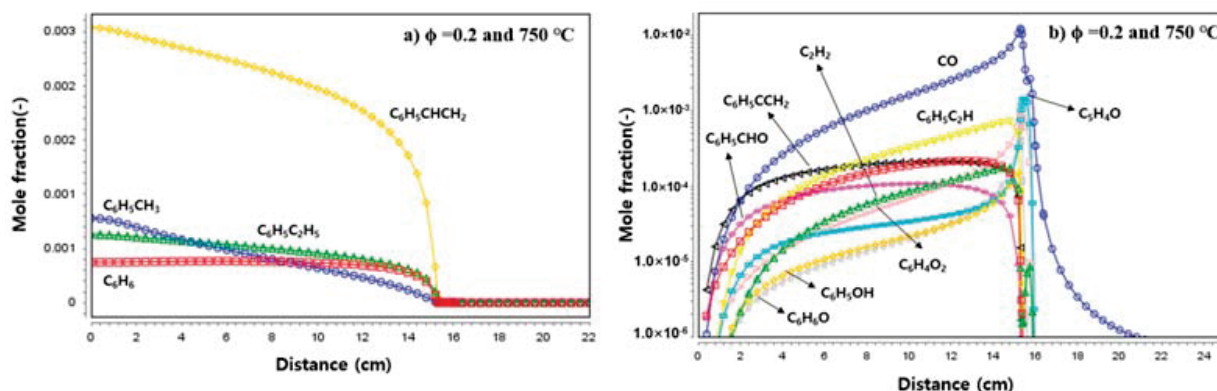


Figure 9. Concentrations of fed UHCs (a) and those of newly formed UHCs and CO (b) at a ϕ value of 0.2 and temperature of 750 °C as a function of the reactor distance.

The reaction pathways of $C_6H_5CH_3$ and $C_6H_5C_2H_5$ into C_6H_6 and that of C_6H_6 into CO_2 are depicted in Figure 10. The largest amount of UHC generated by the pyrolysis of CER, with the basic structure of polystyrene, is $C_6H_5C_2H_5$, as shown in Figure 1. $C_6H_5C_2H_5$ is decomposed into C_6H_6 and CO via $C_6H_5CH_2$, and $C_6H_5C_2H_3$, respectively, as shown in Figure 10a,b. The $C_6H_5C_2H_3$ was the primary decomposition product of $C_6H_5C_2H_5$. As shown in Figure 10a,b, a significant amount of C_6H_6 is generated during the course of the thermal decomposition of $C_6H_5C_2H_5$ and $C_6H_5CH_3$. This explains the delayed decomposition of C_6H_6 shown in Figure 9a. The concentration of C_6H_6 was nearly constant to the length of 10 because the decomposition rate of the fed C_6H_6 is nearly equal to the

formation rate of C_6H_6 due to the decomposition of the fed hydrocarbons until the length of 10 cm. The steep increase in the CO_2 concentration during the course of the decomposition of the fed UHCs was due to the rapid increase in the generation of CO with the temperature according to the reaction pathway shown in Figure 10.

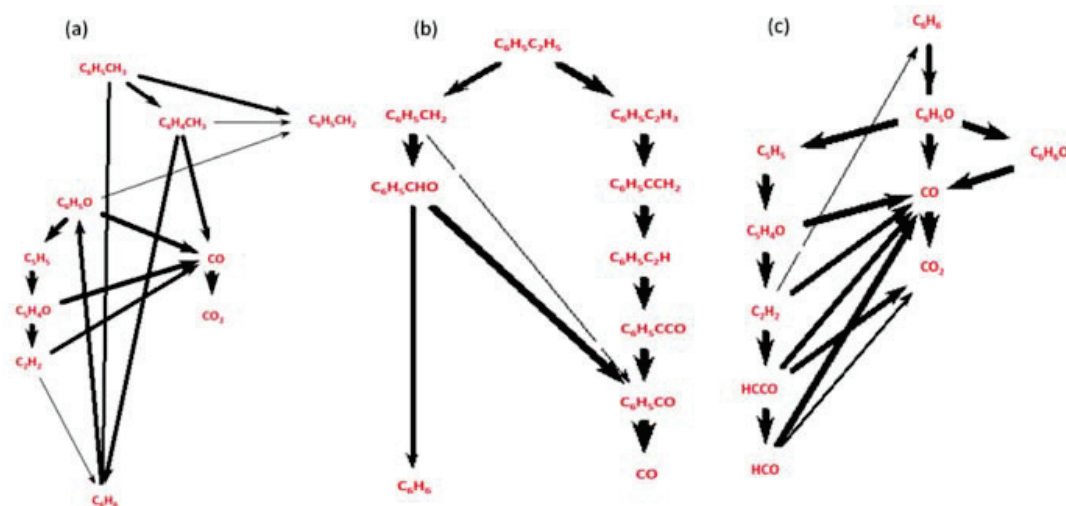


Figure 10. Reaction pathways of $C_6H_5CH_3$ (a) and $C_6H_5C_2H_5$ (b) into C_6H_6 , and that of C_6H_6 (c) into CO_2 .

The concentrations of the fed UHCs at ϕ value of 0.5 and reactor temperature of $750^\circ C$ as a function of the reactor distance are shown in Figure 11a. The critical point of the reactor length is approximately 30 cm for the substantial destruction of the fed UHCs under this condition. Figure 11b shows that the aromatic hydrocarbons generated are also substantially decomposed at the reactor length just before 30 cm. However, 3000 ppm of carbon monoxide (CO) remaining after the reactor length of 16 cm is not further oxidized to 40 cm at a ϕ value of 0.5. The carbon monoxide (CO) cannot be substantially oxidized at a ϕ value of 0.5 and at $750^\circ C$ regardless of the reactor length (residence time).

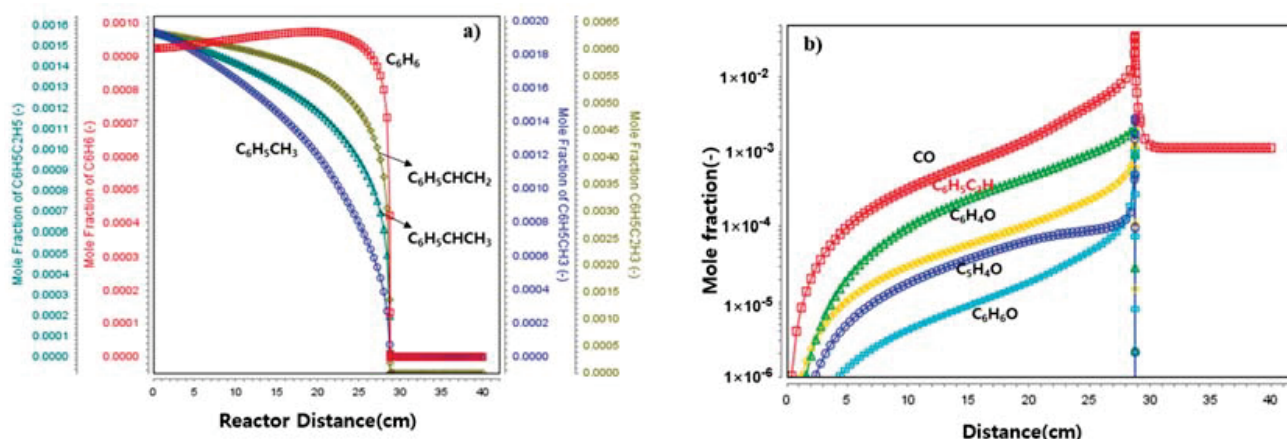


Figure 11. Concentrations of fed UHCs (a) and those of newly formed UHCs and CO (b) at a ϕ value of 0.5 and temperature of $750^\circ C$ as a function of the reactor distance.

The UHC concentration when $\phi = 0.5$ as a function of the PFR length and PFR temperature is plotted in Figure 12a. This 3-D contour plot shows a wide range of UHC combustor operating conditions for the substantial destruction of UHCs. As an example, UHCs are completely decomposed at a temperature of $\geq 800^\circ C$ and PFR length of 10 cm. However, the most critical parameter is the air equivalence ratio, which significantly influences the emission of CO, as shown in Figure 12b,c. In order to lower the emission

concentration of CO to a level below the emission standard (100 ppm), $\phi = \leq 0.35$ is required at 800 °C. The design and operating parameters of the PFR-type UHC combustor were determined as follows: A PFR length of 10 cm (ID = 5 cm), a heating temperature of 800 °C, and a ϕ value of 0.3. The determined appropriate condition will result in the substantial destruction of UHCs and the oxidation of PICs without excess installation and operating costs.

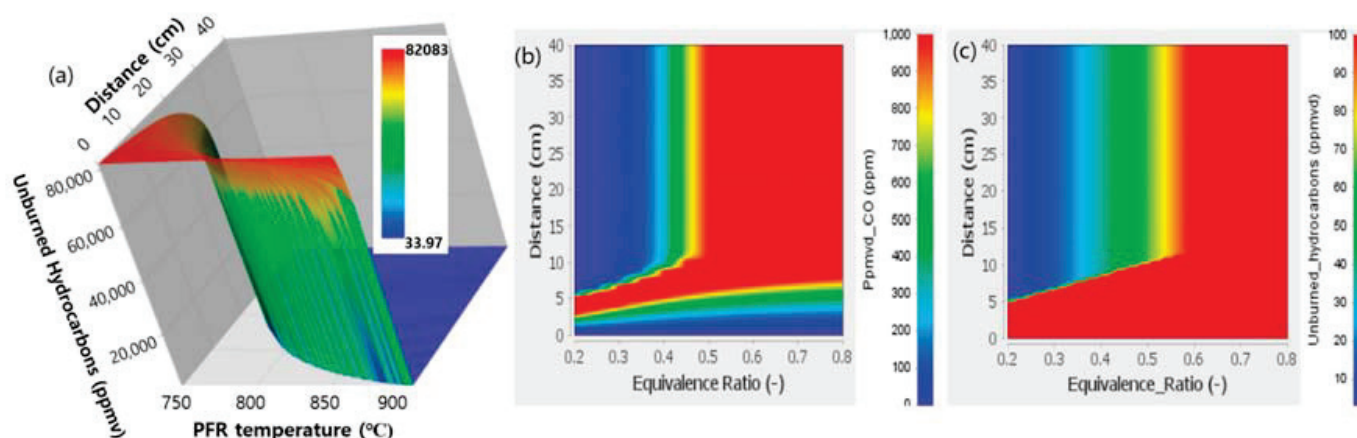


Figure 12. UHC concentration at $\phi = 0.5$ as a function of the plug flow reactor (PFR) length and PFR temperature (a), and concentrations of CO (b) and UHCs (c) at 800 °C as a function of the PFR distance and air equivalence ratio (ϕ).

3.4. Determination of the Appropriate Halogenation Condition

The halogenation treatment condition was thermodynamically modelled to determine the ranges of reactor operating temperatures and the feed halogen gas concentration, which is also required for a detailed design and the selection of reactor materials. The mechanism of the vaporization of the elements is the distribution of the elements as a result of chemical reactions within the thermal treatment system. The exact distribution requires knowledge of all constituents, of all the possible reactions, and the reaction rate constants, as conducted for the determination of operating condition for the UHC combustor in this study. Accurate comprehension of the chemical reaction rate data is not available for inorganic elements with gases at high temperatures. In the absence of reaction rate data, it is often assumed that all reactions achieve chemical equilibrium in a relatively short period of time when compared to the total residence time of the reactants [22]. This is a possible approach to the problem, as numerous chemical reactions take place in the system despite the fact that all of the reaction data are not available [23].

The equilibrium model analysis in this study is based on the following assumptions: (1) Thermodynamic equilibrium is maintained in the halogenation reactor, and (2) all of the radioactive species present in the carbonized resins or gas-phase elements in the reactor are intimately mixed. If a given mixture of species undergoes a change that minimizes the total Gibbs free energy, this represents an equilibrium state and corresponds to the complete conversion of the reactants to products. The Gibbs energy function of a system is expressed as

$$G = \sum_{k=1}^K \bar{g}_k N_k, \quad (6)$$

where \bar{g}_k is the partial molar Gibbs energy function and N_k is the number of moles of each species k in the system; K is the total number of species. For ideal-gas mixtures or ideal solutions, the partial molar Gibbs function is given by

$$\bar{g}_k = g_k(T, P) + RT \ln X_k, \quad (7)$$

where $g_k(T, P)$ is the Gibbs function for the pure species k evaluated at the system temperature and pressure, R is the universal gas constant, and X_k is the mole fraction of the k th species. The equilibrium solution at a given temperature and pressure is the distribution of N_k that minimizes the system Gibbs energy function G subject to atomic population constraints (and a non-negative N_k). The atomic population constraints are as follows:

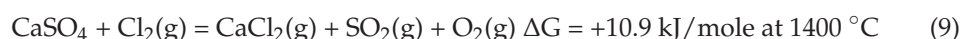
$$\sum_{k=1}^K n_{jk} N_k = P_j, \quad j = 1, \dots, M \quad (8)$$

Here, n_{jk} is the number of the j th atoms that appear in the k th molecule, P_j denotes the total population in moles of the j th atom in the system, and M is the total number of different elements present in the system. HSC-Chemistry 7.1 software was used for the model calculation [24]. The simulated compositions of the carbonized spent CER and chlorination gas are shown in Table 1. The simulated mixing ratio of the condensed phase material (carbonized resin) to the chlorination gas was unity.

Table 1. Chemical composition of carbonized CER and chlorination gas for the equilibrium model calculation for the determination of the appropriate chlorination reactor condition.

Carbonized CER (Mole %)				Chlorination Gas (mole %)	
Non-Radioactive Compounds (wt.%)		Radioactive Compounds ($\times 10^{-6}$)			
C	0.80	$^{134/137}\text{Cs}_2\text{SO}_4$	0.007	Cl_2	0.1
Na_2SO_4	0.025	$^{58/60}\text{CoSO}_4$	0.012	N_2	0.8998
CaSO_4	0.0006	$^{90}\text{SrSO}_4$	0.008	O_2	0.0001
$\text{Fe}(+^{59}\text{Fe})\text{SO}_4$	0.0023	$^{54}\text{MnSO}_4$	0.01	H_2O	0.00005
$\text{Cr}_2(\text{SO}_4)_3$	0.0011	$^{65}\text{ZnSO}_4$	0.006	CO_2	0.00002
MgSO_4	0.00046	$^{95}\text{Zr}(\text{SO}_4)_2$	0.004		
NiSO_4	0.000041				

The calculated results for the equilibrium mole fractions of the nonradioactive compounds and radioactive compounds are shown in Figure 13a,b respectively. Carbon, the major component of carbonized CER, plays an important role in the conversion of inorganic elements into volatile chlorides. As shown in Table 1, inorganic elements exist in the form of their respective sulfides, which are relatively stable at high temperatures. Figure 13a shows the increased mole fractions of $\text{S}(\text{g})$ and $\text{CO}(\text{g})$. This indicates that metal sulfides are readily reduced and chlorinated in the presence of carbon and chlorine. The following reaction, expressed by Equations (9) and (10), shows the significant role of carbon during the volatilization of metals in the form of nonvolatile sulfate. Calcium sulfate (CaSO_4) is a non-volatile compound at approximately ≤ 1500 °C. As an example, as shown in Equation (9), CaSO_4 is not converted into its volatile chloride (CaCl_2) in the presence of chlorine at 1400 °C. However, in the presence of carbon, CaSO_4 is readily converted into its volatile chloride (CaCl_2), even at a much lower temperature of 1000 °C.



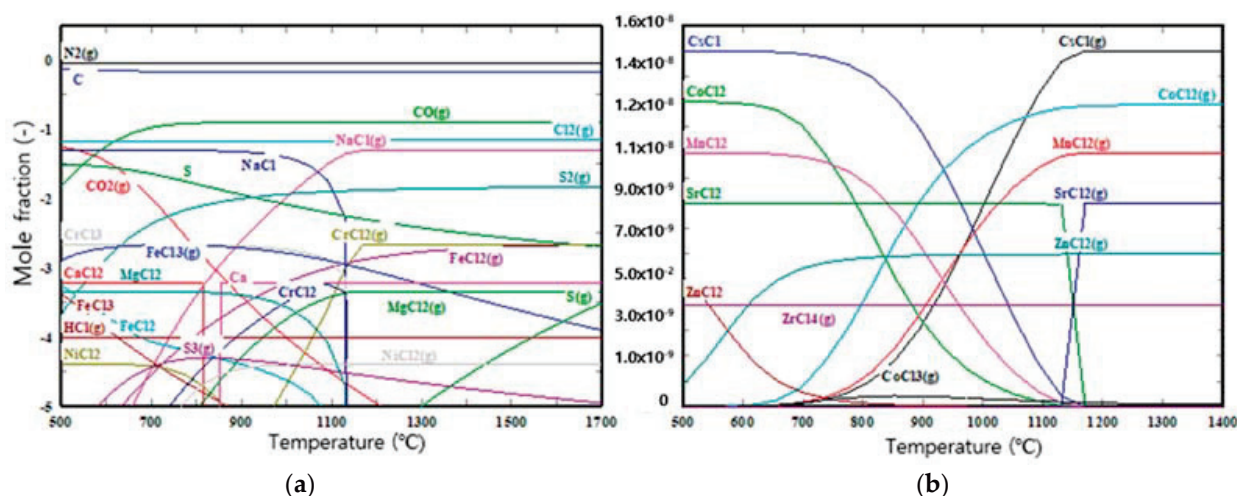


Figure 13. Calculated results for equilibrium mole fractions of nonradioactive compounds (a) and radioactive compounds (b).

Figure 13b shows the thermodynamically stable forms of the radioactive elements and their respective volatile chlorides at a temperature of ≥ 1130 °C. If we continuously flow chlorine gas through the bed of the carbonized resin granules at ≥ 1200 °C, we can readily remove metallic and radioactive elements from the granules.

4. Installation of a Bench-Scale Process and Test Operation

4.1. Process Description

The thermochemical decontamination process is a two-stage process of carbonization and halogenation. Figure 14 shows the arrangement of unit for the proposed thermochemical processes. The key units are a carbonization/halogenation reactor, the UHCs (unburned hydrocarbons), a combustor, and a wet acid gas scrubber. The detailed designs of the carbonization/halogenation reactor and PFR-type UHC combustor were created based on the results of a numerical modeling study. During the first stage of the treatment, the pyrolysis and carbonization of the spent CER, significant amounts of H₂O, SO₂, and UHCs are generated. To prevent the oxidation loss of graphite materials in the multifunctional reactor, a vacuum condition is maintained without supplying nitrogen during the course of carbonization. The complete sealing of the multifunctional reactor and the installation of a vacuum pumping system, as shown in Figure 14, were required for this purpose.

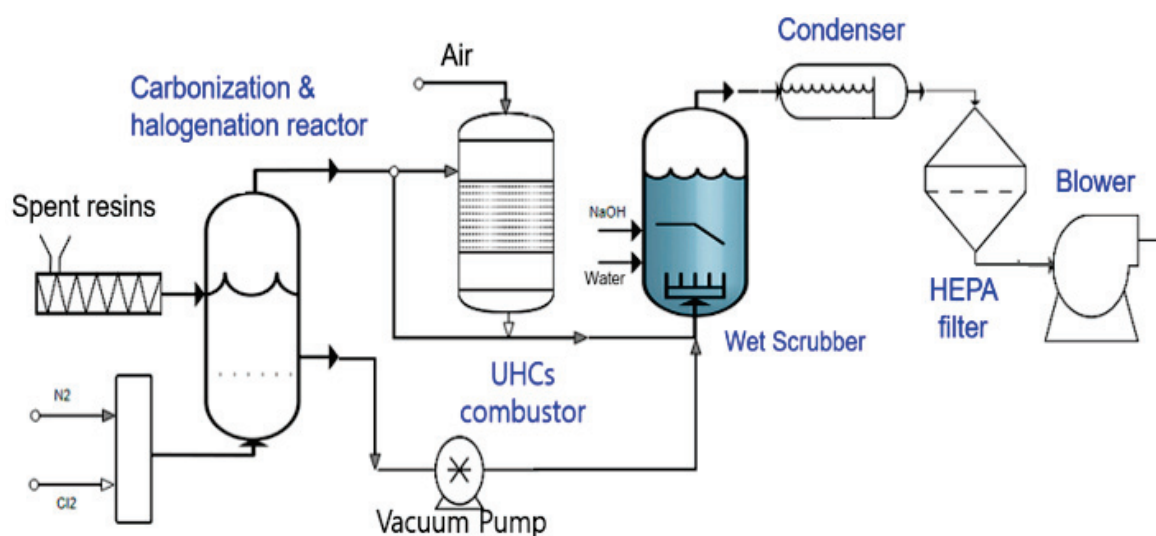


Figure 14. Arrangement of units for the proposed thermochemical processes.

UHCs are treated by the PFR-type combustor with a 5 cm ID and a 20 cm L with a supply of combustion air of $\phi = 0.3$ according to the determined a condition. SO_2 is collected in a conventional wet scrubber with an alkaline (NaOH) solution. During the second stage of the treatment, halogenation of pyrocarbon bearing radionuclides at a higher temperature generates vapors of metal/radionuclide halides. The vapors of these metallic species then condense into particulates as the off-gas cools. This is done by passing them through the wet scrubber, which is operated under atmospheric temperatures. Some portion of the particulates is collected in the wet scrubber and the remainder is collected in the HEPA filter with a collection efficiency of $\geq 99.97\%$ for $0.3 \mu\text{m}$ particles. In this manner, the generated flue gas bearing hazardous constituents with the acid gas (SO_2), UHCs, and vapors of hazardous/radioactive metal species are substantially collected at a level below the emission standards.

Two important advantages of the proposed process are the smaller plant size and the lower volume of the final radwaste requiring disposal. The generated volume of off-gas is much smaller because most of the carbon species in the CER are not gasified or combusted. This results in a smaller plant size when compared to that of a conventional radwaste incineration plant. In the proposed process, only inorganic elements are vaporized and collected as secondary radioactive waste. No carbon-bearing fly-ash due to the turbulence of combustion gas is generated during the proposed thermochemical process. Therefore, no primary filtering system, such as a bag-filter system, is required. These advantages result in a much smaller volume of secondary waste as well as a much smaller size of the off-gas treatment system.

4.2. Detailed Design of the Multifunctional Reactor and Test Results

The detailed design of the multifunctional reactor for the carbonization of the CER, images of the inside of the reactor after the feeding of the CER and after the treatment, and the results of the SEM-EDS (Scanning Electron Microscope-Energy Dispersive X-ray Spectrometer) analysis of the carbonized CER and the chlorination-treated carbonized CER are shown in Figure 15. As shown in Figure 15a, all reactor components are made of graphite, as graphite is the only material available that can endure halogen gases at very high temperatures. The processing materials, spent CERs, are spherical granules with diameters 0.3~0.8 cm in size. Therefore, a type of vertical packed-bed reactor, through which a carrier gas or a reacting gas flows up, is used as a multifunctional reactor. This multifunctional reactor conducts two different reacting processes in a stepwise manner.

Basic performance tests using CER doped with nonradioactive Co and Cs with an initial mass content of 0.1% of each metal were conducted under the determined appropriate carbonization and halogenation treatment conditions. Simulated spent CERs doped with nonradioactive Co and Cs were loaded into the packed-bed reactor. The reactor was then heated to $800 \text{ }^\circ\text{C}$ and this temperature was sustained for 40 min under a N_2 flowing condition according to the appropriate carbonization temperature and time profile shown in Figure 6. After this carbonization step was complete, the temperature of the reactor was raised further to $1500 \text{ }^\circ\text{C}$ by flowing Cl_2 and this stage was sustained for one hour. The results of a SEM-EDX analysis of carbonized CER and halogenation-treated carbonized CER shown in Figure 15d,e present the substantial removal of surrogate metals in the spent CER, Co, and Cs, by the applied carbonization and halogenation treatment. The results of these tests demonstrate that the noble thermochemical process proposed in this study is a viable process that effectively removes radioactive elements from spent CER. The required processing time for the halogenation treatment for the substantial removal of all radionuclides from spent CER to reduce their concentrations to levels below the free-release criteria will be determined by demonstration treatment of actual radioactive spent CER.

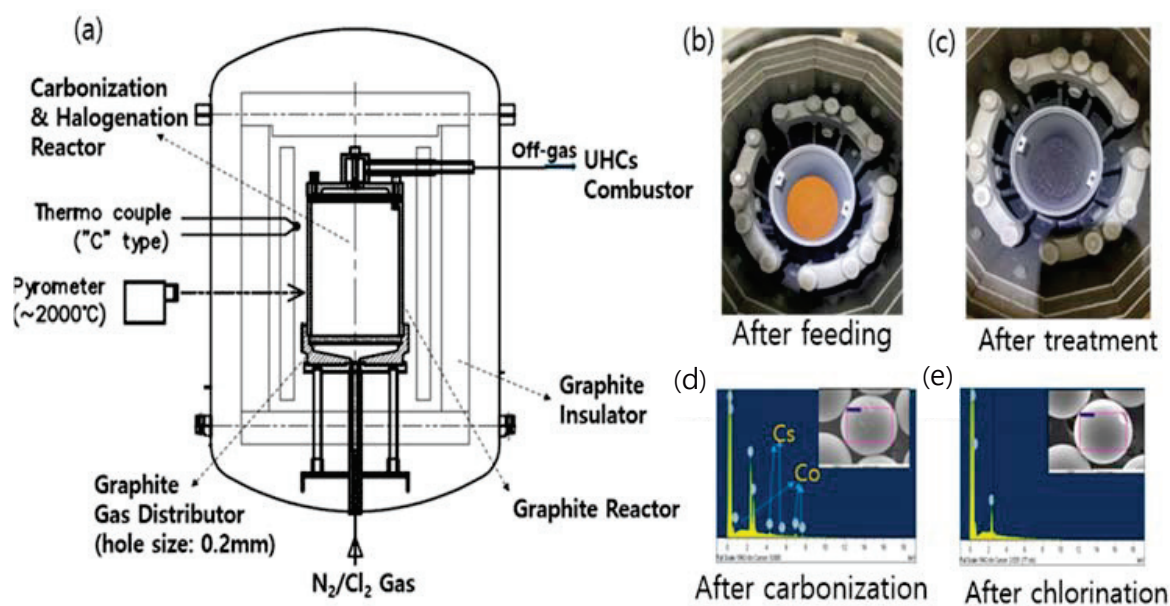


Figure 15. Detailed design of the multifunctional reactor implementing carbonization of CER (a), pictures of the reactor after the feeding of the CER (b) and after the treatment (c), and the SEM-EDS results of the carbonized CER (d) and chlorination-treated carbonized CER (e).

5. Conclusions

A novel thermochemical process for the removal of radionuclides from spent cation-exchange resins was proposed in this study. A step-by-step experimental and numerical modeling study was conducted for the design and establishment of the proper operation conditions for the carbonization and halogenation reactor and the UHC combustor. Based on the results of experimental and modeling study, an integrated process consisting of a multifunctional reactor made of graphite, which can safely conduct the halogenation treatment at a very high temperature, was realized. The optimum operating conditions could be established based on the results of a thermal analysis of the CER, a nonisothermal kinetic analysis, a numerical modeling study of a PFR-type combustor, and a thermodynamic equilibrium composition analysis. The results of this study present detailed design of a novel multifunctional reactor and operating conditions of a bench-scale carbonization and halogenation process. The results of basic performance tests using nonradioactive surrogates showed that the thermochemical process proposed here is an executable process that effectively removes radioactive elements from spent CER.

Author Contributions: Conceptualization, methodology and software, H.-C.Y.; experiment, H.-C.Y., H.-O.P. and K.-T.P.; discussion: H.-C.Y., H.-J.K., H.-C.E. and S.-J.K.; writing and editing, H.-C.Y.; project administration, H.-C.Y. and K.L. All authors have read and agreed to the published version of the manuscript.

Funding: This research received no external funding.

Acknowledgments: This research was supported by the National Research Foundation of Korea (NRF), which is funded by the Ministry of Science, ICT and Future Planning (MSIP) of the Republic of Korea (NRF-2017-M2A8A5015147) and by the Korean Institute of Energy Technology Evaluation and Planning (KETEP-2020311010050).

Conflicts of Interest: The authors declare no conflict of interest.

References

- Zhang, J.; Qian, H. Thermal behavior of weak basic ion exchange resin. *J. Therm. Anal. Calorim.* **2014**, *115*, 875–880. [[CrossRef](#)]
- Mohammad, A.; Inamuddin, A.A.; Nuashad, M.; Eldesoky, G.E. Forward ion-exchange kinetics of heavy metal ions on the surface of carboxymethyl cellulose Sn(IV) phosphate composite nano-rod-like exchanger. *J. Therm. Anal. Calorim.* **2012**, *110*, 715–723. [[CrossRef](#)]

3. Wang, J.; Wan, Z. Treatment and disposal of spent radioactive ion-exchange resins produced in the nuclear industry. *Prog. Nucl. Energy* **2015**, *78*, 47–55. [CrossRef]
4. Chun, U.K.; Choi, K.S.; Yang, K.H.; Park, J.K.; Song, M.J. Waste minimization pretreatment via pyrolysis and oxidative pyrolysis of organic ion exchange resin. *Waste Manag.* **1998**, *18*, 183–196. [CrossRef]
5. Antonetti, P.; Claire, Y.; Massit, H.; Lessart, P.; Van Cang, C.P.; Perichaud, A. Pyrolysis of cobalt and caesium doped cationic ion-exchange resin. *J. Anal. Appl. Pyrolysis* **2000**, *55*, 81–92. [CrossRef]
6. Barton, R.G.; Clark, W.G.; Seeker, W.R. Fate of metals in waste combustion systems. *Combust. Sci. Technol.* **1990**, *74*, 328–336. [CrossRef]
7. Georg, B.; Rainer, S. Pyrolysis of spent ion exchange resins. In Proceedings of the Nuclear Plant Chemistry Conference 2012 (NPC 2010), Quebec City, QC, Canada, 3–7 October 2012; pp. 23–27.
8. Masami, M.; Kiyomi, F.; Makoto, K. Decomposition of Ion Exchange Resins by Pyrolysis. *Nucl. Technol.* **1986**, *75*, 187–982.
9. Peterson, S.; Kemmler, G. *Experience of Resin Pyrolysis*; Waste Management: Tuscon, AZ, USA, 1984.
10. Matsuda, M.; Funabashi, K.; Yusa, H. Influence of functional sulfonic acid group on pyrolysis characteristics for cation exchange resin. *J. Nucl. Sci. Technol.* **1987**, *24*, 124–128. [CrossRef]
11. Michlink, D.L.; Marchall, R.W.; Smith, K.R.; Turner, V.C.; Vander Wall, E.M. *The Feasibility of Spent Resins Incineration at Nuclear Power Plants*; Waste Management: Tuscon, AZ, USA, 1983; pp. 439–441.
12. Chiara, S.; Alessio, F.; Alberto, C.; Tiziano, F.; Eliseo, R. A wide range kinetic modeling study of pyrolysis and oxidation of benzene. *Combust. Flame* **2013**, *160*, 1168–1190.
13. Ho, T.C.; Kuo, T.H.; Hopper, J.R. Thermodynamic study of the behavior of uranium and plutonium during thermal treatment under reducing and oxidizing modes. *Waste Manag.* **2000**, *50*, 355–361. [CrossRef]
14. Barbin, N.M.; Terentiev, D.I.; Alexeev, S.G.; Barbina, T.M. Thermodynamic analysis of radionuclides behaviour in products of vapour phase hydrothermal oxidation of radioactive graphite. *J. Radioanal. Nucl. Chem.* **2016**, *307*, 1459–1470. [CrossRef]
15. Yang, H.C.; Lee, S.Y.; Choi, Y.C.; Yang, I.H.; Chung, D.C. Thermokinetic analysis of spent ion-exchange resins for the optimization of carbonization reactor condition. *J. Therm. Anal. Calorim.* **2017**, *127*, 587–595. [CrossRef]
16. Vyazovkin, S.; Burnham, A.K.; Criado, J.M.; Pérez-Marquedá, L.A.; Popescu, C.; Sbirrazzuoli, N. ICTAC Kinetics Committee recommendations for performing kinetic computations on thermal analysis data. *Thermochim. Acta* **2011**, *520*, 1–19. [CrossRef]
17. Friedman, H.L. Kinetics of thermal degradation of char-forming plastics from thermogravimetry—Application to a phenolic plastic. *J. Polym. Sci.* **1964**, *6*, 183–195. [CrossRef]
18. Roduit, B.; Borgeat, C.; Berger, B.; Folly, P.; Alonso, B.; Aebischer, J.N.; Stoessel, F. Advanced kinetic tools for the evaluation of decomposition reactions. *J. Therm. Anal. Calorim.* **2005**, *80*, 229–236. [CrossRef]
19. Yang, H.C.; Lee, M.W.; Eun, H.C.; Kim, J.H.; Lee, K.; Seo, B.K. Thermal decontamination of spent activated carbon contaminated with radiocarbon and tritium. *Processes* **2020**, *8*, 1359. [CrossRef]
20. ANSYS. *Chemkin-Pro, Chemistry Solution for More Efficient Designs*; ANSYS, Inc.: Canonsburg, PA, USA, 2016. Available online: <https://www.ansys.co17m/-/media/ansys/corporate/resourcelibrary/brochure/chemkin-pro-brochure.pdf> (accessed on 11 November 2020).
21. Westbrook, C.K.; Pitz, W.J.; Herbinet, O.H.J.; Curran, H.J.; Silke, E.J. A detailed chemical kinetic reaction mechanism for n-alkane hydrocarbons from n-Octane to n-Hexadecane. *Combust. Flame* **2009**, *156*, 181–199. [CrossRef]
22. Yang, H.C.; Eun, H.C.; Lee, D.G.; Oh, W.Z.; Lee, K.W. Behavior of radioactive elements during thermal treatment of nuclear graphite—thermodynamic model analysis. *J. Nucl. Sci. Technol.* **2005**, *42*, 869–876. [CrossRef]
23. Durlak, S.K.; Biswas, P.; Shi, J. Equilibrium analysis of the affect of moisture and sodium content on heavy metal emissions from municipal solid waste incinerators. *J. Hazard. Mater.* **1996**, *56*, 1–20. [CrossRef]
24. Outokumpu Research. *HSC Chemistry 7.1—Chemical Reaction and Equilibrium Software with Extensive Thermodynamic Database*; Outotec Research Center: Pori, Finland, 2015.

Article

Transesterification Using Ultrasonic Spray of Triolein Containing CaO Particles into Methanol Vapor in a 3-Phase Reactor

Ravisut Vitidsant *, Satoshi Kodama and Hidetoshi Sekiguchi

Department of Chemical Science and Engineering, School of Materials and Chemical Technology, Tokyo Institute of Technology, Meguro-ku, Tokyo 152-8550, Japan; skodama@chemeng.titech.ac.jp (S.K.); hsekiguc@chemeng.titech.ac.jp (H.S.)

* Correspondence: vitidsant.r.aa@m.titech.ac.jp

Abstract: Ultrasonic spraying was used in a three-phase reactor to produce small droplets of triolein mixed with CaO as a solid catalyst at temperatures above the boiling point of methanol for enhancement of the transesterification of triolein. Droplets fell in the methanol countercurrent flow and were collected at the bottom of the reactor, followed by circulation to the ultrasonic spray system. The experimental parameters included triolein flow rates of 2.5–9.0 mL/min, reaction temperatures of 70–100 °C, and catalyst contents of 1.0–7.0 wt%. The methanol feed rate was set to be constant. The results suggested that the enhancement was successful after using the three-phase reactor by generating a high contact surface area for the droplets, which was a key factor for determining the performance. Comparing the results with conventional transesterification in the liquid phase using the same CaO at 60 °C, the three-phase reactor produced a methyl ester yield 2–5% higher during the 60 min trial period. However, the yield became lower after 60 min because the mass transfer of methanol to the droplets was limited. The transesterification kinetics were estimated based on the experimental data—assuming a first-order reaction—and the results indicated a range of the rate constant, an apparent activation energy, and a pre-exponential factor of $1.21\text{--}3.70 \times 10^{-2} \text{ min}^{-1}$, 36.1 kJ mol^{-1} , and 64.9 min^{-1} , respectively, suggesting that the three-phase reactor was effective for fast transesterification at the initial stage.

Keywords: ultrasonic spraying; three-phase reactor; triolein; transesterification; CaO; methanol vapor

Citation: Vitidsant, R.; Kodama, S.; Sekiguchi, H. Transesterification Using Ultrasonic Spray of Triolein Containing CaO Particles into Methanol Vapor in a 3-Phase Reactor. *Processes* **2021**, *9*, 181. <https://doi.org/10.3390/pr9010181>

Received: 31 December 2020

Accepted: 15 January 2021

Published: 19 January 2021

Publisher's Note: MDPI stays neutral with regard to jurisdictional claims in published maps and institutional affiliations.



Copyright: © 2021 by the authors. Licensee MDPI, Basel, Switzerland. This article is an open access article distributed under the terms and conditions of the Creative Commons Attribution (CC BY) license (<https://creativecommons.org/licenses/by/4.0/>).

1. Introduction

Modern society is currently consuming a great deal of energy. Fossil fuels are one of the types of fuels that have long been used by humans. The enormous consumption of fossil fuels, however, causes a major problem: global warming. Biodiesel has the potential to be one of the clean, sustainable energy sources for human civilization, and it has proven to be an attractive substitute because of its renewability and combustion performance being nearly similar to conventional diesel oil. Generally, biodiesel is produced by the transesterification of vegetable oil, algal oil, or animal fat [1] by using a homogenous catalyst such as sodium hydroxide. The disadvantage of the homogenous process is that the catalyst remains with the product after the reaction. A washing stage is required to purify the product before usage. Also, wastewater from the washing cannot be directly released into the environment. This problem could be solved by changing the homogenous catalysts to heterogeneous catalysts. Alkaline earth metal oxide is considered a candidate because the strength of the basic site is related to the electronegativity of the conjugated metal cation. The basic strength of the data from CO₂-TPD (Temperature Programmed Desorption) is in the sequence of MgO < CaO < SrO [2]. The use of CaO [3] as a solid catalyst leads to an economic advantage, due to the ease of recycling the catalyst [4,5] for

simultaneous transesterification and its environmental friendliness. However, because of the heterogeneously catalyzed transesterification that consists of three phases (oil–catalyst–methanol), the reaction rate is quite slow for the mass transfer among the phases. The application of CaO for the transesterification is thus restricted due to the requirement of a long reaction time and the high molar ratio of methanol to oil [6,7].

One way to promote the reaction is to increase the reaction temperature [8]. The typical reaction temperature in the traditional process is less than 60 °C, as the methanol boiling point is 64.7 °C. Methanol evaporates when the temperature exceeds the boiling point, and hence a three-phase reactor was designed where the methanol vapor could react with the liquid triolein and CaO upon heating the reactor over the boiling point of methanol. An ultrasonic spray device was equipped to produce small oil droplets, including CaO. The methanol vapor flowed upward in the countercurrent to the triolein droplets in the reactor. The surface area of the droplets was enlarged, owing to the ultrasonic spraying, which was expected to enhance the mass transfer of the methanol vapor as well as the transesterification reaction. The effectiveness of the proposed reactor was evaluated.

2. Materials and Methods

2.1. Catalyst Preparation

The CaO catalyst was prepared by the calcination of CaCO₃ (Wako Pure Chemical) [9], which was first loaded into a ceramic crucible and then put into the furnace for calcination at 800 °C for 2 h. The calcinated CaO was kept in a desiccator before the experiments, which had a Brunauer–Emmett–Teller (BET) surface area of 12 m²/g.

2.2. Transesterification Reaction in the Three-Phase Reactor

Triolein was used as the representative of vegetable oils for the reactant. Transesterification of triolein by a methanol vapor with CaO was carried out in the three-phase reactor, as shown in Figure 1. The experiments were conducted in a chemical fume hood for safety. A mixture of 100 mL of triolein (Cica-Reagent) with a specific weight percentage of CaO was loaded in the reactor before starting. The volume of the reactor was 2 L. The glass reactor was wrapped with a ribbon heater to keep the reactor temperature constant. The reactor was heated to the desired temperature prior to the reaction. A magnetic stirrer was placed at the bottom of the reactor to mix the CaO and triolein well. The peristaltic pump brought the mixture of triolein and CaO to the ultrasonic spray device, which generated small droplets of the mixture. The droplets fell from the tip of the ultrasonic nozzle in the methanol vapor atmosphere and then accumulated at the bottom, followed by circulation of the liquid with CaO to the ultrasonic spray device. This circulation was maintained until the desired reaction time. Methanol (Wako Pure Chemical) was vaporized and heated up to the desired temperature and then fed close to the bottom of the reactor. The methanol vapor flowed in the countercurrent direction of the falling droplets. The methanol vapor from the reactor was recovered by the condenser.

The experiments were conducted for 60 min, and the measurements were taken every 15 min. The experimental parameters investigated were triolein flow rates of 2.5, 6, and 9 mL/min, reaction temperatures of 70, 80, 90, and 100 °C, and catalyst loadings of 1, 3, 5, and 7 wt%, whereas methanol injection was kept constant at a liquid feed rate of 4.5 mL/min, which approximately corresponds to a volumetric flow rate of 3.08 L/min for the methanol vapor at the boiling point. A comparative experiment of the conventional transesterification in the liquid phase at 60 °C (below methanol's boiling point) was carried out by setting up the conditions, using a methanol to triolein ratio of 6:1, 5 wt% CaO, and mixing with the magnetic stirrer.

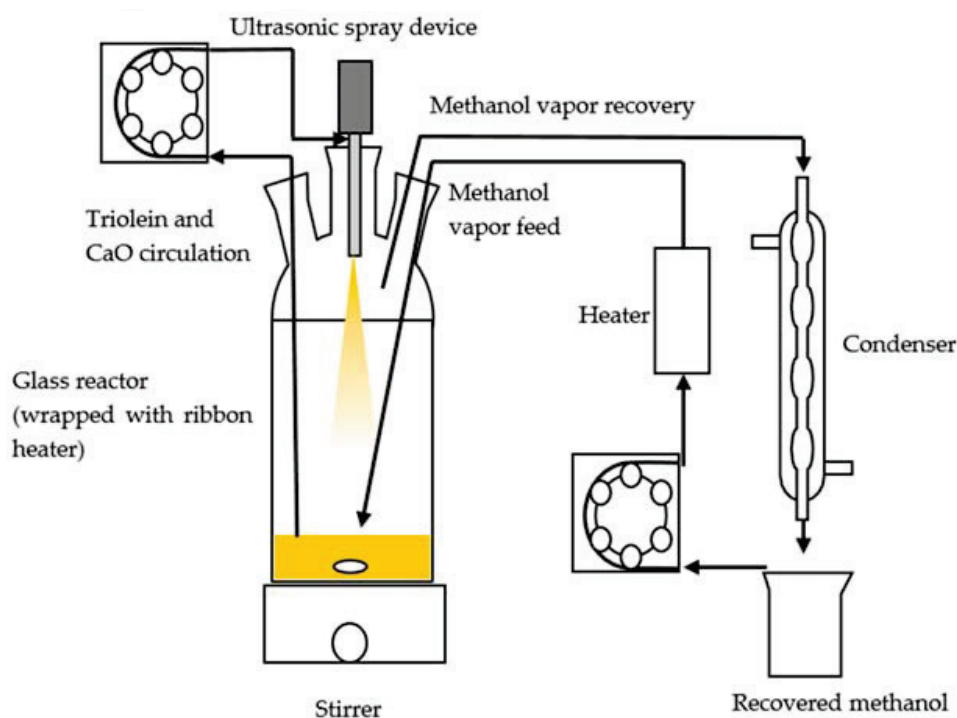


Figure 1. Schematic of the experimental apparatus with the three-phase reactor.

2.3. FAME (Fatty Acid Methyl Ester) Analysis

The yield of methyl ester was determined every 15 min by sampling approximately 2 mL of the product. The catalyst was removed from the sample using a syringe with a microfilter. As a standard, about 600 μL each of the sample and methyl heptadecanoate (Wako Pure Chemical) were prepared. Both the sample and the standard were weighed and mixed, and they were then diluted by 1.5 mL of *n*-heptane (Wako Pure Chemical) followed by analysis of the mixture. The methyl ester content in the mixture was calculated from the peak area obtained by a GC (Gas Chromatography) (Shimadzu GC-14B) equipped with a capillary column (DB-WAX 60 m) and a flame ionization detector. The carrier gas was nitrogen. The temperature of the injector and the detector were both set to 250 $^{\circ}\text{C}$. The column temperature was initially maintained at 180 $^{\circ}\text{C}$ for 2 min and then increased to 230 $^{\circ}\text{C}$ at a heating rate of 10 $^{\circ}\text{C}/\text{min}$. The complete analysis was conducted for about 9 min. The methyl ester yield was calculated in the same manner as Mun's calculation [10].

3. Results and Discussion

3.1. Effect of the Flow Rate of Triolein on Methyl Ester

Figure 2 shows the effect of the triolein flow rate on the methyl ester yield at 90 $^{\circ}\text{C}$ and 5 wt% CaO. The yield gradually increased with time. It was observed that a flow rate of 6.0 mm/min gave the highest yield, compared with those at other flow rates during the experimental time.

Figure 3a–c shows the pictures of the droplets using an optical microscope at triolein flow rates of 2.5, 6.0, and 9.0 mL/min, respectively. Table 1 shows the number and average diameter of the droplets by measuring the sizes of the droplets shown in Figure 3. The average diameter increased with an increasing flow rate, while the higher number of droplets was generated at 6.0 mL/min, compared to that at 9.0 mL/min. The total surface area of the droplets, which were estimated on the basis of the average diameter of the droplets and the flow rate, indicates that the highest surface area was obtained at a flow rate of 6.0 mL/min, causing the highest yield, as shown in Figure 2.

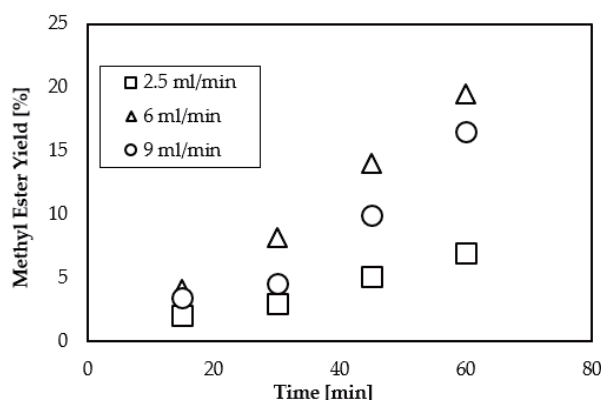


Figure 2. Effect of the triolein flow rate on the methyl ester yield at 90 °C and 5 wt% CaO.

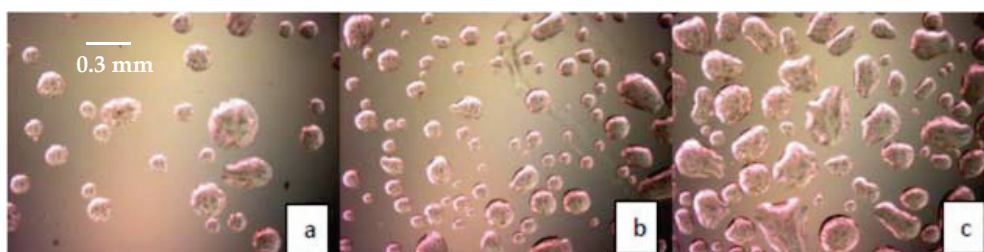


Figure 3. Pictures of droplets at triolein flow rates of (a) 2.5 mL/min, (b) 6 mL/min, and (c) 9 mL/min.

Table 1. Average diameters and surface areas of sprayed droplets.

Triolein Flow Rate (mL/min)	Average Diameter of Droplets (mm)	Volume of One Droplet (mL)	Number of Droplets Sprayed (1/min)	Surface Area of One Droplet (cm ²)	Total Surface Area per min (cm ² /min)
2.5	0.20	4.2×10^{-6}	6.0×10^6	1.2×10^{-3}	7.5×10^2
6.0	0.20	4.3×10^{-6}	1.4×10^7	1.3×10^{-3}	1.8×10^3
9.0	0.35	2.3×10^{-5}	4.0×10^6	3.5×10^{-3}	1.5×10^3

3.2. Effect of CaO Loading on Methyl Ester Yield

Catalyst loading is a principal factor for determining the transesterification process. To investigate the effect of CaO loading on the methyl ester yield, the experiments were carried out at four different catalyst loadings of 1, 3, 5, and 7 wt% at a triolein flow rate of 6.0 mL/min and a temperature of 90 °C. The distribution of CaO particles (Figure 4) increased with the increase of CaO loading. As shown in Figure 5, the yields did not significantly change between the four catalyst loadings in the beginning of the reaction and not until 30 min passed, depicting a trend that higher CaO loading results in a higher yield. The effect of CaO loading is a little pronounced from 45–60 min.

In particular, the yield proportionally increased from 10.0% to 14.1% at 45 min and 14.5% to 19.5% at 60 min, respectively, with increased CaO loading from 1 wt% to 5 wt%. The distribution of the higher CaO loading in the droplets improved the contact between the triolein and CaO, resulting in a higher yield of methyl ester. Similar results were reported by Stamenkovic [11] and Sarve [12]. Concerning the CaO loadings of 5 and 7 wt%, there were no significant yield differences during the first 45 min of the reaction. Moreover, the yields of the 5 and 7 wt% CaO loadings were 19.5% and 17.8%, respectively, at 60 min. This might have been caused by the reduction of the droplet diameter. It was observed that the average diameter of the droplet at a 5 wt% CaO loading was smaller than that at 7 wt%. After calculating the total surface area, it was found that a CaO loading of 5 wt% gave a

higher surface area than that at 7 wt%, and hence a higher methyl ester yield was obtained at a CaO loading of 5 wt%.

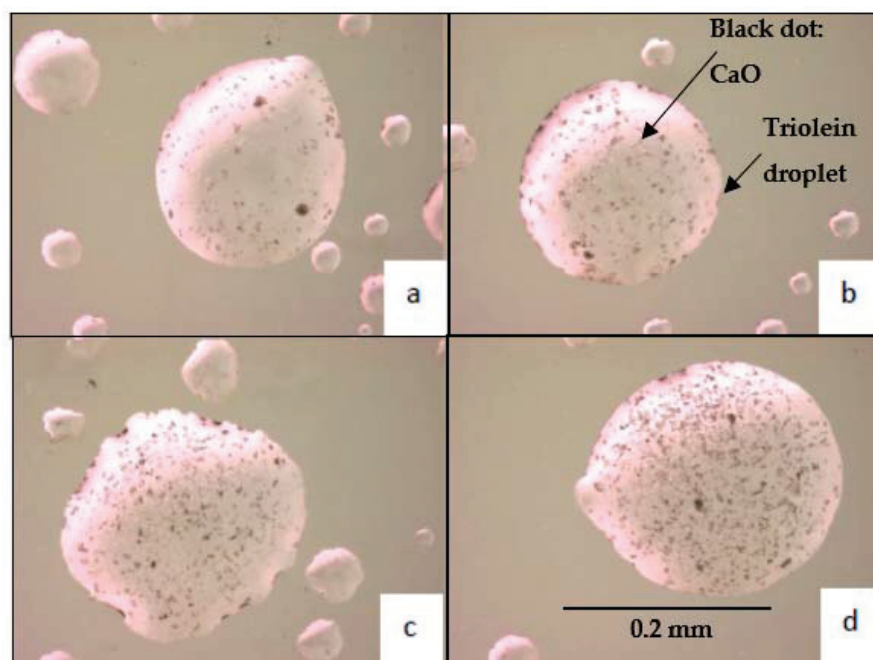


Figure 4. Pictures of droplets at CaO loadings of (a) 1 wt%, (b) 3 wt%, (c) 5 wt%, and (d) 7 wt%.

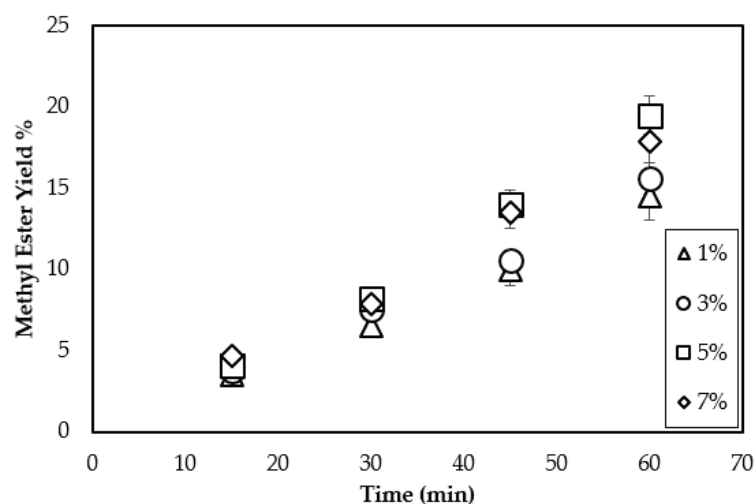


Figure 5. Effect of the catalyst loading on the methyl ester yield (90 °C and a triolein flow rate of 6.0 mL/min).

3.3. Effect of Temperature on the Methyl Ester Yield

Figure 6 shows the effect of the reaction temperature on the methyl ester yield at a triolein flow rate of 6.0 mL/min and 5 wt% CaO. It was observed that the yield increased with the reaction temperature and was higher with a longer reaction time. At 60 min, the yield increased from 12.5% to 23.8% as the temperature increased from 70 °C to 100 °C, because the increase in temperature accelerated the transesterification rate in the endothermic reaction [13], although an increase in the operating temperature resulted in a decrease in the solubility of the methanol [14].

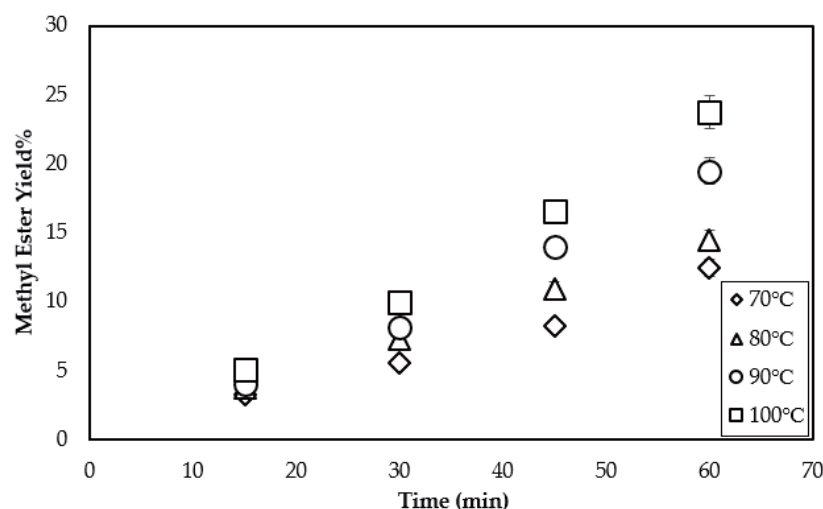


Figure 6. Effect of reaction temperature on the methyl ester yield (triolein flow rate of 6.0 mL/min and 5 wt% CaO).

3.4. Comparison between Three-Phase with Ultrasonic Spraying and a Conventional Reactor

The reaction time was extended to 120 min in order to find the behaviors of the reaction with the three-phase reactor using ultrasonic spraying at 90 °C. Additionally, the liquid phase reaction was carried out at 60 °C in a conventional reactor using a methanol to triolein ratio of 6:1. Figure 7 shows that the methyl ester yield of the three-phase reactor using ultrasonic spraying was 2–10% higher than the conventional batch reactor during 60 min of reaction. However, after 60 min, the yield still gradually increased with time in the three-phase reactor, whereas the yield suddenly increased after 60 min in the conventional reactor.

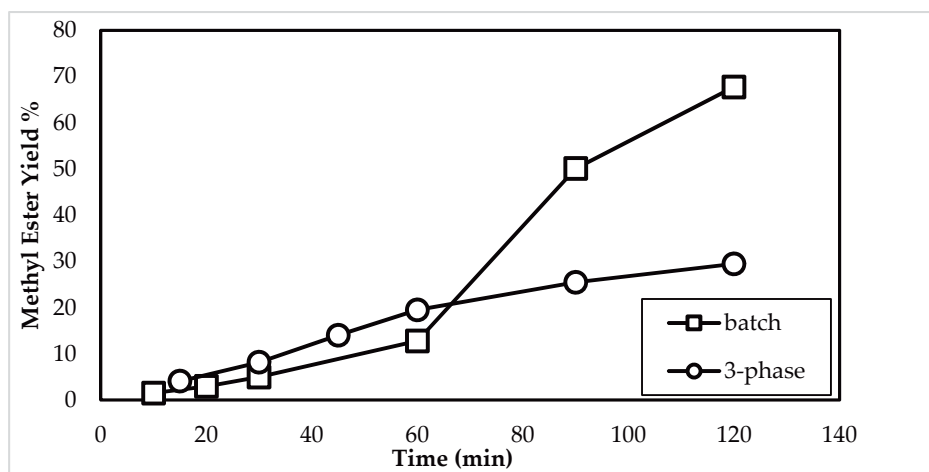


Figure 7. Comparison of methyl ester yields in the three-phase (90 °C) and conventional (60 °C) reactors.

Generally, triolein and methanol are not miscible and form two liquid phases at the initial stage of transesterification in the conventional reactor. Therefore, the mixing process is an important factor for enhancing mass transfer among two phases and heterogeneous catalysts, resulting in an accelerating reaction, as reported by Sarve et al. [14], Nouredini and Zhu [15], and Hingu et al. [16]. However, as methyl ester is formed, it acts as a mutual solvent for triolein and methanol, and there is a single phase where the transesterification is accelerated. This phenomenon corresponds to the sudden increase in the yield for the conventional reactor. On the other hand, as explained later, methanol mass transfer controls the transesterification, owing to the low solubility of methanol, causing a gradual increase

in the yield for the three-phase reactor even above a yield of 20%. From these results, it is concluded that the three-phase reactor is especially effective for the initial stage of transesterification. As a result, the transesterification process is preferable to be carried out using the three-phase reactor to achieve a certain yield, followed by the reaction in the batch reactor to reduce the reaction time with desired yield.

3.5. Relationship between the Time-Totalized Surface Area of the Droplets and the Methyl Ester Yield

The experimental results from Section 3.1 showed that the methyl ester yield depended on the triolein flow rate, as well as the surface area of the droplets generated per time. Thus, a quantitative analysis from Table 1 was used to calculate the time-totalized surface area (total surface area of the droplets produced until a certain reaction time). The area was considered to be the total area of contact between the methanol vapor and the triolein droplets during the experiment. Figure 8 shows the relation between the methyl ester yield and the time-totalized surface area for all triolein flow rate conditions. The yield behaves in one curve against the time-totalized surface area, suggesting that the time-totalized surface area was a key parameter in the three-phase reactor. It was found that the highest yield was with 19.5 wt% at the highest time-totalized surface area and a triolein flow rate of $10.8 \times 10^4 \text{ cm}^2$ at 6 mL/min.

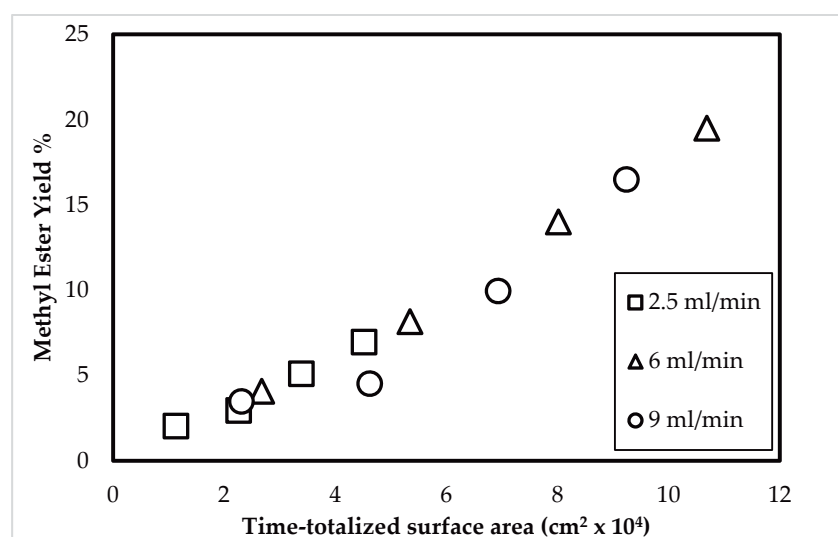


Figure 8. Effect of the time totalized surface area of the droplets on the methyl ester yield.

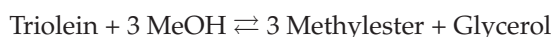
In the three-phase reactor, the transesterification took place using the following three steps:

- Step 1: Methanol mass transfer happens from the vapor phase to the triolein liquid droplets;
- Step 2: The dissolved methanol diffuses and reaches the catalysts in droplets;
- Step 3: The methanol reacts with the triolein in the presence of the catalysts.

Usually, Step 3 determines the overall transesterification rate because the intrinsic reaction rate is low. Owing to the low solubility of methanol to triolein, Step 1 became the rate-determining step, and the high reaction temperature enhanced the rate of Step 3. Therefore, the yield was strongly related to the time-totalized surface area, which directly affected the mass transfer of methanol.

4. Determination of the Kinetic Parameters

To evaluate the effectiveness of the three-phase reactor, the overall reaction rate of the transesterification was estimated, assuming that the reaction followed pseudo first-order kinetics, as proposed by Veljkovic et al. [17]:



The first-order rate equation is written as

$$-r_A = -\frac{dC_T}{dt} = kC_T = k\left(C_{T0} - \frac{1}{3}C_E\right) \quad (1)$$

where C_{t0} is the initial concentration of triolein, C_t is the concentration of triolein at time $t = C_{T0} - 1/3 C_E$, and C_E is the concentration of methyl ester at time t .

By integrating Equation (1), the solution is as follows:

$$-\ln \frac{C_{T0} - \frac{C_E}{3}}{C_{T0}} = kt \quad (2)$$

Figure 9 shows the relation between the data $\left(-\ln \frac{C_{T0} - \frac{C_E}{3}}{C_{T0}}\right)$ and t , where the slope of the linear line is k (at a constant temperature) for the series of experiments conducted at different temperatures of 70, 80, 90, and 100 °C at a triolein flow rate of 6 mL/min and 5 wt% CaO. The results of k are shown in Table 2, where the coefficient of determination R^2 nearly indicated unity, suggesting that the assumption of first-order kinetics is acceptable. The results indicated that a higher temperature enhanced k , as expected.

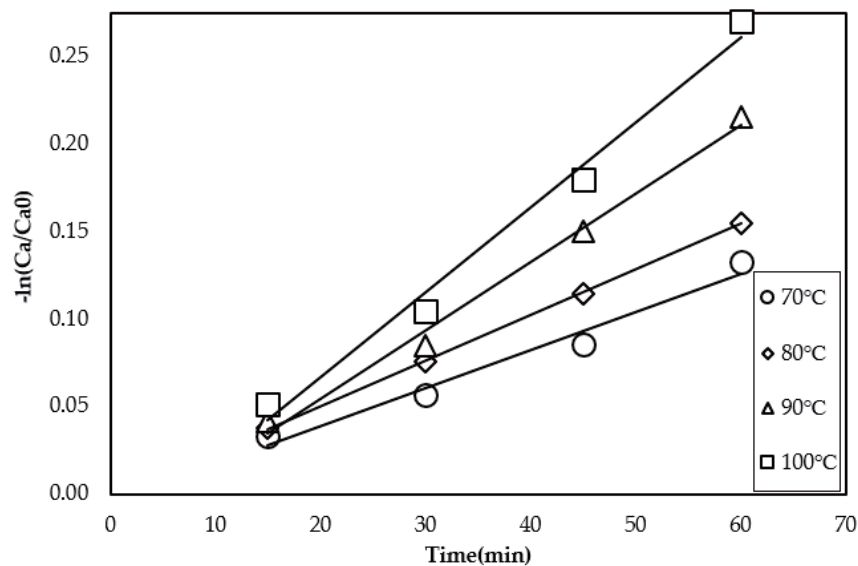


Figure 9. Concentration ratio of triolein versus the reaction time at different reaction temperatures and at a triolein flow rate of 6 mL/min and 5 wt% CaO.

Table 2. First-order rate constants for triolein transesterification with methanol on CaO. (Triolein flow rate of 6 mL/min and 5 wt% CaO.)

Temperature	70 °C	80 °C	90 °C	100 °C
$k, \text{ min}^{-1}$	1.21×10^{-2}	1.75×10^{-2}	2.63×10^{-2}	3.27×10^{-2}
r^2	0.99	0.99	0.99	0.97

The activation energy of the reaction was estimated using the following Arrhenius Equation (3) with the data of k :

$$k = k_0 e^{-\frac{E_a}{RT}}$$

$$\ln k = \ln k_0 - \frac{E_a}{RT} \quad (3)$$

where k_0 is the pre-exponential factor (min^{-1}), E_a is the apparent activation energy (kJmol^{-1}), R is the gas constant ($8.314 \text{ kJmol}^{-1}\text{K}^{-1}$), and T is the reaction temperature (K). As shown in Figure 10, the simple linear regression between $\ln k$ and $\frac{1}{T}$ was found to be a straight line, from which k_0 and E_a were estimated as 64.9 min^{-1} and 36.1 kJ mol^{-1} , respectively. Table 3 summarizes the range of k and E_a , calculated with the results of another similar piece of research. Vujicic [18] studied the kinetics of the production of sunflower biodiesel as a two-phase reaction with CaO. Their work had a higher activation energy ($101.0 \text{ kJ mol}^{-1}$) because the composition of sunflower oil has several types of fatty acids, resulting in harder transesterification than triolein, which has only oleic acid. The two-phase study was also investigated by Anilkumar [19], using waste cooking oil as a raw material and CaO from eggshells prepared by calcination at $800 \text{ }^\circ\text{C}$, followed by hydration at $60 \text{ }^\circ\text{C}$, and then calcination at $600 \text{ }^\circ\text{C}$ again as catalysts. It should also be noted that the value for E_a (54.1 kJ mol^{-1}) was higher than this study because several triglyceride components were present in the oil. In the case of an ultrasound-assisted homogenous reaction, Parkar [20] observed a lower k value and a higher E_a value as compared to the present study. The rate constant of this work ($1.21\text{--}3.70 \times 10^{-2} \text{ min}^{-1}$) was a little higher than other works using CaO, owing to the larger contact area and higher temperature. However, k was not enhanced as much under these conditions because the low solubility of methanol in triolein reduced the mass transfer of methanol.

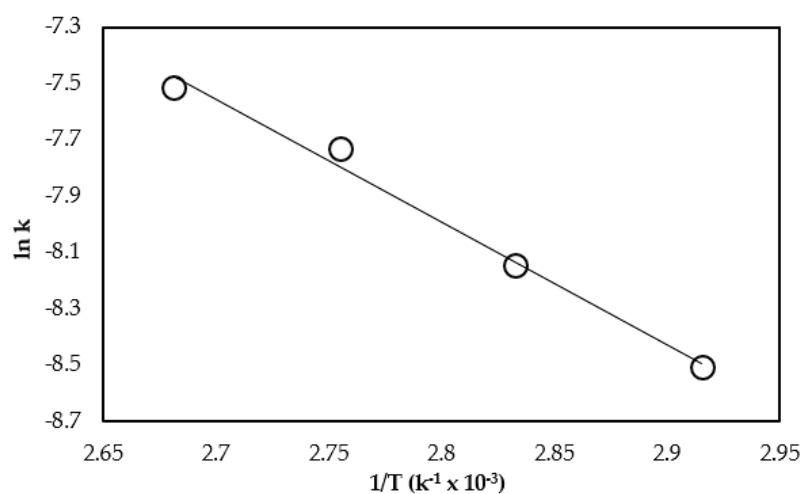


Figure 10. Arrhenius plots between $\ln k$ versus $1/T$.

Table 3. Rate constants and activation energies of the reaction for any catalyst and type of transesterification.

Raw Material or Type of Transesterification	Catalyst	Rate Constant k (min^{-1})	Activation Energy E_a (kJmol^{-1})	Reference
Triolein	CaO	$1.21\text{--}3.70 \times 10^{-2}$	36.1	Present work
Sunflower	CaO	$0.27\text{--}5.92 \times 10^{-2}$	101.0	[18]
Waste cooking oil	CaO from eggshells	$0.92\text{--}2.25 \times 10^{-2}$	54.1	[19]
Soybean oil (ultrasound-assisted)	NaOH (homogenous)	$0.37\text{--}5.2 \times 10^{-3}$	55.4	[20]

5. Conclusions

The transesterification of triolein with methanol and CaO in a three-phase reactor was investigated. It was found that the optimum triolein flow rate producing the highest yield of methyl ester was mainly a result of the highest contact area of the triolein droplets generated by an ultrasonic spray. The three-phase reactor produced a yield 2–5% higher than the conventional reactor during a 60 min period, which confirmed the advantage of the three-phase reactor using an ultrasonic spray, in which the time-totalized surface area was the key factor to determine the yield. Comparing the temporal behavior of the yield in the conventional reactor, the combination of the three-phase reactor for the initial stage of the reaction and the batch reactor for the successive stage would be effective for fast transesterification.

Author Contributions: Conceptualization, R.V.; S.K. and H.S.; methodology, R.V.; writing—original draft preparation, R.V.; writing—review and editing, R.V.; S.K. and H.S. All authors have read and agreed to the published version of the manuscript.

Funding: This research received no external funding.

Data Availability Statement: Data is contained within the article.

Conflicts of Interest: The authors declare no conflict of interest.

References

1. LeTu, T.; Kenji, O.; Yasuhiro, S.; Norimichi, T.; Yasuaki, M.; Hiroshi, B. A two-step continuous ultrasound assisted production of biodiesel fuel from waste cooking oils: A practical and economical approach to produce high quality biodiesel fuel. *Bioresour. Technol.* **2010**, *101*, 5394–5401.
2. Hattori, H. Solid base catalysts: Generation, characterization, and catalytic behavior of basic sites. *J. Jpn. Pet. Inst.* **2004**, *47*, 67–81. [\[CrossRef\]](#)
3. Kouzu, M.; Hidaka, J.; Komichi, Y. Calcium oxide functionalized with strontium as heterogeneous transesterification catalyst for biodiesel production. *Fuel* **2012**, *93*, 1–12. [\[CrossRef\]](#)
4. Kouzu, M.; Hidaka, J.; Komichi, Y.; Nakano, H.; Yamamoto, M. A process to transesterify vegetable oil with methanol in the presence of quick lime bit functioning as solid base catalyst. *Fuel* **2009**, *88*, 1983–1990. [\[CrossRef\]](#)
5. Zabeti, M.; Daud, W.M.A.W.; Aroua, M.K. Activity of solid catalysts for biodiesel production: A review. *Fuel Process. Technol.* **2009**, *90*, 770–777. [\[CrossRef\]](#)
6. Liu, X.; He, H.; Wang, Y.; Zhu, S. Transesterification of soybean oil to biodiesel using SrO as a solid base catalyst. *Catal. Commun.* **2007**, *8*, 1107–1111. [\[CrossRef\]](#)
7. Niu, S.L.; Huo, M.J.; Lu, C.M.; Liu, M.Q.; Li, H. An investigation on the catalytic capacity of dolomite in transesterification and the calculation of kinetic parameters. *Bioresour. Technol.* **2014**, *158*, 74–80. [\[CrossRef\]](#) [\[PubMed\]](#)
8. Kouzu, M.; Hidaka, J. Transesterification of vegetable oil into biodiesel catalyzed CaO: A review. *Fuel* **2012**, *93*, 1–12. [\[CrossRef\]](#)
9. Ngamcharussrivichai, C.; Nunthasanti, P.; Tanachai, S.; Bunyakiat, S. Biodiesel production through transesterification over natural calciums. *Fuel Process. Technol.* **2010**, *91*, 1409–1415. [\[CrossRef\]](#)
10. Mun, Y.C.; Eng, S.C.; Cher, P.S. Biodiesel production catalysed by low-cost liquid enzyme Eversa[®] Transform 2.0: Effect of free fatty acid content on lipase methanol tolerance and kinetic model. *Fuel* **2021**, *283*, 119266.
11. Stamenkovic, O.S.; Todorovic, Z.B.; Veljkovic, V.B. A kinetic study of sunflower oil methanolysis catalyzed by barium hydroxide. *Chem. Eng. Technol.* **2014**, *37*, 2143–2151. [\[CrossRef\]](#)
12. Sarve, A.N.; Sonawane, S.S.; Varma, M.N. Ultrasound assisted biodiesel production from Sesame (*Sesamum indicum* L.) oil using barium hydroxide as a heterogeneous catalyst: Comparative assessment of prediction abilities between response surface methodology (RSM) and artificial neural network (ANN). *Ultrason. Sonochemistry* **2015**, *26*, 218–228. [\[CrossRef\]](#) [\[PubMed\]](#)
13. Feng, Y.; He, B.; Cao, Y.; Li, J.; Liu, M.; Yan, F. Biodiesel production using cation exchange resin as heterogeneous catalyst. *Bioresour. Technol.* **2010**, *101*, 1518–1521.
14. Sarve, A.N.; Mahesh, N.V.; Shriram, S.S. Ultrasound assisted two-stage biodiesel synthesis from non-edible *Schleichera triguga* oil using heterogeneous catalyst: Kinetics and thermodynamic analysis. *Ultrason. Sonochemistry* **2016**, *29*, 288–298. [\[CrossRef\]](#) [\[PubMed\]](#)
15. Nouredini, H.; Zhu, D. Kinetics of transesterification of soybean oil. *J. Am. Oil Chem. Soc.* **1997**, *74*, 1457–1463. [\[CrossRef\]](#)
16. Hingu, S.M.; Gogate, P.R.; Rathod, V.K. Synthesis of biodiesel from waste cooking oil using sonochemical reactors. *Ultrason. Sonochemistry* **2010**, *17*, 827–832. [\[CrossRef\]](#) [\[PubMed\]](#)
17. Veljkovic, V.B.; Stamenkovic, O.S.; Todorovic, Z.B.; Lazic, M.L.; Skela, D.U. Kinetics of sunflower oil methanolysis catalyzed by calcium oxide. *Fuel* **2009**, *88*, 1554–1562. [\[CrossRef\]](#)

18. Vujcic, D.j.; Comic, D.; Zarubica, A.; Micic, R.; Boskovic, G. Kinetics of biodiesel synthesis from sunflower oil over CaO heterogeneous catalyst. *Fuel* **2010**, *89*, 2054–2061. [[CrossRef](#)]
19. Gupta, A.R.; Rathod, V.K. Waste cooking oil and waste chicken eggshells derived solid base catalyst for the biodiesel production: Optimization and kinetics. *Waste Manag.* **2018**, *79*, 169–178. [[CrossRef](#)] [[PubMed](#)]
20. Parkar, P.A.; Choudhary, H.A.; Moholkar, V.S. Mechanistic and kinetic investigations in ultrasound assisted acid catalyzed biodiesel synthesis. *Chem. Eng. J.* **2012**, *187*, 248–260. [[CrossRef](#)]

Article

Optimization of the Production of 1,1-Diethoxybutane by Simulated Moving Bed Reactor

Jasper Spitters, Jonathan C. Gonçalves, Rui P. V. Faria * and Alírio E. Rodrigues

Laboratory of Separation and Reaction Engineering—Laboratory of Catalysis and Materials (LSRE-LCM), Department of Chemical Engineering, Faculty of Engineering, University of Porto, Rua Dr. Roberto Frias s/n, 4200-465 Porto, Portugal; up201811199@fe.up.pt (J.S.); jcgs@fe.up.pt (J.C.G.); arodrig@fe.up.pt (A.E.R.)

* Correspondence: ruifaria@fe.up.pt; Tel.: +351-22-508-14-00

Abstract: Simulated moving bed technology is applied in the field of pharmaceutical, petrochemical and fine chemistry. It shows capability in separating multicomponent mixtures up to high purities. In this work, an attempt was made to optimize the production of 1,1-diethoxybutane (DEB), using the simulated moving bed technology. A fixed bed model is made with good agreement with experimental results. This fixed bed model was expanded to a simulated moving bed model. This model was used to determine the optimum conditions regarding the switching time and flowrates in each section. From this model, the optimum switching time was found to be 2.4 min, and the ratio of liquid flowrate over the solid flowrate in Section 1 to Section 4 of the SMBR was found to be 4.24, 1.77, 3.03 and 1.35, respectively. Under those conditions, the productivity was 19.8 kg DEB per liter of adsorbent per day, and the desorbent consumption was 6.1 L of ethanol per kg of DEB. The results were obtained with a minimum purity of the extract and raffinate of 97%.

Keywords: 1,1-diethoxybutane; heterogeneous catalysts; adsorption; process intensification; simulated moving bed reactor

Citation: Spitters, J.; Gonçalves, J.C.; Faria, R.P.V.; Rodrigues, A.E.

Optimization of the Production of 1,1-Diethoxybutane by Simulated Moving Bed Reactor. *Processes* **2021**, *9*, 189. <https://doi.org/10.3390/pr9020189>

Received: 30 November 2020

Accepted: 13 January 2021

Published: 20 January 2021

Publisher's Note: MDPI stays neutral with regard to jurisdictional claims in published maps and institutional affiliations.



Copyright: © 2021 by the authors. Licensee MDPI, Basel, Switzerland. This article is an open access article distributed under the terms and conditions of the Creative Commons Attribution (CC BY) license (<https://creativecommons.org/licenses/by/4.0/>).

1. Introduction

One of the most relevant environmental issues is global warming due to the increase of CO₂ in the atmosphere. Combustion of fossil fuels accounts for 82% of the increase of CO₂ concentration [1]; therefore, a lot of research is focused on finding alternative fuels. The interest is even further increased due to the predicted shortage of fossil fuel reserves.

A form of these alternative fuels are biofuels such as bio alcohols and biodiesel. Nowadays, bioethanol is the most employed bio alcohol and it can be used in car engines pure or as a blend. Bioethanol is suitable for this use due to the high octane number and the high heat of vaporization [2].

Another biofuel is a biodiesel consisting of methyl esters or ethyl esters of long chain fatty acids. These are produced via a transesterification between an alcohol and vegetable oils [3]. The use of biodiesel instead of petroleum diesel is attractive, due to the renewable nature and lower toxicity, and because it produces no sulphur, no net CO₂ and releases less hydrocarbons and non-gaseous emissions [4]. However, biodiesel has some drawbacks, namely high particles and NO_x emissions [5]. Additionally, petroleum diesel has better properties regarding oxidization stability, energy content and operability at low temperatures [6]. A promising method to overcome these drawbacks is the blending of biodiesel with other compounds like acetals. The use of 1,1-diethoxyethane has shown promising results, but the flashpoint is below the European regulation limit [7]. Therefore, the use of acetals with higher molecular weights is an interesting option. In this context, 1,1-diethoxybutane (DEB) has been identified as a potential alternative additive.

Acetals are produced via the reaction of two molecules of a monohydric alcohol and an aldehyde catalyzed by an acid. The reaction is shown in Figure 1.

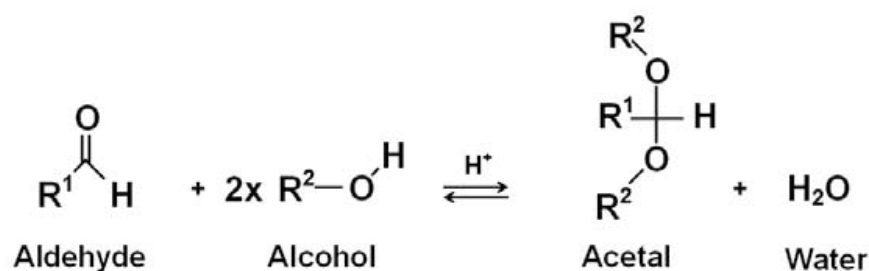


Figure 1. Overall acetalization reaction scheme.

The most optimal way to perform this reaction is via a heterogeneous catalyst, due to the separation difficulties and possible miscibility issues of a homogenous catalyst [8–10]. Ion-exchange resins have been reported as one of the most suitable types of catalysts for the acetalization reaction. For the particular case of the synthesis of DEB, the use of Amberlyst-47 as catalyst has been proposed and deeply studied by different research groups due to its fast kinetics and to the negligible amounts of by-products formed in its presence [11,12].

Because of the equilibrium limitations of this reaction, normal batch operation results in low conversion. Therefore, the implementation of Process Intensification strategies, as the simultaneous separation of one of the products during the reaction, seems a good option to enhance the conversion. The open literature reports reactive distillation [13] and membrane reactors [14] as potential multifunctional reactors for the synthesis of DEB. In all cases, the removal of water from the reaction media was the key step to increase the conversion.

The synthesis of this acetal by reactive distillation, by membrane reactors or by more or less complex combinations of reaction, pervaporation and distillation units has been thoroughly studied over the last decade [13–15]; however, despite the economic potential demonstrated by some of these processes, the performance of both conventional and multifunctional reactors was rather limited. For instance, the reported limiting reactant conversion for reactive distillation units was always below 50% [13], while for membrane reactors, the limiting reactant conversion was typically comprised between 40% and 80% [14,16]. These values are higher than those attained in conventional reactors operated under similar conditions but are quite low for these types of multifunctional reactors and reactive systems. The exothermic character of the DEB synthesis acetalization reaction and the relatively high temperatures at which reactive distillation and membrane reactor processes typically operate (above 343 K) lead to considerable thermodynamic limitations since at higher temperatures the equilibrium conversion will be lower.

A less energy intensive alternative way to accomplish this is by using the principle of chromatography. Chromatography is a process where two components can be separated based on affinity with a solid phase. The two components are carried via a solvent through a solid phase. The component with less affinity to the solid phase will move faster compared to the component with more affinity. This principle can be applied in this case, where water is the more retained component and 1,1-diethoxybutane (DEB) is the less retained component with ethanol as solvent. As previously mentioned, Amberlyst-47 has shown good properties regarding enhancing the reaction [11]. Amberlyst-47 will act as a catalyst, as well as the adsorbent of water.

The acetalization reaction can be carried out in a fixed bed, where Amberlyst-47 is packed in a column, and a mixture of ethanol and butanal will flow through [17]. The disadvantage of this is that the process can only be carried out in batch mode, and after a certain time, the process needs to be stopped because the catalyst/adsorbent will be saturated. From this point on, water will be present in the product and the process has to be stopped; the catalyst/adsorbent has to be cleaned so the process can be restarted. This is very time consuming, implies the use of large amounts of regeneration solvent, and thus this is not a viable option. Therefore, a true moving bed reactor (TMBR) was investigated, where in a column the solid phase is pumped around in a counter-current

operation. The column has two inlet streams, namely, the feed and the desorbent, and two outlet streams, namely, the extract and raffinate. The column can be divided in four sections. In Section 1, the recycled liquid and the fresh desorbent enter the column at one end. In this section, the solid phase is cleaned by the liquid flow, so the solid leaving the column is saturated in the desorbent and can be recycled to Section 4. In Section 2, the desorption of the less-absorbed component takes place, to prevent the extract from being contaminated by this component, together with the chemical reaction. In Section 3, the chemical reaction proceeds and the adsorption of the more-adsorbed component take place to prevent the raffinate from being contaminated with this component. In Section 4, the solid recycle enters the column at one end, and the liquid is cleaned so that the liquid leaving the column can be recycled to Section 1. In Figure 2, a schematic representation of a true moving bed is shown.

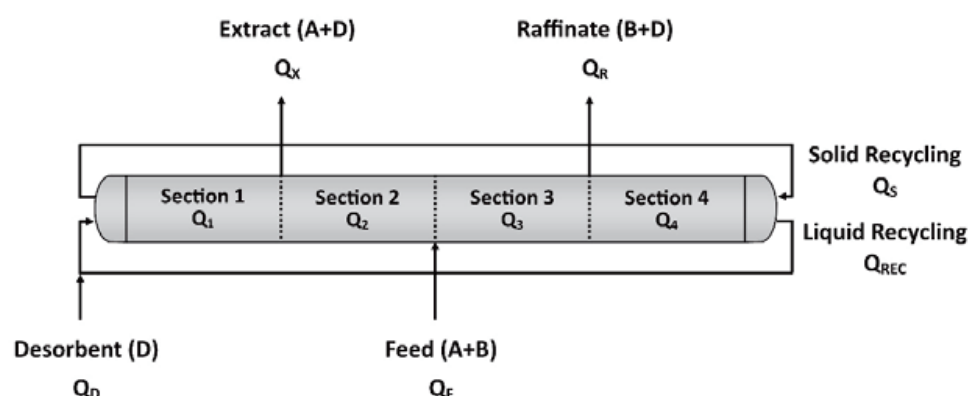


Figure 2. Schematic representation of a true moving bed.

The TMBR operating mode would enable continuous operation; however, moving the solid phase around presents many mechanical difficulties, which makes the process not viable. Therefore, the simulated moving bed (SMB) was invented. In this process, the movement of the solid phase is simulated by changing the input and output locations of all the streams. A schematic review is shown in Figure 3.

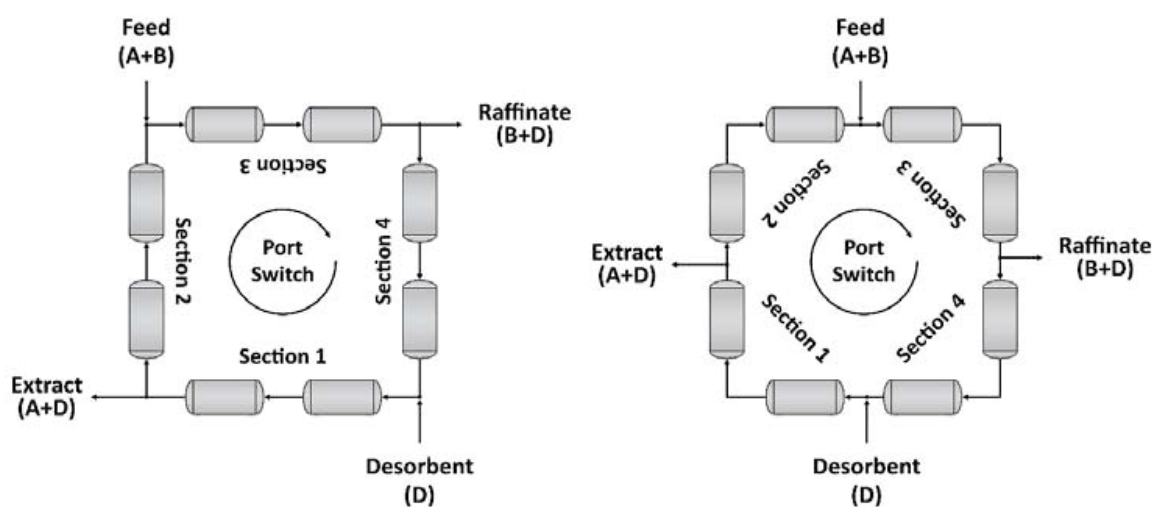


Figure 3. Simulated moving bed process.

In Figure 3, a process of eight identical columns is represented, where each two columns represent one section. These sections have the same function as in the TMBR. In this case, every section has the same number of columns, and a 2-2-2-2 configuration is

used; however, in some cases it can be more efficient to have more columns, for example, in Sections 2 and 3, and use a 1-3-3-1 configuration. After a certain time, designated switching time, all the inlet and outlet ports are shifted by one column, in the same direction as the liquid flow. This simulates the movement of the solid flow, while the solid flow is stationary. Because of the switching, there is no real steady state, but only a cyclic steady state. When this state is achieved, the concentration profile that is observed in eight consecutive switches will be exactly the same (for an eight-column unit presented as example). The cyclic steady state is achieved after a short number of cycles (typically 10–30 cycles). After eight switches, the inlet and outlet ports are at the same place again, and the whole cycle starts again. Therefore, it is called a cyclic steady state because the unit internal concentration profiles and outlet concentration histories are cyclically the same from that moment on.

The SMB separation principle can be applied to the multifunctional reactors concept and include the reaction in a so-called simulated moving bed reactor (SMBR). In fact, this technology has been implemented for the production of fuel additives [18] and has been demonstrated to be particularly effective for the synthesis of acetals [19–21]. For the synthesis of DEB, Amberlyst-47 will be used as stationary phase (catalyst and adsorbent) and ethanol is used as desorbent. This has the advantage of shifting the reaction equilibrium to the preferred side of the reaction, and almost all the butanal will react. The raffinate will contain ethanol and DEB, where the extract will contain ethanol and water. Ethanol from both of these streams can be separated and recycled back to the unit in order to reduce the overall SMBR desorbent consumption.

In this work, the synthesis of DEB by SMBR will be studied and optimized. A mathematical model will be developed and validated against experimental data obtained from the open literature [22], which will then be used for this purpose. A two-level SMBR optimization procedure will be adopted [23], based on the Separation Volumes concept [24,25], together with a sensitivity analysis of some of the most relevant operating parameters.

2. Methods

2.1. Mathematical Model

In order to model an SMBR, a fixed bed column has to be modelled and validated. The thermodynamic properties and validation data are based on previous work [22]. In this model, the assumption of constant packing and bed length is made. For each compound, a second-order partial differential equation is set up for the concentration in the bulk, an ordinary differential equation for the average concentration inside the particle, and an algebraic equation for the adsorbed concentration in equilibrium with the average concentration inside the particle pores. The mass balance for the bulk phase for component i is presented in Equation (1).

$$\frac{\partial C_i}{\partial t} + \frac{\partial(uC_i)}{\partial z} + \frac{(1-\varepsilon)}{\varepsilon} \frac{3}{r_p} K_{L,i}(C_i - \bar{C}_{p,i}) = D_{ax} \frac{\partial}{\partial z} \left(C_T \frac{\partial x_i}{\partial z} \right) \quad (1)$$

The particle mass balance for component i is presented in Equation (2).

$$\frac{3}{r_p} K_{L,i}(C_i - \bar{C}_{p,i}) = \varepsilon_p \frac{\partial \bar{C}_{p,i}}{\partial t} + (1-\varepsilon) \frac{\partial q_i}{\partial t} - v_i \frac{\rho_b}{1-\varepsilon} r(\bar{C}_{p,i}) \quad (2)$$

where q_i is the concentration of component i in the solid. With the following boundary conditions in Equations (1)–(3),

$$t = 0 \quad C_i = \bar{C}_{p,i} = C_0 \quad (3)$$

$$z = 0 \quad uC_i - D_{ax} C_T \frac{\partial X_i}{\partial z} \Big|_{z=0} = uC_{i,F} \quad (4)$$

$$z = L \quad \left. \frac{\partial C_i}{\partial z} \right|_{z=L} = 0 \quad (5)$$

where C_0 refers to pure eluent concentration, which means there is only ethanol present. In the equations, u refers to the interstitial velocity, K_L is the global mass transfer coefficient, D_{ax} is the axial dispersion coefficient, t is the time variable, z is the axial coordinate, v_i is the stoichiometric coefficient, ρ_b is the bulk density and $r(\bar{C}_{p,i})$ is the reaction rate based on the average particle concentration. The reaction rate is shown in Equation (6),

$$r = k_c \frac{a_{EtOH} a_B \frac{a_W a_{DEB}}{K_{eq} a_{EtOH}}}{(1 + K_{S,W} a_W)^2} \quad (6)$$

where a_i corresponds to the activity coefficient. These coefficients are based on the average particle concentration and are calculated via the universal quasichemical functional-group activity coefficient (UNIFAC) method. The equilibrium constant K_{eq} , the water equilibrium constant $K_{S,D}$ and the reaction kinetic constant k_c were determined in a previous study [11] and are represented by Equations (7)–(9).

$$K_{eq} = 7.73 * 10^{-2} \exp\left(\frac{1036.8}{T(K)}\right) \quad (7)$$

$$K_{S,D} = 1.454 * 10^{-4} \exp\left(\frac{2920.68}{T(K)}\right) \quad (8)$$

$$K_C = 3.21 * 10^5 \exp\left(\frac{-4561.06}{T(K)}\right) \quad (9)$$

To describe the adsorption equilibrium, the multicomponent Langmuir isotherm was considered and is shown in Equation (10).

$$q_i = \frac{Q_i K_i \bar{C}_{p,i}}{1 + \sum_{j=1}^n K_j \bar{C}_{p,j}} \quad (10)$$

In this equation, Q_i represents the total molar capacity for each component per volume of adsorbent and K_i represents the equilibrium constant for each component. These values, determined in a previous work [22], are presented in Table 1.

Table 1. Multicomponent Langmuir isotherm parameters for the species involved in the synthesis of 1,1-diethoxybutane (DEB) at 303 K [22].

Component	Q (mol L _{Solid} ⁻¹)	K (L mol ⁻¹)
Ethanol	10.58	7.24
Butanal	3.08	0.12
Water	34.47	8.18
DEB	3.59	0.06

For the model to be accurate, the interstitial velocity variation has to be accounted for and is calculated via the total mass balance assuming ideal additivity. This is represented by Equation (11).

$$\frac{du}{dz} = -\frac{(1-\varepsilon)}{\varepsilon} \frac{3}{r_p} \sum_{i=1}^{NC} K_{L,i} V_{mol,i} (C_i - \bar{C}_{p,i}) \quad (11)$$

where V_{mol} is the molar volume of component I , with the following boundary condition:

$$z = 0 \quad u = Q_{in} / (A * \varepsilon) \quad (12)$$

where A is the cross-sectional area, ε is the porosity of the bed and Q_{in} and Q_{out} represents the volumetric flow in and the volumetric flow out, respectively, in l/s .

The axial dispersion coefficient was based on an experimentally determined Péclet number. The Péclet number relates the ratio between convection and diffusion, and is shown in Equation (13).

$$Pe = \frac{L_c u}{D_{ax}} \quad (13)$$

The assumption of a global mass transfer has been made, where the internal and external mass transfer are combined into one coefficient. The coefficient is defined in Equation (14).

$$\frac{1}{K_L} = \frac{1}{K_e} + \frac{1}{\varepsilon_p K_i} \quad (14)$$

To determine the internal mass transfer, an approximation for the average value was used in Equation (15).

$$K_i = \frac{5 \varepsilon_p D_m}{\tau r_p} \quad (15)$$

where τ represents the tortuosity factor which was set to 2 by experimental data fitting.

The external mass transfer coefficient was approximated via the Wilson and Geankopolis relation, shown in Equation (16).

$$Sh_p = \frac{1.09}{\varepsilon} (Re_p Sc)^{0.33} \quad 0.0015 < Re < 55 \quad (16)$$

In Equation (16), Sh_p , Re_p and Sc are, respectively, the particle Sherwood number, the particle Reynolds number and the Schmidt number, which are determined via Equations (17)–(19).

$$Sh_p = \frac{K_e d_p}{D_m} \quad (17)$$

$$Re_p = \frac{\rho d_p u}{\eta} \quad (18)$$

$$Sc = \frac{\eta}{\rho D_m} \quad (19)$$

The infinite dilution diffusivities are estimated by the Scheibel correlation in Equation (20).

$$D_{A,B}^0 = \frac{8.2 * 10^{-8} T}{\eta_b V_{Mol,A}^{\frac{1}{3}}} \left(1 + \left(\frac{3V_{Mol,B}}{V_{Mol,A}} \right)^{\frac{1}{3}} \right) \quad (20)$$

In which $D_{A,B}^0$ is the diffusion coefficient for a dilute A in solvent B . Since we have a multicomponent system, the Perkins and Geankopolis mixing rule is applied, as shown in Equation (21).

$$D_{A,m} \eta_m^{0.8} = \sum_{i=1}^n x_i D_{A,i}^0 \eta_i^{0.8} \quad (21)$$

Since the infinite dilution diffusivity is only valid for low concentrations, the mixture diffusivity of ethanol cannot be calculated in this way. Since ethanol is used as the solvent, it will always be present in high concentrations, so for ethanol the mixture diffusivity is approximated by the self-diffusion coefficient. The self-diffusion is calculated via Equation (22), based on a previous work. [26].

$$\frac{D_{AA} \eta_A}{k_B T} = \frac{1}{2\pi} \left(\frac{\tilde{N}_A}{\tilde{V}_A} \right)^{\frac{1}{3}} \quad (22)$$

In which D_{AA} represents the self-diffusion coefficient, K_B represents the Boltzmann constant, \tilde{N}_A represents the Avogadro number and \tilde{V}_A represents the molar volume. The results are in the same order of magnitude as those reported in other studies [27].

As seen in Equation (21), the mixture viscosity is used to determine the mixture diffusivity. The mixture viscosity is determined using the Gruenberg–Nissan correlation, shown in Equation (23).

$$\ln(\eta_m) = \sum_i x_i \ln(\eta_i) \quad (23)$$

For the SMBR, the balances for the nodes are given in Equations (24)–(27). For the extract, the balance is:

$$C_{iII,in} = C_{iI,out} \quad (24)$$

For the raffinate:

$$C_{iIV,in} = C_{iIII,out} \quad (25)$$

For the eluent:

$$C_{iI,in} = \frac{u_{IV}}{u_I} C_{iIV,out} + \frac{u_D}{u_I} C_i^D \quad (26)$$

For the feed:

$$C_{iIII,in} = \frac{u_{II}}{u_{III}} C_{iII,out} + \frac{u_F}{u_{III}} C_i^F \quad (27)$$

2.2. Performance Parameters

To optimize the process, the performance parameters need to be determined. Since there is no steady state, the performance parameters are based on average concentrations in the raffinate and extract streams. The raffinate purity is determined via Equation (28).

$$PUR = \frac{C_{DEB,R}}{C_{B,R} + C_{W,R} + C_{DEB,R}} \quad (28)$$

where the concentrations represent the average concentrations of butanal, water and ethanol in the raffinate within a cycle.

The extract purity is determined via Equation (29).

$$PUX = \frac{C_{W,X}}{C_{B,X} + C_{W,X} + C_{DEB,X}} \quad (29)$$

where the concentrations represent the average concentrations of butanal, water and ethanol in the extract within a cycle. The purity values resulting from the equations indicate the purity obtained after removing the ethanol, as commonly considered for this type of process. When ethanol is included in the equation, the purity is much lower.

The butanal conversion is determined via Equation (30).

$$X = \left(1 - \frac{Q_x C_{B,X} + Q_R C_{B,R}}{Q_F C_{B,F}}\right) \quad (30)$$

where Q_x represents the extract flowrate, Q_R the raffinate flowrate, Q_F the feed flowrate and $C_{B,F}$ the butanal concentration in the feed.

The DEB productivity is determined via Equation (31).

$$PR = \frac{Q_R C_{DEB,R}}{(1 - \varepsilon) V_{unit}} \quad (31)$$

where $C_{D,R}$ represents the DEB concentration in the raffinate stream and V_{unit} represents the volume of all the columns.

The desorbent consumption is determined via Equation (32).

$$DC = \frac{(Q_D C_{EtOH,D} + Q_F (C_{EtOH,F} - 2XC_{B,F}) V_{mol,EtOH})}{PR(1 - \epsilon) V_{unit}} \quad (32)$$

where Q_D represents the flowrate of the eluent going into the SMBR and $V_{mol,A}$ represents the molar volume of ethanol.

2.3. Numerical Solution

The model was written in gPROMS (general PROcess Modeling System). The axial coordinate was discretized using a second-order centered finite difference method (CFDM). The discretization results in a system of ordinary differential equations integrated over time using the DASOLV integrator implementation in gPROMS.

3. Results and Discussion

In this section, the results regarding the fixed bed adsorptive reactor model validation and the optimization results attained through the extrapolation of the previously validated single column model to the multicolumn SMBR unit will be presented.

3.1. Fixed Bed Adsorptive Reactor Model Validation

In order to optimize the SMBR, the model of a single fixed bed has to be validated with experimental data. The experimental data were obtained from a previous work [22]. Three different experiments were compared, namely: a breakthrough curve of water with ethanol, a breakthrough curve of DEB with ethanol and a reaction experiment. The experimental conditions used are presented in Table 2.

Table 2. Experimental conditions used for the fixed bed simulations.

Experiment	1	2	3
Bed length (cm)	10.95	11.18	11.1
Column diameter (cm)	2.6	2.6	2.6
Temperature (K)	303	303	303
Bed porosity	0.42	0.42	0.42
Particle porosity	0.5	0.5	0.5
Péclet number	64.4	64.4	64.4
Flowrate (mL min ⁻¹)	5.1	7.59	7
$C_{0,ethanol}$ (mol/L)	0.579	0	16.958
$C_{0,water}$ (mol/L)	0	55.26	0
$C_{0,DEB}$ (mol/L)	5.535	0	0
$C_{F,ethanol}$ (mol/L)	16.958	16.897	11.4
$C_{F,water}$ (mol/L)	0	0.212	3.61
$C_{F,DEB}$ (mol/L)	0.001	0	0

For these experiments, the concentration at the outlet of the bed is registered, these are the outlet concentrations. The model and the experimental results are plotted from Figures 4–6.

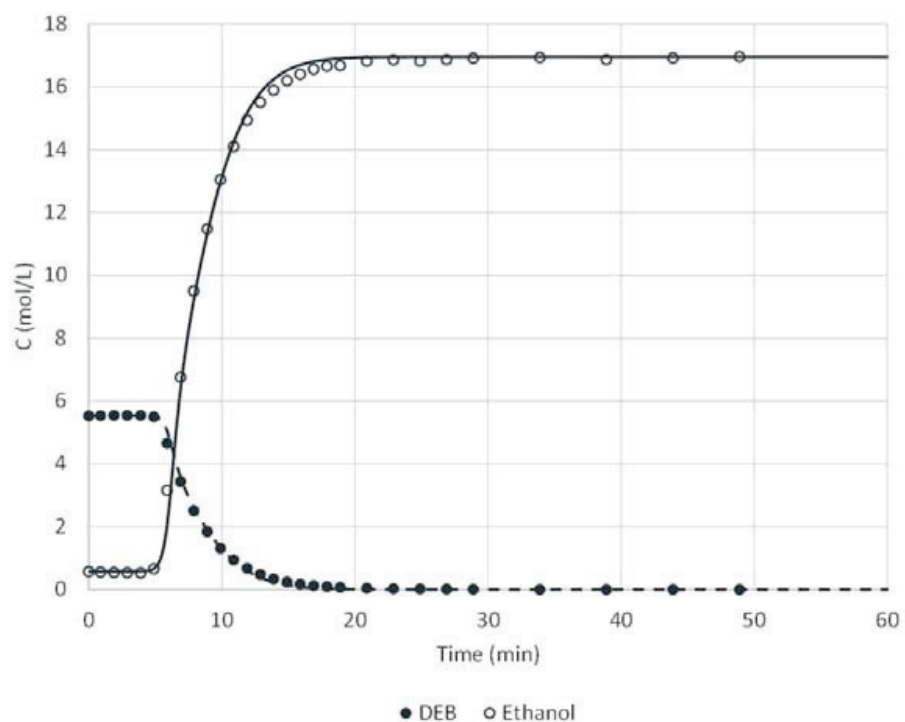


Figure 4. Breakthrough curve between ethanol and DEB experimental conditions provided in Table 2 for experiment 1 [22].

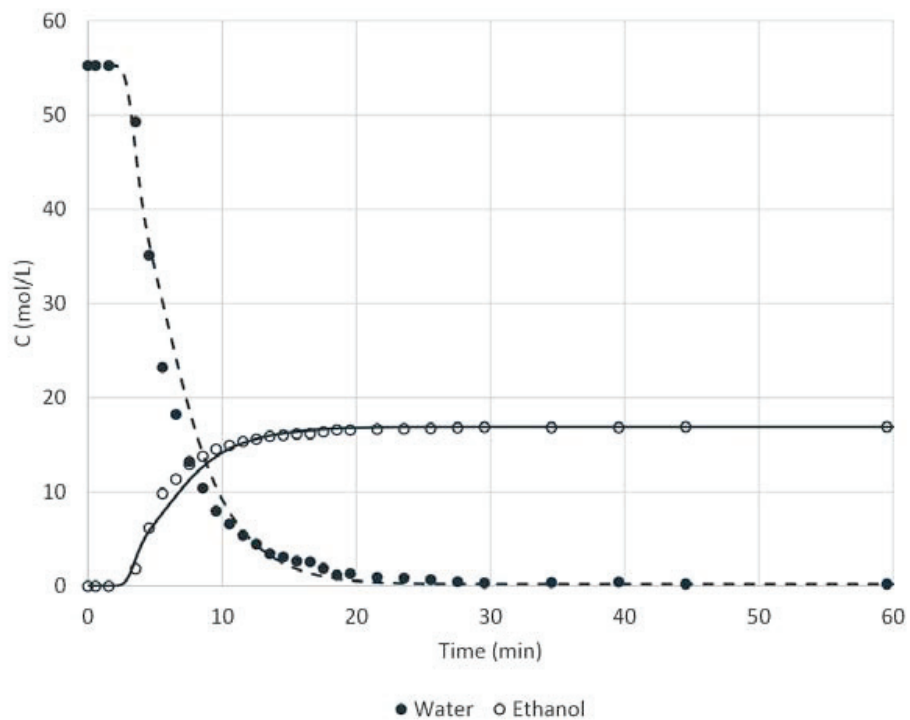


Figure 5. Breakthrough curve between ethanol and water experimental conditions provided in Table 2 for experiment 2 [22].

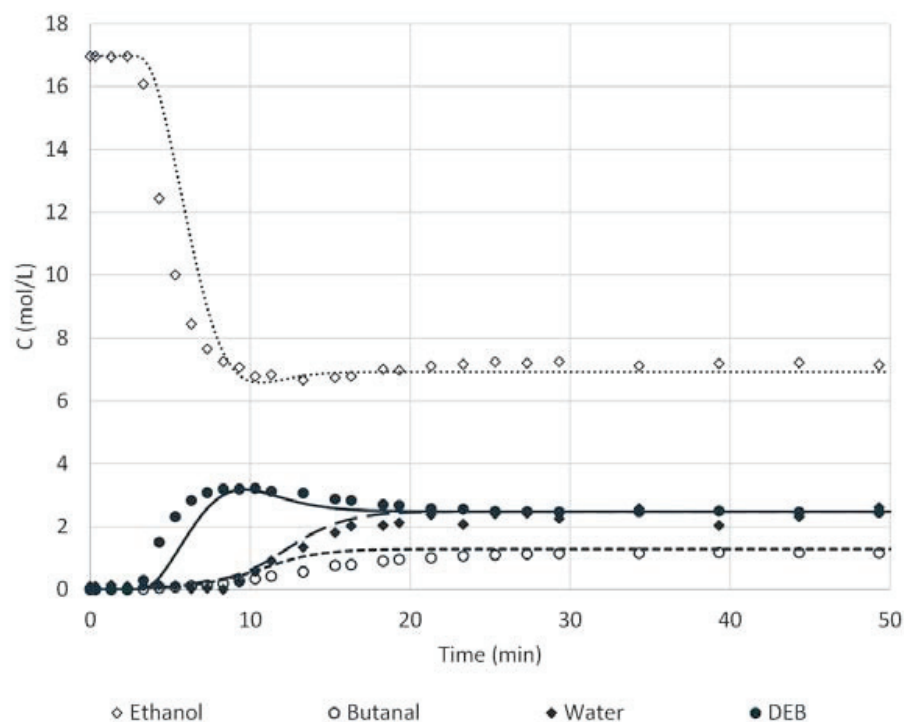


Figure 6. Reaction breakthrough curve experimental conditions provided in Table 2 for experiment 3 [22].

It can be seen from these plots that there is good agreement between the model results and the experimental results. To quantify this agreement, Equation (33) is used to determine the correlation factor.

$$R_{Correl}^2 = 1 - \left(\frac{\sum_{i=1}^{NC} \sum_{j=1}^{NE} \sum_{k=1}^{NP} (C_{out,i,j,k}^{exp} - C_{out,i,j,k}^{mod})^2}{\sum_{i=1}^{NC} \sum_{j=1}^{NE} \sum_{k=1}^{NP} (C_{out,i,j,k}^{exp} - \bar{C}_{out,i,j,k}^{mod})^2} \right) \quad (33)$$

The correlation factor is calculated for all of the three breakthrough experiments using values from the model described in this work, and the values from [22]. The biggest difference between the two models is the way the diffusion coefficient of ethanol is determined. In this model, it is determined using the self-diffusion coefficient, which is more suitable considering the high concentrations of ethanol present throughout the system. This should represent the phenomena more accurately compared to when it is computed via the infinite dilution diffusivity.

From Table 3 it can be concluded that the fixed bed model fairly represents the experiments. The lower values in the reaction, compared to the binary curves, are mainly caused by the deviation in the ethanol and DEB curves within the first 500 s. This deviation has a major impact on the correlation factor but it was already observed in the results attained by Graça et al. [22], being slightly improved in this work through the modifications made in the estimation of ethanol diffusion coefficient.

Table 3. Correlation factors attained for the breakthrough curves used for the fixed bed reactor model validation.

	This Work	Previous Work [22]
Ethanol and Water	0.991	0.989
Ethanol and Deb	0.998	0.999
Reaction	0.954	0.949

3.2. Sensitivity Analysis to the SMBR Operating Parameters

In order to guarantee that the cyclic steady state was reached every time, the same simulation was run for 12, 20 and 40 cycles. No differences could be observed between 20 and 40 cycles' separation regions. Some were observed between 12 and 20 cycles, albeit quite small. Hence, it was decided to use 20 cycles, in order to be sure that in every scenario, the cyclic steady state was reached. In Table 4 the experimental conditions are presented.

Table 4. Simulated moving bed reactor (SMBR) conditions.

Parameter	Value
Temperature (K)	303
Configuration	3-3-3-3
Column Length (cm)	23.0
Column diameter (cm)	2.6
Bed porosity	0.42
Particle porosity	0.5
Péclet number	64.4
Ethanol feed concentration (mol/L)	12.266
Butanal feed concentration (mol/L)	3.064

In Figure 7, the history of the purity of the raffinate and the extract stream are plotted against the number of cycles. It can be seen that 20 cycles are enough in order for the system to reach the cyclic steady state.

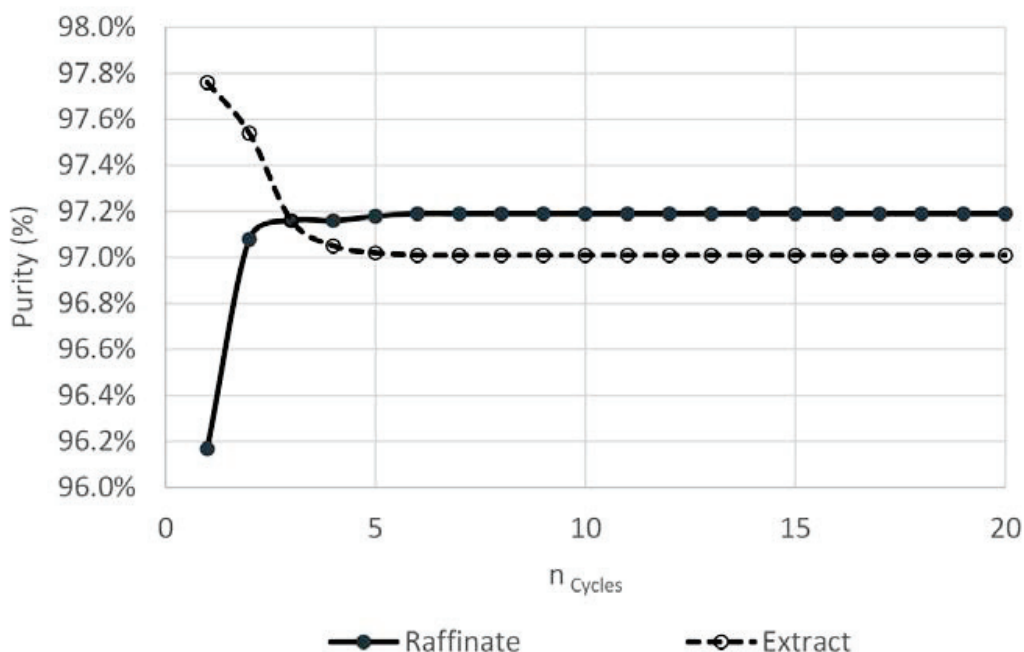


Figure 7. Outlet streams' purity histories over the number of cycles.

Now that the fixed bed model is validated, the SMBR can be modelled. In the SMBR, one of the most important parameters is the γ value. This parameter represents the velocity of the liquid over the flow rate of the solid, in each section from 1 to 4. The equation for the gamma value is presented in Equation (34).

$$\gamma_j = \frac{u_j}{u_s} \quad (34)$$

where the solid flow in an SMB is represented by Equation (35).

$$u_s = \frac{L_c}{t_{switch}} \quad (35)$$

The main function of Sections 1 and 4 is to clean the solid and the desorbent, respectively, as stated above. In this section, the optimal switching time will be determined. For this, the value of γ_1 and γ_4 should be a set value, to ensure that at all times the desorbent and solvent are cleaned properly. This is called a sensitivity analysis, because the influence of the switching time on the performance parameters is determined. These values are determined via Equations (36) and (37),

$$\gamma_{1min} = \frac{(1 - \varepsilon)}{\varepsilon} \left(\varepsilon_p + (1 - \varepsilon_p) \frac{q_{W,1}}{C_{p,W,1}} \right) \quad (36)$$

$$\gamma_{4max} = \frac{(1 - \varepsilon)}{\varepsilon} \left(\varepsilon_p + (1 - \varepsilon_p) \frac{q_{DEB,1}}{C_{p,DEB,1}} \right) \quad (37)$$

with a safety factor included, which is set to 20%. If the system is working properly, in Sections 1 and 4, only ethanol should be present, so in the isotherm, the denominator is only represented by the contribution of ethanol. However, Equations (36) and (37) are only valid for TMBR. Because the solid is not really moving in the SMBR, the relative liquid velocity to the solid is represented by Equation (38).

$$u_L = u_L^* + u_s^* \quad (38)$$

In this equation, the * refers to the flow in the TMBR. If this Equation is divided by the solid flow rate, the ratio between the liquid flow rate and the solid flow rate appears on the left-hand side of the equation. In that case, it can be seen that the γ value in SMBR is equal to the gamma value of a TMBR plus 1. So, to determine γ_1 and γ_4 , a value of 1 must be added to Equations (36) and (37). This results in a value of 3.465 and 1.635 for γ_1 and γ_4 , respectively. When these values are used, Sections 1 and 4 work properly, and the desorbent and solid are cleaned completely. For the rest of the simulations in this section, these values should be maintained. This means that the recycle flow rate and the eluent flow rate are set for each specific switching time value. The γ_2 and γ_3 values need to be determined regarding a purity requirement of the extract and the raffinate. The ratios in Sections 2 and 3 can be changed by altering the feed flowrate and the extract flowrate. From these flowrates, the raffinate flowrate is calculated by closing the mass balance.

When the purity requirement is set, a region within the γ_2 - γ_3 plane that satisfies the purity requirement is delimited. This is called the separation region in the case of SMB and reactive-separation region in the case of SMBR. In Figure 8 an idealized situation of the separation region is shown.

In Figure 8, the triangle (formed by the vertexes a, b and w) is the separation region. Within that region, the raffinate and extract satisfy the purity requirements. The real separation region will not be a perfect triangle as the one in this figure, because of non-idealities in the process, due to mass transfer, for example. Even though it will not be a triangle, it will have a tip, which is the point furthest away from the diagonal. From an economical point of view, this is the most interesting point to operate, because the productivity is the highest, and the desorbent consumption is the lowest. However, at this point, one of the purities is at the limit of the purity requirement. Therefore, to ensure that the desired purity is attained, regardless of the possible flowrate fluctuations when operating real SMBR units, the operating point should be slightly closer to the diagonal.

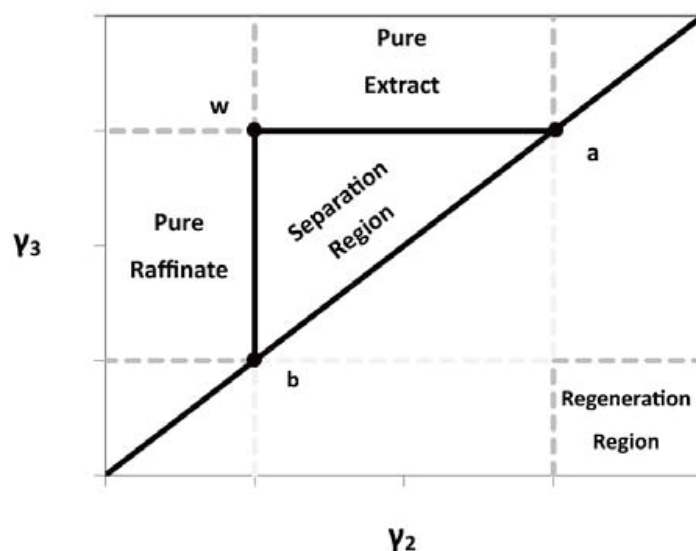


Figure 8. Separation region for linear isotherms assuming the equilibrium theory is valid.

To determine this reactive-separation region, multiple simulations are run with different flow rates. Because the γ_1 and γ_4 are set, the recycle and eluent flow are also set. The simulations are run until the cyclic steady state is reached, and then the raffinate and extract purities are known. At the beginning of the simulation, the extract and feed flowrates are set, and the raffinate flowrate is calculated, in order to close the mass balance. At the first simulation, a low value should be set to the feed flow and extract flow. This way, both γ_2 and γ_3 values are high, and should be outside the reactive-separation region. The next simulation should have a higher extract flowrate with the same feed flowrate. This way, the point on the graph moves parallel to the diagonal. At a certain extract flowrate, the point gets inside of the graph, and at some point, with an even higher extract flow rate, the point gets outside the region. At this moment, the boundaries of the reactive-separation region are known, with a certain feed flowrate. The next point is with the same extract flowrate that is just outside the region, but with a higher feed flowrate. Increasing the feed flowrate moves the point perpendicular to the diagonal. Because it is known that at best, the reactive-separation region is a triangle, as presented in Figure 8, this point should still be outside of the region. Now the extract flowrate is decreased, and will move inside the region, and eventually get outside of the region again. From that point, the feed flowrate is increased, and after that, the extract flowrate will be increased again. This goes on until a certain point where the purity requirements will not be met anymore by changing the extract flowrate. From that moment, the maximum feed flowrate is reached, corresponding to the vertex of the region. At this moment, the separation region can be drawn (with several discrete points corresponding to simulations with different γ and switching time values combinations that ran until the cyclic steady state was reached), and the performance parameters of the vertex will be compared with other vertexes, obtained using different switching times, in a first approach. It has to be noted that conversion is an important factor, but since the conversion is computed regarding butanal (the limiting reactant), and the desorbent is ethanol, the conversion will almost go to completion in all the cases.

As was stated before, the separation region will not be a perfect triangle. But since we are not interested in constructing the whole separation region for every simulation, it is only done once, while in the remaining situations only the points closer to the vertex of the reactive-separation region were simulated to reduce the computation time. In Figure 9 the reactive-separation region is shown with a switching time of 4.5 min. The reactive-separation region was drawn by setting a purity requirement of 97% for both raffinate and extract.

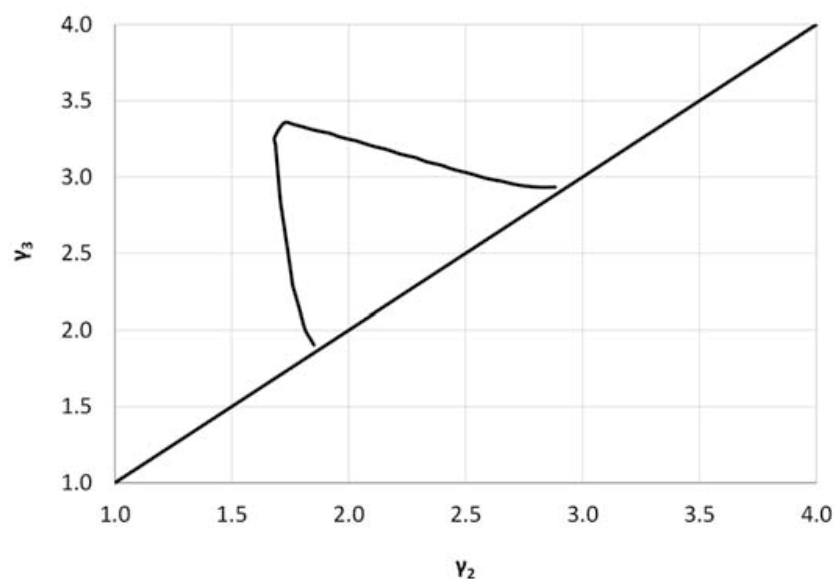


Figure 9. Separation region using a switching time of 4.5 min and a 20% safety factor for γ_1 and γ_4 .

From Figure 9, it can be observed that the separation region is not an ideal triangle, but it still has a vertex, which represents the optimal operating point for this switching time. Changing the switching time will change the separation region regarding the γ_2 and γ_3 values, but the shape will be similar. The main thing that will change is its area, because a more appropriate switching time will result in a larger separation region. The conditions used for the simulation are presented in Table 4. For the further simulations that are done in this work, these conditions were maintained.

In Figure 10, the productivity and desorbent consumption are plotted against the switching time. Every point on this graph represents the productivity and the desorbent consumption corresponding to the vertex of the reactive-separation region attained for that particular switching time.

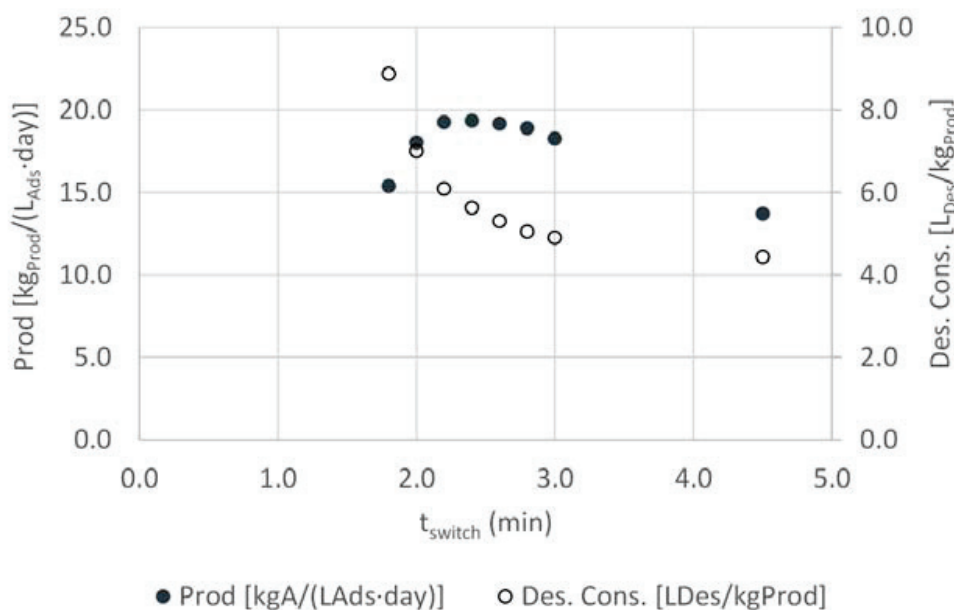


Figure 10. Sensitivity analysis regarding the influence of switching time on the productivity and the desorbent consumption, by setting a 20% safety factor for γ_1 and γ_4 .

From Figure 10, a maximum is observed regarding the productivity at a switching time of 2.4 min. If the switching time is further decreased, in order to have enough contact time between the reactants and the catalyst, the feed flowrate has to be lower. When the switching time is further increased, the contact time becomes longer than needed, so this reduces the efficiency of the process, and so it reduces the productivity, as well. From this, it can be concluded that a switching time of 2.4 min is the optimum.

3.3. Optimization of DEB Synthesis by SMBR: Separation Volumes

In the sensitivity analysis performed in the previous section, where the operating performances were determined for multiple switching times, the values of γ_1 and γ_4 were kept constant, considering a 20% safety factor relatively to the values provided by the Equilibrium Theory (Equations (34) and (35)). The optimization procedure that will be implemented in this section will allow the maximization of the productivity and the minimization of the desorbent consumption through the optimization of γ_2 and γ_3 values as a function of γ_1 and γ_4 , defining a minimum purity requirement of 97%.

The two-level SMBR optimization procedure was adopted was based on the Separation Volumes concept [24,25]. This methodology (previously used in the optimization of SMB separations [28]) can be interpreted as an extrapolation of the Reactive-Separation Regions methodology, commonly used of the determination of the optimum flow rate ratios in Sections 2 and 3 of the SMBR (for predetermined γ_1 , γ_4 and switching time values), coupled with a sensitivity analysis to the flow rate ratios in Sections 1 and 4. The limit values for the latter variables can be determined through the Equilibrium Theory, as explained earlier, which defines the maximum eluent recycling flow rate in Section 4 and the minimum desorbent flow rate in Section 1, which allow the regeneration of the liquid and solid phases, respectively. Therefore, in the Reactive Separation Volumes methodology, several reactive-separation regions are determined for different combinations of γ_1 and γ_4 values, sequentially approaching the limit values imposed by the Equilibrium Theory to these variables. The procedure to determine each of these reactive-separation regions is described in detail in the previous section and basically consists of determining the (γ_2, γ_3) sets that meet the target species purity specifications for each (γ_1, γ_4) set. Repeating the process for different (γ_1, γ_4) combinations, as detailed before, will allow the determination of the reactive separation volumes.

The optimization process can then be divided into two levels: the first is the optimization of the productivity or, in other words, the maximization of the difference $(\gamma_3 - \gamma_2)$, since this corresponds to the highest feed flow rate that the unit can treat; and the second is the optimization of the desorbent consumption, which corresponds to the minimum $(\gamma_1 - \gamma_4)$, since the desorbent flow rate will decrease as this difference decreases. At the end of this procedure, the optimum flow rates are known for the predetermined optimum switching time (which is 2.4 min, according to the results reported in the previous section).

In Figures 11 and 12, two 3D plots are presented, where the desorbent consumption and the productivity are plotted against the values of γ_1 and γ_4 .

From these plots, it can be seen that the optimum productivity is reached with a γ_1 value of 4.24 and a γ_4 of 1.35. From the plot with the desorbent consumption it can be seen that this point is not the optimum point, but the optimum point regarding the desorbent consumption corresponds to a significantly lower productivity. Since ethanol is used as a desorbent and this is a widely available bulk chemical, the optimum point is chosen regarding the highest productivity. At this point a productivity of 19.8 kg DEB per liter of adsorbent per day, a desorbent consumption of 6.1 L of ethanol per kg of DEB is reached.

Using this optimum point, the internal concentration profile is plotted in Figure 13.

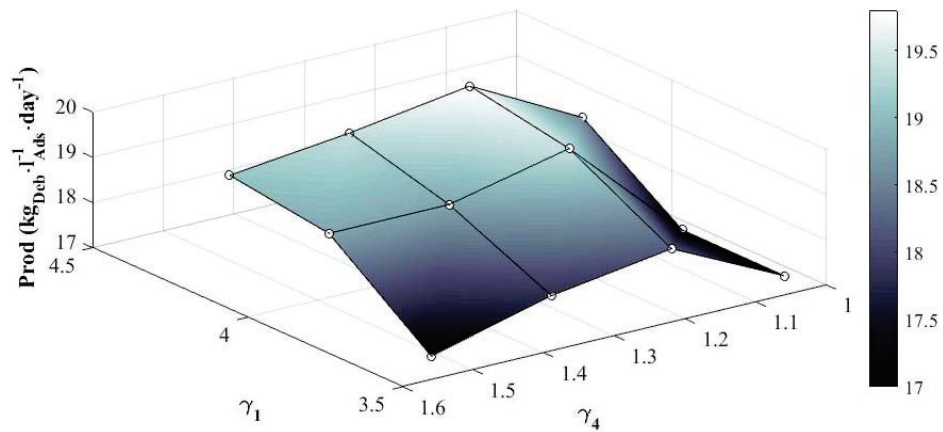


Figure 11. Productivity performance against γ_1 and γ_4 at the optimum γ_2 and γ_3 .

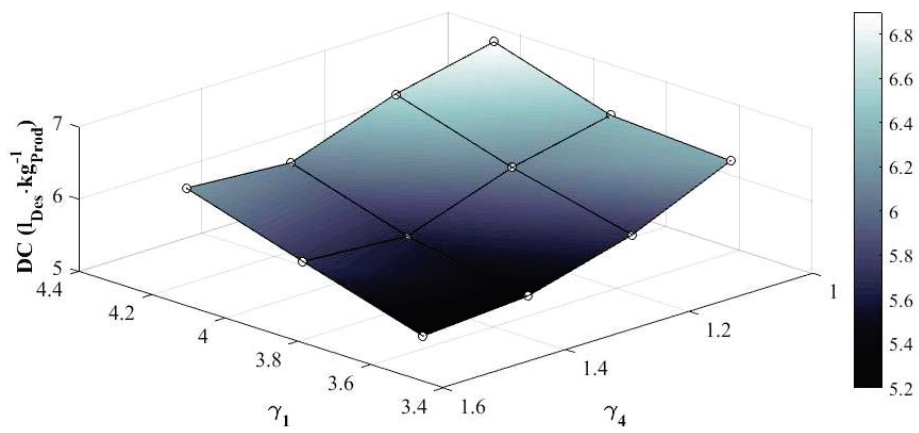


Figure 12. Desorbent consumption performance against γ_1 and γ_4 at the optimum γ_2 and γ_3 .

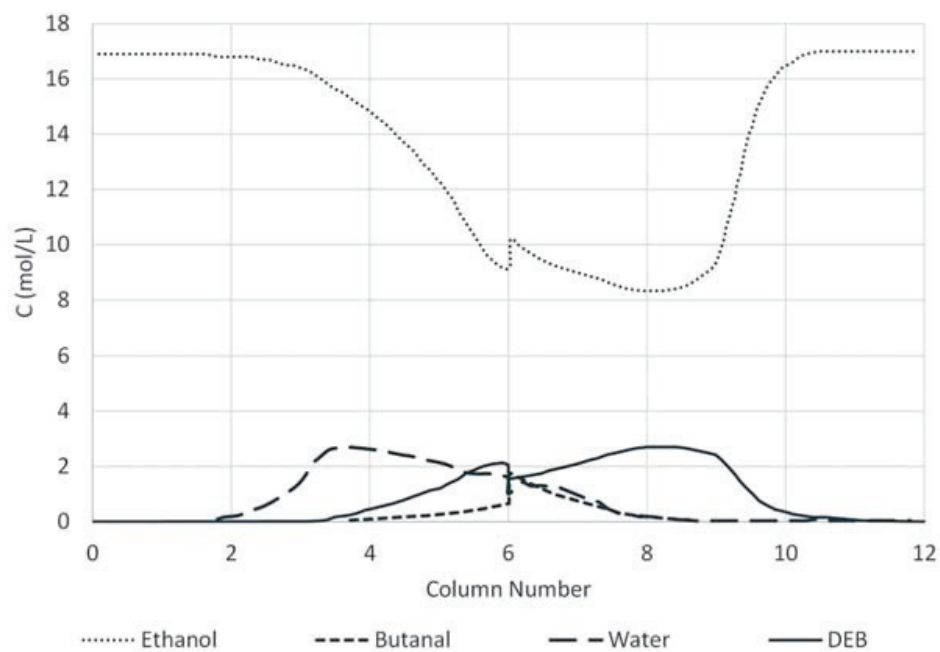


Figure 13. Cyclic steady state profile at half switching time.

In Figure 13, the concentrations are taken at half the switching time, during the last cycle. In this figure, the x-axis divides the graph into four sections, which correspond to the four sections mentioned earlier. It is important to see that at the extract port at column 3, almost no DEB should be present, since this would decrease the purity of the extract. The same goes for the raffinate port at column 9, where no water should be present. From Figure 13 it is also clear that the purity does not include the ethanol, which comprises a high fraction of both outgoing streams.

The limiting reactant conversion value attained for the SMBR process optimized within this work was 99.99%. Hence, the multifunctional reactor proposed and studied in this work clearly outperforms reactive distillation units [12,13] and membrane reactors [14,16] previously reported in the open literature, in terms of reactants conversion. The main reason for the high conversion values attained in the SMBR is related to its operating conditions, more specifically, its operating temperature. Since the acetalization reaction between ethanol and butanol is exothermic, the chemical reaction thermodynamic equilibrium will benefit from lower operating temperatures, which will lead to higher equilibrium conversions. As the SMBR unit studied in this work operates at 303 K, the chemical reaction thermodynamic limitations are less penalizing in terms of the overall process performance than those observed for reactive distillation units and membrane reactors which typically operate above 343 K. Moreover, the products' separation by adsorption, which is also an exothermic phenomenon, is simultaneously favored by lower operating temperatures. These facts are at the foundation of the SMBR-enhanced performance. Furthermore, lower operating temperatures may also represent a considerable advantage in terms of the overall energy consumption of the process.

As stated in previous studies [15], the main cost of the DEB consists of the raw material costs. Therefore, it is important to use the ethanol and butanal as efficiently as possible. Since ethanol is used as desorbent in the SMBR, butanal almost reaches full conversion. So, butanal is used as efficiently as possible. In both the raffinate and extract streams, the products are diluted in ethanol, so this can be recycled in order to optimize the process. The ethanol in the extract stream can be purified using a hydrophilic membrane. This method does not have issues with azeotropes compared to distillation, and has shown its capabilities in previous studies [29]. This way, the ethanol can be used as desorbent again. From the raffinate stream, the DEB needs to be separated from the ethanol. This can be achieved using distillation, since the boiling point of ethanol is at 78 °C and the boiling point of DEB is at 143 °C.

4. Conclusions

The production of 1,1-diethoxybutane using the simulated moving bed reactor technology was investigated, using ethanol and butanal as starting materials.

The simulated moving bed reactor model used in this work was based on a single column fixed bed model developed in a previous work. This model was validated against experimental data showing good agreement with the experimental results.

A two-level optimization procedure based on the Separation Volumes concept was successfully implemented to this case study. The optimum ratios between the liquid flow rate over the solid flow rate in Sections 1–4 were found to be 4.24, 1.77, 3.03 and 1.35, respectively, for a switching time of 2.4 min. Using these results, a productivity of 19.8 kg 1,1-diethoxybutane per liter of adsorbent per day and a desorbent consumption of 6.1 L of ethanol per kg of 1,1-diethoxybutane were estimated for the simulated moving bed reactor, considering a minimum purity of the extract and raffinate of 97%. Despite the promising performance demonstrated by the simulated moving bed reactor for the synthesis of 1,1-diethoxybutane, it must be noted that there are other variables that can affect the productivity and desorbent consumption that were not taken into account in this study. These include the configuration, feed concentration and the dimensions of the column.

Reactive distillation units and membrane reactors have been reported in the open literature as the most efficient multifunctional reactors for the synthesis of 1,1-diethoxybutane; however, the results attained for the simulated moving bed reactor in this work revealed that adsorption-based reactive processes can outperform the technologies previously proposed for the synthesis of this acetal. Since this process involves a thermodynamically limited exothermic reaction, it will take advantage from the lower operating temperatures typically associated with chromatographic separations (due to the exothermic nature of the adsorption). The simulated moving bed reactor can reach complete limiting reactants conversion at 303 K, while the remaining state-of-the-art technologies typically do not overcome 50% to 70%, because their operating temperature is above 343 K.

Author Contributions: A.E.R. conceptualized and coordinated all the aspects of the work, R.P.V.F. developed the gPROMS mathematical models used in the work and defined the optimization strategy adopted, J.S. performed all the simulations and prepared the original manuscript, J.C.G. revised the methodology and the results. All authors were involved in the review and editing of the final manuscript. All authors have read and agreed to the published version of the manuscript.

Funding: This work was financially supported by: Base Funding—UIDB/50020/2020 of the Associate Laboratory LSRE-LCM—funded by national funds through FCT/MCTES (PIDDAC).

Informed Consent Statement: Not applicable.

Data Availability Statement: The data presented in this study are available on request from the corresponding author.

Acknowledgments: The authors acknowledge FCT/MCTES (PIDDAC) for the financial support: Base Funding—UIDB/50020/2020 of the Associate Laboratory LSRE-LCM.

Conflicts of Interest: The authors declare no conflict of interest.

Glossary

List of symbols

a	Activity
A	Cross-sectional area (dm ²)
C	Concentration (mol L ⁻¹)
CO ₂	Carbon dioxide
CFDM	Centered finite difference method
$D_{i,m}$	Diffusion coefficient of compound i in a mixture
D_{ax}	Axial dispersion coefficient
DC	Desorbent consumption (L _{des.} Kg ⁻¹ _{DEB})
DEB	1,1-diethoxybutane
k_B	Boltzmann constant ($1.38064852 \times 10^{-23}$ m ² kg s ⁻² K ⁻¹)
K	Adsorption equilibrium constant (L mol ⁻¹)
k_C	Reaction kinetic constant (mol g ⁻¹ s ⁻¹)
K_E	External mass transfer (dm s ⁻¹)
K_{eq}	Equilibrium constant
K_i	Internal mass transfer (dm s ⁻¹)
K_L	Overall mass transfer coefficient (dm s ⁻¹)
$K_{S,D}$	Water adsorption constant
L	Length of the column (dm)
NO _x	Nitrogen oxides
PR	Productivity (Kg _{DEB} L _{ads.} ⁻¹ day ⁻¹)
PUR	Raffinate purity (%)
PUX	Extract purity (%)
Q	Flow rate (L s ⁻¹)
q	Particle solid concentration (mol L ⁻¹)
Q_i	Molar Adsorption capacity of compound i (mol L ⁻¹)
r	Reaction rate (mol g ⁻¹ s ⁻¹)
Re	Reynolds number

Sc	Schmidt number
Sh	Sherwood number
$SMBR$	Simulated moving bed reactor
T	Temperature (K)
t	Time (s)
$TMBR$	True moving bed reactor
u	Interstitial Velocity (dm s^{-1})
V_{mol}	Molar volume ($\text{dm}^3 \text{mol}^{-1}$)
X	Conversion (%)
x	Molar fraction
z	Dimensionless axial coordinate (dm s^{-1})
Greek letters	
β	Safety factor
γ	Ratio between liquid and solid interstitial velocities
ε	Porosity (volume void volume bed ⁻¹)
η	Viscosity (cP)
ρ	Density (g L^{-1})
τ	Tortuosity
Subscripts	
B	Butanal
D	Desorbent
$EtOH$	Ethanol
F	Feed
i	Component i
m	Mixture
p	Particle
R	Raffinate
Rec	Recycle
W	Water
X	Extract

References

1. EIA. *Emissions of Greenhouse Gases in the United States*; EIA: Washington, DC, USA, 2001–2002.
2. Claesson, K. *Effects of Nutrients Supplementation on Fermentability of Lignocellulosic Hydrolysates under High Gravity Conditions*; Chalmers University of Technology: Gothenburg, Sweden, 2012.
3. Ma, F.; Hanna, M.A. Biodiesel production: A review. *Bioresour. Technol.* **1999**, *70*, 1–15. [[CrossRef](#)]
4. Atabani, A.E.; Silitonga, A.S.; Badruddin, I.A.; Mahlia, T.M.I.; Masjuki, H.H.; Mekhilef, S. A comprehensive review on biodiesel as an alternative energy resource and its characteristics. *Renew. Sustain. Energy Rev.* **2012**, *16*, 2070–2093. [[CrossRef](#)]
5. McCormick, R.L.; Graboski, M.S.; Alleman, T.L.; Herring, A.M.; Tyson, K.S. Impact of biodiesel source material and chemical structure on emissions of criteria pollutants from a heavy-duty engine. *Environ. Sci. Technol.* **2001**, *35*, 1742–1747. [[CrossRef](#)] [[PubMed](#)]
6. Moser, B.R.; Erhan, S.Z. Branched chain derivatives of alkyl oleates: Tribological, rheological, oxidation, and low temperature properties. *Fuel* **2008**, *87*, 2253–2257. [[CrossRef](#)]
7. Frusteri, F.; Spadaro, L.; Beatrice, C.; Guido, C. Oxygenated additives production for diesel engine emission improvement. *Chem. Eng. J.* **2007**, *134*, 239–245. [[CrossRef](#)]
8. Kolah, A.K.; Asthana, N.S.; Vu, D.T.; Lira, C.T.; Miller, D.J. Reaction kinetics of the catalytic esterification of citric acid with ethanol. *Ind. Eng. Chem. Res.* **2007**, *46*, 3180–3187. [[CrossRef](#)]
9. Andrade, J.; Arntz, D.; Kraft, M.; Prescher, G. Method for Preparation of Acetals. U.S. Patent 45,799,79A, 1 April 1986.
10. Silva, V.M.; Rodrigues, A.E. Kinetic studies in a batch reactor using ion exchange resin catalysts for oxygenates production: Role of mass transfer mechanisms. *Chem. Eng. Sci.* **2006**, *61*, 316–331. [[CrossRef](#)]
11. Rahaman, M.; Graça, N.; Pereira, C.; Rodrigues, A.E. Thermodynamic and kinetic studies for synthesis of the acetal (1, 1-diethoxybutane) catalyzed by Amberlyst 47 ion-exchange resin. *Chem. Eng. J.* **2015**, *264*, 258–267. [[CrossRef](#)]
12. Agirre, I.; Barrio, V.L.; Güemez, B.; Cambra, J.F.; Arias, P.L. Bioenergy II: The development of a reactive distillation process for the production of 1, 1 diethoxy butane from bioalcohol: Kinetic study and simulation model. *Int. J. Chem. React. Eng.* **2010**, *8*. [[CrossRef](#)]
13. Agirre, I.; Barrio, V.L.; Güemez, B.; Cambra, J.F.; Arias, P.L. Catalytic reactive distillation process development for 1,1 diethoxy butane production from renewable sources. *Bioresour. Technol.* **2011**, *102*, 1289–1297. [[CrossRef](#)]
14. Agirre, I.; Güemez, M.B.; Motelica, A.; van Veen, H.M.; Vente, J.F.; Arias, P.L. The conceptual design of a continuous pervaporation membrane reactor for the production of 1,1-diethoxy butane. *AIChE J.* **2012**, *58*, 1862–1868. [[CrossRef](#)]

15. Agirre, I.; Uemez, M.B.E.; Motelica, A.; van Veen, H. A techno-economic comparison of various process options for the production of 1,1-diethoxy butane. *J. Chem. Technol. Biotechnol.* **2012**, *87*, 943–954. [[CrossRef](#)]
16. Agirre, I.; Güemez, M.B.; van Veen, H.M.; Motelica, A.; Vente, J.F.; Arias, P.L. Acetalization reaction of ethanol with butyraldehyde coupled with pervaporation. Semi-batch pervaporation studies and resistance of HybSi®membranes to catalyst impacts. *J. Membr. Sci.* **2011**, *371*, 179–188. [[CrossRef](#)]
17. Regufe, M.J.; Faria, R.; Ribeiro, A.M.; Loureiro, J.M. Synthesis of the Biofuel Additive 1,1-Diethoxybutane in a Fixed-Bed Column with Amberlyst-15 Wet. *Chem. Eng. Technol.* **2016**, *39*, 1509–1518. [[CrossRef](#)]
18. Zhang, Z.; Hidajat, K.; Ray, A.K. Application of Simulated Countercurrent Moving-Bed Chromatographic Reactor for MTBE Synthesis. *Ind. Eng. Chem. Res.* **2001**, *40*, 5305–5316. [[CrossRef](#)]
19. Graça, N.S.; Pais, L.S.; Silva, V.M.T.M.; Rodrigues, A.E. Analysis of the synthesis of 1,1-dibutoxyethane in a simulated moving-bed adsorptive reactor. *Chem. Eng. Process. Process Intensif.* **2011**, *50*, 1214–1225. [[CrossRef](#)]
20. Silva, V.M.T.M.; Rodrigues, A.E. Novel process for diethylacetal synthesis. *AIChE J.* **2005**, *51*, 2752–2768. [[CrossRef](#)]
21. Pereira, C.S.M.; Gomes, P.S.; Gandi, G.K.; Silva, V.M.T.M.; Rodrigues, A.E. Multifunctional reactor for the synthesis of dimethylacetal. *Ind. Eng. Chem. Res.* **2008**, *47*, 3515–3524. [[CrossRef](#)]
22. Graça, N.S.; Delgado, A.E.; Constantino, D.S.; Pereira, C.S.; Rodrigues, A.E. Synthesis of a renewable oxygenated diesel additive in an adsorptive reactor. *Energy Technol.* **2014**, *2*, 839–850. [[CrossRef](#)]
23. Minceva, M.; Rodrigues, A.E. Two-level optimization of an existing SMB for p-xylene separation. *Comput. Chem. Eng.* **2005**, *29*, 2215–2228. [[CrossRef](#)]
24. Azevedo, D.C.S.; Rodrigues, A.E. Design of a simulated moving bed in the presence of mass-transfer resistances. *AIChE J.* **1999**, *45*, 956–966. [[CrossRef](#)]
25. Rodrigues, A.E.; Pereira, C.; Minceva, M.; Pais, L.S.; Ribeiro, A.M.; Ribeiro, A.; Silva, M.; Graça, N.; Santos, J.C. *Simulated Moving Bed Technology: Principles, Design and Process Applications*; Elsevier Science: Oxford, UK, 2015.
26. Shi, Q.; Gonçalves, J.C.; Ferreira, A.F.P.; Plaza, M.G.; Rodrigues, A.E. Xylene isomerization over Beta zeolites in liquid phase. *Ind. Eng. Chem. Res.* **2018**, *57*, 5568–5579. [[CrossRef](#)]
27. Guevara-Carrion, G.; Vrabec, J.; Hasse, H. Prediction of self-diffusion coefficient and shear viscosity of water and its binary mixtures with methanol and ethanol by molecular simulation. *J. Chem. Phys.* **2011**, *134*, 074508. [[CrossRef](#)] [[PubMed](#)]
28. Coelho, L.C.D.; Filho, N.M.L.; Faria, R.P.V.; Ferreira, A.F.P.; Ribeiro, A.M.; Rodrigues, A.E. Separation of tartronic and glyceric acids by simulated moving bed chromatography. *J. Chromatogr. A* **2018**, *1563*, 62–70. [[CrossRef](#)]
29. Gravelle, S.; Yoshida, H.; Joly, L.; Ybert, C.; Bocquet, L. Carbon membranes for efficient water-ethanol separation. *J. Chem. Phys.* **2016**, *145*, 124708. [[CrossRef](#)]

Article

Removal of Dissolved Oxygen from Water by Nitrogen Stripping Coupled with Vacuum Degassing in a Rotor–Stator Reactor

Zemeng Zhao ¹, Zhibang Liu ², Yang Xiang ², Moses Arowo ³ and Lei Shao ^{2,*}

¹ Clean Utilization Research Institute, China Coal Energy Research Institute Co., Ltd., Xi'an 710054, China; hunter_zzm@163.com

² Research Center of the Ministry of Education for High Gravity Engineering and Technology, College of Chemical Engineering, Beijing University of Chemical Technology, Beijing 100029, China; 2019400002@mail.buct.edu.cn (Z.L.); xiangy@mail.buct.edu.cn (Y.X.)

³ Department of Chemical & Process Engineering, Moi University, Eldoret 3900, Kenya; musarowo@yahoo.com

* Correspondence: shaol@mail.buct.edu.cn; Tel.: +86-10-6442-1706

Citation: Zhao, Z.; Liu, Z.; Xiang, Y.; Arowo, M.; Shao, L. Removal of Dissolved Oxygen from Water by Nitrogen Stripping Coupled with Vacuum Degassing in a Rotor–Stator Reactor. *Processes* **2021**, *9*, 1354. <https://doi.org/10.3390/pr9081354>

Academic Editors: Elio Santacesaria, Riccardo Tesser and Vincenzo Russo

Received: 8 June 2021

Accepted: 30 July 2021

Published: 1 August 2021

Publisher's Note: MDPI stays neutral with regard to jurisdictional claims in published maps and institutional affiliations.



Copyright: © 2021 by the authors. Licensee MDPI, Basel, Switzerland. This article is an open access article distributed under the terms and conditions of the Creative Commons Attribution (CC BY) license (<https://creativecommons.org/licenses/by/4.0/>).

Abstract: Oxygen is a harmful substance in many processes because it can bring out corrosion and oxidation of food. This study aimed to enhance the removal of dissolved oxygen (DO) from water by employing a novel rotor–stator reactor (RSR). The effectiveness of the nitrogen stripping coupled with vacuum degassing technique for the removal of DO from water in the RSR was investigated. The deoxygenation efficiency (η) and the mass transfer coefficient (K_La) were determined under various operating conditions for the rotational speed, liquid volumetric flow rate, gas volumetric flow rate, and vacuum degree. The nitrogen stripping coupled with vacuum degassing technique achieved values for η and K_La of 97.34% and 0.0882 s^{-1} , respectively, which are much higher than those achieved with the vacuum degassing technique alone ($\eta = 89.95\%$ and $K_La = 0.0585 \text{ s}^{-1}$). A correlation to predict the K_La was established and the predicted K_La values were in agreement with the experimental values, with deviations generally within 20%. The results indicate that RSR is a promising deaerator thanks to its intensification of gas–liquid contact.

Keywords: deoxygenation efficiency; vacuum– N_2 – H_2O – O_2 system; rotor–stator reactor; mass transfer; correlation

1. Introduction

Oxygen plays a key role in the treatment of wastewater [1,2]. Nevertheless, oxygen is a harmful substance and removal of dissolved oxygen (DO) from water is an essential step carried out in power plants in order to prevent corrosion in boilers and pipes, improve heat transfer and enhance plant efficiency [3–5]. This operation is not only adopted in the power industry but is also necessary in the semiconductor, pharmaceutical, biotechnology and food industries, which also have stringent requirements for DO levels in water [6,7]. It is thus indispensable to remove DO from water prior to its use in many industries.

Various physical techniques, such as thermal degassing, vacuum degassing and nitrogen stripping, are currently employed by industries to remove DO from water. It has been reported that nitrogen stripping is the most effective approach for DO removal among these techniques [8]. Coupled techniques, such as thermal degassing with vacuum degassing or thermal degassing with nitrogen stripping, are also promising means for DO removal [8,9]. However, these techniques are conventionally carried out in packed towers/columns that exhibit poor mass transfer performance and, as a result, suffer limitations related to low efficiency, bulkiness, high costs and inflexibility in operation [10–12]. It is therefore necessary to develop a simple and efficient technique to remove DO from water, and a gas–liquid contactor capable of good mass transfer performance is desirable.

The rotor–stator reactor (RSR) is a novel multiphase contactor comprising a series of rotor rings and stator rings alternately configured in a radial direction [13]. In an RSR, a high-gravity environment several orders of magnitude greater than the Earth’s gravitational field can be created as a result of the huge centrifugal force produced by rapid rotation of the rotor. Consequently, the liquid stream in the RSR is broken into small elements and thin films [14–16]. There is also increased turbulence of the gas and liquid streams, in addition to rapid renewal of the gas–liquid interface [17,18]. All of these properties can greatly enhance the mass transfer rate in an RSR. Thus, RSRs have successfully been employed in degradation of organic pollutants [19,20], nanomaterial synthesis [21], CO₂ capture [22] and other applications.

This work therefore employed an RSR to intensify the removal of DO from water through nitrogen stripping coupled with vacuum degassing (vacuum–N₂–H₂O–O₂ system). The effects of various operating conditions, such as the rotational speed of the RSR, the liquid volumetric flow rate, the gas volumetric flow rate and the vacuum degree of the RSR, on the deoxygenation efficiency, as well as on the mass transfer coefficient, were investigated. Separate experiments involving nitrogen stripping (N₂–H₂O–O₂ system) and vacuum degassing (vacuum–H₂O–O₂ system) were also carried out for comparison. Additionally, a correlation to predict the mass transfer coefficient ($K_L a$) in the RSR was also established.

2. Materials and Methods

2.1. Structure of RSR

The structure of the RSR is shown in Figure 1a. The RSR consisted primarily of a liquid distributor, rotor seat, shaft, seal, rotor and stator. The rotor was comprised of six circular rings (named rotor rings) located on a rotor seat, which was connected to a motor by a shaft, while the stator consisted of five layers of pins (named stator rings) mounted concentrically on a cover cap. As shown in Figure 1b, the open space between pins in the same layer and the perforations in the rotor provide the flow channels for fluids in the RSR [15].

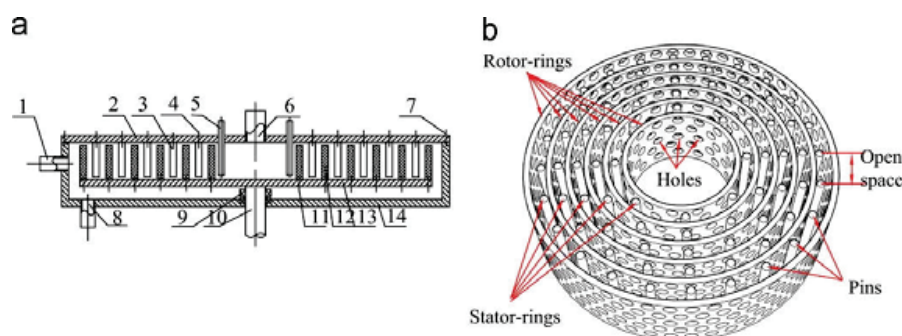


Figure 1. Schematic diagrams of an RSR. (a) Structure of an RSR; (b) 3D diagram of rotor rings and stator rings: (1) gas inlet; (2) cover cap; (3) stator; (4, 7, 11) bolts; (5) liquid distributor; (6) gas outlet; (8) liquid outlet; (9) seal; (10) shaft; (12) rotor; (13) rotor seat; (14) casing.

As shown in Table 1, the inner diameter of the rotor rings ranged from 70 to 190 mm and thus could provide centrifugal acceleration ranging from 28.48 to 1395.68 m²/s. The stator rings (diameter ranges from 80 to 176 mm) allow the redistribution of liquid in an RSR.

Table 1. Specifications of the RSR.

Item	Unit	Value
Layer number of rotor rings	-	6
Layer number of stator rings	-	5
Number of perforations in rotor rings	-	180, 240, 294, 348, 408, 462
Number of pins in stator rings	-	12, 16, 20, 24, 24
Diameter of perforations in rotor rings	mm	4
Diameter of pins in stator rings	mm	5
Inner diameter of rotor rings	mm	70, 94, 118, 142, 166, 190
Inner diameter of stator rings	mm	80, 104, 128, 152, 176
Inner diameter of the RSR	mm	300
Axial depth of rotor rings	mm	61
Axial depth of stator rings	mm	60
Axial depth of the RSR	mm	65
Internal volume of the RSR	cm ³	4592

2.2. Experimental Procedure

Figure 2 shows the experimental setup for the vacuum–N₂–H₂O–O₂ system. The liquid inlet and outlet of the RSR were connected to a centrifugal pump and sealed tank, respectively, whereas the gas inlet and outlet were connected respectively to a nitrogen gas cylinder and a vacuum system, which was made up of a vacuum pump and a buffer tank. The buffer tank helped to maintain the pressure balance in the DO removal system. Tap water was pumped via the liquid distributor into the RSR vacuumized below atmospheric pressure and allowed to flow radially outward through the rotor rings and stator rings, while nitrogen gas was introduced into the RSR via a gas inlet and allowed to flow inward through the rotor rings and stator rings. The nitrogen gas stream made contact in a counter-current with the water stream in the RSR, leading to removal of DO from the water by both vacuum degassing and nitrogen stripping. The gas and liquid streams finally exited the RSR via the gas and liquid outlets, respectively. The DO concentration in the tap water and deoxygenated water was measured using a DO detector (Rex, SJG-203A, CHN; detection limits: 0~19.99 mg/L). The composition of the gas used in this study was 99.5% N₂ and 0.5% O₂.

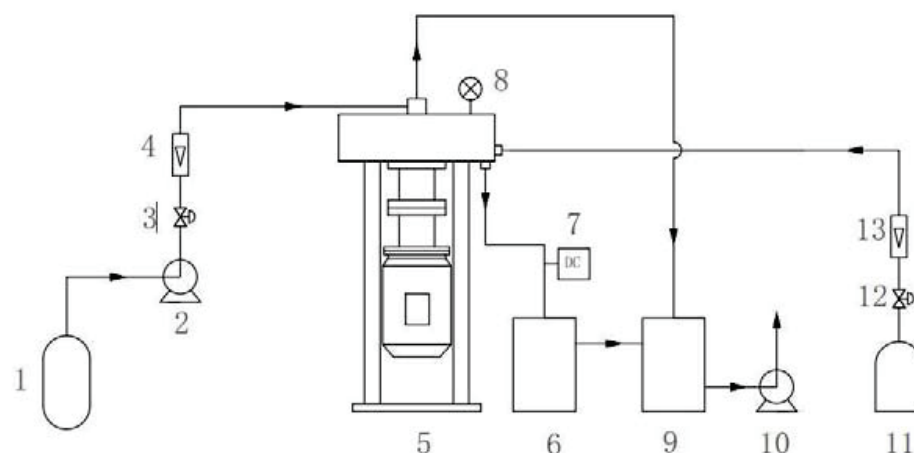


Figure 2. Experimental set up: (1) Water tank; (2) centrifugal pump; (3, 12) valve; (4) liquid flow meter; (5) RSR; (6) sealed tank; (7) DO detector; (8) vacuum gauge; (9) buffer tank; (10) vacuum pump; (11) nitrogen cylinder; (13) gas flow meter.

Experiments involving nitrogen stripping or vacuum degassing were performed in the same way as with the vacuum–N₂ technique.

The operating conditions were set as follows: rotational speed = 200–1400 rpm, liquid volumetric flow rate = 0.35–0.6 m³/h, gas volumetric flow rate = 1–7 m³/h, vacuum degree

= 0.02–0.06 MPa, inlet liquid temperature = 300 ± 2 K (ambient temperature) and initial DO concentration in tap water = 7.85–8.01 mg/L.

2.3. Calculation of $K_L a$ and η

The equation for the experimental $K_L a$ (Equation (1)) was obtained by referring to literature [23]:

$$K_L a = \frac{Q_L}{H\pi R^2} \times \frac{x_{in} - x_{out}}{(x - x_e)_{in} - (x - x_e)_{out}} \ln \left(\frac{(x - x_e)_{in}}{(x - x_e)_{out}} \right) / c_M \quad (1)$$

where x_e is the equilibrium molar fraction of O_2 in liquid which was obtained using Equation (2):

$$x_e = \frac{L}{mG} (x - x_{out}) \quad (2)$$

The deoxygenation efficiency (η) was determined by the molar concentration of O_2 at the liquid inlet (c_{in}) and the outlet (c_{out}) (Equation (3)):

$$\eta = \frac{c_{in} - c_{out}}{c_{in}} \times 100\% \quad (3)$$

3. Results and Discussion

3.1. Effect of Rotational Speed

The effect of the rotational speed on η and $K_L a$ is illustrated in Figure 3. Both η and $K_L a$ increased from 96.32% and 0.0803 s^{-1} to 97.34% and 0.0882 s^{-1} , respectively, with an increase in rotational speed from 200 to 600 rpm, beyond which both η and $K_L a$ showed little change with increasing rotational speed. Higher rotational speeds caused a larger centrifugal force, which split the liquid into finer elements and thinner films. Consequently, there was increased turbulence in the gas and liquid streams, a larger gas–liquid interfacial area and a faster renewal rate of the gas–liquid interface, resulting in thinner gas and liquid boundary layers. All of these factors led to an enhanced gas–liquid mass transfer rate and thereby a larger $K_L a$ and higher η .

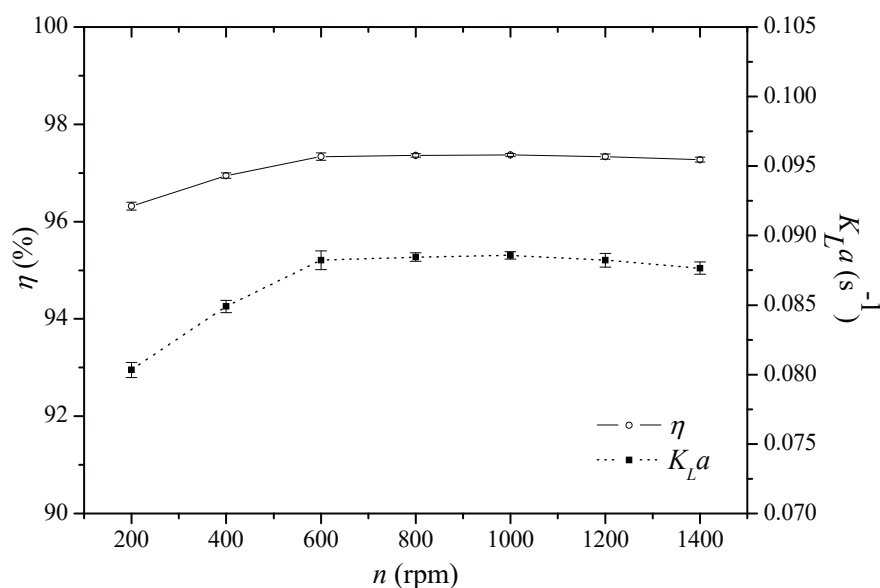


Figure 3. Effect of rotational speed on η and $K_L a$ ($L = 0.4 \text{ m}^3/\text{h}$; $G = 3 \text{ m}^3/\text{h}$; $P = 0.06 \text{ MPa}$; initial DO concentration = 7.96 mg/L).

Nonetheless, increasing rotational speed brought about increased liquid velocity, which reduced liquid residence time in the RSR and liquid holdup declined accordingly,

perhaps leading to a decrease in the gas–liquid interfacial area. The effect of the phenomena at rotational speeds greater than 600 rpm offset the aforementioned benefits of higher rotational speeds in this study, resulting in almost stable η and K_La .

According to Henry's law, the lowest equilibrium oxygen concentration in liquid is 0.2028 mg/L at 25 °C. Thus, the highest deoxygenation efficiency is 97.47% for tap water with an initial DO concentration of 8.01 mg/L. The deoxygenation efficiency of 97.34% in this study was close to the highest one, suggesting the good deoxygenation effect of the RSR.

3.2. Effect of Liquid Volumetric Flow Rate

Figure 4 shows the effect of the liquid volumetric flow rate on η and K_La . It was noted that η decreased by 4.22% (from 97.39 to 93.28%) while K_La increased by 27.98% (from 0.0772 to 0.0988 s⁻¹) with an increase in liquid volumetric flow rate from 0.35 to 0.6 m³/h. A higher liquid volumetric flow rate resulted in more liquid droplets and, consequently, a larger gas–liquid interface area, leading to an increase in K_La . Moreover, oxygen is sparingly soluble in water and the removal of DO from water is controlled by a liquid film. Thus, a higher liquid volumetric flow rate can result in a larger K_La . However, at a given gas–liquid equilibrium, vacuum degree and gas volumetric flow rate, a higher liquid volumetric flow rate led to a decline in η . A higher liquid volumetric flow rate led to a shorter liquid residence time in the RSR. This probably caused more liquid to exit the RSR before the maximum DO removal was achieved.

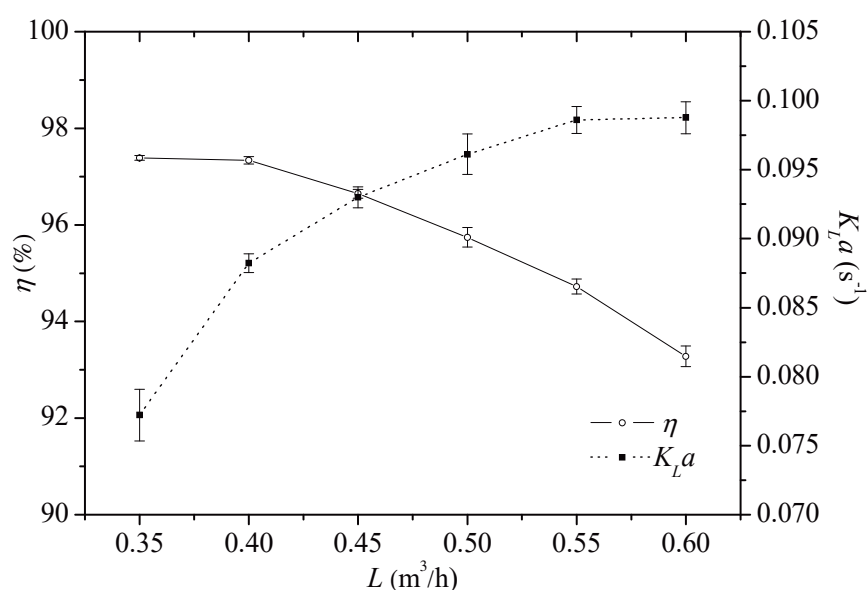


Figure 4. Effect of liquid volumetric flow rate on η and K_La ($n = 600$ rpm; $G = 3$ m³/h; $P = 0.06$ MPa; initial DO concentration = 7.96 mg/L).

3.3. Effect of Gas Volumetric Flow Rate

As shown in Figure 5, both η and K_La increased from 95.97 to 97.34% and 0.0791 to 0.0882 s⁻¹, respectively, with an increase in the gas volumetric flow rate from 1 to 3 m³/h, and thereafter they remained almost stable with further increases in the gas volumetric flow rate. This was because a higher gas volumetric flow rate resulted in increased turbulence in the gas and liquid streams, leading to a larger gas–liquid interfacial area and faster renewal rate of the gas–liquid interface, thereby resulting in the observed increase in η and K_La . However, as the gas volumetric flow rate further increased over 3 m³/h, the oxygen might have reached equilibrium between the gas and liquid phases. Thus, the increase in the gas–liquid interfacial area and the renewal rate of the gas–liquid interface had no effect on

the oxygen transfer from water to gas. Therefore, both η and $K_L a$ remained stable when the gas volumetric flow exceeded $3 \text{ m}^3/\text{h}$.

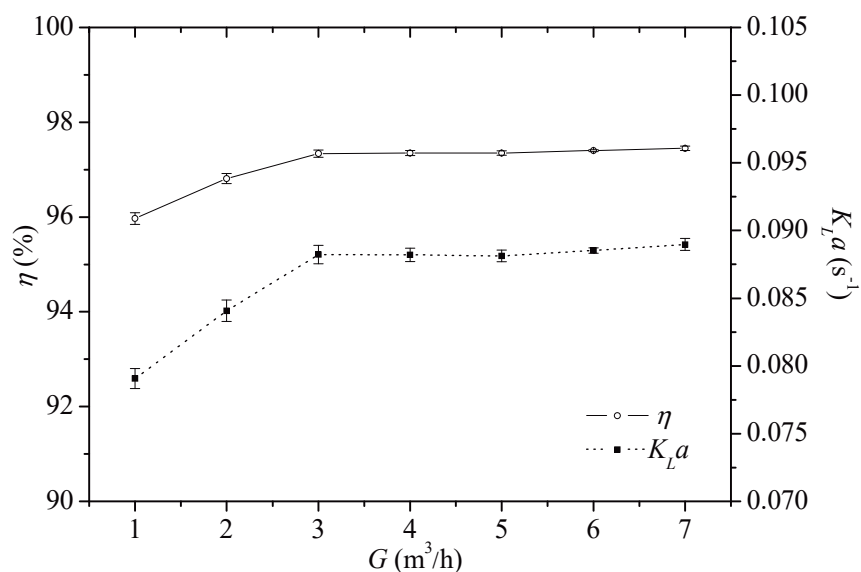


Figure 5. Effect of gas volumetric flow rate on η and $K_L a$ ($n = 600 \text{ rpm}$; $L = 0.4 \text{ m}^3/\text{h}$; $P = 0.06 \text{ MPa}$; initial DO concentration = 7.96 mg/L).

3.4. Effect of Vacuum Degree

The effect of the vacuum degree on η and $K_L a$ is shown in Figure 6. Both η and $K_L a$ increased from 95.03 to 97.06% and 0.0728 to 0.0856 s^{-1} , respectively, when the vacuum degree rose from 0.02 MPa to 0.04 MPa . This was because a higher vacuum degree causes more water vapor and lower oxygen partial pressure in the gas phase. Therefore, a high vacuum degree and more water vapor in the gas phase resulted in an increased mass transfer driving force and, consequently, higher η . A higher vacuum degree also results in a thinner mass transfer boundary layer [24]. Consequently, there was reduced mass transfer resistance and, hence, $K_L a$ was larger, which is also conducive to oxygen removal from water.

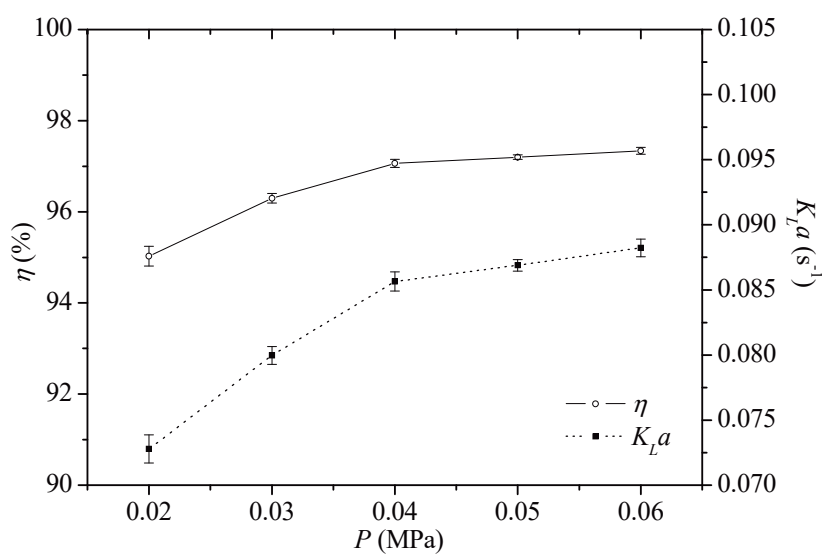


Figure 6. Effect of vacuum degree on η and $K_L a$ ($n = 600 \text{ rpm}$; $L = 0.4 \text{ m}^3/\text{h}$; $G = 3 \text{ m}^3/\text{h}$; initial DO concentration = 7.96 mg/L).

However, the DO concentration was low and the mass transfer driving force was small when the vacuum reached a high degree. Furthermore, the oxygen approached equilibrium between the gas and liquid phases under such conditions. Hence, both η and $K_L a$ increased slowly from 97.06 to 97.34% and 0.0856 to 0.0882 s^{-1} , respectively, with an increase in the vacuum degree from 0.04 to 0.06 MPa.

3.5. Comparison of Different Deoxygenation Systems in RSR

Figure 7 shows the values for η and $K_L a$ achieved by the N_2 - H_2O - O_2 , vacuum- H_2O - O_2 and vacuum- N_2 - H_2O - O_2 systems in the RSR, respectively. It is evident that the vacuum- N_2 - H_2O - O_2 system achieved the highest values for $K_L a$ and η among the three systems. This can be attributed to the synergistic effect of nitrogen stripping and vacuum degassing, as oxygen partial pressure in the gas phase of the vacuum- N_2 - H_2O - O_2 system at a certain vacuum degree was lower than that of the N_2 - H_2O - O_2 system at atmospheric pressure or the vacuum- H_2O - O_2 system at the same vacuum degree. Thus, according to Henry's law, the equilibrium concentration of DO in water in the vacuum- N_2 - H_2O - O_2 system was lower than that in the N_2 - H_2O - O_2 system at atmospheric pressure or the vacuum- H_2O - O_2 system at the same vacuum degree. In addition, it was also deduced that there was stronger turbulence in the vacuum- N_2 - H_2O - O_2 system in the RSR due to a faster gas velocity. This resulted in a larger gas-liquid interfacial area and a higher renewal rate of the gas-liquid interface, thereby leading to higher $K_L a$ and η .

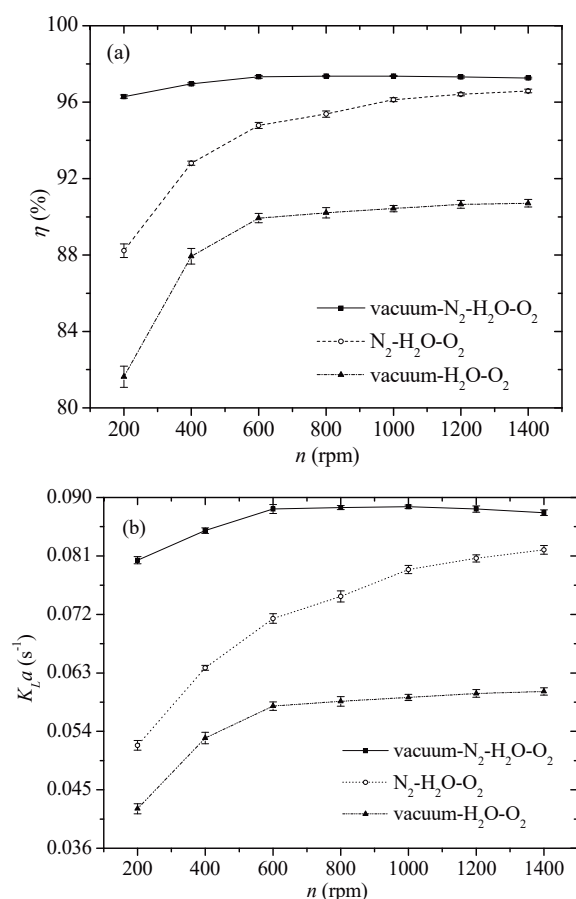


Figure 7. Comparison of the (a) η and (b) $K_L a$ of the N_2 - H_2O - O_2 , vacuum- H_2O - O_2 and vacuum- N_2 - H_2O - O_2 . $L = 0.4$ m^3/h , $G = 3$ m^3/h , $P = 0.06$ MPa and initial DO concentration = 7.96 mg/L in the vacuum- N_2 - H_2O - O_2 system; $L = 0.4$ m^3/h , $G = 3$ m^3/h and initial DO concentration = 7.85 mg/L in the N_2 - H_2O - O_2 system; and $L = 0.4$ m^3/h , $P = 0.06$ MPa and initial DO concentration = 8.01 mg/L in the vacuum- H_2O - O_2 system).

3.6. Correlation for $K_L a$

It was assumed that the mass transfer coefficient $K_L a$ in the RSR was influenced by 14 major factors, as shown in Table 2. The values of these factors were based on the experimental conditions and physical properties of the gas and liquid.

Table 2. Major influence factors of $K_L a$.

Factor	Symbol	Value	Unit	Dimension
Liquid inlet velocity	u_L	3.1~5.3	m/s	$[LT^{-1}]$
Angular velocity of rotor	ω	21~147	s^{-1}	$[T^{-1}]$
Geometric radius of rotor	R	0.115	m	$[L]$
Liquid density	ρ_L	997	kg/m^3	$[ML^{-3}]$
Liquid viscosity	μ_L	8.94×10^{-4}	$kg/(m \cdot s)$	$[ML^{-1}T^{-1}]$
Liquid surface tension	σ	71.97	kg/s^2	$[MT^{-2}]$
Gravitational acceleration	g	9.81	m/s^2	$[LT^{-2}]$
Temperature	T	25~29	$^{\circ}C$	$[^{\circ}]$
Inlet air humidity	φ	-	%	-
Gas inlet velocity	u_G	8.85~61.95	m/s	$[LT^{-1}]$
Gas density	ρ_G	0.5~1.25	kg/m^3	$[ML^{-3}]$
Gas viscosity	μ_G	1.78×10^{-5}	$kg/(m \cdot s)$	$[ML^{-1}T^{-1}]$
Oxygen diffusivity in water	D_{AB}	2.41×10^{-9}	m^2/s	$[L^2T^{-1}]$
Vacuum degree	P	0~0.06	MPa	$[L^{-1}MT^2]$

The basic dimensions of the variables were $[T]$, $[L]$ and $[M]$. According to the Buckingham pi theorem [25], $K_L a$ can be expressed as follows (Equation (4)):

$$Sh = \frac{K_L a R^2}{D_{AB}} = \alpha (Re_L)^\beta (Re_G)^\gamma (Sc_G)^\epsilon (Eu_L)^\theta (Fr_L)^\xi \quad (4)$$

The coefficients of the correlation were obtained by fitting the experimental data to give the following equation (Equation (5)):

$$Sh = 0.99 (Re_L)^{0.69} (Re_G)^{-1.62} (Sc_G)^{-1.41} (Eu_L)^{-0.88} (Fr_L)^{-0.14} \quad (5)$$

As shown in Figure 8, the predicted $K_L a$ values were in agreement with the experimental $K_L a$ values, with deviations generally within 20%. Thus, the correlation can be used to predict $K_L a$ in an RSR.

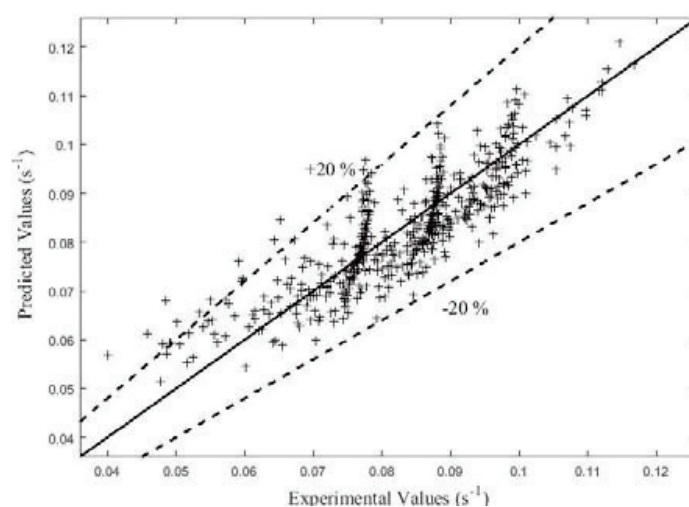


Figure 8. Diagonal graph of experimental and predicted $K_L a$ values.

Table 3 shows that the accuracy of the correlation obtained in this study was similar to that of other studies in the literature. Furthermore, the correlation could predict $K_L a$ at atmospheric pressure as well as at reduced pressure.

Table 3. Comparison of different deoxygenation systems in various high gravity devices.

Reference	This Study	Lin et al.	Guan et al.
System	Vacuum–N ₂ –H ₂ O–O ₂	N ₂ –H ₂ O–O ₂	Vacuum–H ₂ O–O ₂
High gravity device	RSR	RSR	Rotating packed bed
Liquid flow rate, m ³ /h	0.35~0.6	0.75~2.0	0.02~0.10
Gas flow rate, m ³ /h	1~7	1.5~4.0	-
Rotational speed, rpm	200~1400	300~1450	800~1400
Vacuum degree, MPa	0.02~0.06	0	0.08~0.1
Range of mass transfer coefficient, s ⁻¹	0.073~0.098	0.077~0.34	0.031~0.202
Reference	-	[26]	[27]

4. Conclusions

This study employed a coupled vacuum–N₂ technique to remove DO from water in an RSR. The effects of various operating conditions, including the rotational speed, the liquid volumetric flow rate, the gas volumetric flow rate and the vacuum degree, on the values of η and $K_L a$ were investigated. The optimum operating conditions in terms of deoxygenation efficiency and energy consumption were determined as a rotational speed of 600 rpm, a liquid volumetric flow rate of 0.4 m³/h, a gas volumetric flow rate of 3 m³/h and a vacuum degree of 0.06 MPa. Under these conditions, the vacuum–N₂–H₂O–O₂ system achieved values for η and $K_L a$ of 97.34% and 0.0882 s⁻¹, respectively. Additionally, a correlation to predict the $K_L a$ in the RSR was established, and the results show that the predicted values were in agreement with the experimental values, with deviations generally within 20%. These results indicate that the coupled technique carried out in an RSR is a feasible approach to remove DO from water under reasonable operating conditions thanks to the enhanced synergistic effect of nitrogen stripping and vacuum degassing under a high gravity environment.

Author Contributions: Conceptualization, L.S.; methodology, Z.Z.; validation, Z.L.; formal analysis, Y.X.; investigation, Z.Z.; writing—original draft preparation, Z.Z.; writing—review and editing, M.A.; supervision, L.S.; project administration, L.S.; funding acquisition, L.S. All authors have read and agreed to the published version of the manuscript.

Funding: This research was funded by the National Natural Science Foundation of China, grant number 22078009.

Data Availability Statement: Not applicable.

Acknowledgments: The authors gratefully acknowledge the financial support from the National Natural Science Foundation of China (No. 22078009).

Conflicts of Interest: The authors declare no conflict of interest.

Nomenclature

c_M	Total mole concentration of mixture, mol/L
c_{in}	Molar concentration of O ₂ at the liquid inlet of RSR, mol/L
c_{out}	Molar concentration of O ₂ at the liquid outlet of RSR, mol/L
D_{AB}	Oxygen diffusivity in water, m ² /s
Eu_L	Liquid Euler number, $\frac{p}{\rho_L u_L^2}$
Fr_L	Liquid Froude number, $\frac{u_L^2}{\omega^2 R^2}$

G	Liquid volumetric flow rate, m^3/h
g	Gravitational acceleration, m/s^2
H	Height of RSR, m
$K_L a$	Overall volumetric mass transfer coefficient, s^{-1}
L	Liquid volumetric flow rate, m^3/h
m	Phase equilibrium constant of oxygen
n	Rotational speed of RSR, rpm
P	Vacuum degree, MPa
Q_L	Liquid molar flow rate, mol/s
R	Radius of RSR, m
Re_G	Gas Reynolds number, $\frac{R u_G \rho_G}{\mu_G}$
Re_L	Liquid Reynolds number, $\frac{R u_L \rho_L}{\mu_L}$
Sc_G	Gas Schmidt number, $\frac{\mu_G}{\rho_G D_{AB}}$
Sh	Sherwood number, $\frac{K_L a R^2}{D_{AB}}$
T	Temperature, $^{\circ}\text{C}$
u_G	Gas inlet velocity, m/s , $u_G = G / \pi r_G^2$
u_L	Liquid inlet velocity, m/s , $u_L = L / \pi r_L^2$
x	Molar fraction of O_2 in liquid
x_e	Equilibrium molar fraction of O_2 in liquid
x_{in}	Molar fraction of O_2 at the liquid inlet of RSR
x_{out}	Molar fraction of O_2 at the liquid outlet of RSR
$\alpha, \beta, \gamma, \varepsilon, \theta, \zeta$	Fitting coefficients
σ	Liquid surface tension, kg/s^2
η	Deoxygenation efficiency, %
μ_G	Gas viscosity, $\text{kg}/(\text{m}\cdot\text{s})$
μ_L	Liquid viscosity, $\text{kg}/(\text{m}\cdot\text{s})$
ρ_G	Gas density, kg/m^3
ρ_L	Liquid density, kg/m^3
φ	Inlet air humidity, %
ω	Angular velocity of rotor, s^{-1}
[L]	Length dimension
[M]	Mass dimension
[T]	Time dimension
[Θ]	Temperature dimension

References

- Caraman, S.; Luca, L.; Vasiliev, I.; Barbu, M. Optimal-Setpoint-Based Control Strategy of a Wastewater Treatment Process. *Processes* **2020**, *8*, 1203. [[CrossRef](#)]
- Kang, D.; Kim, K. Real Wastewater Treatment Using a Moving Bed and Wastewater-Borne Algal-2. Bacterial Consortia with a Short Hydraulic Retention Time. *Processes* **2021**, *9*, 116. [[CrossRef](#)]
- Abdi, A.; Karimi, A.; Razzaghi, M. Continuously deoxygenation of water in a reactor packed with glucose oxidase immobilized in MnO_2 /calcium alginate composite. *J. Environ. Chem. Eng.* **2016**, *4*, 2356–2361. [[CrossRef](#)]
- Lee, J.; Baek, S.M.; Boo, C.; Son, A.; Jung, H.; Park, S.S.; Hong, S.W. Water deoxygenation using a hollow fiber membrane contactor to prevent pipe corrosion for sustainable management of district heating systems: A pilot-scale study. *J. Clean. Prod.* **2020**, *277*, 124049. [[CrossRef](#)]
- Liang, M.; Yuan, J.; Li, L.; Lai, Z.; Sun, X.; Zhang, H. The preparation of a catalyst doped with Cu and Al on MCM-41 and its catalytic reduction removal of dissolved oxygen in reclaimed water at low temperatures. *New J. Chem.* **2021**, *45*, 11336. [[CrossRef](#)]
- Zekos, I.; Stack, M.M. A note on a design protocol for deoxygenation of water. *Electrochem. Commun.* **2019**, *103*, 12–16. [[CrossRef](#)]
- Jokar, S.; Aghel, B.; Fathi, S.; Karimi, M. Removal of dissolved oxygen from industrial raw water in a microchannel. *Environ. Technol. Innov.* **2021**, *23*, 101672. [[CrossRef](#)]
- Butler, I.B.; Schoonen, M.A.A.; Rickard, D.T. Removal of dissolved oxygen from water: A comparison of four common techniques. *Talanta* **1997**, *41*, 211–215. [[CrossRef](#)]
- Stucki, J.W.; Golden, D.C.; Roth, C.B. Preparation and Handling of Dithionite-Reduced Smectite Suspensions. *Clays Clay Miner.* **1984**, *32*, 191–197. [[CrossRef](#)]
- Mahdizadeh, F.; Eskandarian, M. Glucose oxidase and catalase co-immobilization on biosynthesized nanoporous SiO_2 for removal of dissolved oxygen in water: Corrosion controlling of boilers. *J. Ind. Eng. Chem.* **2014**, *20*, 2378–2383. [[CrossRef](#)]
- Moon, J.S.; Park, K.K.; Kim, J.H.; Seo, G. Reductive removal of dissolved oxygen in water by hydrazine over cobalt oxide catalyst supported on activated carbon fiber. *Appl. Catal. A-Gen.* **2000**, *201*, 81–89. [[CrossRef](#)]

12. Tan, X.; Li, K. Investigation of novel membrane reactors for removal of dissolved oxygen from water. *Chem. Eng. Sci.* **2000**, *55*, 1213–1224. [[CrossRef](#)]
13. Song, Y.H.; Chu, G.W.; Chen, J.M.; Chen, J.F. A Rotor-Stator Reactor and Its Application. Chinese Patent 200410042631.6, 20 December 2006. (In Chinese)
14. Chu, G.W.; Song, Y.H.; Yang, H.J.; Chen, J.M.; Chen, H.; Chen, J.F. Micromixing efficiency of a novel rotor–stator reactor. *Chem. Eng. J.* **2007**, *128*, 191–196. [[CrossRef](#)]
15. Li, Y.; Wang, S.; Sun, B.; Arowo, M.; Zou, H.; Chen, J.; Shao, L. Visual study of liquid flow in a rotor-stator reactor. *Chem. Eng. Sci.* **2015**, *134*, 521–530. [[CrossRef](#)]
16. Zhao, Z.; Sun, B.; Arowo, M.; Chu, G.; Chen, J.; Shao, L. Study on the hydrodynamic characteristics of a rotor-stator reactor by electrical conductance and response time technique. *Chem. Eng. Process.* **2016**, *109*, 158–163. [[CrossRef](#)]
17. Zhao, Z.; Wang, J.; Sun, B.; Arowo, M.; Shao, L. Mass transfer study of water deoxygenation in a rotor–stator reactor based on principal component regression method. *Chem. Eng. Res. Des.* **2018**, *132*, 677–685. [[CrossRef](#)]
18. Li, Y.; Si, J.; Arowo, M.; Liu, Z.; Sun, B.; Song, Y.; Chu, G.; Shao, L. Experimental investigation of effective gas-liquid specific interfacial area in a rotor-stator reactor. *Chem. Eng. Process.* **2020**, *148*, 107801. [[CrossRef](#)]
19. Arowo, M.; Zhao, Z.; Li, G.; Chu, G.; Sun, B.; Shao, L. Ozonation of o-phenylenediamine in the presence of hydrogen peroxide by high gravity technology. *Chin. J. Chem. Eng.* **2018**, *26*, 601–607. [[CrossRef](#)]
20. Zhao, Z.; Wang, L.; Fan, J.; Song, Y.; Chu, G.; Shao, L. Degradation of indigo carmine by coupling Fe(II)-activated sodium persulfate and ozone in a rotor-stator reactor. *Chem. Eng. Process.* **2020**, *148*, 107791. [[CrossRef](#)]
21. Liu, C.; Li, Y.; Zhang, Y.; Zeng, X.; Chen, J.; Shao, L. Synthesis of Ni-CeO₂ nanocatalyst by the microemulsion-gas method in a rotor-stator reactor. *Chem. Eng. Process.* **2018**, *130*, 93–100. [[CrossRef](#)]
22. Feng, Q.; Wang, Y.; Wang, L.; Zhao, W.; Arowo, M.; Shao, L. CO₂ absorption into K₂CO₃/KHCO₃ solution enhanced by organic phase in a rotor-stator reactor. *Sep. Sci. Technol.* **2020**, *55*, 1239–1248. [[CrossRef](#)]
23. Zhao, Z.; Zhang, X.; Li, G.; Chu, G.; Sun, B.; Zou, H.; Arowo, M.; Shao, L. Mass transfer characteristics in a rotor-stator reactor. *Chem. Eng. Technol.* **2017**, *40*, 1078–1083. [[CrossRef](#)]
24. Zhang, D.; Liu, Y.; Xie, W. Preparation of γ -alumina ultrafiltration membrane by Sol–Gel process modified with polyvinyl alcohol. *Membr. Sci. Technol.* **2007**, *27*, 7–10. (In Chinese)
25. Bansal, S.; Roy, S.; Larachi, F. Support vector regression models for trickle bed reactors. *Chem. Eng. J.* **2012**, *207–208*, 822–831. [[CrossRef](#)]
26. Lin, H.; Song, Y.; Chu, G.; Chen, J. Experimental Investigation on Gas-Liquid Mass Transfer Characteristics of Rotor-Stator Reactor. *J. Chem. Eng. Chin. Univ.* **2007**, *5*, 882–886. (In Chinese)
27. Guan, W. Study on Vacuum Deaeration Process in Rotating Packed Bed. Master’s Thesis, Beijing University of Chemical Technology, Beijing, China, 2014. (In Chinese)

MDPI
St. Alban-Anlage 66
4052 Basel
Switzerland
Tel. +41 61 683 77 34
Fax +41 61 302 89 18
www.mdpi.com

Processes Editorial Office
E-mail: processes@mdpi.com
www.mdpi.com/journal/processes



MDPI
St. Alban-Anlage 66
4052 Basel
Switzerland

Tel: +41 61 683 77 34
Fax: +41 61 302 89 18

www.mdpi.com



ISBN 978-3-0365-4156-3